Geoscience BC

ENERGY & WATER

Summary of Activities 2021

Geoscience BC

GEOSCIENCE BC SUMMARY OF ACTIVITIES 2021: ENERGY AND WATER

Geoscience BC Report 2022-02

This publication is also available, free of charge, as colour digital files in Adobe Acrobat® PDF format from the Geoscience BC website: http://www.geosciencebc.com/updates/summary-of-activities/.

Every reasonable effort is made to ensure the accuracy of the information contained in this report, but Geoscience BC does not assume any liability for errors that may occur. Source references are included in the report and the user should verify critical information.

When using information from this publication in other publications or presentations, due acknowledgment should be given to Geoscience BC. The recommended reference is included on the title page of each paper. The complete volume should be referenced as follows:

Geoscience BC (2022): Geoscience BC Summary of Activities 2021: Energy and Water; Geoscience BC, Report 2022-02, 102 p.

Summary of Activities: Energy and Water (Geoscience BC)
Annual publication

ISSN 2562-2757 (Print)
ISSN 2562-2765 (Online)

Geoscience BC
1101–750 West Pender Street
Vancouver, British Columbia V6C 2T7
Canada

Front cover photo and credit: Team from the Geoscience BC–funded GHGMap project prepare to demonstrate the GHGMapper™ aerial drone, which can detect and quantify methane emissions, at a FortisBC gas distribution plant in Metro Vancouver Regional District. Photo by D. Stenzel (March 2021).

Foreword

Geoscience BC is pleased to once again present results from our ongoing projects and scholarship recipients in our annual *Summary of Activities* publication. Papers are published in two separate volumes: *Minerals*, and this volume, *Energy and Water*. Both volumes are available in print and online via www.geosciencebc.com.

Summary of Activities 2021: Energy and Water

This volume, *Summary of Activities 2021: Energy and Water*, contains 10 papers from Geoscience BC–funded projects and scholarship recipients that are within Geoscience BC's strategic focus areas of energy and water. The papers are divided into five sections, based on Geoscience BC's strategic objectives of

1) Identifying New Natural Resource Opportunities,
2) Advancing Science and Innovative Geoscience Technologies,
3) Facilitating Responsible Natural Resource Development,
4) Enabling Clean Energy, and
5) Understanding Water.

In the 'Identifying New Natural Resource Opportunities' section, Wilson et al. introduce a new Geoscience BC project aimed at compiling an initial inventory dataset of lithium and other dissolved-metal brine data for northeastern British Columbia (BC). Zoshi et al. highlight another new project in the 'Advancing Science and Innovative Geoscience Technologies' section; it focuses on a pilot project to test a zero-liquid-discharge technology that could provide BC's oil and gas sector with an economic and sustainable alternative for produced water disposal. Mackie et al. examine the local stratigraphic and facies context that coincides with elevated levels of hydrogen-sulphide distribution within the Montney Formation.

The 'Facilitating Responsible Natural Resource Development' section contains three papers focused on induced seismicity in northeastern BC. Mehrabifard and Eberhardt consider the effects of stiffness on injection-induced seismicity, and Wang et al. develop a model to better understand seismogenic behaviours of injection wells in the Kiskatinaw Seismic Monitoring and Mitigation Area. Esmaeilzadeh and Eaton evaluate the relationship between structural corridors, pressure terranes and geomechanical parameters in the Septimus field.

In the 'Enabling Clean Energy' section, Whiticar and Wiebe summarize the wealth of information now available in the enhanced BC Natural Gas Atlas. Grasby et al. expand earlier geothermal studies in southwestern BC to Mount Cayley, and Hanneson and Unsworth discuss magnetotelluric investigations of geothermal systems in southeastern BC and at Mount Meager. Finally, in the 'Understanding Water' section, Lapp et al. provide an update on collaborative water monitoring work in northeastern BC.

Geoscience BC Energy and Water Publications 2021

Geoscience BC published the following eight Energy and Water reports in 2021:

- Sixteen technical papers in the **Geoscience BC Summary of Activities 2020: Energy and Water** volume (Geoscience BC Report 2021-02)
- **Garibaldi Geothermal Energy Project – Phase 1: Final Report,** by S.E. Grasby, S.M. Ansari, R.W. Barendregt, A. Borch, A. Calahorrano-DiPatre, Z. Chen, J.A. Craven, J. Dettmer, H. Gilbert, C. Hanneson, M. Harris, F. Hormozzade, S. Leiter, J. Liu, M. Muhammad, S.L. Quane, J.K. Russel, R.O. Salvage, G. Savard, V. Tschirhart, M.J. Unsworth, N. Vigouroux-Caillibot, G. Williams-Jones, A. Williamson and Z.E. Vestrum (Geoscience BC Report 2021-08)
- **Assessment of Fugitive Natural Gas on Near-Surface Groundwater Quality,** by B. Ladd, C.J.C. Van De Ven, J. Chao, J. Soares, T. Cary, N. Finke, C. Manning, A.L. Popp, C. Chopra, A.G. Cahill, K.U. Mayer, A. Black, R. Lauer, C. van Geloven, L. Welch, S. Crowe, B. Mayer and R.D. Beckie (Geoscience BC Report 2021-10)
- **Development of an Induced Seismicity Susceptibility Framework and Map for NEBC using an Integrated Machine Learning and Mechanistic Validation Approach,** by A. Amini, A. Mehrabifard and E. Eberhardt (Geoscience BC Report 2021-11)

- **Real-Time Monitoring of Seismic Activity in the Kiskatinaw Area, Northeastern British Columbia (NTS 093P, 094A),** by D.W. Eaton, R.O. Salvage, K. MacDougall, T.H. Swinscoe, J. Dettmer, Z. Esmaeilzadeh, C. Furlong, M. Hamidbeygi, P. Igweze and P. Wozniakowska (Geoscience BC Report 2021-12)
- **Wastewater Disposal in the Maturing Montney Play Fairway of Northeastern British Columbia,** by Petrel Robertson Consulting Ltd. (Geoscience BC Report 2021-14)
- **Peace Region Scientific Groundwater Monitoring Network Installation Study,** by M. Goetz, A.J. Allen, B. Ladd, P.S. Gonzalez, A.G. Cahill, D. Kirste, L. Welch, B. Mayer, C. van Gelovan and R.D. Beckie (Geoscience BC Report 2021-16)
- **Monitoring Induced Seismicity in the Montney, Northeast British Columbia,** by A.M.M. Bustin, D. Jones, G. Chalmers, A. Amini and R.M. Bustin (Geoscience BC Report 2021-18)

All releases of Geoscience BC reports, maps and data are published on our website and announced through our website and e-mail updates. Most final reports and data can be viewed or accessed through our Earth Science Viewer at https://gis.geosciencebc.com/esv/?viewer=esv.

Acknowledgments

Geoscience BC would like to thank all authors and reviewers of the *Summary of Activities* for their contributions to this volume. COVID-19 once again made this a challenging year for all our field programs and laboratory research, and Geoscience BC continues to be grateful for the perseverance of our researchers and scholarship recipients in continuing their projects.

RnD Technical is also acknowledged for its work in editing and assembling both volumes. As well, Geoscience BC would like to acknowledge the Province of British Columbia and our project funding partners for their ongoing support of public geoscience, and express our appreciation for the leaders and volunteers in British Columbia's mineral exploration, mining and energy sectors who support our organization through their guidance, use and recognition of the data and information that we collect and distribute.

Carlos Salas
Chief Scientific Officer
Geoscience BC
www.geosciencebc.com

Contents

Northeastern British Columbia Lithium Formation-Water Database: Forging the Plan, Process and Path (NTS 093P, Parts of 093I, 094A, B, G–J, O, P)

T. Wilson, Canadian Discovery Ltd., Calgary, Alberta, twilson@canadiandiscovery.com

C. Williams, Canadian Discovery Ltd., Calgary, Alberta

E. Pelletier, Matrix Solutions Inc., Calgary, Alberta

D. Murfitt, Matrix Solutions Inc., Calgary, Alberta

K. Rakhit, Canadian Discovery Ltd., Calgary, Alberta

H. Abercrombie, Matrix Solutions Inc., Calgary, Alberta

Wilson, T., Williams, C., Pelletier, E., Murfitt, D., Rakhit, K. and Abercrombie, H. (2022): Northeastern British Columbia lithium formation-water database: forging the plan, process and path (NTS 093P, parts of 093I, 094A, B, G–J, O, P); *in* Geoscience BC Summary of Activities 2021: Energy and Water, Geoscience BC, Report 2022-02, p. 1–8.

Introduction—Forging the Plan

Lithium has garnered significant interest in recent years as it is an essential constituent in lithium-ion batteries—a necessary component in the plan to decarbonize energy infrastructure in the coming decades. Having been deemed a critical mineral for the future clean energy economy (Natural Resources Canada, 2021), it is important to catalogue prospective lithium resources and explore possible synergies with existing oil and gas operations to benefit the forthcoming electrified economy.

Formation waters collected from oil and gas wells have been tested for lithium content but currently only a handful of sites with lithium data exist within the public domain in British Columbia (BC; Eccles and Jean, 2010), compared to the more than 100 and 1500 sites in Saskatchewan and Alberta, respectively (Figure 1; Eccles and Jean, 2010; Jensen, 2012, 2016; Jensen and Rostron, 2017). This sparse BC dataset necessitates additional sampling and analysis of lithium deposits throughout the province to garner a better understanding of lithium concentration and the geological mechanisms driving enrichment. This study, which is a joint venture between Canadian Discovery Ltd. (CDL) and Matrix Solutions Inc. (Matrix), aims to deliver an initial inventory dataset of lithium and other dissolved-metal brine data in northeastern BC through a large-scale sampling program. The study will involve attempts to collect and analyze water samples from approximately 350 to 500 oil and gas wells throughout active oil and gas fields in northeastern BC, targeting key reservoirs from the Cretaceous to Devonian. This foundational dataset will be incorporated into the broader geological context of northeastern BC to reveal preliminary de-risking parameters for future exploration initiatives. This study is currently in its preliminary stages with the initial scoping process completed and the site access negotiations underway with field sampling slated to commence following completion of access agreements. The final report is scheduled to be completed in the spring of 2023. Defining current lithium concentrations and quantities in subsurface brines enables the evaluation of novel resource potential, which will use existing infrastructure and expertise in current operations, while supporting job creation and development in an emerging industry.

This publication is also available, free of charge, as colour digital files in Adobe Acrobat® PDF format from the Geoscience BC website: http://geosciencebc.com/updates/summary-of-activities/.

Background

Lithium occurs naturally in a variety of rock types, brines and groundwater; however, most concentrations are not economic. The content of lithium in the Earth's upper crust has been estimated to be between 20 and 70 ppm by weight (Kamienski et al., 2004). Lithium enrichment occurs in felsic continental crust, with particular appreciations in highly differentiated granites and pegmatites. Lithium brine deposits by contrast are saline groundwater accumulations that are enriched in dissolved lithium, often orders of magnitude higher than background oceanic concentrations of approximately 0.1 ppm. Globally these are present in a variety of settings, such as the Andean salar brines in South America, with concentrations of more than 400 ppm (Kesler et al., 2012), and various formation waters (wastewater) produced during oil and gas or geothermal operations, with concentrations ranging from 10 to 400 ppm (Blondes et al., 2018).

The mechanism of lithium enrichment in brines is not fully understood, but a variety of sources and processes for enrichment have been identified and proposed. These are derived in part from the physical characteristics of lithium, which is exceptionally mobile and has a strong affinity to

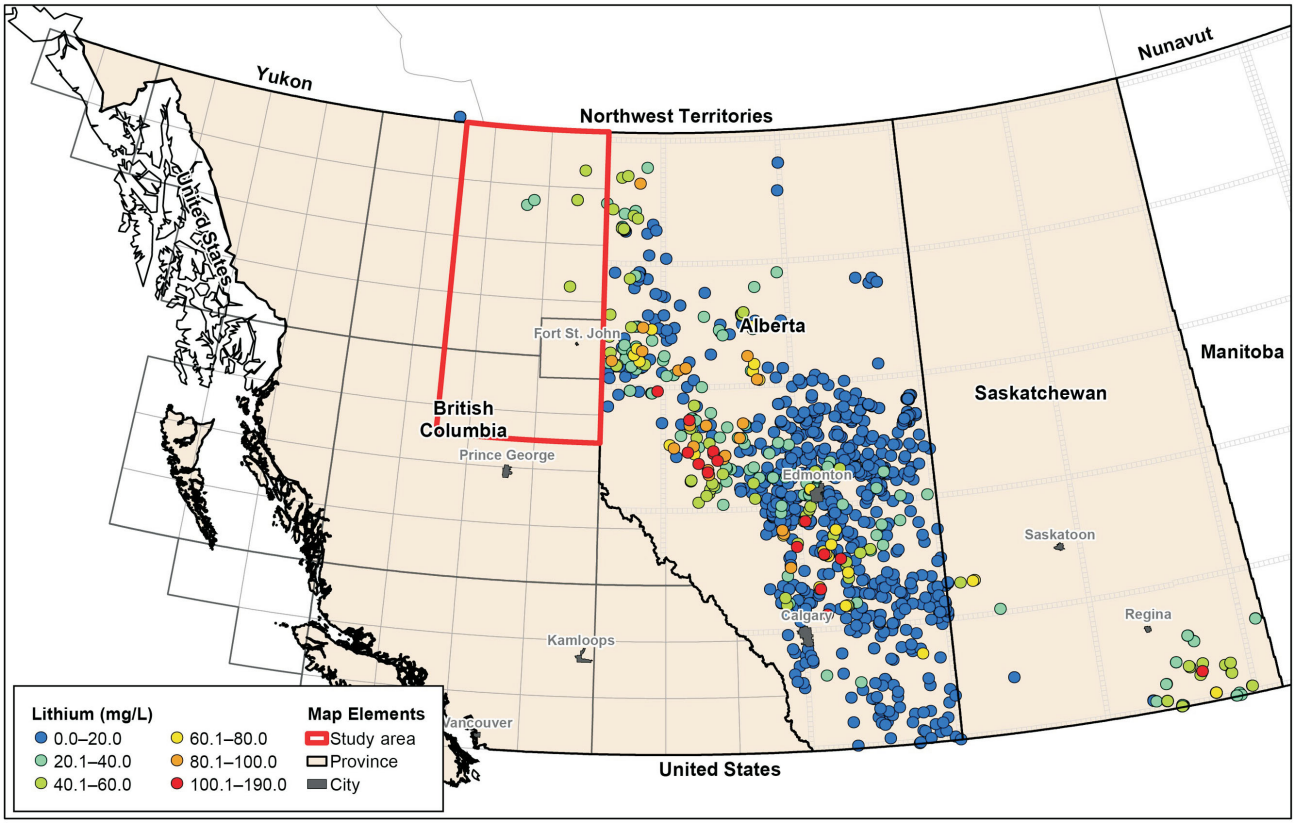

Figure 1. Concentration of lithium in formation waters collected from pre-existing oil and gas wells throughout the Western Canada Sedimentary Basin. Currently, only a handful of lithium data points exist in the study area in northeastern British Columbia (outlined in red; data from Eccles and Jean, 2010), as compared to more than 1600 in Alberta and Saskatchewan (data from Eccles and Jean, 2010; Jensen, 2012, 2016; Jensen and Rostron, 2017).

remain in solution in either magmatic or brine systems (Teng et al., 2004). This property also extends to lithium being preferentially dissolved and stripped away through erosional and/or fluid-rock interactions. Geological criteria have been identified for various lithium-enriched brine deposits and these criteria are evident in northeastern BC, as outlined in Table 1.

Recent efforts in Alberta and Saskatchewan have noted brines enriched in lithium are particularly evident in carbonate-hosted reservoirs subjected to varying degrees of dolomitization and hydrothermal fluid interactions, potentially with a complex brine history (Eccles and Berhane, 2011; Huff, 2016, 2019). Studies in Alberta and Saskatchewan have led to early discoveries and exploration expenditures, with companies such as E3 Metals Corp. (E3 Metals) and Prairie Lithium Corporation (Prairie Lithium) moving to pilot direct lithium extraction (DLE) technologies for lithium brine. As outlined in Table 1, northeastern BC hosts all of the identified geological criteria conducive to lithium enrichment and in some respects presents the potential to host more favourable conditions than Alberta and Saskatchewan. Of additional interest is that northeastern BC benefits from possessing a higher geothermal gradient than other provinces in the Western Canada Sedimentary Basin, and the associated possible synergies with geothermal initiatives.

Projects such as this one address significant gaps in early inventory data and are vital to providing foundational information for research and regulatory and policy development for the exploration and ultimate development of prospective lithium resources in northeastern BC.

Methodology—Forging the Process

This project is the first of its kind in northeastern BC and consists of a three-phase approach, which will take place over the course of approximately 24 months. The three phases include

1) co-ordination and scoping,
   a) project co-ordination, logistics and safety standards,
   b) prospective formation review and high-level scoping of wells to sample,
   c) operator engagement, access negotiations and field logistics,
2) field sampling and data analysis,
   a) field sampling program,
   b) laboratory analysis,
   c) data processing, quality assurance–quality control (QA-QC) and analysis,

Table 1. Geological criteria identified for lithium-enriched brine deposits with examples from northeastern British Columbia (BC).

Geological criteria for potential lithium enrichment (modified from Bradley et al., 2013)	Criteria present in BC?	Examples identified in northeastern BC
Tectonically driven subsidence	✓	Multiple subsidence episodes and tectonic settings, including intracratonic and intraoceanic basins, rifting and continental margins (Nelson and Colpron, 2007)
Associated igneous, volcanic or geothermal activity	✓	High geothermal gradient, generally higher than Alberta and Saskatchewan
Interactions with basement-derived hydrothermal fluids along basement conduit features	✓	Basement structural features such as the Peace River Arch and the Hay River fault zone; the latter of which was the conduit for fluids that led to significant mineralization at the Pine Point Mississippi Valley–type deposit (Nelson and Colpron, 2007)
Proximal felsic bedrock and volcanic terranes weathering into sedimentary basins	✓	Various volcanic and plutonic elements exist in northeastern BC through accreted terranes and igneous intrusions (Goodfellow et al., 1995; Nelson and Colpron, 2007)
Periods of restricted basin conditions and arid to semi-arid paleoclimates where evaporation exceeds precipitation, often recorded by evaporite deposits, which display cyclic brining-upward sequences concentrating lithium into remaining brine fractions	✓	Restricted basin conditions were present during the deposition of the Muskeg Formation; cyclic intervals are noted and thickening is observed along the Hay River fault zone and other subsiding blocks along strike-slip faults (Petrel Robertson Consulting Ltd., 2003)
Presence of adequate aquifer units	✓	Significant reservoir enhancements through hydrothermal dolomitization and solution brecciation (Petrel Robertson Consulting Ltd., 2003)
Sufficient time to allow concentration	✓	Geological history in northeastern BC spans 1.8 Ga; various potential Phanerozoic reservoirs that range in age from Middle Devonian to Late Cretaceous

3) geological interpretation and lithium potential (final report),
   a) incorporate data into the broader geological and hydrogeological framework,
   b) advance the understanding of geological controls and natural variability of lithium in formation waters,
   c) preliminary assessment of aquifer volumes, producibility and economic viability of lithium extraction.

Currently, the project is wrapping up the first phase with project co-ordination and high-level scoping of the targeted aquifers completed and operator engagement underway.

Prospective Formations and High-Level Scoping of Wells

The initial objective was to sample at least 10 to 12 prospective groups/formations/members, but the search was broadened to include over 20 (Figure 2). This broader incorporation ensures limitations, which exist by virtue of limited well numbers in some intervals, are better managed. The intervals span from the Cretaceous to the Devonian and include groups/formations/members of various lithologies. In Alberta and Saskatchewan, the highest lithium concentrations are generally associated with Devonian carbonate rocks, however, exceptions have been noted and this project is intended to provide a first-pass and unbiased fundamental database for northeastern BC.

Active wells have been exported from geoLOGIC systems ltd.'s geoSCOUT for the targeted groups/formations/members, resulting in an initial dataset of 10 299 wells. The Montney Formation alone constitutes nearly 50% of these wells. Figure 3 illustrates the distribution of wells within the study area and the breakdown between oil and gas producers. From the initial dataset, production data was analyzed on a formation-by-formation and field-by-field basis in order to determine wells with relatively high monthly water production and water-gas ratios (WGR). Water production was the main factor considered during initial scoping, as it is imperative the water sample is as representative of true formation water as possible. Newly completed wells were avoided to reduce the probability of sampling flowback water (containing hydraulic fracturing fluid) instead of formation water. The initial 10 299 wells were reviewed and vetted during the scoping process on the basis of water production and spatial and stratigraphic distribution within the study area; the result was a filtered down list of 692 wells. Each formation, where possible, was incorporated into the vetted well list. The distribution of these 692 vetted wells is shown in Figure 4. The goal is to sample approximately 500 of these 692 vetted wells.

Operator Engagement

The success of this project is dependent on the extent of participation from operators within the study area. To facilitate effective communications, concise operator engagement

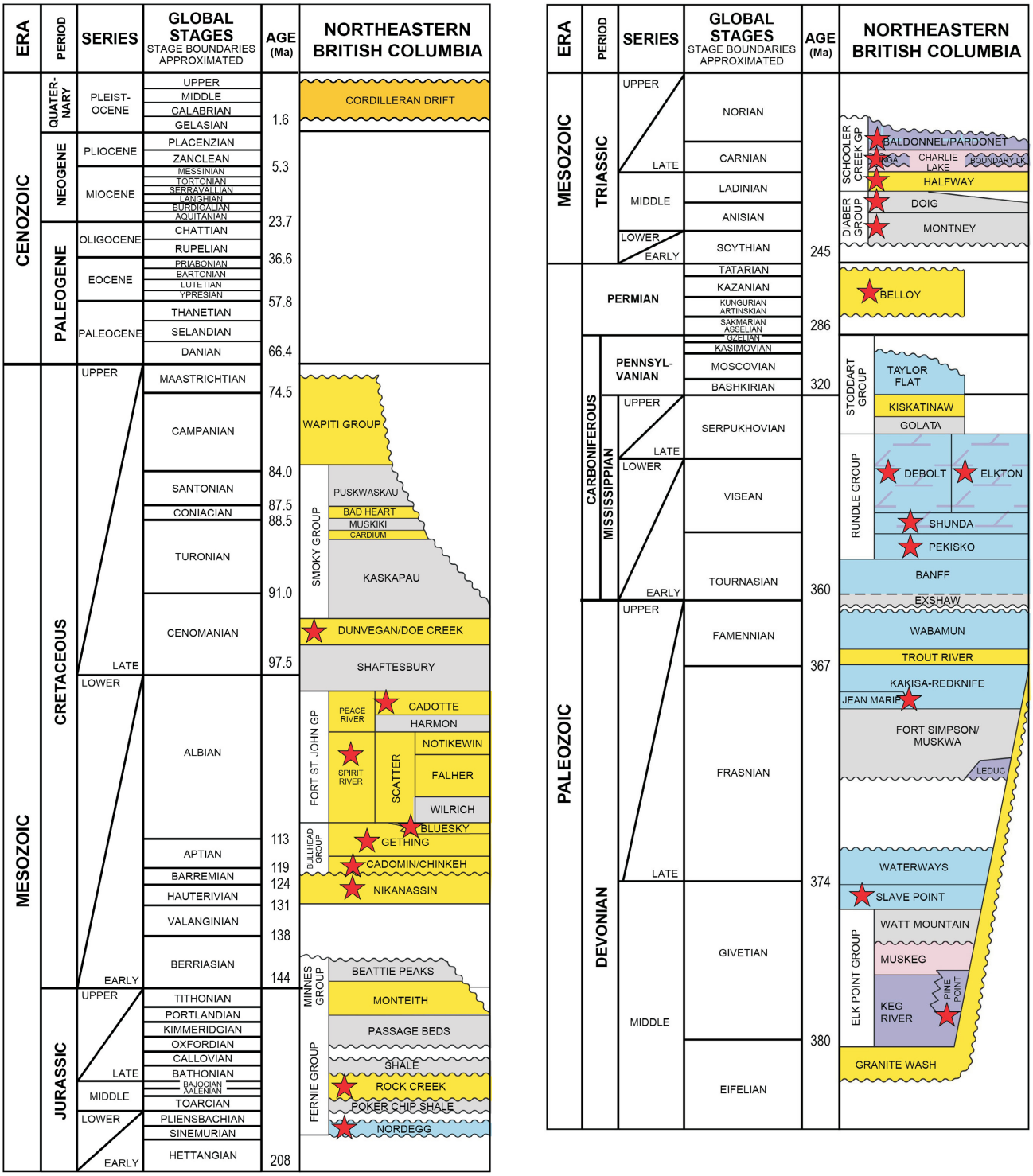

Figure 2. Stratigraphy of northeastern British Columbia (modified and reproduced with permission from Core Laboratories Petroleum Services, 2017). Targeted groups/formations/members are indicated with a star.

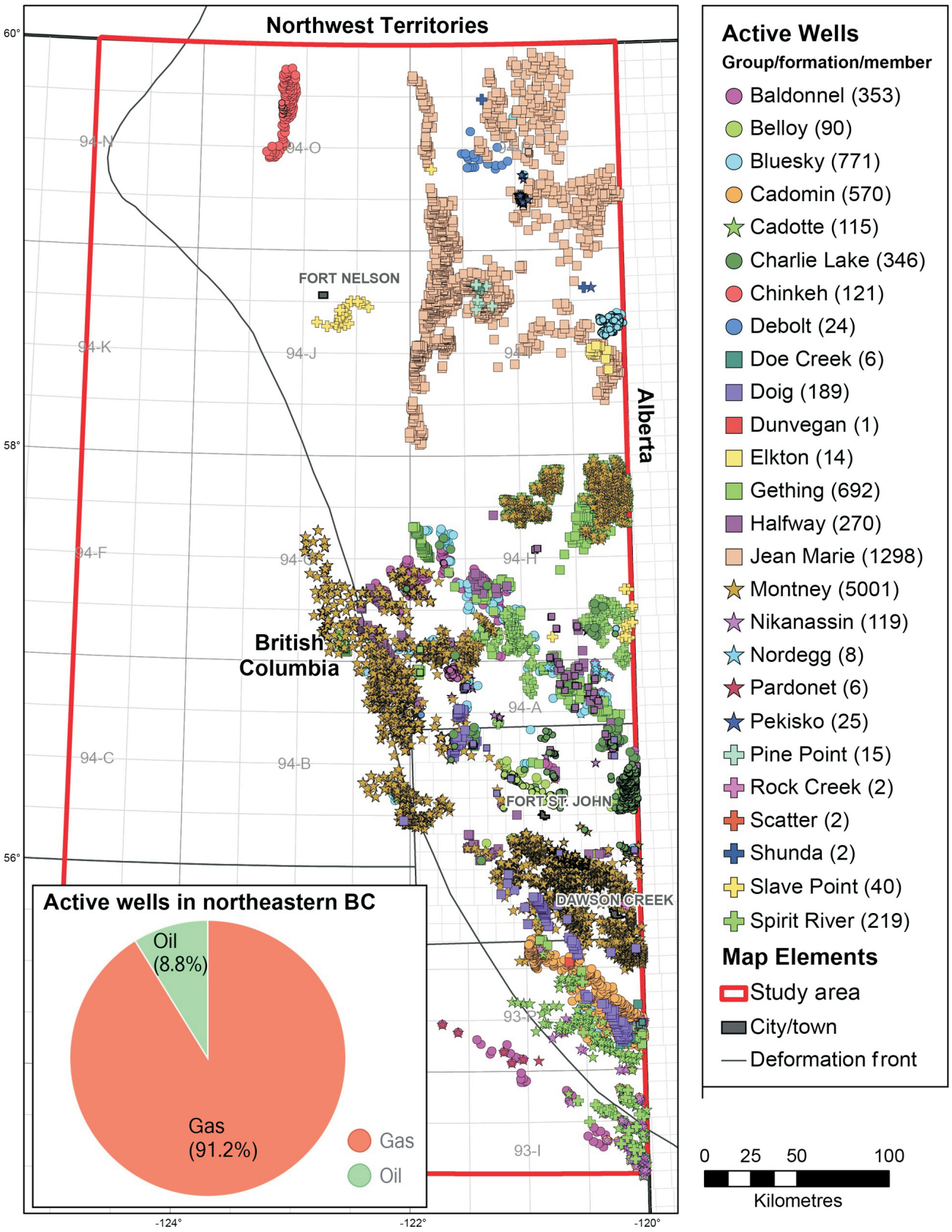

Figure 3. Active oil and gas wells by group/formation/member in northeastern British Columbia (BC; well data supplied by geoLOGIC systems ltd. © 2021). Inset shows breakdown between oil and gas producers.

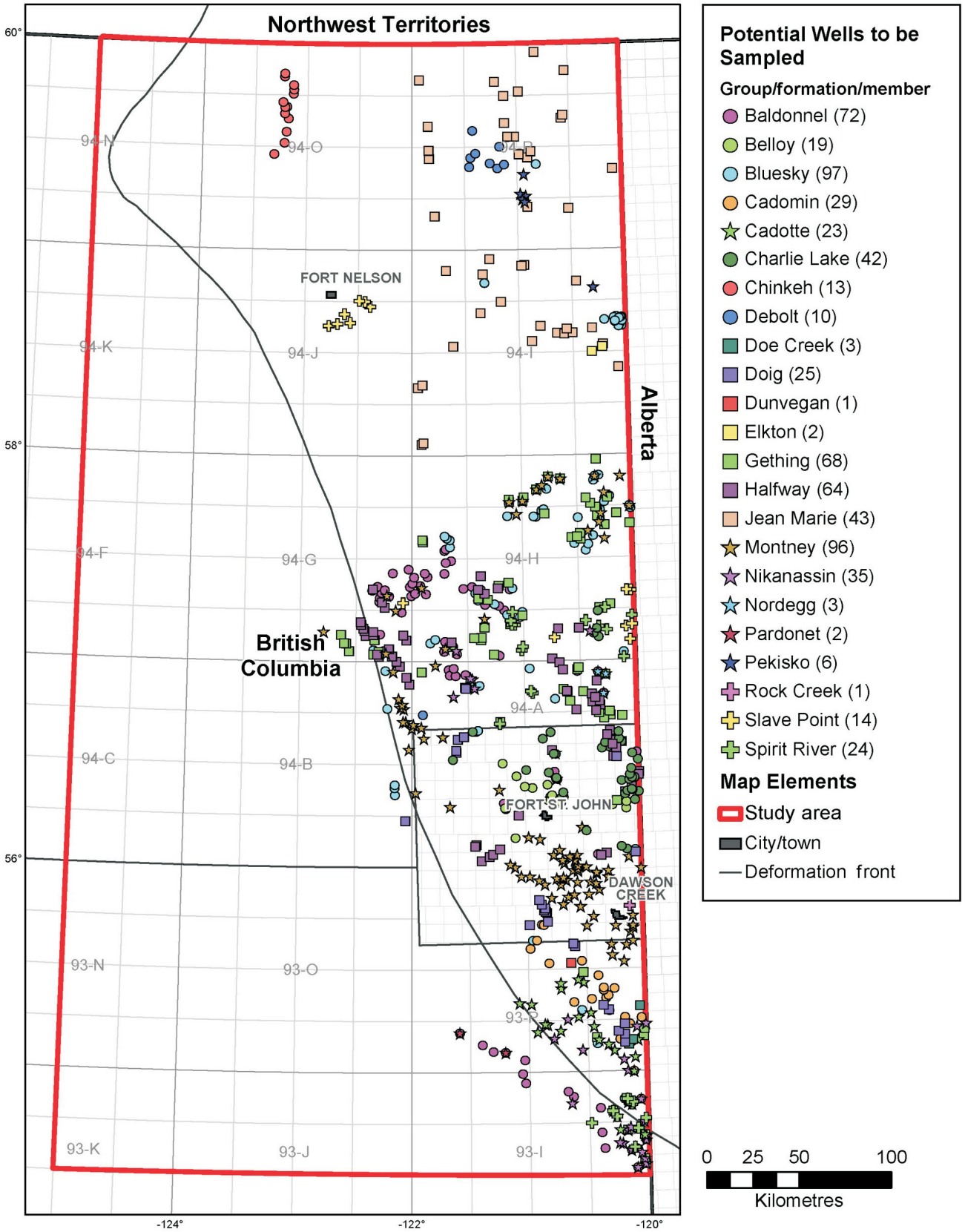

Figure 4. Vetted oil and gas wells by group/formation/member in northeastern British Columbia (well data supplied by geoLOGIC systems ltd. © 2021).

packages have been prepared on an operator and field basis. The purpose of these packages is to provide operators with the necessary information in a digestible form, to help spur further engagement. Project information includes the value proposition for the operators, the vetted list of wells prospective for sampling, an overview of project scope, impact and deliverables, and health and safety procedures. The vetted well lists provided to the operators are not meant to be prescriptive, but rather intended to provide a starting point from which the operators can inform the process based on current operational knowledge and efficiencies.

The list of vetted wells includes nearly 40 different operators. In order to successfully carry out this large undertaking, certain operators have been prioritized, either due to a large inventory of wells or their operations in formations with a low number of completions (such as the Pekisko Formation). At the time of writing, the operator engagement process was underway and will continue in conjunction with the field sampling program, which is expected to start early in 2022. Voluntary submission of existing lithium data is also encouraged to provide a robust lithium database for northeastern BC.

Future Work—Forging the Path Ahead

The next major step in this project is to officially kick off the field sampling program while continuing to engage operators as required. The field sampling will take place between November 2021 and May 2022, and will rely on the expertise of Matrix field staff and the co-operation of operators. Following collection, samples will be sent to a local commercial laboratory for a full suite of water chemistry analyses, including lithium-ion concentration. Routine water analysis includes pH, electrical conductivity, Ca, Mg, Na, K, Fe, SO_4, Cl, Mn, carbonate, bicarbonate, NO_3, NO_2, NO_3+NO_2-N, alkalinity, hardness and calculated total dissolved solids (TDS). The added analysis of dissolved metals will include Al, Sb, As, Ba, Be, Bi, B, Cd, Ca, Cr, Co, Cu, Fe, Pb, Li, Mg, Mn, Mo, Ni, K, Se, Si, Ag, Na, S, Sr, Sn, Tl, Ti, U, V and Zn. Once all samples have been collected and analyzed, CDL will leverage in-house expertise to create a fully vetted water chemistry database, which will be incorporated into the broader geological context of northeastern BC. The final report will include water chemistry mapping, graphical analysis, initial interpretations regarding the geochemical and genetic implications for enrichment of lithium in formation-water brines and preliminary resource calculations.

Characterizing and mapping lithium concentrations is important for the potential use of existing oil and gas infrastructure in the application of DLE. Early examples of such projects are being undertaken by E3 Metals in Alberta and Prairie Lithium in Saskatchewan. The former is advancing a project with average concentrations of 74.6 mg/L over a significant land footprint with preliminary indicated resources of 2.2 million tonnes of lithium carbonate equivalent (LCE) with the potential to support resource development for upward of 20 years (MacMillan et al., 2020). Prairie Lithium successfully piloted a DLE project in 2020 reporting recovery factors of over 99%, which ultimately led to their recent acquisition of 898 km^2 (220,000 acres) of mineral permits (Prairie Lithium Corporation, 2021). The best comparative commercial example would be the Standard Lithium Corporation–LANXESS Corporation joint venture in southern Arkansas, with the largest brine production and processing facilities in North America. This is now the flagship for Standard Lithium Corporation, with over 109 km^2 (27,000 acres) of brine leases in the Smackover formation aiming to produce 20 900 t/yr of lithium carbon equivalent (LCE) over 25 years (Dworzanowski et al., 2019).

Acknowledgments

The authors would like to acknowledge financial support from Geoscience BC, Northern Development Initiative Trust and LithiumBank Resources Corp. along with the technical support of the advisors on this project's Advisory Committee. The authors would also like to thank S. Donaldson at Canadian Discovery Ltd. for taking the time to review this paper.

References

Blondes, M.S., Gans, K.D., Engle, M.A., Kharaka, Y.K., Reidy, M.E., Saraswathula, V., Thordsen, J.J., Rowan, E.L. and Morrissey, E.A. (2018): U.S. Geological Survey national produced waters geochemical database (ver. 2.3, January 2018); U.S. Geological Survey, data release, URL <https://doi.org/10.5066/F7J964W8>.

Bradley, D., Munk, L., Jochens, H., Hynek, S. and Labay, K.A. (2013): A preliminary deposit model for lithium brines; U.S. Geological Survey, Open-File Report 2013-1006, 9 p., URL <https://pubs.usgs.gov/of/2013/1006/OF13-1006.pdf> [September 2017].

Core Laboratories Petroleum Services (2017): Stratigraphic correlation chart; Core Laboratories Petroleum Services, Geological Sciences Department, 1 p., URL <https://www.spec2000.net/downloads/StratChart.pdf> [March 2021].

Dworzanowski, M., Eccles, D.R. and Kotowski, S. (2019): Preliminary economic assessment of LANXESS Smackover project; NI 43-101 report prepared by Worley for Standard Lithium Ltd., 230 p.

Eccles, D.R. and Berhane, H. (2011): Geological introduction to lithium-rich formation water with emphasis on the Fox Creek area of west-central Alberta (NTS 83F and 83K); Energy Resources Conservation Board, ERCB/AGS Report 2011-10, 28 p.

Eccles, D.R. and Jean, G.M. (2010): Lithium groundwater and formation-water geochemical data (tabular data, tab delimited format); Energy Resources Conservation Board, ERCB/AGS Digital Data 2010-0001, URL <https://ags.aer.ca/publication/dig-2010-0001> [March 2021].

Goodfellow, W.D., Cecile, M.P. and Leybourne, M.I. (1995): Geochemistry, petrogenesis, and tectonic setting of lower Paleozoic alkalic and potassic volcanic rocks, Northern Canadian Cordilleran Miogeocline; Canadian Journal of Earth Sciences, v. 32, p. 1236–1254.

Huff, G.F. (2016): Evolution of Li-enriched oilfield brines in Devonian carbonates of the south-central Alberta Basin, Canada; Bulletin of Canadian Petroleum Geology, v. 64, p. 438–448.

Huff, G.F. (2019): Origin and Li-enrichment of selected oilfield brines in the Alberta Basin, Canada; Alberta Energy Regulator/Alberta Geological Survey, AER/AGS Open File Report 2019-01, 35 p.

Jensen, G.K.S. (2012): Initial results of a brine sampling project: investigating the mineral potential of brines in southeastern Saskatchewan; *in* Summary of Investigations 2012, Volume 1, Saskatchewan Geological Survey, Saskatchewan Ministry of the Economy, Miscellaneous Report 2012-4.1, Paper A-8, 8 p.

Jensen, G.K.S. (2016): Results from the 2016 field season for the brine sampling project: investigating the mineral potential of brines in Saskatchewan; *in* Summary of Investigations 2016, Volume 1, Saskatchewan Geological Survey, Saskatchewan Ministry of the Economy, Miscellaneous Report 2016-4.1, Paper A-3, 7 p.

Jensen, G.K.S. and Rostron, B. (2017): Investigating the mineral potential of brines in Saskatchewan: results from the 2017 field season for the brine sampling project; *in* Summary of Investigations 2017, Volume 1, Saskatchewan Geological Survey, Saskatchewan Ministry of the Economy, Miscellaneous Report 2017-4.1, Paper A-1, 6 p.

Kamienski, C.W., McDonald, D.P., Stark, M.W. and Papcun, J.R. (2004): Lithium and lithium compounds; *in* Kirk-Othmer Encyclopedia of Chemical Technology, American Cancer Society, 40 p.

Kesler, S.E., Gruber, P.W., Medina, P.A., Keoleian, G.A., Everson, M.P. and Wallington, T.J. (2012): Global lithium resources: relative importance of pegmatite, brine and other deposits; Ore Geology Reviews, v. 48, p. 55–69, URL <https://dx.doi.org/10.1016/j.oregeorev.2012.05.006>.

MacMillan, G., Vorster, W., Bransby-Williams, D., Pattinson, S. and Owen, G. (2020): Preliminary economic assessment Clearwater Lithium Project; NI-43-101 report prepared for E3 Metals Corp., 169 p.

Natural Resources Canada (2021): Canada announces critical minerals list; Natural Resources Canada, news release, March 11, 2021, URL <https://www.canada.ca/en/natural-resources-canada/news/2021/03/canada-announces-critical-minerals-list.html> [May 2021].

Nelson, J. and Colpron, M. (2007): Tectonics and metallogeny of the British Columbia, Yukon and Alaskan Cordillera, 1.8 Ga to the present; *in* Mineral Deposits of Canada: A Synthesis of Major Deposit-Types, District Metallogeny, the Evolution of Geological Provinces, and Exploration Methods, W.D. Goodfellow (ed.), Geological Association of Canada, Mineral Deposits Division, Special Publication no. 5, p. 755–791.

Petrel Robertson Consulting Ltd. (2003): Exploration assessment of deep Devonian gas plays; BC Ministry of Energy, Mines and Low Carbon Innovation, Oil and Gas Report 2003-1, 48 p.

Prairie Lithium Corporation (2021): Prairie Lithium validates 99.7% lithium extraction from brine in 5 minutes; Prairie Lithium Corporation, press release, May 19, 2021, URL <https://www.businesswire.com/news/home/20210519005239/en/Prairie-Lithium-Validates-99.7-Lithium-Extraction-From-Brine-in-5-Minutes> [November 2021].

Teng, F.Z., McDonough, W.F., Rudnick, R.L., Dalpé, C., Tomascak, P.B., Chappell, B.W. and Gao, S. (2004): Lithium isotopic composition and concentration of the upper continental crust; Geochimica et Cosmochimica Acta, v. 68, p. 4167–4178.

Novel Zero-Liquid-Discharge Pilot Project for Produced Water Management, Northeastern British Columbia

J. Zoshi, Saltworks Technologies Inc., Richmond, British Columbia, joshua.zoshi@saltworkstech.com

B. Sparrow, Saltworks Technologies Inc., Richmond, British Columbia

H. Tsin, Saltworks Technologies Inc., Richmond, British Columbia

Zoshi, J., Sparrow, B. and Tsin, H. (2022): Novel zero-liquid-discharge pilot project for produced water management, northeastern British Columbia; *in* Geoscience BC Summary of Activities 2021: Energy and Water, Geoscience BC, Report 2022-02, p. 9–12.

Introduction

Canada's Montney play is one of the richest shale gas plays in North America. On its British Columbian (BC) side, however, tight geology limits disposal zones for produced water. Operators reuse produced water where possible but when in excess they often resort to deep disposal underground. As shale gas extraction increases, reuse opportunities diminish and the disposal capability of northeastern BC's geology is forecasted to become more stressed. Saltworks Technologies Inc. (Saltworks) is presently advancing a project to pilot test a novel zero-liquid-discharge (ZLD) technology aimed at providing BC's oil and gas sector with an economic and sustainable alternative for produced water disposal.

BC Produced Water Disposal Management

On the BC side of the Montney play, tight geology closer to the Rocky Mountains results in limited access and reliability of Class II disposal wells for produced water. The cost to permit and install new disposal wells is substantial and, where possible, operators are reusing and sharing flowback and produced waters in order to reduce operating costs. However, where that is not possible, produced water must be disposed of, either by ponding or trucking to neighbouring disposal wells (Kniewasser and Riehl, 2018). Ponds present containment failure risk and a potential hazard to waterfowl, whereas trucking, the primary disposal method, is greenhouse-gas (GHG) intensive and involves land disturbance and the risk of spills. Conventional evaporators for concentrating produced water to reduce volume prior to trucked disposal have been trialed in shale plays other than the Montney play. However, they have not been widely adopted due to a typical feed water salinity limit of 20% salt by mass (below that of many produced waters), corrosion and resulting reliability challenges, and hazardous air emissions of volatile organic compounds (VOCs), such as benzene, common in produced waters. Another challenge with concentrating produced water is the increased risk of causing scaling in disposal wells. As BC's oil and gas sector continues to grow, disposal well capacity is likely to become more constrained and concentrated produced waters are less likely to find disposal outlets in a supply constrained market (Petrel Robertson Consulting Ltd., 2021).

Salt Reuse Opportunity

On average, 5 million tonnes of road salt are used each year in Canada (Environment and Climate Change Canada, 2018). In BC, sodium chloride is used for road salting, bleach production in the pulp and paper industry and chlor-alkali chemical production, but BC is not a producer of sodium chloride and must import it (WaterSMART Solutions Ltd., 2012). Salt transportation contributes to GHG emissions. Analysis of BC Montney play water samples performed by Saltworks (Richmond, BC) showed $10–30 of recoverable salt per cubic metre of produced water, a relatively small mass of contaminants requiring removal to enable reuse, and dissolved components comprising approximately 95% sodium chloride and calcium chloride, the primary constituents of road salt (Transportation Association of Canada, 2013).

The Case for Zero Liquid Discharge

A safe, economic and reliable ZLD solution could be an effective means of preserving BC's disposal well capacity while reducing the environmental impacts associated with existing produced water handling methods. The ZLD treatment of produced water provides the following benefits: it significantly reduces GHG-intensive truck hauling by transporting a much smaller relative volume of solid salt for reuse or landfill; it avoids potential scaling of disposal wells by concentrated fluids; and it debottlenecks production constrained by disposal and pond concentration limits. In addition, reusing residual salt for local consumption can further offset costs of treatment and disposal, enabling a circular economy. The ZLD technology is equally applicable to mining and manufacturing industries, enabling further economic and environmental benefits.

This publication is also available, free of charge, as colour digital files in Adobe Acrobat® PDF format from the Geoscience BC website: http://geosciencebc.com/updates/summary-of-activities/.

Table 1. Results of AirBreather pilot plant testing completed in the Marcellus shale basin, northern Pennsylvania. Abbreviation: n.d., no data.

Pilot test	1	2
Uptime (%)	97	96
Feed water - total dissolved solids (TDS; mg/L average)	210 667	326 333
Feed water - benzene, toluene, ethylbenzene and xylene (BTEX; ug/L)	823	n.d.
Concentrated brine - TDS (mg/L average)	391 333	384 333
Treated water - TDS (mg/L average)	367	90
Treated water - BTEX (ug/L)	n.d.	n.d.
Volume reduction factor (average)	1.93	1.18

Novel ZLD Technology

Saltworks has developed a novel thermal evaporator-crystallizer technology, trade named 'AirBreather', designed to overcome the limitations of conventional evaporators. The novel technology is compatible with waters having over 20% salt mass, achieves 100% liquid volume reduction by crystallizing and extracting solids, uses waste heat to offset input thermal energy and employs corrosion-proof wetted components. Its key differentiator from commercially available evaporators is its novel air emissions management process, which mitigates the release of VOCs through zero contact of saline water with atmospheric air. Beneficially, and unlike conventional open-to-air evaporators, no vapour plume is produced.

Initial modelling by Saltworks estimates that a system sized to evaporate 100 m^3/day that reduces the concentration of salt in produced water from 20 to 40% by mass prior to disposal could offset 940 t CO_2e per year, compared to hauling unconcentrated produced water by truck[2]. The authors estimate the novel technology operated as a ZLD solution will further reduce trucking by up to 75% (one truck equivalent moving solid salt for reuse or to a landfill instead of four trucks hauling concentrated produced water for disposal).

Previous Work

The novel technology has been successfully tested at a prototype scale, producing solid salt from nonsynthetic wastewaters from industrial applications, including oil and gas and manufacturing. A containerized pilot plant with 0.3 m^3/day capacity was built (Figure 1) and two successful onsite tests were completed in the Marcellus shale basin, northern Pennsylvania (Figure 2), concentrating live produced water into a more concentrated brine (Table 1). The pilot plant generated treated water that met local surface discharge (Centralized Waste Treatment Effluent Guidelines [United States Environmental Protection Agency, 2020]) and air emissions criteria (National Emission Stan-

Figure 1. Interior of the main processing equipment container at AirBreather pilot plant, Marcellus shale basin, northern Pennsylvania.

Figure 2. AirBreather pilot plant consisting of two 12.2 m (40 ft.), International Organization for Standardization (ISO), shipping container units, Marcellus shale basin, northern Pennsylvania.

[2] *AirBreather GHG offset calculations are based on a truck round trip distance of 150 km, 135.25 g CO_2e/tonne-km emission factor, produced water density of 1100 kg/m^3 and concentrated brine density of 1200 kg/m^3.*

dards for Hazardous Air Pollutants [United States Environmental Protection Agency, 2021]), making it the first process to receive a full-scale permit in a challenging jurisdiction where previous open-to-air evaporation systems failed to meet air emission requirements. In separate testing, Saltworks produced salt meeting BC road salt specifications from Montney play produced water, without trace deleterious elements (the firm has technology to remove naturally occurring radioactive materials [NORM]).

Present Project

A project is presently underway to adapt the novel technology for ZLD treatment of produced water. The project's goals are to de-risk a full-scale implementation and enable a future alternative for produced water management in BC's oil and gas sector. The project is supported by Geoscience BC, the Natural Gas Innovation Fund, Sustainable Development Technology Canada and industry partners.

Project objectives include i) upgrading pilot plant systems to enable ZLD operation on produced water; ii) producing solid salt from live produced water supplied by industry partners while meeting water discharge and air emissions requirements; iii) producing industrially reusable salt; and iv) mapping the economics of the total process, including the salt reuse market potential.

Upgrades to the pilot project include adding an upstream NORM management subsystem, a downstream solids management system and modifications to mechanical, electrical and control systems. The project draws on lessons learned from past industrial water treatment technology development and solid salt production experience by Saltworks. Project activities are presently underway at Saltworks' Richmond, BC, facility.

Completed Activities

The following activities have been completed:

- design of mechanical, electrical and control systems required for ZLD operation;
- installation and integration of ZLD-specific components into the pilot plant, including additional tanks, pump skids, electrical systems, and solids containment and handling equipment (Figure 3);
- checks and calibrations of transmitters and sensors, mechanical systems and safety systems;
- establishment of maintenance procedures, spare parts and wear component lists and kits; and
- commissioning with fresh water, including thermal start-up and testing of pretreatment, NORM and VOC subsystems.

Current Activities

Six batches of Montney play produced water totalling 6000 L were received from industry partners (Figure 4) and are presently undergoing independent lab analysis. The upgraded pilot plant is now ready to produce, in successive stages: treated produced water without NORM; distilled water extracted from produced water; VOC-treated distilled water for evaporation and release; and solid salt for beneficial reuse. The pilot plant will also produce waste in trace amounts: solids from selective precipitation and separation of NORM (dependent on water chemistry) and sludge from removal of VOCs.

Remaining Activities

Remaining project activities include developing pilot plant testing procedures and performing ZLD testing on each batch of water. In parallel to the testing, pilot plant process control tuning and additional component upgrades will be

Figure 3. AirBreather pilot solids management subsystem showing centrifuge (left) and process tank (right).

Figure 4. British Columbia Montney play produced water received from industry partners.

performed as necessary and following learnings from the testing procedures. Final activities include results analysis and reporting, analysis of solid salt produced and updating the economic model for full-scale implementation and salt reuse.

Summary

As British Columbia's natural gas sector grows and produced water disposal becomes more challenging, an economic and green alternative for produced water management could be made available to the sector. As a zero-liquid-discharge solution, novel AirBreather evaporator-crystallizer technology has the potential to preserve disposal well capacity, while reducing costs and greenhouse gas emissions associated with trucked wastewater hauling, and enabling a circular economy through industrial salt reuse.

Acknowledgments

Funding for this project was provided by Geoscience BC, the Natural Gas Innovation Fund and Sustainable Development Technology Canada. The authors would like to thank the industrial project partners for providing representative waters, technical advice and guidance for the project. The authors also thank M. Man for his review of this submission.

References

Environment and Climate Change Canada (2018): Code of practice: road salts environmental management; Environment and Climate Change Canada, URL <https://www.canada.ca/en/environment-climate-change/services/pollutants/road-salts/code-practice-environmental-management.html> [October 2018].

Kniewasser, M. and Riehl, B. (2018): Risks to water and public health from unconventional gas in B.C.: a review of new research on hydraulic fracturing impacts; The Pembina Institute, 19 p., URL <https://www.pembina.org/reports/unconventional-natural-gas-water-risks-2018.pdf> [May 2018].

Petrel Robertson Consulting Ltd. (2021): Wastewater disposal in the maturing Montney play fairway of northeastern British Columbia; Geoscience BC, Report 2021-14, 237 p., URL <http://www.geosciencebc.com/i/project_data/GBCReport2021-14/GBCR%202021-14%20Wastewater%20Disposal%20in%20the%20Maturing%20Montney%20Play%20Fairway%20of%20NEBC.pdf> [November 2021].

Transportation Association of Canada (2013): Syntheses of best practices - road salt management; Transportation Association of Canada, 6 p., URL <https://www.tac-atc.ca/sites/tac-atc.ca/files/site/doc/resources/roadsalt-1.pdf> [April 2013].

United States Environmental Protection Agency (2020): Centralized Waste Treatment Effluent Guidelines; United States Environmental Agency, URL <https://www.epa.gov/eg/centralized-waste-treatment-effluent-guidelines> [April 2021].

United States Environmental Protection Agency (2021): National Emission Standards for Hazardous Air Pollutants; United States Environmental Protection Agency, URL <https://www.epa.gov/stationary-sources-air-pollution/national-emission-standards-hazardous-air-pollutants-neshap-9> [April 2021].

WaterSMART Solutions Ltd. (2012): Sodium chloride market: an overview of the sodium chloride (salt) market in western Canada (v.02); Oil Sands Leadership Initiative, 20 p., URL <https://content.energy.alberta.ca/xdata/IETP/IETP%202012/06-098%20Water%20Mgmt.%20Through%20Water%20Treatment%20Technologies/Appendices/APPENDIX%20H_OWM-MD-Salt%20Market%20Study-v02%20(2012-12-21)%20(2).pdf> [December 2012].

Relation of Stratigraphy and Facies Heterogeneities to Hydrogen Sulphide Distribution in the Montney Formation of Northeastern British Columbia (Parts of NTS 093, 094)

S.J. Mackie[1], **Department of Geoscience, University of Calgary, Calgary, Alberta, samantha.mackie@ucalgary.ca**

C.M. Furlong, Department of Geoscience, University of Calgary, Calgary, Alberta

P.K. Pedersen, Department of Geoscience, University of Calgary, Calgary, Alberta

O.H. Ardakani, Natural Resources Canada, Geological Survey of Canada–Calgary, Alberta

Mackie, S.J., Furlong, C.M., Pedersen, P.K. and Ardakani, O.H. (2022): Relation of stratigraphy and facies heterogeneities to hydrogen sulphide distribution in the Montney Formation of northeastern British Columbia (parts of NTS 093, 094); *in* Geoscience BC Summary of Activities 2021: Energy and Water, Geoscience BC, Report 2022-02, p. 13–22.

Introduction

The Lower Triassic Montney Formation within the Western Canada Sedimentary Basin (WCSB) is a prolific hydrocarbon reservoir hosting 12 719 billion m^3 (449 tcf) of natural gas, 2308 million m^3 (14 521 million barrels) of natural-gas liquids and 179 million m^3 (1125 million barrels) of oil (National Energy Board et al., 2013). Within Triassic reservoirs of the WCSB, the hydrogen sulphide (H_2S) content of sour gas, which is a highly corrosive and toxic gas leading to costly safety, environmental, and production measures, can range from less than 1 to up to 29% (Kirste et al., 1997; Desrocher et al., 2004). There is a range of processes that can generate H_2S, including thermochemical sulphate reduction (TSR), microbial sulphate reduction and thermal chemical alteration of organic matter in oil or kerogen (Orr, 1977; Worden and Smalley, 1996; Machel, 2001). In most sour gas reservoirs globally, sulphate-rich fluids dissolved from evaporite minerals are a key contributor to H_2S gas formation (Hutcheon et al., 1995; Machel et al., 1995; Worden and Smalley, 1996).

Within the Montney Formation, previous studies have interpreted the source of the dissolved sulphate contributing to the H_2S as evaporite beds in the overlying Charlie Lake Formation (Kirste et al., 1997; Desrocher et al., 2004; Chalmers et al., 2021). Earlier studies (Kirste et al., 1997; Desrocher et al., 2004) focused on H_2S-gas stable isotope geochemistry and did not account for the diagenetic process associated with the dissolved sulphate. Recent studies have re-evaluated Montney Formation H_2S sourcing by examining sulphate minerals associated with H_2S generation and found a mix of both Devonian and Triassic isotopic signatures (Liseroudi et al., 2020, 2021; Chalmers et al., 2021). The samples in these studies from northeastern British Columbia (BC) were selected to primarily focus investigations on the Upper Montney, with limited data from the Middle Montney or Lower Montney (Liseroudi et al., 2020, 2021; Chalmers et al., 2021). A recent study integrating stratigraphy and sulphur-isotope geochemistry highlighted the complex diagenetic history of the Montney, which is laterally discontinuous and highly variable regionally (Kingston et al., 2021). Local, detailed intramember stratigraphy or facies associated with each sample were not considered within the scope of these studies. However, local stratigraphy and the distribution of facies have been shown to influence reservoir properties (Wood, 2013; Wood and Sanei, 2016) and, likely, H_2S distribution. Previously mapped updip Montney gas-migration fairways (Wood and Sanei, 2016; Sereda and Fur, 2017; Euzen et al., 2019, 2021) may additionally impact elevated H_2S occurrences. The aim of this study is to better understand the local stratigraphic and facies context that coincides with elevated levels of H_2S distribution within the Montney Formation of northeastern BC (Figure 1) and to further build upon this by integrating and comparing the outcome with other Montney fluid-distribution studies.

Geological Background

The Lower Triassic Montney Formation unconformably overlies the Paleozoic Belloy Formation and is in turn unconformably overlain by either the Sunset Prairie Formation or Doig phosphate zone in northeastern BC (Armitage, 1962; Furlong et al., 2018a, b; Zonneveld and Moslow, 2018). The Montney Formation consists of a westward-thickening wedge of dolomitic siltstone, sandstone and bioclastic-rich intervals, which represent deposition within the lower shoreface, offshore transition and offshore marine environments (Davies et al., 1997; Davies et al.,

[1]*The lead author is a 2021 Geoscience BC Scholarship recipient.*

This publication is also available, free of charge, as colour digital files in Adobe Acrobat® PDF format from the Geoscience BC website: http://geosciencebc.com/updates/summary-of-activities/.

2018; Zonneveld and Moslow, 2018). Regionally, there are three Montney members, the Lower Montney, Middle Montney and Upper Montney, which are well-established third-order sequences, recording an overall westward progradation of the Montney over time (Davies et al., 1997; Crombez et al., 2016; Zonneveld and Moslow, 2018). Overlying the Montney, is the Middle Triassic Sunset Prairie Formation (a mixed siliciclastic-carbonate interval), Doig phosphate zone (a phosphate-rich interval at the base of the Doig Formation), Doig Formation (clastic offshore to shoreface succession) and Halfway Formation (clastic shoreface succession; Figure 2; Armitage, 1962; Furlong et al., 2018a, b). Stratigraphically above the Middle Triassic formations lies the Upper Triassic Charlie Lake Formation, which consists of a series of evaporitic deposits (Hunt and Ratcliffe, 1959; Armitage, 1962) emplaced during a tectonically active time, as evidenced by the presence of the angular Coplin unconformity (Davies, 1997). The Triassic represents an overall regression event as the paleoshoreline moves westward through time, with the youngest Triassic sediments being eroded before deposition of the Jurassic Fernie Formation (Armitage, 1962).

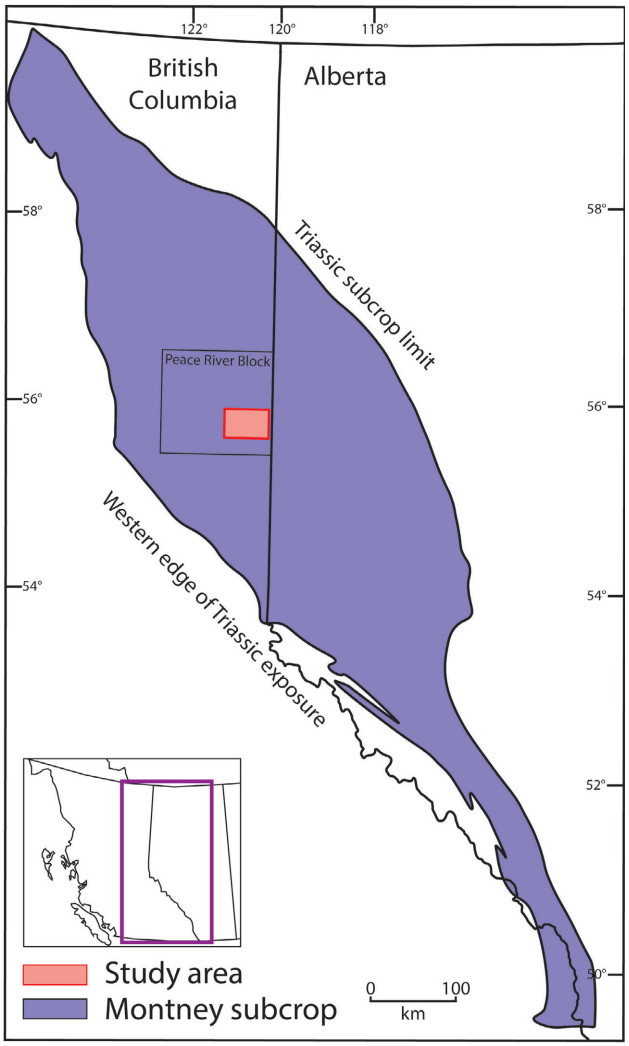

Figure 1. Location of the study area in northeastern British Columbia (modified from Wood and Sanei, 2016).

Study Area and Methodology

The area studied in this research is in northeastern BC, within the Peace River block, spanning from Twp. 79 to 81, Rge. 14 to 18 W 6th Mer. (Figure 3). This study area was selected based on the availability of a relatively dense dataset of Montney wells, a well-established structural history and the presence of varied H_2S concentrations within the different Montney members. Within this study area, the Montney Formation unconformably overlies the Paleozoic Belloy Formation and unconformably underlies the Sunset Prairie Formation (Furlong et al., 2018a, b).

Within the northeastern BC study area, 865 vertical wells penetrate the Montney Formation and 1656 lateral wells produce from the Montney Formation. Using these wells logs, a regional stratigraphic framework was established with the Lower Montney, lower Middle Montney, upper Middle Montney, and Upper Montney units by picking tops, guided by previous work by Davies et al. (2018), Euzen et al. (2018), Proverbs et al. (2018), Zonneveld and Moslow (2018) and Furlong et al. (2021). Once the regional Montney stratigraphy was established, parasequences within individual Montney units were initially selected based on coarsening-upward trends within the core, which were tied to wireline-log signatures, then correlated and extrapolated throughout the study area. Depending on

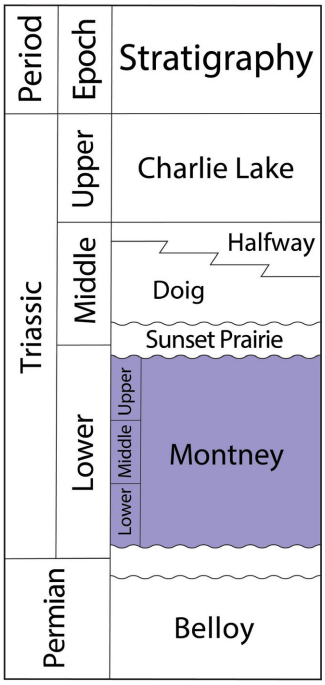

Figure 2. Stratigraphic column of the Montney Formation and surrounding formations in northeastern British Columbia (modified from Furlong et al., 2018a, b).

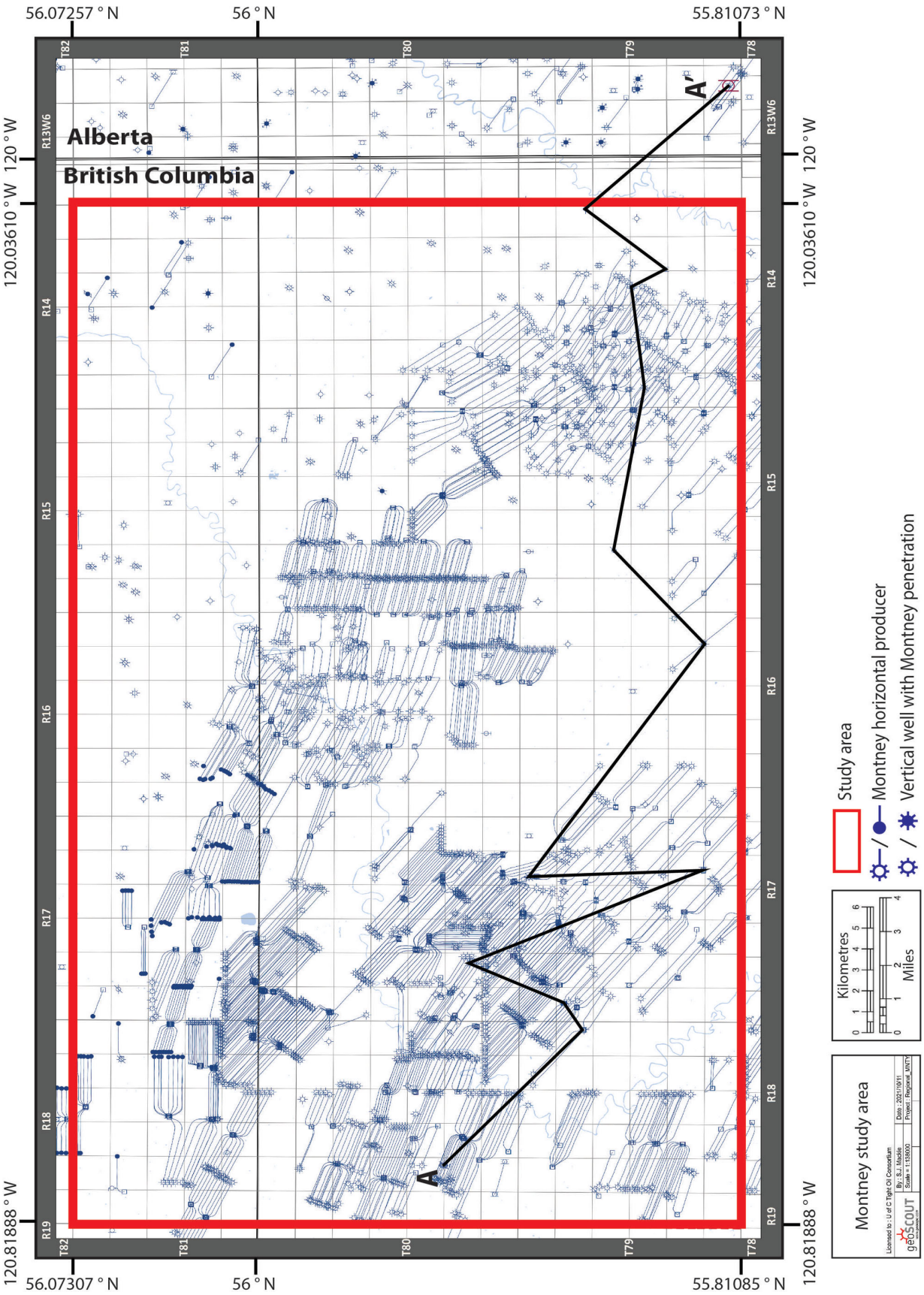

Figure 3. Study area in northeastern British Columbia, showing Montney Formation horizontal producers and vertical wells. The cross-section (A–A') in the southern portion of the study area can be viewed in Figure 4 (geoLOGIC systems ltd., 2021).

their availability, a combination of gamma-ray, resistivity, photoelectric and neutron density/porosity logs were used in the process of correlating the logs. In general, the log patterns display an overall coarsening-upward trend (gamma decreasing and resistivity increasing upward within the log package).

Once parasequences were established throughout the study area, the facies were examined in detail. Using the Montney facies scheme established by Furlong et al. (2021), Montney facies were picked in seven cores throughout the study area. The Furlong et al. (2021) facies scheme includes detailed facies that can be binned into three categories: fine-grained silt, coarse-grained silt and carbonate-rich intervals. These binned categories allow for broad facies correlations on a larger scale. Once the facies were picked in the core, the binned facies categories were correlated to wireline-log signatures using a combination of available gamma-ray, resistivity, photoelectric and neutron density/porosity logs. After establishing the wireline-log signatures, the binned facies were correlated in the vertical wells throughout the study area; establishing the facies regionally in the study area leads to a better understanding of the vertical and lateral facies heterogeneities present. These heterogeneities were then placed in the context of the established parasequences. Using both the parasequences and facies-distribution area is key to understanding the H_2S-distribution maps.

Accessing publicly available gas-analysis data through the geoSCOUT platform developed by geoLOGIC systems ltd., the maximum recorded H_2S value for each well was obtained (geoLOGIC systems ltd., 2021). As the recorded H_2S values are highly dependent on sample-container type (e.g., natural gas cylinder, IsoTrap®), sample-point location (e.g., wellhead vs. plant) and well-production time, the maximum H_2S values were used since the research goal of this study was improved risk mitigation. Within the study area, approximately 20% of the Montney wells (334 wells) had sour gas concentrations greater than 0.01%, which was the minimum threshold recorded. The wells were categorized based on the Montney units in which they are landed and from which they produce. The wells were categorized visually by placing horizontal wells within a cross-section of vertical offsets containing the stratigraphic framework that was established based on previous work by Davies et al. (2018), Euzen et al. (2018), Proverbs et al. (2018), Zonneveld and Moslow (2018) and Furlong et al. (2021), and used to determine which landing zone was targeted based on the wireline-log signatures. These subdivisions include the Lower Montney, lower Middle Montney, upper Middle Montney and Upper Montney. Once all Montney wells were placed within a Montney unit, the maximum H_2S data was plotted and contoured logarithmically for each Montney unit due to the high fluctuation in values (0.01–1%). A compilation of major Triassic normal faults associated with pull-apart basins (Furlong et al., 2018a, b), including the southern edge of the Fort St. John graben, were then overlain onto the maps to incorporate the regional structural events.

Results

Facies Distribution and Stratigraphic Correlations

Facies, classified/identified in core based on the facies scheme from Furlong et al. (2021), highlight the geological variability within the Montney Formation. Within an individual core, coarsening-upward sequences are visible at the millimetre to centimetre scale and generally record an overall coarsening upward of the entire Montney. Correlating the core facies to the wireline-log signatures allowed for facies to be correlated across the study area, highlighting the vertical and lateral facies heterogeneities present within the Montney Formation. Within the study area, the stratigraphic framework was produced by picking parasequences within each Montney unit: four parasequences were picked within the Lower Montney, three within the lower Middle Montney, four within the upper Middle Montney and eight within the Upper Montney. Examining the correlated facies in combination with the picked parasequences makes it possible to place the facies within the stratigraphic framework (Figure 4). Generally, within individual Montney units, facies are more distal near the bottom of the unit and increase upward through the unit as they near the shoreline. Each Montney unit has the fine-grained, silt-dominated facies in the lower portion and the increased coarse-grained, silt-component facies situated stratigraphically above. However, the carbonate-rich intervals are only present within the upper portion of the Lower Montney and the upper Middle Montney in this study area. Additionally, the stratigraphic framework shows that similar facies at a similar depth are not necessarily within the same parasequence and, thus, may present slight geological differences.

Trends in H_2S

The H_2S data were split according to the Montney Formation unit to which they belonged, and maps were constructed to logarithmically contour the data (Figure 5). The Lower Montney had the smallest dataset with only nine wells, of which eight, or 88%, have H_2S (≥0.01%); the H_2S concentration spanned from 0.01 to 1.00%. The Lower Montney wells are landed in the eastern portion of the study area and represent a limited dataset; there are too few wells landed in the Lower Montney near the normal faults to confidently correlate structural trends to H_2S distribution.

The lower Middle Montney had 241 wells, of which 123, or 51%, had H_2S (≥0.01%). The data from the lower Middle Montney exhibited an arc trend across the study area that

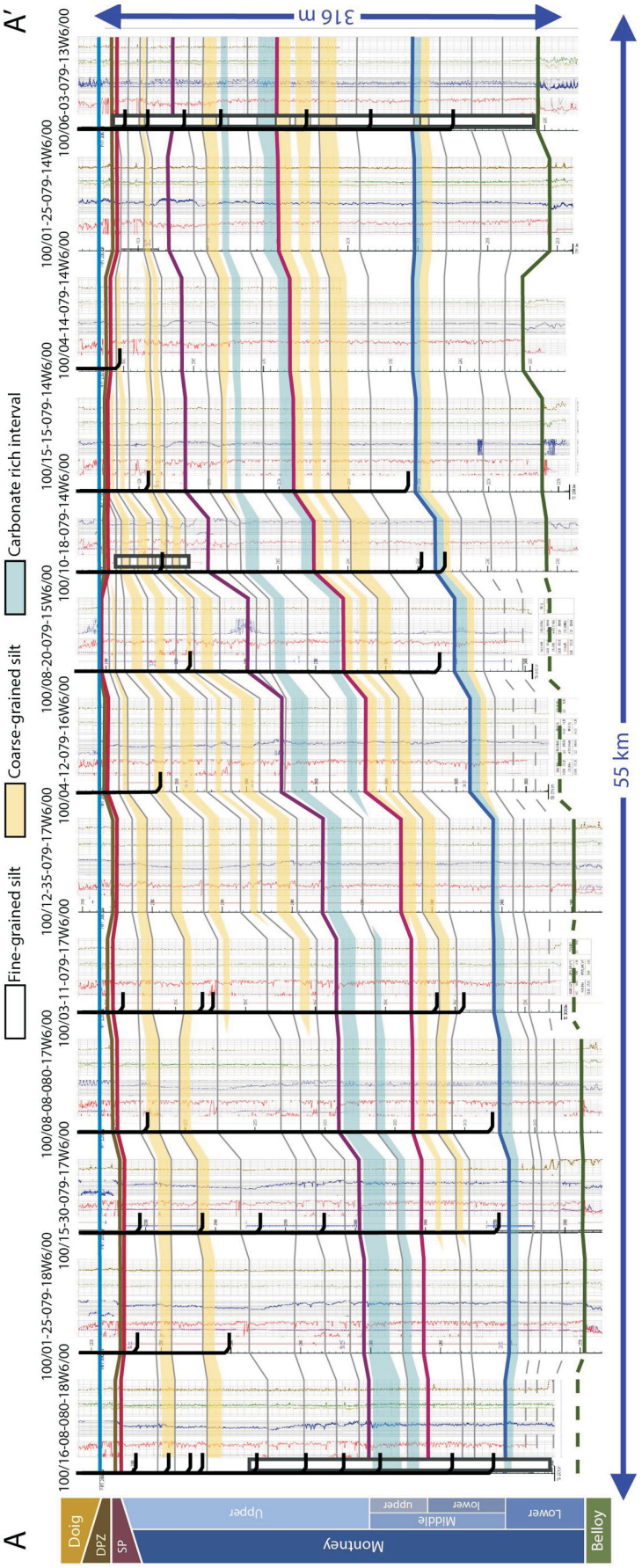

Figure 4. Stratigraphic cross-section highlighting the Montney Formation units and the parasequences within individual Montney units in northeastern British Columbia. The Montney facies, based on a scheme developed by Furlong et al., (2021) were mapped across the study area and constrained laterally within individual parasequences. The variability in vertical and lateral facies heterogeneities highlights the complexity of the Montney Formation. Montney lateral facies are schematically projected onto cross-section A–A' (location shown in Figure 3), highlighting various operational target zones. Well logs are accessed through the geoSCOUT program (geoLOGIC systems ltd., 2021). Abbreviations: DPZ, Doig phosphate zone; SP, Sunset Prairie.

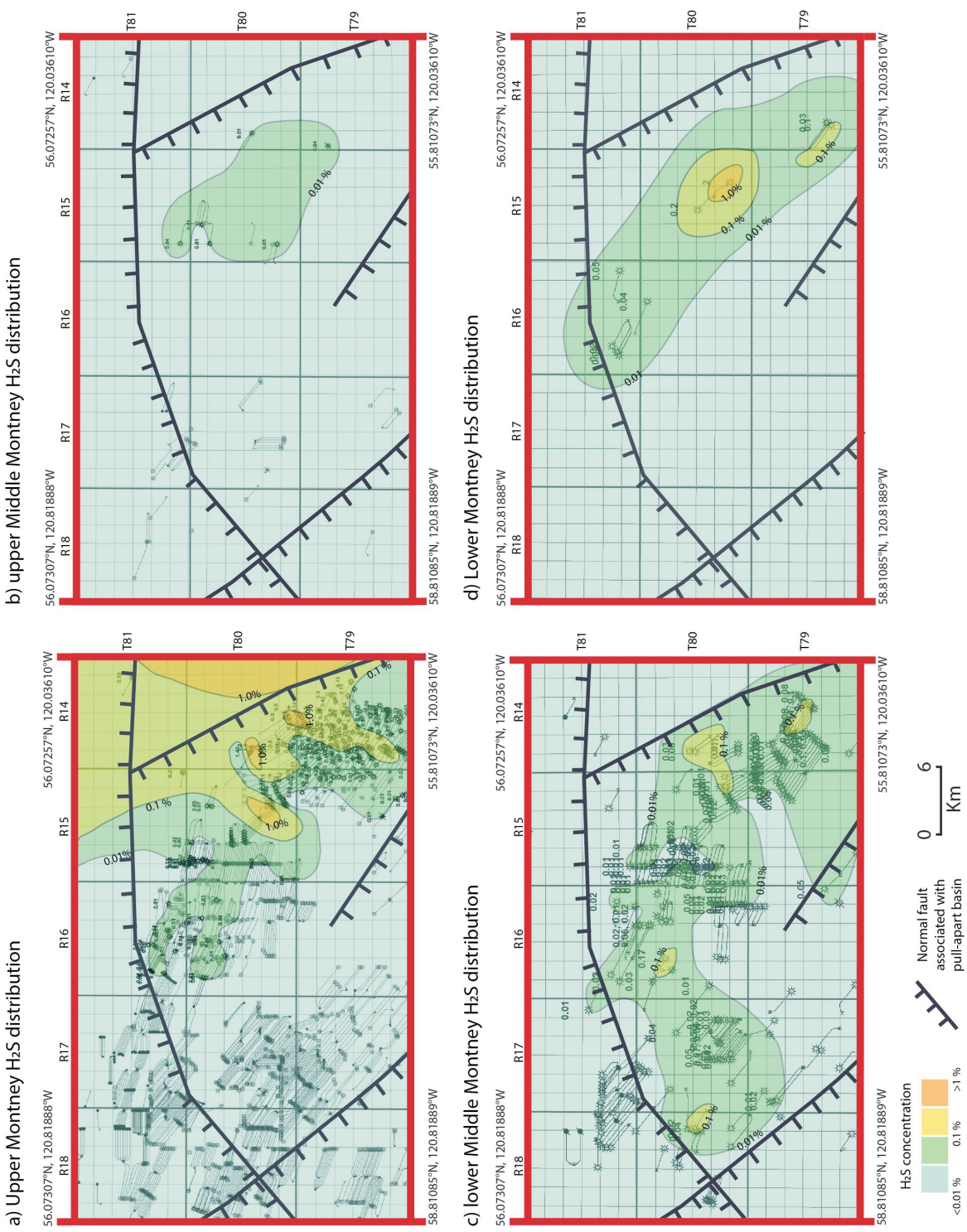

Figure 5. Montney Formation H_2S distribution within the study area, northeastern British Columbia, split according to individual Montney units and contoured logarithmically with an overlay of major normal faults compiled from Furlong et al. (2018a, b): **a)** Upper Montney H_2S map, showing a drastic increase in H_2S content toward the east of the study area; **b)** upper Middle Montney H_2S map, showing a small dataset primarily with H_2S in the eastern portion of the study area; **c)** lower Middle Montney H_2S map, displaying an arc shape across the study area, which may change as more wells are drilled in the northern portion; and **d)** Lower Montney H_2S map, using a very limited dataset that shows high enrichment of H_2S in the eastern portion of the study area.

marginally aligns with the pattern of faulting. However, the trend may become more linear and may fill in toward the north and south as more wells are drilled and the gas is tested over time. The H_2S concentration spread varies from 0.01 to 0.1%.

The upper Middle Montney consists of a sparse dataset with a total of 41 wells, of which 6, or 15%, are enriched in H_2S (≥0.01%). The H_2S concentration ranges from 0.01% to just under 0.1%. The wells containing H_2S are concentrated in the eastern portion of the study area. There are too few wells landed in the upper Middle Montney near the normal faults to confidently correlate structural trends with H_2S distribution.

The Upper Montney has the largest dataset with 1365 wells landed, of which 197, or 14%, are enriched in H_2S (≥0.01%). The Upper Montney wells with H_2S are concentrated in the eastern portion of the study area and rapidly increase in concentration from 0.01% to 1%. Generally, although there are faults in the eastern portion of the study area enriched in H_2S, the fact there are insufficient Upper Montney wells directly near the eastern fault means this trend cannot be fully correlated and the matter requires further investigation.

Discussion

Examining the H_2S-production distribution maps for each Montney unit alongside the regional cross-section allows to better visualize the trends from the datasets. In the Upper Montney, the elevated H_2S is primarily in the eastern portion of the study area. Upper Montney wells that reveal the same binned, coarse-grained silt facies within a single parasequence can have absent, low or high H_2S content, highlighting the lateral variability. The H_2S content increases eastward and may be linked to the overlying thinning of the Doig–Halfway formations to the east (Edwards et al., 1994), allowing for sulphate-rich fluids sourced from anhydrite beds in the Charlie Lake Formation to diffuse downward into the Montney Formation (Desrocher et al., 2004). Between the 100 08 20 079 15 W6 00 well and the 100 04 14 079 14 W6 00 well (BC Oil and Gas Commission, 2021), the Doig and Halfway formations thin by approximately 12%, from about 118 to around 103 m. In addition to the thinning overlying units, there are structures in the east that may additionally be linked to the elevated H_2S content; further work needs to be done to fully understand this relationship. Within the Charlie Lake Formation, tectonic activity is evident, as indicated by the presence of the angular Coplin unconformity (Davies, 1997), and may have provided conduits for early sulphate-rich fluid migration. This is consistent with recent sulphur-isotope fingerprinting analysis that shows that Upper Montney samples in northeastern BC have a Triassic signature (Chalmers et al., 2021), but contrasts with previous studies in west-central Alberta, which have shown a Devonian signature on sulphur-isotope data that has been interpreted as upward fluid migration through faults acting as conduits (Liseroudi et al., 2020), thus highlighting the regional diagenetic variability within the Montney Formation (Kingston et al., 2021).

A recent study by Liseroudi et al. (2021), based on the relationship between the $\delta^{34}S$ values of the present-day produced-gas H_2S and other sulphur-bearing species from the Montney and neighbouring formations, proposed a dual in situ and migrated TSR-derived origin for the H_2S gas, with substantial contributions of in situ H_2S in the Montney Formation. Within a single Upper Montney parasequence in a similar binned facies over a distance of under 10 km, the increasing H_2S content eastward suggests that in situ H_2S-generating mechanisms increase eastward. These in situ mechanisms may be increased due to early dissolution from the Charlie Lake anhydrite associated with a combination of the overlying thinning Halfway–Doig formations, bringing the Charlie Lake Formation closer to the Montney (Edwards et al., 1994), and faults acting as fluid conduits. However, further research needs to be completed to better understand this relationship.

In the lower Middle Montney and Lower Montney, H_2S content increases with proximity to the contact between the lower Middle Montney and Lower Montney, and the contact with the underlying Paleozoic Belloy Formation. Additionally, the carbonate-rich facies present along the boundary between the lower Middle Montney and Lower Montney may act as an in situ sulphate source. Wells landed stratigraphically higher within the lower Middle Montney do not have high H_2S concentrations. In comparison, wells landed closer to the base of the lower Middle Montney and in the Lower Montney produced relatively higher concentrations of H_2S gas. Another potential sulphate source is the underlying Belloy Formation, which is known to contain anhydrite (Naqvi, 1972). Previously mapped isopachs of Lower Montney in this study area thin westward by approximately 100 m (BC Oil and Gas Commission, 2012). However, due to the limited number of Lower Montney produ-cers in this study and marginal variations in the lower Middle Montney H_2S concentrations (0.01–0.1%), there is no distinct trend between Lower Montney thickness and H_2S content. Further work is required to properly understand the Montney H_2S-Belloy Formation relationship. Within the lower Middle and Lower Montney, two examples were found in which H_2S concentrations increased temporally during production (Table 1). The increase in H_2S content may be due to diffusion upward through time as the wells are produced or may be derived from faults acting as fluid conduits, similar to the situation that has been established in Alberta (Liseroudi et al., 2020).

Table 1. Examples from two wells in northeastern British Columbia show Lower Montney and lower Middle Montney H_2S production varying with time. Publicly available gas-analysis data accessed through the geoSCOUT program (geoLOGIC systems ltd., 2021). Abbreviation: UWI, unique well identifier.

UWI	Unit	Test date	H2S (%)
100 03 17 079 14 W6 00	lower Middle Montney	12-Sep-2019	0
100 03 17 079 14 W6 00	lower Middle Montney	17-Sep-2020	0.02
102 12 08 079 14 W6 00	Lower Montney	01-Sep-2019	Trace
102 12 08 079 14 W6 00	Lower Montney	20-Sep-2020	0.1

Conclusions and Future Work

Within the northeastern BC study area, H_2S concentrations in the Upper Montney increase toward the east as the Halfway and Doig formations thin, bringing the overlying anhydrite beds of the Charlie Lake Formation nearer to the Montney Formation. The Upper Montney of northeastern BC has been shown to contain sulphate minerals with a Triassic signature, supporting in situ H_2S that is TSR derived (Liseroudi et al., 2021) and not solely sourced from fluids that migrated up from underlying strata. Within the study area, H_2S in the Lower Montney and lower Middle Montney Formation increases downward, approaching the carbonate facies at both the lower Middle Montney–Lower Montney boundary and the underlying Paleozoic Belloy Formation, which is another anhydrite-rich carbonate unit. Although the dataset from the Lower Montney is limited, the H_2S concentration of produced gases is shown to increase over time in a few isolated examples, potentially implying that fluids drawn to the wellbore include H_2S diffusing or migrating through faults upward, which is consistent with previous regional findings (Liseroudi et al., 2020, 2021). Further work is required to better understand this process and sulphur-isotope fingerprinting of wells landed in the lower Middle Montney and Lower Montney formations is recommended for future studies. Understanding from where the stratigraphically lower H_2S is sourced may help better understand H_2S distribution in northeastern BC. In addition, further delineating of structures in the Lower Montney may provide insight into whether the fluids are migrating through faults acting as conduits or if they are diffusing sporadically from the underlying Belloy Formation. Comparing previously published mapped updip gas-migration fairways (Wood and Sanei, 2016; Sereda and Fur, 2017; Euzen et al., 2019, 2021) with the H_2S distribution mapped in this study may also provide insight on fluid-migration pathways. Improved understanding of the facies and stratigraphic controls on H_2S distribution within northeastern BC is key to enhancing prediction and mitigation of this highly toxic gas, improving environmental and worker safety, as well as improving the economic perspective for operators in this area.

Acknowledgments

The authors would like to thank T. Euzen for providing insightful comments that helped to greatly improve this manuscript. Geoscience BC, Natural Resources Canada and the sponsors of the Tight Oil Consortium at the University of Calgary are thanked for their financial support of this research. The authors would also like to thank geoLOGIC systems ltd. for making the geoSCOUT GIS program used to search and analyze the well data for this study available.

Natural Resources Canada, Lands and Minerals Sector contribution 20210378

References

Armitage, J.H. (1962): Triassic oil and gas occurrences in northeastern British Columbia, Canada; Journal of the Alberta Society of Petroleum Geologists, v. 10, p. 35–56.

BC Oil and Gas Commission (2012): Montney formation play atlas NEBC, URL <https://www.bcogc.ca/montney-formation-play-atlas-nebc> [November 2021].

BC Oil and Gas Commission (2021): Well lookup and reports; BC Oil and Gas Commission, URL <http://www.bcogc.ca/online-services> [November 2021].

Chalmers, G.R.L., Bustin, R.M. and Bustin, A.A. (2021): Isotopic fingerprinting of sulphur sources for the hydrogen sulphide gas in the Montney Formation, northeastern British Columbia (NTS 093O, P, 094A, B, G–J, N–P); Geoscience BC Summary of Activities 2020: Energy and Water, Geoscience BC, Report 2021-02, p. 103–108, URL <http://www.geosciencebc.com/summary-of-activities-2021-energy-and-water/> [November 2021].

Crombez, V., Rohais, F., Baudin, F. and Euzen, T. (2016): Facies, well-log patterns, geometries and sequence stratigraphy of a wave-dominated margin: insight from the Montney Formation (Alberta, British Columbia, Canada); Bulletin of Canadian Petroleum Geology, v. 64, p. 516–537, <https://doi.org/10.2113/gscpgbull.64.4.516>.

Davies, G.R. (1997): The Triassic of the Western Canada Sedimentary Basin: tectonic and stratigraphic framework, paleogeography, paleoclimate, and biota; Bulletin of Canadian Petroleum Geology, v. 45, p. 434–460.

Davies, G.R., Moslow, T.F. and Sherwin, M.D. (1997): The Lower Triassic Montney Formation, west-central Alberta; Bulletin of Canadian Petroleum Geology, v. 45, p. 474–505.

Davies, G., Watson, N., Moslow, T.F. and MacEachern, J. (2018): Regional subdivision, sequences, correlation and facies relationships of the Lower Triassic Montney Formation, west-central Alberta to northeastern British Columbia, Canada – with emphasis on the role of paleostructure; Bulletin of Canadian Petroleum Geology, v. 66, p. 23–92.

Desrocher, S., Hutcheon, I., Kirste, D. and Henderson, C.M. (2004): Constraints on the generation of H_2S and CO_2 in the subsurface Triassic, Alberta Basin, Canada; Chemical Geology, v. 204, p. 237–257, URL <https://doi.org/10.1016/j.geochem.2003.11.012>.

Edwards, D.E., Barclay, J.E., Gibson, D.W., Kvill, G.E. and Halton, E. (1994): Triassic strata of the Western Canadian Sedimentary Basin; Chapter 16 *in* Geological Atlas of the Western Canada Sedimentary Basin, G. Mossop and I. Shetsen (comp.), Canadian Society of Petroleum Geologists, Calgary, Alberta and Alberta Research Council, Edmonton, Alberta, p. 159–275.

Euzen, T., Moslow, T.F., Crombez, V. and Rohais, S. (2018): Regional stratigraphic architecture of the Spathian depositions in Western Canada – implications for the Montney resource play; Bulletin of Canadian Petroleum Geology, v. 66, p. 175–192.

Euzen, T., Watson, N., Chatellier, J.Y. Mort, A. and Mangenot, X. (2019): Petroleum system analysis using unconventional gas geochemistry: examples from the Montney play of western Canada; Proceedings of the Society of Petroleum Engineers, American Association of Petroleum Geologists and Society of Exploration Geophysicists Unconventional Resources Technology Conference, July 22–24, 2019, Denver Colorado, URTeEC-649-MS, p. 1276–1290, URL <https://doi.org/10.15530/urtec-2019-649>.

Euzen, T., Watson, N., Fowler, M. and Mort, A. (2021): Petroleum distribution in the Montney hybrid play: source, carrier bed, and structural controls; American Association of Petroleum Geologists Bulletin, v. 105, p. 1867–1892, URL <https://doi.org/10.1306/12222020088>.

Furlong, C.M., Gingras, M.K., Moslow, T.F. and Zonneveld, J.P. (2018a): The Sunset Prairie Formation: designation of a new Middle Triassic formation between the Lower Triassic Montney Formation and Middle Triassic Doig Formation in the Western Canada Sedimentary Basin, northeast British Columbia; Bulletin of Canadian Petroleum Geology, v. 66, p. 193–214.

Furlong, C.M., Gegolick, A., Gingras, M.K., Gonzalez, P., Moslow, T.F., Prenoslo, D., Playter, T. and Zonneveld, J.P. (2018b): Sedimentology and ichnology of the Middle Triassic (Anisian) Sunset Prairie Formation of the Western Canada Sedimentary Basin; Bulletin of Canadian Petroleum Geology, v. 66, p. 215–236.

Furlong, C.M., Pedersen, P.K., and Eaton, D.W. (2021): Sedimentological heterogeneities of the Montney Formation: case study from the Greater Pouce Coupe area; Canadian Society of Petroleum Geologists, 2021 Online Core Conference, June 17–18, 2021, Calgary, Alberta, Program with Abstracts, p. 34–38.

geoLOGIC systems ltd. (2021): geoSCOUT version 8.8; geoLOGIC systems ltd., mapping, data management and analysis software, URL <https://www.geologic.com/products/geoscout/> [August 2021].

Hunt, A.D. and Ratcliffe, J.D. (1959): Triassic stratigraphy, Peace River area, Alberta and British Columbia, Canada; American Association of Petroleum Geologists, AAPG Bulletin, v. 43, p. 563–589, URL <https://doi.org/10.1306/0BDA5CC3-16BD-11D7-8645000102C1865D>.

Hutcheon, I., Krouse, H.R. and Abercrombie, H.J. (1995): Controls of the origin and distribution of elemental sulfur, H_2S, and CO_2 in Paleozoic hydrocarbon reservoirs in western Canada; Chapter 24 *in* Geochemical Transformations of Sedimentary Sulfur, M.A. Vairavamurthy, M.A.A. Schoonen, T.I. Eglinton, G.W. Luther and B. Manowitz (ed.), ACS Symposium Series, v. 612, p. 426–438, URL <https://doi.org/10.1021/bk-1995-0612.ch024>.

Kingston, A.W., Ardakani, O.H., Grasby, S.E. and Mayer, B. (2021): Using elemental and isotopic geochemistry to identify the geochemical signatures of diagenetic events in the Montney Formation and their relationship with H_2S formation and distribution; Geoconvention 2021, September 3–15, 2021 (virtual event), abstract 67397, p. 1–3.

Kirste, D., Desrocher, S., Spence, B., Hoyne, B., Tsang, B. and Hutcheon, I. (1997): Fluid flow, water chemistry, gas chemistry, and diagenesis in the subsurface Triassic in Alberta and British Columbia; Bulletin of Canadian Petroleum Geology, v. 45, p. 742–764.

Liseroudi, M.H., Ardakani, O.H., Sanei, H., Pedersen, P.K., Stern, R.A. and Wood, J.M. (2020): Origin of sulfate-rich fluids in the Early Triassic Montney Formation, Western Canadian Sedimentary Basin; Marine and Petroleum Geology, v. 114, art. 104236, URL <https://doi.org/10.1016/j.marpetgeo.2020.104236>.

Liseroudi, M.H., Ardakani, O.H., Pedersen, P.K., Stern, R.A., Wood, J.M. and Sanei, H. (2021): Microbial and thermochemical controlled sulfur cycle in the Early Triassic sediments of the Western Canadian Sedimentary Basin; Journal of the Geological Society, v. 178, p. 1–20.

Machel, H.G. (2001): Bacterial and thermochemical sulfate reduction in diagenetic settings – old and new insights; Sedimentary Geology, v. 140, p. 143–175, URL <https://doi.org/10.1016/S0037-0738(00)00176-7>.

Machel, H.G., Krouse, H.R., Riciputi, L.R. and Cole, D.R. (1995): Devonian Nisku sour gas play, Canada: a unique natural laboratory for study of thermochemical sulfate reduction; Chapter 25 *in* Geochemical Transformations of Sedimentary Sulfur, M.A. Vairavamurthy, M.A.A. Schoonen, T.I. Eglinton, G.W. Luther and B. Manowitz (ed.), ACS Symposium Series, v. 612, p. 439–454, URL <https://doi.org/10.1021/bk-1995-0612.ch025>.

National Energy Board of Canada, BC Oil and Gas Commission, Alberta Energy Regulator and BC Ministry of Natural Gas Development (2013): Energy briefing note: the ultimate potential for unconventional petroleum from the Montney Formation of British Columbia and Alberta; National Energy Board, BC Oil and Gas Commission, Alberta Energy Regulator and BC Ministry of Natural Gas Development, briefing note, 23 p.

Naqvi, I.H. (1972): The Belloy Formation (Permian), Peace River area, northern Alberta and northeastern British Columbia; Bulletin of Canadian Petroleum Geology, v. 20, p. 58–88, URL <https://doi.org/10.35767/gscpgbull.20.1.058>.

Orr, W.L. (1977): Geologic and geochemical controls on the distribution of hydrogen sulfide in natural gas; *in* Advances in Organic Geochemistry, R. Campos and J. Goni (ed.), Enadimsa, Madrid, p. 571-597.

Proverbs, I.P., Bann, K.L., Fratton, C.M., Frostad, C.J. and Juska, A. (2018): Facies architecture and sequence stratigraphy of the Lower Triassic Montney Formation, NE British Columbia: fundamental controls on the distribution of 'sweet spots' in a world-class unconventional reservoir; Bulletin of Canadian Petroleum Geology, v. 66, p. 237–258.

Sereda, R. and Fur, J. (2017): The Lower Montney turbidite complex of northwest Alberta and northeast British Columbia: evolution of an oil and gas play from conventional to unconventional; Proceedings of the 5th Society of Petroleum Engineers, American Association of Petroleum Geologists and Society of Exploration Geophysicists Unconventional Resources Technology Conference, July 24–26, 2017, Austin, Texas, URTeC-2674327-MS, 8 p., URL <https://doi.org/10.15530/urtec-2017-2674327>.

Wood, J.M. (2013): Water distribution in the Montney tight gas play of the Western Canadian Sedimentary Basin: significance for resource evaluation; Society of Petroleum Engineers, SPE Reservoir Evaluation and Engineering, v. 16, p. 290–302, URL <https://doi.org/10.2118/161824-PA>.

Wood, J.M. and Sanei, H. (2016): Secondary migration and leakage of methane from a major tight-gas system; Nature Communications, v. 7, art.13614, 9 p.

Worden, R.H. and Smalley, P.C. (1996): H_2S-producing reactions in deep carbonate gas reservoirs: Khuff Formation, Abu Dhabi; Chemical Geology, v. 133, p. 157–171, URL <https://doi.org/10.1016/S0009-2541(96)00074-5>.

Zonneveld, J.P. and Moslow, T.F. 2018. Paleogeographic setting, lithostratigraphy, and sedimentary framework of the Lower Triassic Montney Formation of western Alberta and northeastern British Columbia; Bulletin of Canadian Petroleum Geology, v. 66, p. 93–127.

Numerical Study on the Effects of Montney Formation Stiffness on Injection-Induced Seismicity in Northeastern British Columbia (NTS 093, 094A, B, G, H)

A. Mehrabifard[1], Department of Earth, Ocean and Atmospheric Sciences, The University of British Columbia, Vancouver, British Columbia, amehrabifard@eoas.ubc.ca

E. Eberhardt, Department of Earth, Ocean and Atmospheric Sciences, The University of British Columbia, Vancouver, British Columbia

Mehrabifard, A. and Eberhardt, E. (2022): Numerical study on the effects of Montney Formation stiffness on injection-induced seismicity in northeastern British Columbia (NTS 093, 094A, B, G, H); *in* Geoscience BC Summary of Activities 2021: Energy and Water, Geoscience BC, Report 2022-02, p. 23–34.

Introduction

The Lower Triassic Montney Formation is areally extensive, covering approximately 130 000 km^2 from central Alberta to northeastern British Columbia (BC; National Energy Board et al., 2013). This gas-bearing shale is also thick, typically ranging from 100 to 300 m, and, although thinning to zero at its eastern and northeastern subcropping margins, increases to over 300 m on its western margin before it begins outcropping in the Rocky Mountains. However, the permeability of this formation is commonly in the 10^{-21} to 10^{-18} m^2 range. The Montney Formation is considered a prime candidate for horizontal drilling and multistage hydraulic fracturing (HF) treatment in Canada. More than 3200 horizontal, multistage wells have been drilled and completed in the Montney since 2008 (Vishkai and Gates, 2019). Although only less than 1% of these stimulated wells are associated with moment magnitude (M_w) <3 earthquakes (Atkinson et al., 2016), the connection between induced earthquakes and strongly controversial issues, such as shale gas, could impact the public and stakeholder perception of clean energy development, as is already apparent from the current perception of deep geothermal energy (Malo et al., 2015). Projects being delayed or abandoned due to public backlash, such as occurred following HF operations in Preston, United Kingdom (Kettlety et al., 2021) or after targeting enhanced geothermal systems in Pohang, South Korea (Ellsworth et al., 2019) and Basel, Switzerland (Majer et al., 2007), represents a direct economic risk to energy developers. More importantly, such backlash can also have wider impacts if deep geothermal energy, natural-gas development as well as carbon capture and storage are prevented from making a timely contribution to climate-change mitigation strategies (Trutnevyte and Ejderyan, 2017). Accordingly, fluid-injection–induced seismic hazard assessment and mitigation planning are necessary steps in tackling global warming. Such seismic hazard analyses and assessments require a comprehensive knowledge of the mechanistic causes of injection-induced shear slips.

In this study, a sensitivity analysis of Montney Formation stiffness (Young's modulus, E) was carried out and its effects on induced-seismicity behaviour and frequency-magnitude distribution were studied. Formation stiffness was selected based on the results of an in-depth machine-learning analysis; this analysis, using a compiled dataset, was carried out on geological and operational parameters throughout the Montney Formation in BC to determine the effect of each parameter on the injection-induced seismicity distribution recorded in BC for shale-gas development. Correlation between induced earthquake hypocentres and sharp changes in seismic tomography (i.e., proxy for formation stiffness, E) has been observed elsewhere (Matzel et al., 2014). Finally, the goal of this paper is to provide insight into the mechanistic reasoning behind such observations. The generic base model (Figure 1a) developed for the common geological setting in northeastern BC uses the new 3-D hybrid lattice and particle-bonded code XSite^{TM} developed by Itasca Consulting Group, Inc. (Damjanac at al., 2016). The models generated are conceptual but were guided and constrained by reported reservoir characteristics for the Montney Formation in BC. As these models to study the mechanisms of induced seismicity due to fluid injection are designed to be generic, they are not meant to be predictive for any specific site location or set of conditions. By adopting a simpler representation involving a single planar fault, focus was placed on capturing the physics of fluid-pressure perturbation and stress transfer as triggering mechanisms. This model can generate large moment-magnitude events (M_w <3). The input parameters are listed in Table 1. Fluid injection was simulated directly into the fault to gain computational advantages in simulation computing times. This simplified assumption is representative of a scenario where either the borehole, a hydraulic fracture or a discrete fracture network (DFN) intersects the fault and transmits fluid pressure radially into the more permeable

[1]*The lead author is a 2021 Geoscience BC Scholarship recipient.*

This publication is also available, free of charge, as colour digital files in Adobe Acrobat® PDF format from the Geoscience BC website: http://geosciencebc.com/updates/summary-of-activities/.

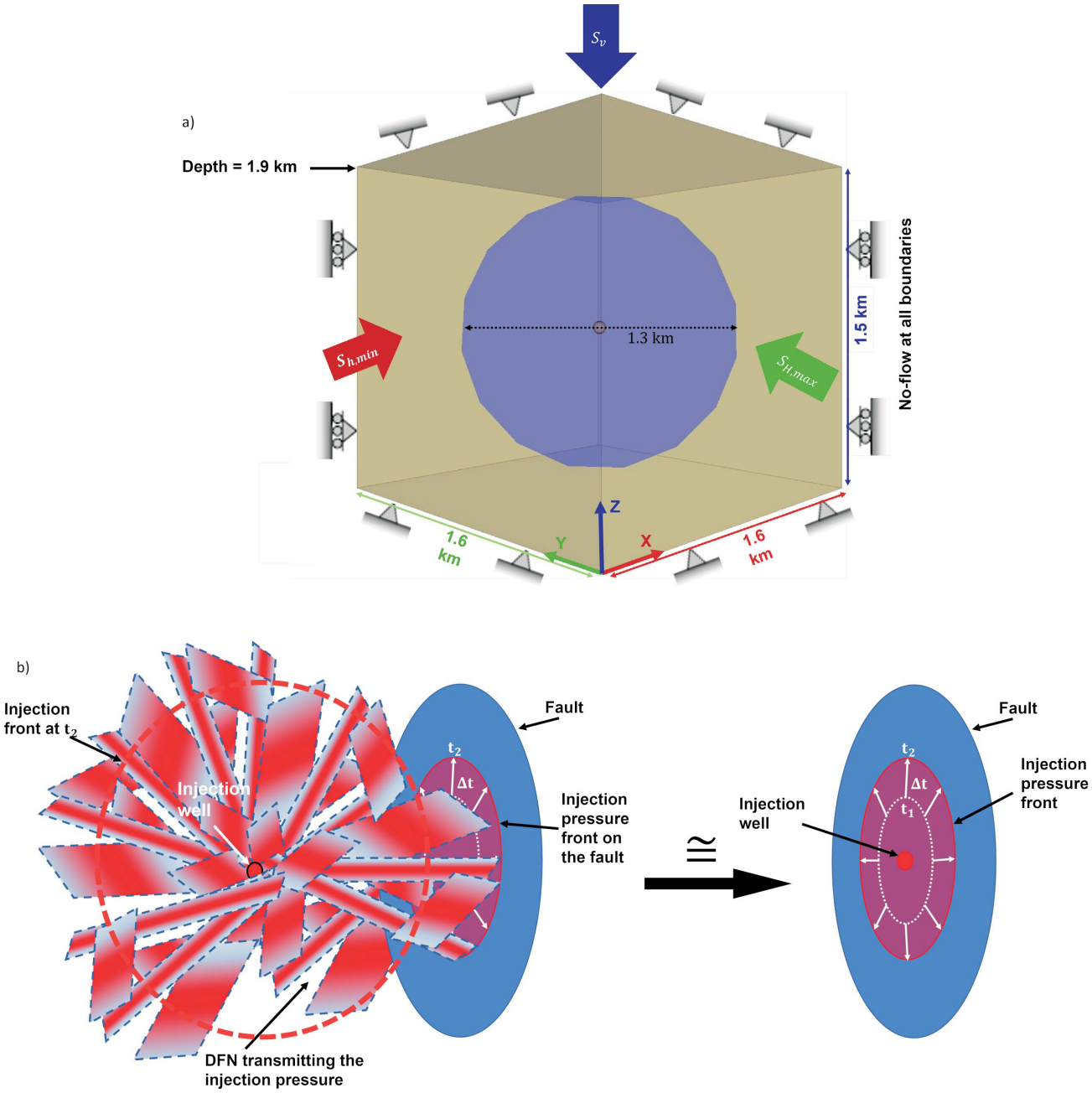

Figure 1. a) Schematic of the XSite™-generated model of the geometry and boundary conditions characteristic of the Montney Formation in British Columbia. The directions of the principal stresses (S) are shown (note that each stress is parallel to the Cartesian axes of the model as indicated by the matching arrow and axes colours). The geometry and dimension of the fault are shown (strength properties are listed in Table 1). The far-field displacement boundary conditions are fixed at the top and bottom faces (grey symbols), and free to move in the z-direction along the side faces. All the boundaries are impermeable. **b)** Fluid-injection method used for the XSite modelling. In this scenario, a discrete fracture network (DFN) intersects with a fault, transmitting fluid pressure as a cone-shaped pressure front that radiates outward from the injection point and intersects and perturbs an area of the fault, which increases (Δt) from t_1 (white dotted circle) to t_2 (red dashed circle) with increasing injection time (t).

Table 1. XSite™ model inputs for fluid injection and induced-seismicity simulation, including in situ stress conditions as well as rock-mass and fault properties.

Property	Description
Model geometry	1.6 km × 1.6 km × 1.5 km
Fault radius, initial aperture	r = 650 m, a = 0.0001 m
Fault strength properties	μ = tan(27°) [1, 2], c = 9.5 MPa [3], T = 2.5 MPa [2]
Injection rate at point of intersection with fault [4]	q_{inj} = 0.2 m^3/s [5]
$\partial S_v/\partial Z$ (z axis)	Strike-slip: 25 MPa/km; reverse: 25 MPa/km [1, 6]
$\partial S_H/\partial Z$ (y axis)	Strike-slip: 33 MPa/km; reverse: 33 MPa/km; reverse max: 38 MPa/km [1, 6]
$\partial S_h/\partial Z$ (x axis)	Strike-slip: 20 MPa/km; reverse: 28 MPa/km [1, 6]
Pore-pressure gradient	15 MPa/km [1, 6]
Depth at top of the model	1.9 km
Formation density	2600 kg/m^3 [1, 2, 7]
Elastic properties	E = 32 GPa, v = 0.22 [1, 2, 7]
Matrix internal friction angle	47° [1, 7]
Unconfined compression strength (UCS)	120 MPa [7]
Fracture toughness	1.25 $MPa.m^{0.5}$ [8, 9]
Tensile strength	1.5 MPa [9]
Matrix permeability and porosity	k = 50 nD [1, 10], Φ = 5% [10, 11]

[1]McLellan (2016), Rogers et al. (2014)

[2]Vaisblat et al. (2019)

[3]Determined based on sensitivity analysis. Note that the cohesion adds more brittle behaviour to the fault and thus a more sudden release of energy. This value is selected to simulate a conservative scenario (see also Tenthorey and Cox, 2006).

[4]The model is designed to examine the fluid-injection rates, pressures and volumes as experienced by the fault. The implementation of the fluid injection represents a conservative scenario where the borehole or the hydraulic fracture intersects with the discrete fault network (DFN) connected with the fault (see Figure 1b).

[5]Zoback and Kohli (2019)

[6]Fox and Watson (2019); the gradients implemented simulate injection into an over-pressured reservoir. This represents a conservative scenario. The vertical stress gradient is calculated from the average density of the formations from the ground surface to the reservoir depth.

[7]Trican Geological Solutions Ltd. (unpublished report, 2013)

[8]Chen and Wong (2018)

[9]Abdelaziz et al. (2019)

[10]Javaheri et al. (2017)

[11]Vishkai and Gates (2019)

fault (Figure 1b). As the injection continues, the zone of interaction (or the injection pressure front) transmitted to the fault gets larger. The injection-flow rate used was 0.2 m^3/s (~75.5 bbl/min), which represents an average value for well stimulations lasting two hours (Zoback and Kohli, 2019).

Results and Discussion

The influence of elastic stiffness (E) on the rock mass hosting a critically stressed fault (a subvertical fault, which is usually hard to detect prior to the operation and hosts M_w <3 events in northeastern BC) was investigated. Rock-mass stiffness is known to be a key influencing factor in fault-slip rockburst hazards encountered in deep mining. Figure 2 shows laboratory-measured Young's modulus (E) values, which range from 16 to 50 GPa, for cores obtained from the Montney Formation at reservoir depths between 2.3 and 2.6 km (Trican Geological Solutions Ltd., unpublished report, 2013). McKean and Priest (2019) reported an even higher range (42 to 72 GPa), albeit for samples obtained from Montney surface outcrops. To ensure a thorough analysis of the parameter space, five different Young's modulus values were selected covering the reported ranges (see Figure 3). As previously noted, the rock properties were assumed to be homogeneous and isotropic in each model representing a different stiffness of the rock-mass domain.

As the parameter of interest was formation stiffness, the model geometry used assumed the same fault orientation for each model scenario (dip direction of 45°, clockwise from the maximum horizontal stress, and dip angle of 80°). Modelling for this fault orientation considered both the strike-slip and reverse fault stress regimes. Once the in situ stresses and pore pressures are initialized and fluid injection begins, the fluid pressures acting on the fault begin to increase. As the fluid pressure increases, the effective shear

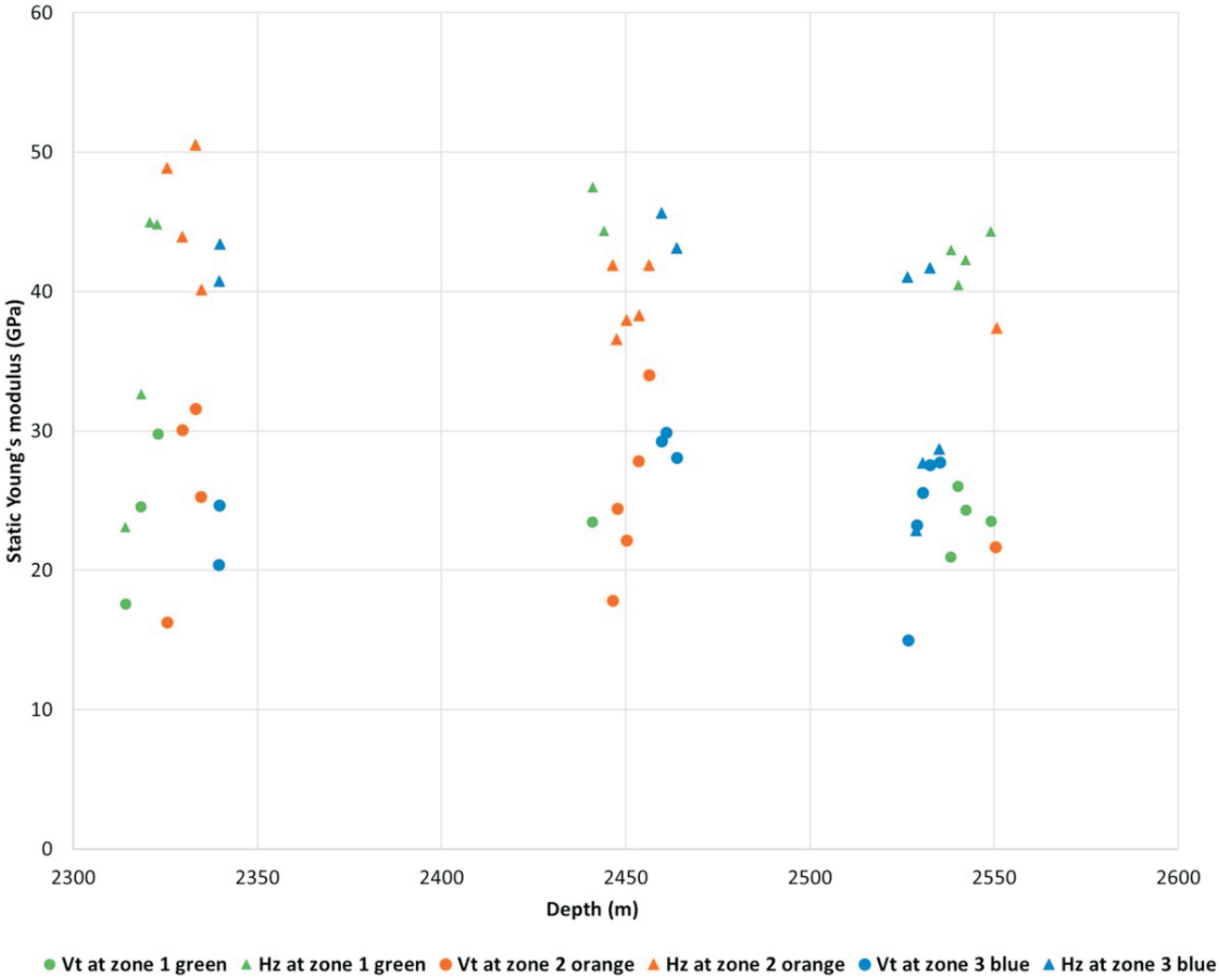

Figure 2. Laboratory-measured Young's modulus (E) values for rock cores retrieved from the same well in the Montney Formation, northeastern British Columbia (Trican Geological Solutions Ltd., unpublished report, 2013). The coloured circles and triangles correspond to values of samples tested vertically (Vt) and horizontally (Hz), respectively, relative to the core axis. The colours represent three different zones (1–3) designated as having different rock facies. Abbreviation: GPa, gigapascal.

strength of the fault decreases until the shear-slip criterion is satisfied:

$$\tau - [(\sigma_n - P_f \cdot \tan(27^\circ) + 9.5] \geq 0$$

where τ refers to shear stress on the fault, the σ_n value is the normal stress on the fault and P_f stands for fluid pressure on the fault. Once this criterion is met, shear slip occurs.

It was observed that as the rock-mass stiffness increases, fluid pressure in the fault becomes greater as there is more resistance to rock-mass deformation:

$$\varepsilon_v = \sigma / K$$

where ε_v is the volumetric strain, the σ value is the mean stress (i.e., the summation of the three principal stresses divided by 3) and K is the bulk modulus. This restricts the ability of the fault aperture to increase, which results in a higher fluid-pressure gradient (ΔP_f) at the site of the fault, resulting in a larger perturbed area over a shorter injection time:

$$q \propto \Delta P_f \quad and \quad q \cdot \Delta t_{inj} = \Delta V = a\pi R^2$$

where q is the fluid flow rate, ΔP_f is the pressure gradient and Δt_{inj} is the injection duration. At the same time, the stiffer rock mass adjacent to the fault provides more confinement (i.e., higher normal stresses) and, therefore, resistance to slip, resulting in more elastic strain energy being stored. Figure 3 illustrates the increasing amount of strain energy stored for a given amount of shear strain (ε_o) as a function of increasing rock-mass shear stiffness (G). It should be noted that the stored elastic strain energy is proportional to the area under the shear stress versus shear strain curve of the rock. Thus, for the same slip area (πR^2)

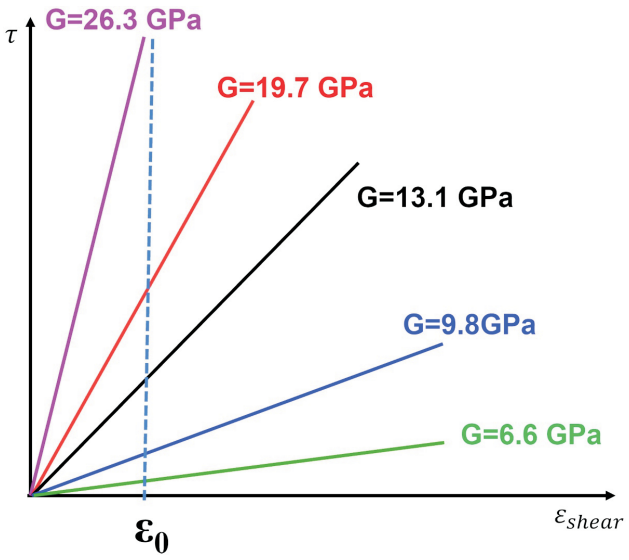

Figure 3. Schematic illustration of the stored elastic strain energy for different rock-mass stiffnesses. The stored elastic strain energy is proportional to the area under the shear stress (τ) versus shear strain curve of the rock. Thus, as rock-mass shear stiffness (G) increases, so does the strain energy stored in the rock mass for the same amount of shear strain (ε_0). Abbreviation: GPa, gigapascal.

and displacement (D), it is expected that stiffer rock will result in a larger moment release (M_o; i.e, $M_o = GD\pi R^2$).

Reverse Fault Far-Field Stress Regime

Figure 4 plots the moment release as a function of injection time for the reverse fault far-field stress-regime boundary condition. The solid lines correspond to the base-case maximum horizontal stress gradient (i.e., 33 MPa/km in Table 1), whereas the dashed lines represent a higher horizontal stress gradient (MPa/km [Reverse max] in Table 1). The latter represents an adjusted gradient that conforms to the observed horizontal stress ratio ($1.1 \leq S_H/S_h \leq 1.4$; see Rogers et al., 2014), but also results in a differential stress (i.e., $S_1–S_3$) that is the same as for the strike-slip stress-regime scenario (Table 1). This facilitates comparison with results for the strike-slip stress-regime scenario presented later. Another important consideration with respect to interpreting this plot, is that XSite is a quasi-static program, whereas fault-slip rupture events are dynamic. To address this limitation, the maximum moment magnitude for a simulation can be calculated by summing the displacement events over the total fluid-injection time, thus treating the displacements as a cluster of cascading events resulting in a single moment magnitude, even though the fault-slip response in the model occurs over an extended injection time. Figure 4

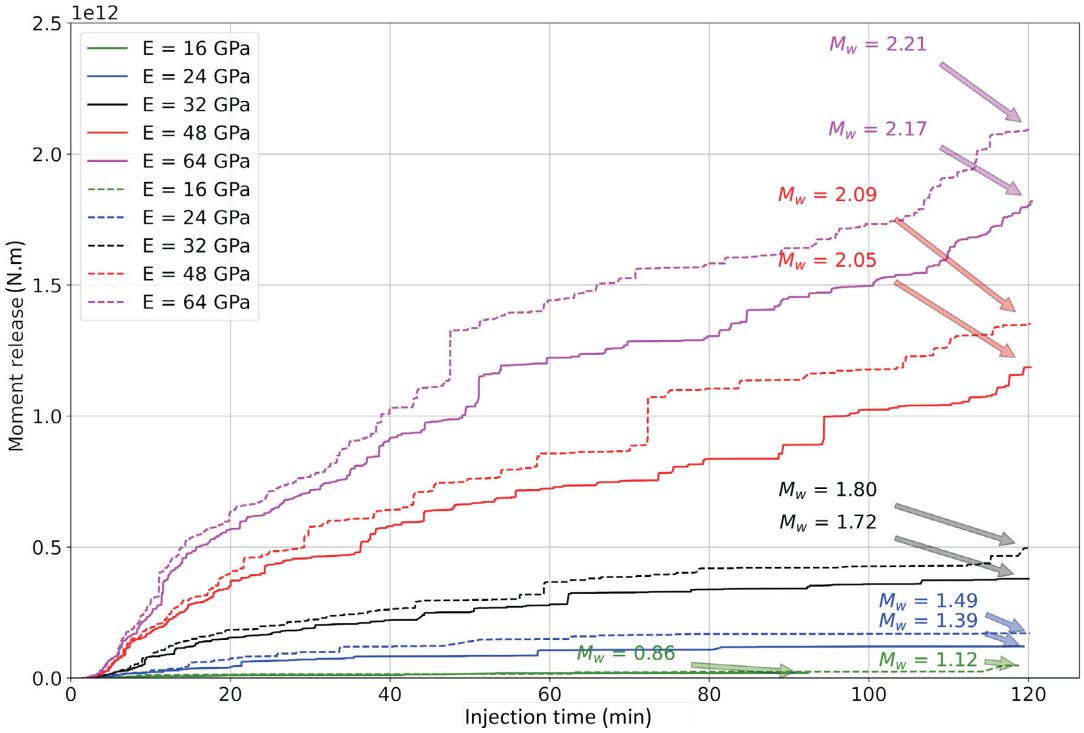

Figure 4. Plot of moment release versus fluid-injection time for models presenting different rock-mass stiffnesses (E). The modelled scenario is for a fault with a dip of 80° and a dip direction of 45° relative to a reverse fault far-field stress regime, assuming either a base-case (solid lines) or maximum (dashed lines) stress gradient. The quasi-static maximum moment magnitude (M_w) is reported for each case. Abbreviations: GPa, gigapascal; N·m, newton-metre.

shows the calculated maximum moment magnitudes (M_w) with arrows pointing at the end of the injection time.

As expected, the overall trend in Figure 4 indicates that higher rock-mass stiffnesses result in the potential for increased moment release and, thus, larger magnitude events. Comparing the solid and dashed lines, the results also suggest that as the differential stress increases, the moment release and maximum event magnitudes increase further. The latter can be explained mechanistically by comparing the shear to normal stress ratio acting on the fault prior to injection, which for the larger differential stress is slightly higher ($\tau/\sigma_n = 0.30$ for the maximum stress gradient compared to $\tau/\sigma_n = 0.18$ for the base-case stress gradient; Figure 5). Consequently, a higher differential stress results in a more critically stressed fault with a larger potential slip area, resulting in larger magnitude events. Viewed another way, a larger differential stress results in a larger stress-drop potential and therefore larger magnitude events. This is shown in Figure 6, which compares the stress drop with fault slip for the larger differential stress case (blue symbols) to that for the smaller differential stress case (green symbols).

Strike-Slip Far-Field Stress Regime

Figure 6 also includes, for comparison, the average stress drops modelled for the strike-slip far-field stress regime. These are seen to be significantly larger for the same rock-mass stiffness than the stress drops for the reverse fault far-field stress regime, including the maximum stress gradient case. This is further shown in Figure 7, which plots the moment release as a function of simulated injection time for each rock-mass stiffness. Comparing Figure 7 with the similar plot for the reverse fault far-field stress boundary condition (Figure 4), the moment release and event magnitudes

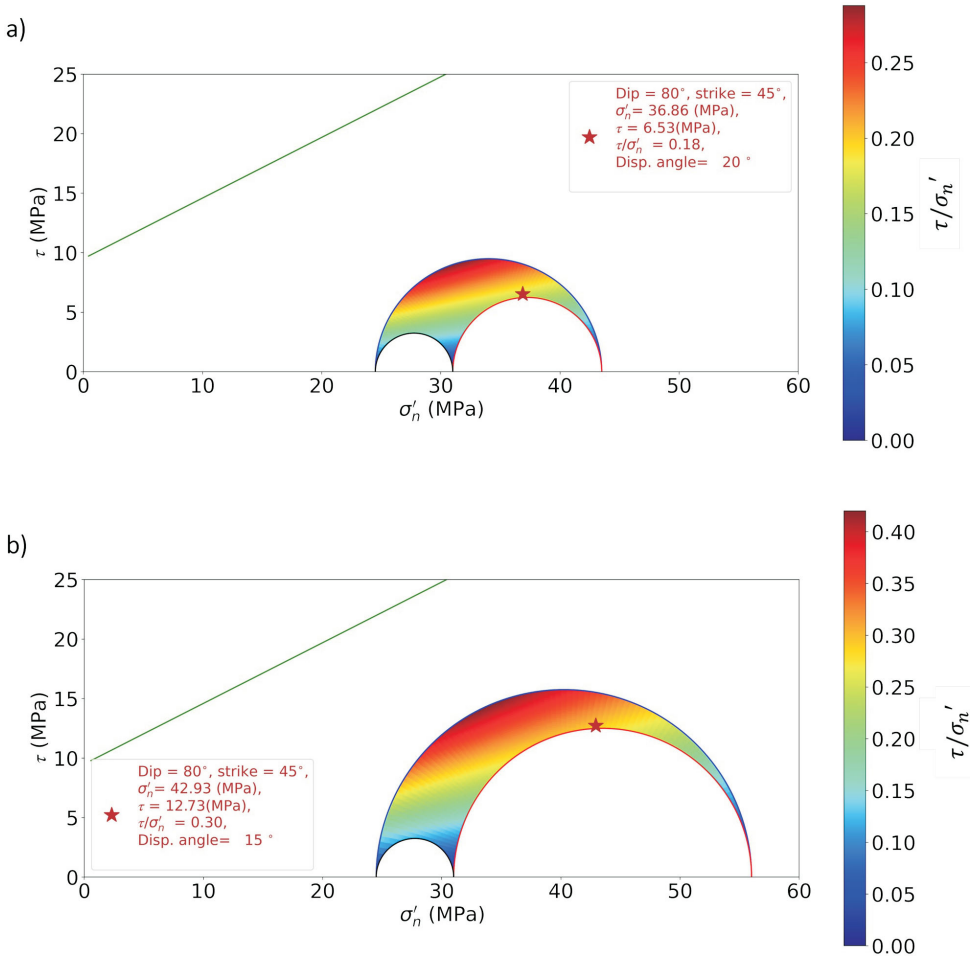

Figure 5. Mohr's circle three dimensional representations of the pre-injection effective normal and shear-stress ratios calculated for a depth of 2.4 km under a reverse fault far-field stress regime for the: **a)** base-case and **b)** maximum stress gradient scenarios. The green line represents the fault-failure envelope (i.e., μ = tan [27°] and c = 9.5 MPa) and its distance to the Mohr's circle prior to fluid injection into the reservoir. The red star indicates the stress state for a fault with a dip of 80° and a dip direction (Dip D) of 45° relative to the reverse fault far-field stresses. Also reported are the corresponding effective normal stress (σ_n') and shear stress (τ) ratio (τ/σ_n') as well as the displacement angle (i.e., the rake angle measured clockwise from the strike). Abbreviation: MPa, megapascal.

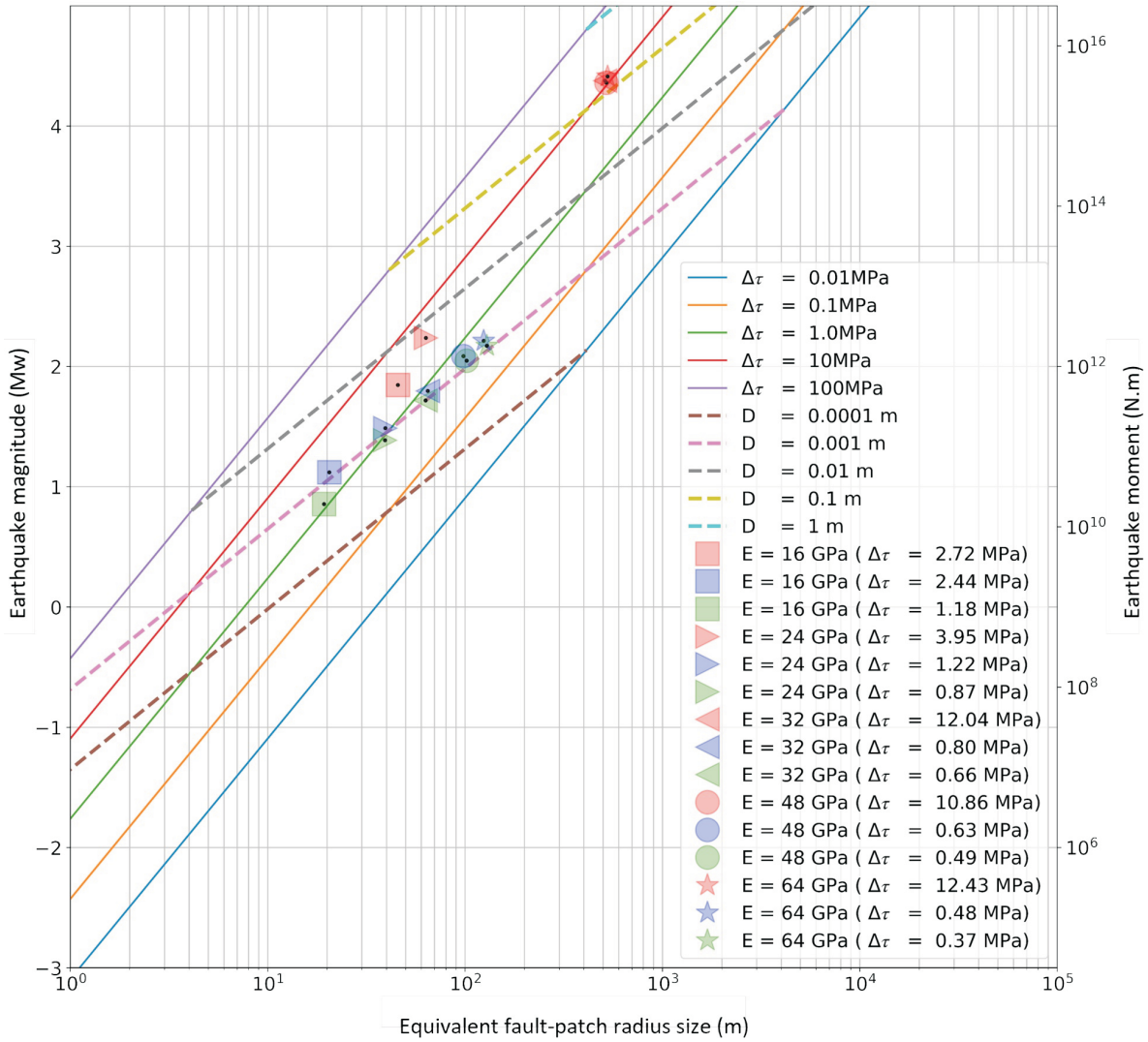

Figure 6. Average stress drop ($\Delta\tau$) and shear displacement (D), and corresponding event magnitude (M_w), derived from the simulation results as a function of rock-mass stiffness (E). The modelled scenario is for a fault with a dip of 80° and a dip direction 45° relative to a reverse fault far-field stress regime and base-case (green symbols) and maximum (blue symbols) stress gradient as well as a strike-slip far-field stress regime (red symbols). These values are based on the maximum induced-seismicity event occurring after 120 minutes of fluid injection. Abbreviations: GPa, gigapascal; MPa, megapascal; N·m, newton-metre.

are significantly higher for the strike-slip far-field stress boundary condition. This relates to the τ/σ_n ratio for the strike-slip far-field stress regime ($\tau/\sigma_n = 0.56$; see Figure 8) being nearly double that of the reverse fault far-field stress regime (see Figure 5). This shows that the strike-slip far-field stress regime, for the assumed fault orientation, results in the fault being more critically stressed, thus requiring a smaller fluid-pressure perturbation to cause slip over a larger area, which results in much larger events.

Figure 7 also shows for the intermediate case of the E = 32 GPa model an interesting deviation from the general trend of increasing moment release that corresponds to increasing rock-mass stiffness. The results for E = 32 GPa show a higher moment release than that recorded in the case of the stiffer E = 48 GPa model. Exploring this further, it can also be seen that there is a difference related to the injection time when the first sudden energy release and the corresponding moment magnitude ($M_{w,sud}$) is experienced. For the two higher stiffness cases (E = 64 and 48 GPa), this occurs after an injection time of 10 minutes, whereas for the intermediate case (E = 32 GPa) it is 20 minutes, and for the two lower stiffness cases (E = 24 and 16 GPa) it is 30 minutes. As previously discussed, for the same fluid-injection rate, the corresponding fluid pressures acting on the fault increase as the stiffness of the surrounding rock mass increases. Figure 9 shows the bottom-hole fluid pressures during the simulated injection (dashed lines), which confirms these are higher for the two stiffer formations during the first ten minutes of injection. What is seen in the models is that the critical pressure ($P_{f,crit}$; Figure 10) to initiate a

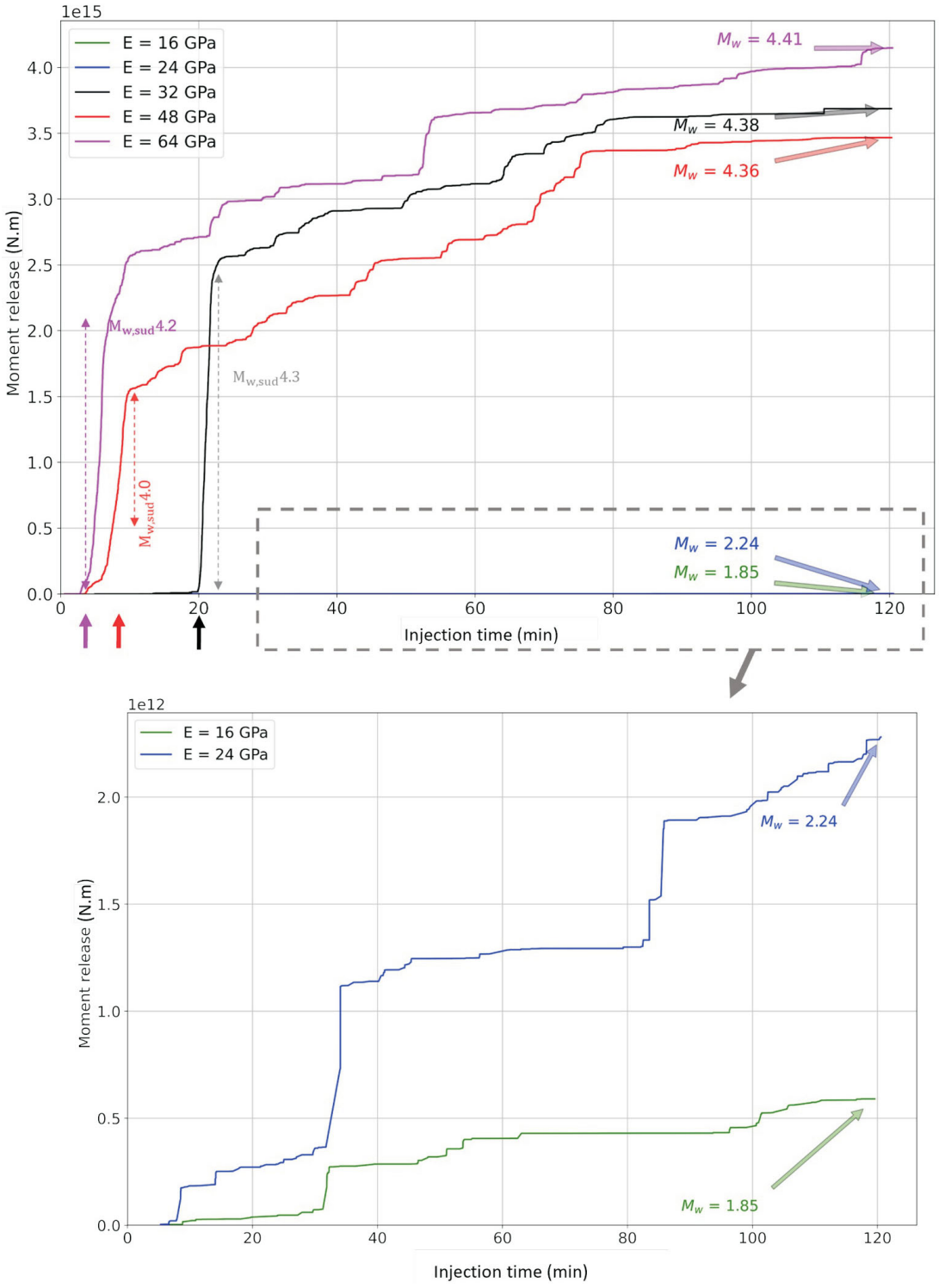

Figure 7. Plot of moment release versus fluid-injection time for models presenting different rock-mass stiffnesses (E). The modelled scenario is for a fault with dip of 80° and a dip direction of 45° relative to a strike-slip far-field stress regime. The quasi-static maximum moment magnitude (M_w) is reported for each case. The dashed arrows represent the sudden energy release and corresponding moment magnitude ($M_{w,sud}$). Panel below the main plot shows moment-release values three orders of magnitude smaller to highlight the details of the response in the case of the lower rock-mass stiffnesses. Note the three orders of magnitude difference in the moment release between the top panel (1e15) and the bottom panel (1e12). Abbreviations: GPa, gigapascal; N·m, newton-metre.

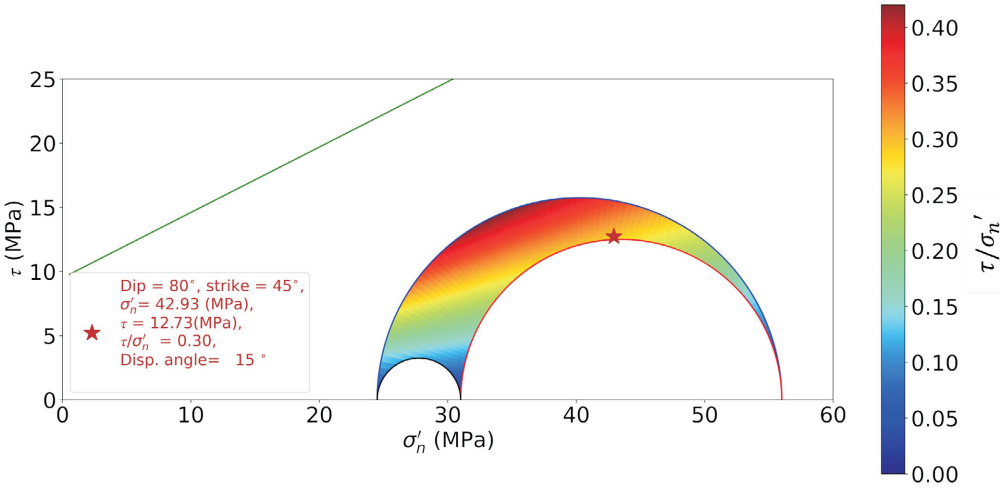

Figure 8. Mohr's circle three-dimensional representation of the pre-injection effective normal and shear-stress ratios calculated for a depth of 2.4 km under a strike-slip far-field stress regime. The green line represents the fault-failure envelope (i.e., μ = tan [27°] and c = 9.5 MPa) and its distance to the Mohr's circle prior to fluid injection into the reservoir. The red star indicates the stress state for a fault with a dip of 80° and a dip direction (Dip D) of 45° relative to the strike-slip far-field stresses. Also reported are the corresponding effective normal stress (σ_n') and shear stress (τ) ratio (τ/σ_n') as well as the displacement angle (i.e., the rake angle measured clockwise from the strike). Abbreviation: MPa, megapascal.

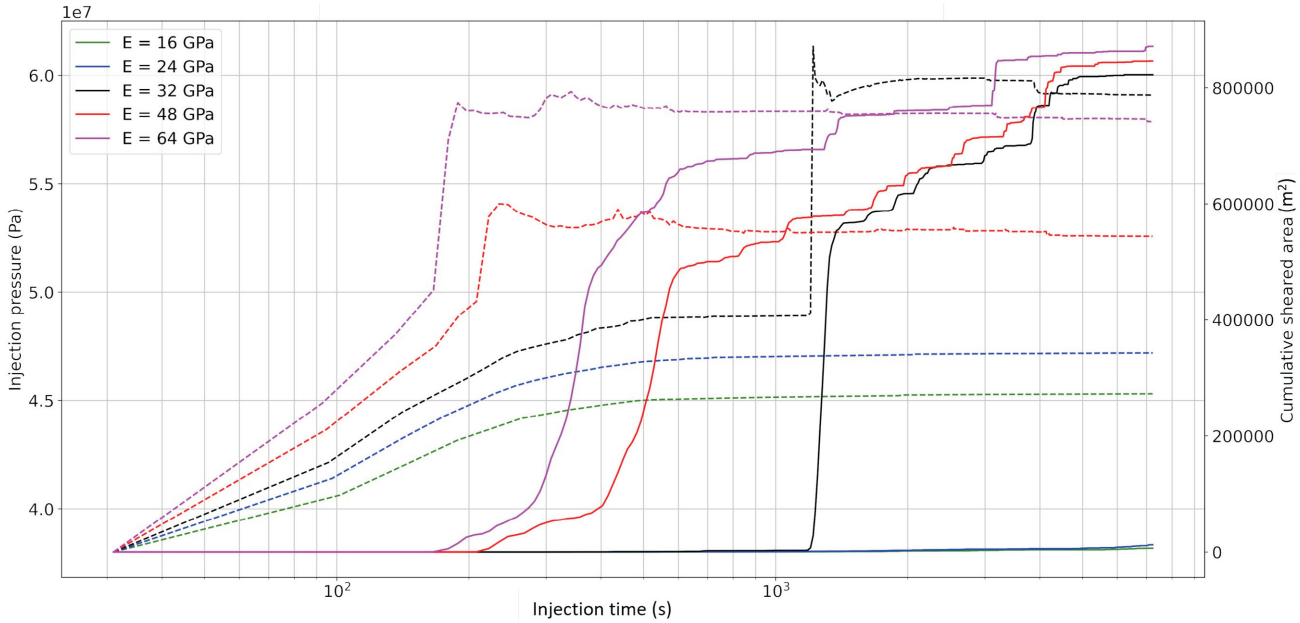

Figure 9. Bottom-hole injection pressures (dashed lines) and cumulative sheared area on the fault (solid lines) as a function of injection time for different rock-mass stiffnesses (E). The modelled scenario is for a fault with a dip of 80° and a dip direction of 45° relative to a strike-slip stress regime. Abbreviations: GPa, gigapascal; Pa, pascal.

fault-slip event is reached with smaller injection volumes for stiffer rocks. At the same time, the smaller injection volumes mean that the areal extent of the increased pore pressures acting on the fault surface is also smaller. Therefore, two factors are at play in the XSite models with respect to the magnitude of the induced-seismicity event (Figure 10):

- the level of stress experienced by the fault in relation to the in situ stress condition and the corresponding stress drop
- the areal extent along the fault experiencing the pore-pressure increase resulting from the fluid injection, which introduces a temporal component related to the injection rate.

As the formation stiffness decreases, it takes a higher fluid pressure acting on the fault to trigger a slip event, which requires a longer injection time and, thus, a larger injection volume can radiate further into the fault, resulting in a

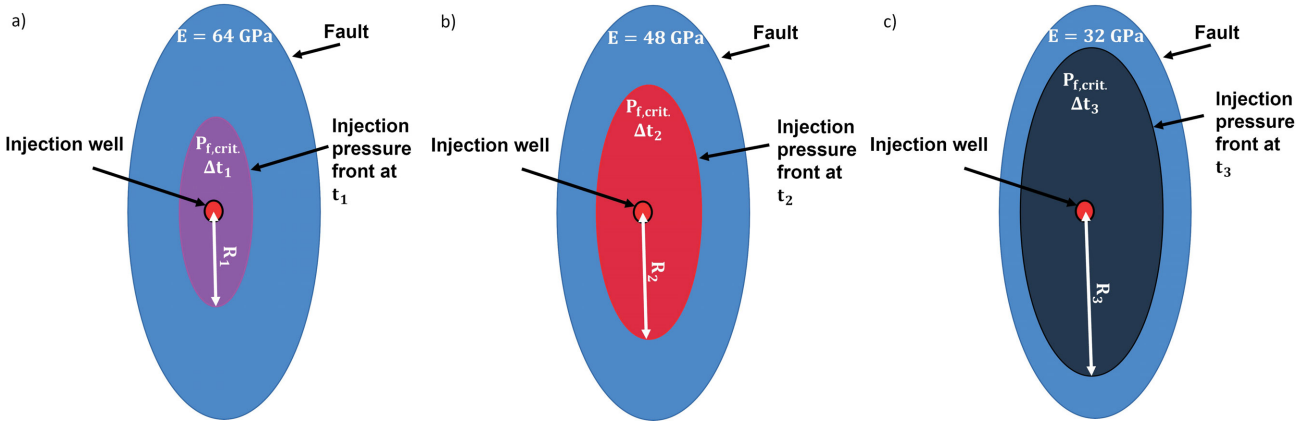

Figure 10. Schematic representation of the fluid-injection front at the time of the first seismic moment release, as observed in Figure 7. The colours of the injection pressure fronts above match those for the rock-mass stiffnesses (E) in Figure 7: **a)** E = 64 GPa model (purple); **b)** E = 48 GPa model (red); and **c)** E = 32 GPa model (black). Each shows the respective area of fluid pressure acting on the fault increasing with injection time (t). The corresponding injection times are, from left to right, $\Delta t_1 \geq \Delta t_2 \geq \Delta t_3$. Abbreviation: GPa, gigapascal.

larger affected fault area. Comparing rock-mass stiffness values E = 64 GPa (Figure 10a) and E = 48 GPa (Figure 10b), the models are comparable in their sensitivity to the fluid pressure and, therefore, they slip at similar times, with the E = 64 case generating a larger slip area (solid lines in Figure 10a) and stress drop as the fault is more critically stressed. In contrast, the E = 24 GPa and E = 16 GPa models are less critically stressed, and thus require longer injection times (larger injection volumes) for pressures acting on the fault to be sufficient, relative to the corresponding aerial extent of fault weakening, to trigger slip.

It should be noted that although the area on the fault affected by the pore-pressure increase is larger for the lower rock-mass stiffness cases, this does not translate into larger induced-seismicity–event magnitudes. Although the influenced area is larger, the area satisfying the shear-slip criterion is smaller, resulting in a smaller seismic moment.

Thus, in the case of the E = 32 GPa model (Figure 10c), an intermediate condition exists. Because the fault in this case is less critically stressed compared to the higher stiffness cases, a longer injection time is possible, allowing more fault area to see an increase in fluid pressure (and decrease in effective stress). At the same time, the rock is still stiff enough to store considerable strain energy. The combined result is that when the induced-seismicity event is triggered, there is more seismic energy suddenly released in the case of the E = 32 GPa model than in that of the E = 48 GPa model.

Conclusion

The numerical modelling results would suggest that these are wells that are possibly in proximity to faults in higher stiffness rock in a strike-slip far-field stress regime (see Figure 7). Although the XSite modelled scenario includes numerous simplifications and generalizations, it is interesting to note that the average formation stiffness for the Montney is approximately 32 GPa (Figure 2) and that the crystalline basement rocks would be even stiffer. These results suggest that, when operating in a strike-slip far-field stress regime in stiffer rocks and there are fewer early events of M_w >1 or 2 than expected, this might indicate that strain energy is accumulating toward a large M_w >4 event. Similarly, in the context of a traffic light protocol (e.g., Walters et al., 2015) and seismic hazard, the detection of a M_w 2 event might be more concerning when the formation targeted by the injection, or adjacent to it, is stiffer (e.g., E >32 GPa). These results assume a good hydraulic communication between the injection wells and the fault leading to the observation of early seismicity (i.e., creating a strong correlation between fluid injection and the observation of induced seismicity). It should also be noted that in these results, activity after shut-in is not considered and large induced-seismicity events can occur after well shut-in (e.g., Häring et al., 2008). The next step in this study will be to examine the effect of formation-stiffness anisotropy on injection-induced seismicity behaviour.

Acknowledgments

The authors would like to thank Geoscience BC, Itasca Consulting Group, Inc. and Golder Associates Ltd. for their financial support. They would also like to thank S. Hendi and M. Gorjian for their input and constructive comments on aspects of this work.

References

Abdelaziz, A., Ha, J., Khair, H.A., Adams, M., Tan, C.P., Musa, I.H. and Grasselli, G. (2019): Unconventional shale hydraulic fracturing under true triaxial laboratory conditions, the value of understanding your reservoir; SPE Annual Technical Conference and Exhibition, Society of Petroleum Engineers, September 30–October 2, 2019, Calgary, Alberta,

abstract no. SPE-19026-MS, URL <https://doi.org/10.2118/196026-ms>.

Atkinson, G.M., Eaton, D.W., Ghofrani, H., Walker, D., Cheadle, B., Schultz, R., Shcherbakov, R., Tiampo, K., Gu, J., Harrington, R.M., Liu, Y., Van Der Baan, M. and Kao, H. (2016): Hydraulic fracturing and seismicity in the Western Canada Sedimentary Basin; Seismological Research Letters, v. 87, no. 3, p. 631–647, URL <https://doi.org/10.1785/0220150263>.

Chen, Q. and Wong, R.C.K. (2018): Mode I and mode II fracture toughness of Montney shale; 52nd U.S. Rock Mechanics/Geomechanics Symposium, June 17–20, 2018, Seattle, Washington, abstract no. ARMA-2018-127, URL <https://onepetro.org/ARMAUSRMS/proceedings-abstract/ARMA18/All-ARMA18/ARMA-2018-127/124120> [October 2020].

Damjanac, B., Detournay, C. and Cundall, P.A. (2016): Application of particle and lattice codes to simulation of hydraulic fracturing; Computational Particle Mechanics, v. 3, no. 2, p. 249–261, URL <https://doi.org/10.1007/s40571-015-0085-0>.

Ellsworth, W.L., Giardini, D., Townend, J., Ge, S. and Shimamoto, T. (2019): Triggering of the Pohang, Korea, Earthquake (M_W 5.5) by enhanced geothermal system stimulation; Seismological Research Letters, v. 90, no. 5, p. 1844–1858, URL <https://doi.org/10.1785/0220190102>.

Fox, A.D. and Watson, N.D. (2019): Induced seismicity study in the Kiskatinaw Seismic Monitoring and Mitigation Area, British Columbia; report prepared for the BC Oil and Gas Commission, 51 p., URL <https://www.bcogc.ca/data-reports/reports/?year=2019> [January 2020].

Javaheri, A., Dehghanpour, H. and Wood, J. M. (2017): Tight rock wettability and its relationship to other petrophysical properties: a Montney case study; Journal of Earth Science, v. 28, no. 2, p. 381–390, URL <https://doi.org/10.1007/s12583-017-0725-9>.

Häring, M.O., Schanz, U., Ladner, F. and Dyer, B.C. (2008): Characterisation of the Basel 1 enhanced geothermal system; Geothermics, v. 37, no. 5, p. 469–495, URL <https://doi.org/10.1016/J.GEOTHERMICS.2008.06.002>.

Kettlety, T., Verdon, J.P., Butcher, A., Hampson, M. and Craddock, L. (2021): High-resolution imaging of the M_L 2.9 August 2019 earthquake in Lancashire, United Kingdom, induced by hydraulic fracturing during Preston New Road PNR-2 operations; Seismological Research Letters, v. 92, no. 1, p. 151–169, URL <https://doi.org/10.1785/0220200187>.

Majer, E.L., Baria, R., Stark, M., Oates, S., Bommer, J., Smith, B. and Asanuma, H. (2007): Induced seismicity associated with enhanced geothermal systems; Geothermics, v. 36, no. 3, p. 185–222, URL <https://doi.org/10.1016/J.GEOTHERMICS.2007.03.003>.

Malo, M., Moutenet, J.-P., Bédard, K. and Raymond, J. (2015): Public awareness and opinion on deep geothermal energy in the context of shale gas exploration in the Province of Québec, Canada; *in* Proceedings of the World Geothermal Congress, April 19–25, 2015, Melbourne, Australia, 8 p.

Matzel, E., Templeton, D., Petersson, A. and Goebel, M. (2014): Imaging the Newberry EGS site using seismic interferometry; *in* Proceedings of the Thirty-Ninth Workshop on Geothermal Reservoir Engineering, February 24–26, 2014, Stanford, California, 4 p.

McGarr, A. (2014): Maximum magnitude earthquakes induced by fluid injection; Journal of Geophysical Research: Solid Earth, v. 119, no. 2, p. 1008–1019, URL <https://doi.org/10.1002/2013JB010597>.

McKean, S.H. and Priest, J.A. (2019): Multiple failure state triaxial testing of the Montney Formation; Journal of Petroleum Science and Engineering, v. 173, p. 122–135, URL <https://doi.org/10.1016/J.PETROL.2018.09.004>.

McLellan, P. (2016): Geomechanical characterization of the Farrell Creek Montney reservoir, northeast British Columbia; SPE Workshop: the Montney Play; Society of Petroleum Engineers, October 18, 2016, Calgary, Alberta, Canada, workshop presentation.

National Energy Board, BC Oil and Gas Commission, Alberta Energy Regulator and BC Ministry of Natural Gas Development (2013): Energy briefing note: the ultimate potential for unconventional petroleum from the Montney Formation of British Columbia and Alberta; National Energy Board, BC Oil and Gas Commission, Alberta Energy Regulator and BC Ministry of Natural Gas Development, briefing note, 23 p., URL <https://www.cer-rec.gc.ca/en/data-analysis/energy-commodities/natural-gas/report/ultimate-potential-montney-formation/the-ultimate-potential-unconventional-petroleum-from-montney-formation-british-columbia-alberta-energy-briefing-note.html> [September 2020].

Rogers, S., McLellan, P. and Webb, G. (2014): Investigation of the effects of natural fractures and faults on hydraulic fracturing in the Montney Formation, Farrell Creek gas field, British Columbia; International Discrete Fracture Network Engineering Conference, October 1–13, 2014, Vancouver, British Columbia, art. 224, 12 p.

Tenthorey, E. and Cox, S.F. (2006): Cohesive strengthening of fault zones during the interseismic period: an experimental study; Journal of Geophysical Research: Solid Earth, v. 111, no. B9, art. B09202, 14 p., URL <https://doi.org/10.1029/2005JB004122>.

Trutnevyte, E. and Ejderyan, O. (2017): Managing geoenergy-induced seismicity with society; Journal of Risk Research, v. 21, no. 10, p. 1287–1294, URL <https://doi.org/10.1080/13669877.2017.1304979>.

Vaisblat, N., Shokri, A.R., Ayranci, K., Harris, N. and Chalaturnyk, R.J. (2019): Significance of rock compositional control on geomechanical properties and hydraulic fracturing of the Montney Formation, Western Canadian Basin; Asia Pacific Unconventional Resources Technology Conference, November 18–19, 2019, Brisbane, Australia, p. 752–784, URL <https://doi.org/10.15530/ap-urtec-2019-198199>.

Vishkai, M. and Gates, I. (2019): On multistage hydraulic fracturing in tight gas reservoirs: Montney Formation, Alberta, Canada; Journal of Petroleum Science and Engineering, v. 174, p. 1127–1141, URL <https://doi.org/10.1016/J.PETROL.2018.12.020>.

Walters, R.J., Zoback, M.D., Baker, J.W. and Beroza, G.C. (2015): Characterizing and responding to seismic risk associated with earthquakes potentially triggered by fluid disposal and hydraulic fracturing; Seismological Research Letters, v. 86, no. 4, p. 1110–1118, URL <https://doi.org/10.1785/0220150048>.

Zoback, M. and Kohli, A. (2019): Unconventional Reservoir Geomechanics: Shale Gas, Tight Oil, and Induced Seismicity; Cambridge University Press, Cambridge, United Kingdom, 492 p., URL <https://doi.org/10.1017/9781316091869>.

Comprehensive Physical Model for the Contrasting Seismogenic Behaviours of Injection Wells in the Kiskatinaw Seismic Monitoring and Mitigation Area, Northeastern British Columbia (NTS 093P, 094A)

B. Wang, School of Earth and Ocean Sciences, University of Victoria, Victoria, British Columbia
beiwang@uvic.ca

H. Kao, Natural Resources Canada, Geological Survey of Canada–Pacific, Sidney, British Columbia

H. Yu, Natural Resources Canada, Geological Survey of Canada–Pacific, Sidney, British Columbia

R. Visser, Natural Resources Canada, Geological Survey of Canada–Pacific, Sidney, British Columbia

S. Venables, British Columbia Oil and Gas Commission, Victoria, British Columbia

Wang, B., Kao, H., Yu, H., Visser, R. and Venables, S. (2022): Comprehensive physical model for the contrasting seismogenic behaviours of injection wells in the Kiskatinaw Seismic Monitoring and Mitigation Area, northeastern British Columbia (NTS 093P, 094A); *in* Geoscience BC Summary of Activities 2021: Energy and Water, Geoscience BC, Report 2022-02, p. 35–48.

Introduction

Induced earthquakes are defined as events caused by anthropogenic activities and their occurrence can be traced back over five decades (Healy et al., 1968; Raleigh et al., 1976). During the past ten years, subsurface fluid injection has drawn increasing attention due to its association with a dramatic increase in regional/local seismicity; for example, the number of earthquakes of magnitude (M_w) >3 increased by a factor of 10 in the central United States. Most of these events have been attributed to wastewater-disposal (WD) operations that are often associated with high injection rates and a large amount of cumulative volume (Ellsworth, 2013; Keranen and Weingarten, 2018). Comparably, hydraulic fracturing (HF) stimulations can also trigger ≥M_w 4 earthquakes, and many cases have been documented in areas such as the Western Canada Sedimentary Basin (WCSB) and southwestern China (e.g., Atkinson et al., 2016; Bao and Eaton, 2016; Schultz et al., 2018; Lei et al., 2019; Wang et al., 2020; Yu et al., 2020).

Progress has been made to characterize the various controlling factors of the HF-related injection-induced earthquakes (IIEs) in the WCSB. For example, Schultz and Eaton (2018) suggested that IIEs preferentially locate within regions with overpressured formations, whereas Schultz et al. (2016) and Galloway et al. (2018) found that specific geological conditions, such as the reef margins and fault-related karst features, tend to correlate with more IIEs due to their ability to guide fluid flow to the faults. Similarly, Peña Castro et al. (2020) and Wang et al. (2020) proposed that several of the largest IIEs in western Canada have occurred on pre-existing faults, with possible direct connection to highly permeable conduit structures. Schultz et al. (2018) further delineated a linear relationship between the cumulative injection volume of a single HF pad and the number of HF-related IIEs. Many studies also suggested that in situ regional stress could be another important factor facilitating seismic slip on a fault (e.g., Zoback and Lund Snee, 2018; Shen et al., 2019). On a regional scale, Kao et al. (2018) pointed out that the tectonic-strain rate plays a key role in controlling the spatial distribution of IIEs in the WCSB.

These innovative breakthroughs provided a first-order understanding of the seismogenic factors associated with IIEs in the WCSB. However, comprehensive investigations to evaluate the relative significance of each of these factors are hindered by the lack of a high-quality catalogue of IIEs and the limited access to well-operation databases. In addition to delineating possible controlling factors of IIEs in western Canada, two key questions related to their causal mechanisms also need to be considered. The first relates to the reason why the seismic response to comparable injection activities within the same shale play varies significantly. An interesting example is the Duvernay play in Alberta, where the Kaybob region is more seismogenic than the Willesden Green or Edson regions (Schultz et al., 2018). The other is concerned with how to forecast the corresponding seismogenic behaviour when multiple formations are targeted by the same HF pad. A typical example is the Kiskatinaw Seismic Monitoring and Mitigation Area (KSMMA) in northeastern British Columbia (BC), where the gas-bearing stratigraphy of the Montney Formation can be subdivided, from top to bottom, into the Upper Montney (UM), upper Middle Montney (UMM), lower Middle Montney (LMM) and Lower Montney (LM) members (Figure 1;

This publication is also available, free of charge, as colour digital files in Adobe Acrobat® PDF format from the Geoscience BC website: http://geosciencebc.com/updates/summary-of-activities/.

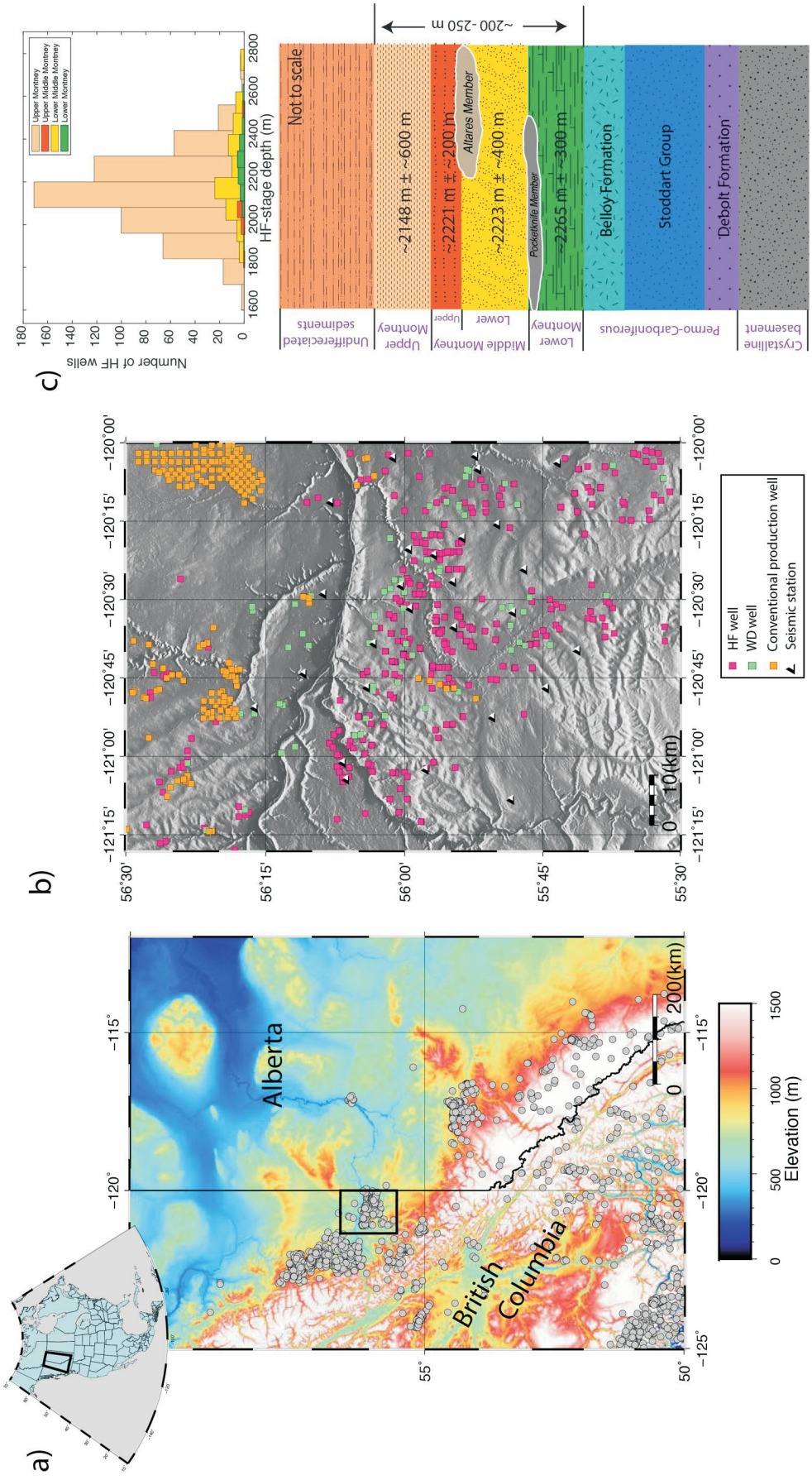

Figure 1. Spatial distribution of earthquakes and injection wells in western Canada. **a)** Grey circles mark epicentres of magnitude 3 or greater seismicity in northeastern British Columbia and western Alberta between 2011 and 2020, as reported by Natural Resources Canada. The black rectangle marks the study area in the Kiskatinaw Seismic Monitoring and Mitigation Area in northeastern British Columbia. **b)** Hydraulically fractured production wells (HF) and wastewater-disposal wells (WD), conventional oil-and-gas production wells and seismic stations in the study area. **c)** Top panel shows the number of HF wells targeting different Montney Formation members as a function of depth; bottom panel shows a stratigraphic column of the Montney Formation and the underlying Permo-Carboniferous formations.

Davies et al., 2018). The HF operations targeting these members offer a natural laboratory in which to differentiate the possible seismic response within different stratigraphic units.

The seismic-station coverage in northeastern BC has been systematically improved since 2013 (Figure 1). Over the years, the newly established stations have lowered the regional earthquake-detection threshold by 1 to 2 units of magnitude (Babaie Mahani et al., 2016; Babaie Mahani, 2021) and thus provide a unique opportunity to enhance the existing earthquake catalogue (Visser et al., 2017, 2020) as well as to investigate, at an unprecedented resolution, the detailed spatiotemporal distribution of IIEs relative to potential influencing factors. In this study, a series of Monte Carlo tests and detailed statistical analysis based on an enhanced earthquake catalogue were used to determine the relative significance of physical factors that control the local seismogenic pattern of IIEs. A comprehensive model was developed, using injection type, regional structural geology and stratigraphic setting as the top three factors explaining observations from the study. Initial observations presumably indicate that injections, even at the same geographic location, can have very different IIE responses, depending on the target's stratigraphic setting. This finding will help bridge the gap in understanding how anthropogenic/hydrogeologic/stratigraphic factors impact the occurrence of IIEs and lead to substantial progress in effectively mitigating injection-related seismic hazard.

Data and Methods

The fluid injection parameters from completion reports in the BC Oil and Gas Commission database (BC Oil and Gas Commission, 2021) were compiled. Wastewater-disposal injection is usually a continuous process lasting for months or years, in contrast to a HF stage that is often finished within a few hours. There is also a big difference in the injection rate (~0.5 m^3/min in the case of WD injections vs. ~10 m^3/min in that of HF injections). In this study, the WD- and HF-injection operations in the stratigraphic unit are quantified by month and stage, respectively, based on the technical/completion reports submitted to the regulator by local operators. In total, 20 293 HF stages were undertaken at 778 horizontal wells and 58 WD-injection wells were active for 1151 months. Detailed information on the stratigraphic setting of all injection wells is retrieved from the BC Oil and Gas Commission (2021) database.

The waveform data used has been retrieved from broadband seismic stations belonging to three local and regional seismograph networks (network codes XL, 1E and PQ, operating at a digitization rate of 100 samples/s). The first step consisted in deploying the sophisticated earthquake-location method, referred to as 'source-scanning based on navigated automatic phase-picking' (Tan et al., 2019), to detect and locate events within the study area that occurred between January 1, 2017 and December 31, 2018. To minimize errors resulting from inaccurate travel times, the 1-D velocity model developed specifically for the KSMMA area by Babaie Mahani et al. (2020) was adopted. About 250 times more events have been detected and located (10 693 events in total; Figure 2a) using the method outlined in this study, compared to the number reported in the standard Natural Resources Canada (NRCan) earthquake catalogue (Natural Resources Canada, 2021) , which is mainly based on visual inspection of seismic phases recorded by much fewer stations.

Next, the newly developed depth-scanning algorithm (DSA; Yuan et al., 2020) is used to refine the focal depth of earthquakes of M_w 2.5 or greater recorded in the enhanced catalogue. The DSA improves the focal-depth accuracy by incorporating the travel-time constraint from depth phases recorded at local and regional distances. The scanning range of focal depth is set at 1 to 35 km and the scanning process consists of three major steps: firstly, the waveforms of all possible depth phases are constructed from the direct P and S phases; secondly, the synthetic depth-phase waveforms are used as templates to scan the observed seismograms for any segments with high waveform similarity; lastly, the depth corresponding to the largest number of depth-phase matches and minimum accumulated travel-time residual is deemed the final solution.

Using the enhanced earthquake catalogue and compiled fluid-injection data, a Monte Carlo test is conducted, following the method presented in Schultz et al. (2016), to verify whether IIEs are statistically correlated with injection activities. Based on the naive assumption that all epicentres are randomly distributed, 10 000 synthetic catalogues (each with the same number of events as the real catalogue) are created. For each synthetic catalogue, the average distance between earthquake epicentre and the nearest injection activity is calculated. These 10 000 event-to-well averaged-distance values from the synthetic catalogues are then compared with the actual distances derived from the real catalogue and injection data.

Finally, by deploying a spatiotemporal correlation filter (STCF), IIEs are associated with corresponding HF stages to determine the role of the stratigraphic setting, as was done in a prior study (Schultz et al., 2018). As a prerequisite, the earthquake must have occurred within a certain time window after the stimulation stage. Once this temporal criterion is satisfied, the earthquake is assigned to the nearest HF stage, so long as the pair also satisfies the spatial criterion.

Results

In this section, the physical factors that control the pattern of IIEs in the KSMMA are systematically delineated. By

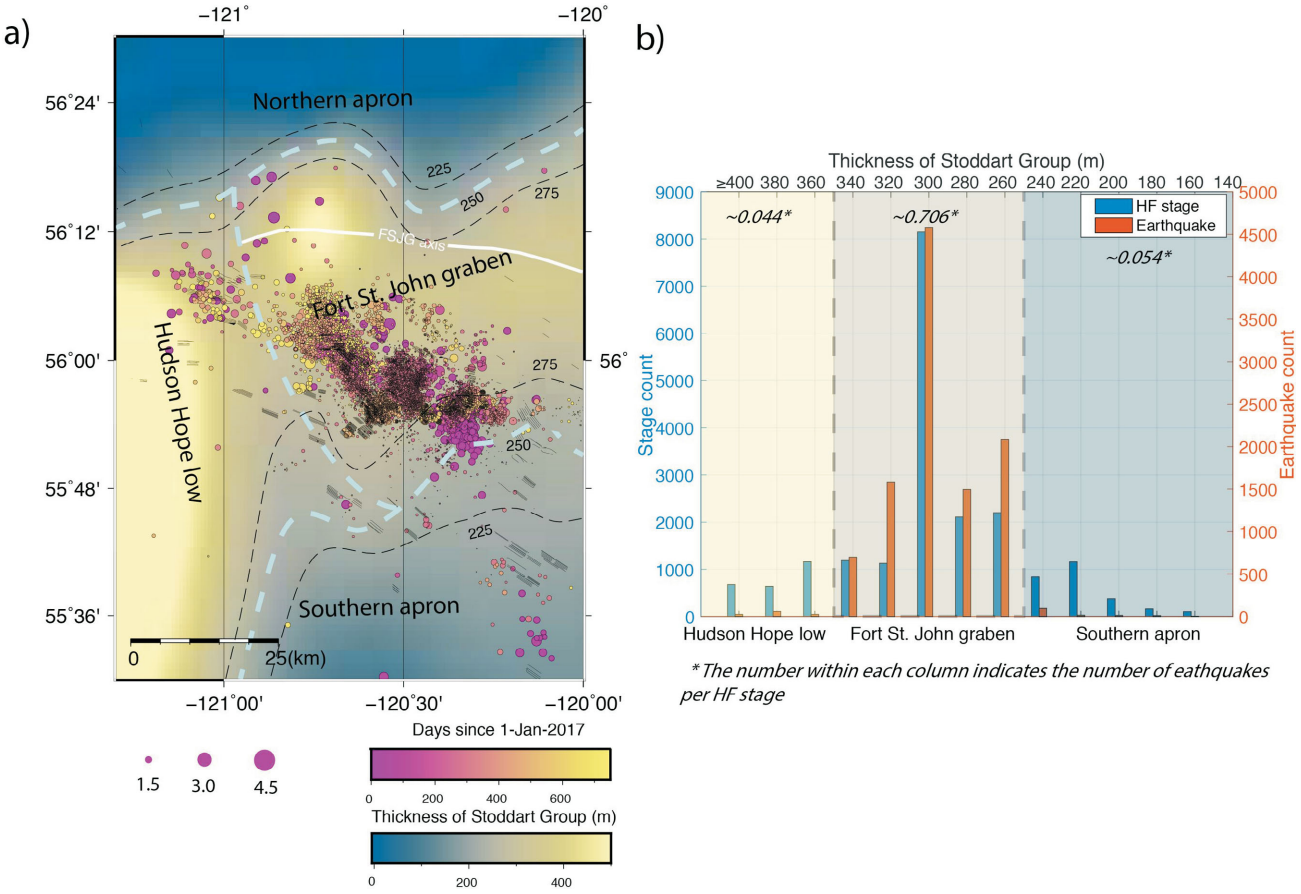

Figure 2. Major geological structures and seismic pattern in the study area, northeastern British Columbia. **a)** Spatiotemporal distribution of injection-induced earthquakes with respect to the regional structural geology. Thick dashed lines represent the inferred boundaries of different tectonic elements based on the thickness (thin dashed lines) of the Stoddart Group (SG). The inferred boundary between the Fort St. John graben (FSJG) and the deeper Hudson Hope low to the west is shown as well as the FSJG axis indicated by the white line (adapted from O'Connell, 1994). **b)** Number of hydraulic-fracturing stages and earthquakes corresponding to different SG thicknesses. Note that the SG thickness of each earthquake is approximated with the measurement corresponding to the closest hydraulic-fracturing (HF) well.

comparing the level of seismicity of comparable injection activities, an attempt is made to determine the relative significance of the recognized factors.

Most Influential Factor: Injection Type

As shown in Figure 3, the Monte Carlo-simulation results suggest that the randomly generated synthetic catalogues all present significantly greater event-to-well distances when compared to the real earthquake catalogue (~10 km vs. ~1 km). The distance difference becomes even greater once a temporal constraint of no longer than five days is imposed on the triggering delay (~35 km vs. ~7 km). Since none of the 10 000 synthetic catalogues yields an averaged event-to-well distance comparable to the observed value, the probability of earthquakes being randomly distributed in the study area must be $<10^{-4}$. This result suggests that the association proposed between earthquake occurrence and injection operations is statistically significant.

The average distance between individual catalogued earthquakes and the nearest HF and WD wells is then calculated, following the approach used in Schultz et al. (2018). The average distance from an earthquake epicentre to the closest WD operation has been found to be approximately four times the distance associated with the closest HF stage (~4 km vs. ~1 km; Figure 3c), which suggests that HF activities might play a more significant role in inducing these events.

Secondary Factor: Regional Structural Geology

In the study area, the predominant geological structure is the Dawson Creek graben complex (DCGC), consisting of the core Fort St. John graben (FSJG), the western zone of greater subsidence (i.e., the Hudson Hope low [HHL]), the northern and southern sediment aprons, and the smaller satellite grabens to the east (Barclay et al., 1990; O'Connell, 1994). The structural development of the DCGC is closely linked to the deposition of the Stoddart Group (SG) and the thin, overlying Belloy Formation (Barclay et al., 1990). Barclay et al. (1990) used the thickness of the SG as a proxy to estimate the boundary of the FSJG, which is an asymmetric structure with a gently sloping, but less constrained,

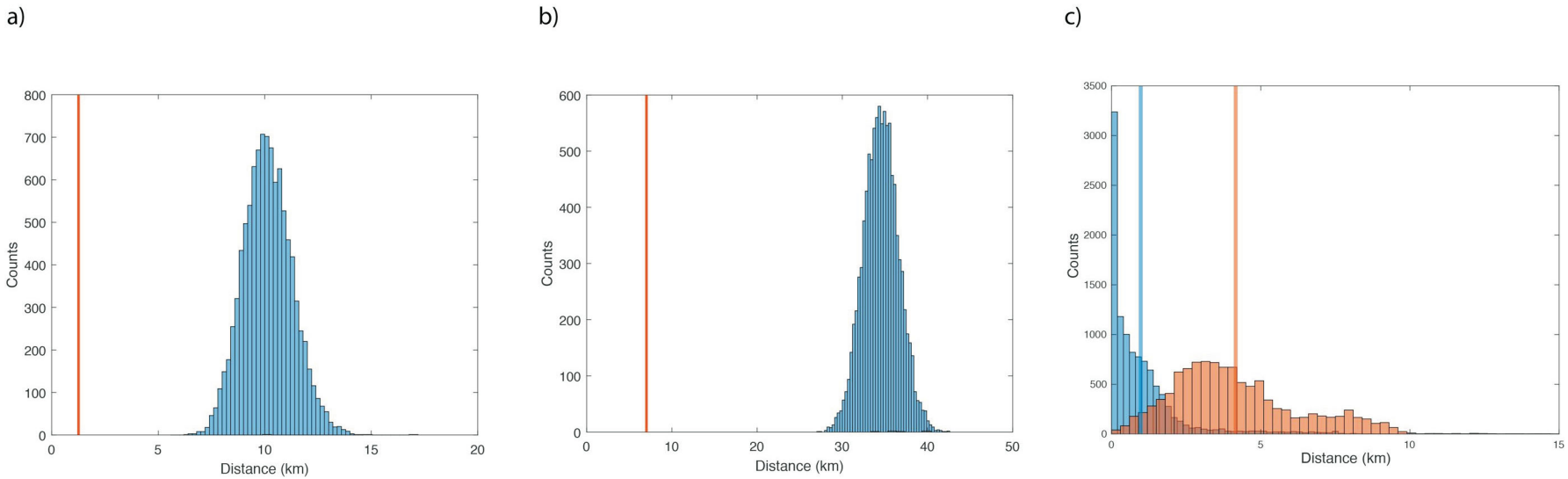

Figure 3. Results of Monte Carlo tests used to examine whether the seismicity observed in the study area, northeastern British Columbia, is correlated with injection operations. **a)** Assuming that earthquake epicentres are randomly distributed, the histogram shows the distribution of the average distance between an epicentre and the nearest injection well from a population of 104 synthetically generated catalogues. This experiment is done without imposing a time constraint. The solid vertical line represents the average distance between an epicentre and the nearest injection well, derived from an enhanced earthquake catalogue (using a total of 10 693 events). **b)** Similar to a), but with a five day time constraint to correlate the earthquake to the nearest injection well. **c)** Distribution of the distance between an earthquake epicentre and the nearest hydraulic fracturing (blue bars) or wastewater-disposal (red bars) well. The two vertical lines represent the average values.

southern apron. Conventionally, different thickness contours of the SG are used to define the northern (150–200 m) and southern (270–300 m) edges of the FSJG (Figure 2a). However, in this study, a more consistent approach is taken and the boundary between the FSJG and the surrounding aprons is set at the SG-thickness contour of 250 m (Figure 2a).

The number of earthquakes and HF stages within the areas of FSJG, HHL and the southern apron (the number of HF wells in the northern apron is insufficient) was counted. As shown in Figure 2b, the level of seismicity is the highest within the FSJG area (corresponding to a SG thickness between 250 and 350 m), whereas the number of earthquakes is almost negligible in the HHL and southern apron areas. In total, 10 439, 110 and 144 events were observed for the FSJG, HHL and southern apron areas, respectively, whereas the corresponding number of HF stages performed in these three areas were recorded as 14 778, 2488 and 2642, respectively. On average, the ratio between the number of earthquakes and HF stages is ~0.706 in the FSJG area, but only ~0.044 and ~0.054 in the areas of the HHL and southern apron. These results suggest that HF injections in the FSJG area have a much greater likelihood of inducing an earthquake.

The next step consists in examining whether the drastically different levels of local seismicity can be explained as the result of the injection of different cumulative volumes of fluids. It turns out that the cumulative injected volume is approximately linearly correlated with the cumulative number of HF stages (Figure 4). Consequently, the total volume of HF injections in the FSJG area is approximately 5.9 times higher than that in the HHL area and ~5.6 times higher than that in the southern apron. The number of earthquakes per one million cubic metres of injected volume is ~1413 for the FSJG area, which is ~15 times higher than the number of events in the HHL (~88) and southern apron (~107) areas. Therefore, the difference between injection volumes cannot fully account for the extreme variations of local seismicity in the three subareas; these ratios again underscore the significance of the area's geological structures.

Third Factor: Stratigraphic Setting

In the KSMMA, the majority of HF stimulations aim at the UM, followed by the LMM, and only a very small number of HF wells target the UMM and LM (Figure 1c). The depth of each Montney member can vary from one location to another, ranging from ~1.5 to ~2.5 km below the surface, as inferred from HF completion reports. Overall, the total thickness of the Montney Formation is ~100–250 m. The seismic response to injections within the different members (or depths) remains unclear.

Figure 5 shows the results of a STCF analysis using time and distance thresholds of 3 days and 3 km, respectively. While the number of HF stages targeting the LMM is only ~1/5 of that targeting the UM, the number of IIEs associated with the LMM HF stimulations is much higher (Figure 5b). Furthermore, a *p*-value was calculated to test the validity of a null hypothesis proposing that HF stages tar-

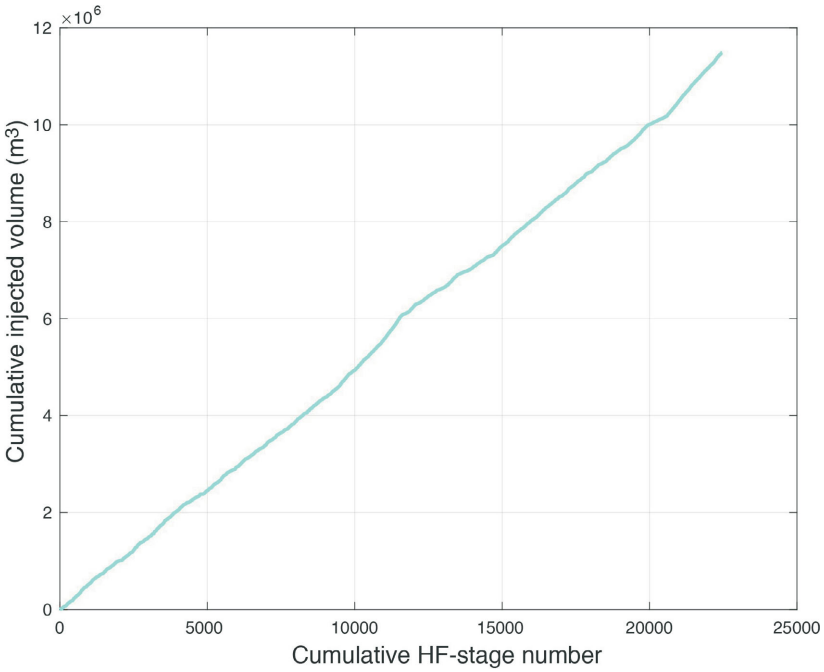

Figure 4. The relationship between the number of cumulative hydraulic fracturing (HF) stages and the cumulative injected volumes within the Kiskatinaw Seismic Monitoring and Mitigation Area, northeastern British Columbia, for 2017 and 2018.

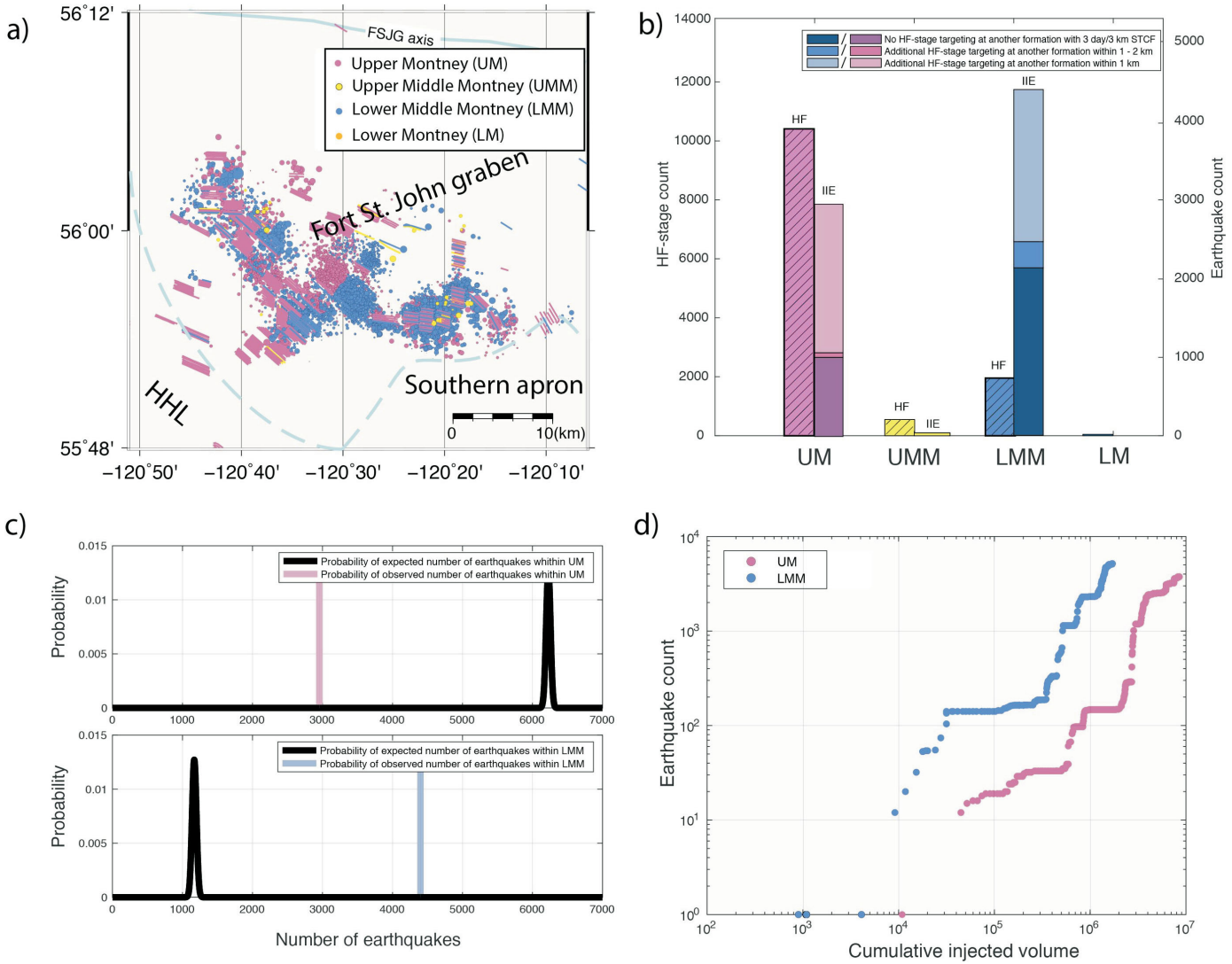

Figure 5. Statistical results after applying a 3 day and 3 km spatiotemporal correlation filter (STCF). **a)** Spatial distribution of epicentres (circles) and surface projections of horizontal hydraulic-fracturing (HF) wells (thin lines) associated with injections into different Montney Formation members, northeastern British Columbia. **b)** Histograms showing the number of HF stages and earthquakes associated with each Montney member. The level of confidence in the correlation between HF stage and injection-induced earthquake (IIE) is reflected in the tone of the colour (darker means higher confidence level). **c)** Probability as a function of the designated number of earthquakes associated with HF (thick black line) in the UM (top panel) and LMM (bottom panel), assuming that earthquakes can be equally triggered by HF stages, regardless of the targeted member. Coloured vertical lines mark the observed number of earthquakes. **d)** Number of earthquakes as a function of the cumulative injected volume for the UM and LMM. Abbreviations: FSJG, Fort St. John graben; HHL, Hudson Hope low; LM, Lower Montney; LMM, Lower Middle Montney; UM, Upper Montney; UMM, Upper Middle Montney.

geting the UM and LMM have the same earthquake-triggering capacity. The number of earthquakes predicted by this hypothesis (solid black lines, Figure 5c) is completely inconsistent with observations made during this study (pink and blue lines, Figure 5c), which suggests that the null hypothesis can be statistically rejected.

Finally, to quantitatively characterize the different seismic responses of the UM and LMM, the volumes used in individual HF stages and the number of IIEs for the two members were compiled separately, and the result is shown in Figure 5d. It is interesting to note that the two lines are similar except that the UM has approximately one time more cumulative volume, given the same IIE count. This difference suggests that the likelihood of IIEs being triggered in the LMM is probably one time greater than that in the UM.

Other Operational Factors

In addition to the injected volume, other operational parameters that could contribute to the discrepancy in IIE-triggering capacity in the three areas were also investigated, including breakdown pressure, injection rate, shut-in pressure and average treating pressure. All these operational parameters appear to have comparable values without following the IIE-distribution pattern (Figure 6). Therefore, the difference is not large enough to justify the dramatic difference noted in the observed seismic pattern.

A Physical Model to Interpret the Contrasting Seismogenic Behaviours

After delineating the controlling factors associated with deep fluid injection, a comprehensive model was developed to interpret the findings. Figure 7 is a schematic diagram summarizing this physical model; three factors are considered in the model. The first, and most important, controlling factor is the injection type; as shown in Figure 3, and suggested by the results of the Monte Carlo tests, the vast majority of IIEs in the KSMMA are associated with HF injections (~80%, given a 3 day and 3 km STCF criterion). The second important controlling factor is the regional structural geology; specifically, HF-related IIEs are more likely to occur if stimulations are performed in the FSJG area than in the neighbouring HHL and southern apron areas. Lastly, the third controlling factor is the stratigraphic setting; once inside the FSJG area, HF stages targeting the LMM are found to statistically cause more IIEs than those targeting other formations, even though the corresponding cumulative injected volume is ~5 times lower.

The fact that HF stimulations in the study area are associated with many more IIEs than WD injections did not come as a surprise, since a similar conclusion had been reported in previous studies (Atkinson et al., 2016; Schultz and Eaton, 2018; Yu et al., 2020; Wang et al., 2021). However, care should be taken when interpreting this observation. A direct communication with the regulator confirms that all WD-well locations in northeastern BC were carefully selected to minimize the chance of causing IIEs. Specifically, they avoid any known fault structures and target reservoirs that are less communicable to surrounding formations with confining layers. Thus, the contrasting seismic responses to HF and WD may be, at least in part, a consequence of the industry's own mitigation practice in the KSMMA.

The higher number of HF-related IIEs in the FSJG area than in the surrounding HHL and apron areas may be explained by the presence of unique geological characteristics. The FSJG has been intensely segmented and faulted into blocks during tectonic subsidence (Barclay et al., 1990). A recent study based on the spatiotemporal distribution of HF-related IIEs and high-resolution 3-D seismic images near Fort St. John reveals multiple buried thrust faults extending from the basement up to the Montney Formation and a pervasive system of transverse structures (Riazi and Eaton, 2020). These faults could act as potential pathways, along which aseismic pore-pressure diffusion can migrate farther, thus increasing the possibility of causing more IIEs in the vicinity (e.g., Ryan Schultz et al., 2016; Lei et al., 2017; Galloway et al., 2018; Eyre et al., 2019; Peña Castro et al., 2020; Yu et al., 2020; Wang et al., 2021). Moreover, one of the largest fault systems in the region, the Gordondale fault, runs subparallel to the axis of the FSJG and extends eastward into central Alberta (Eaton et al., 1999); it could also contribute to the higher potential of IIEs in the FSJG area.

The more active seismogenic behaviour of the LMM, as compared to that of the UM, could be related to its greater depth and unique stratigraphic setting. Many previous studies have suggested that larger IIE sequences tend to nucleate on pre-existing faults, located in the deeper crystalline basement, that are reactivated by fluid injections (e.g., Bao and Eaton, 2016; Schultz et al., 2016; Lei et al., 2017; Skoumal et al., 2018; Lei et al., 2019; Riazi and Eaton, 2020; Wang et al., 2020). In the study area, the recalibrated focal depths of the two largest IIEs (M_w 4.5 on November 30, 2018 and M_w 3.3 on November 30, 2018) are also located deeper than the Montney Formation at ~2.6 and ~3.9 km, respectively, most likely in the crystalline basement. More importantly, there are two newly recognized groups of bioclastic beds, known as the Altares Member (AM) and Pocketknife Member (PKM), intercepting and interfingering with the LMM at the top and bottom sections, respectively (Figures 1c, 7c; Zonneveld and Moslow, 2018). Both members have a distinctly low total organic carbon (TOC) content and high proportion of recrystallized skeletal calcite from shell materials. As calcite-rich fault-gouge joint surfaces generally have higher shear strength than those coated with clayey material (Ikari et al., 2013; Verberne et al., 2014), it is conceivable that deformation caused by fluid injection within the LMM, interfingered with the AM and PKM, is more likely to manifest itself as

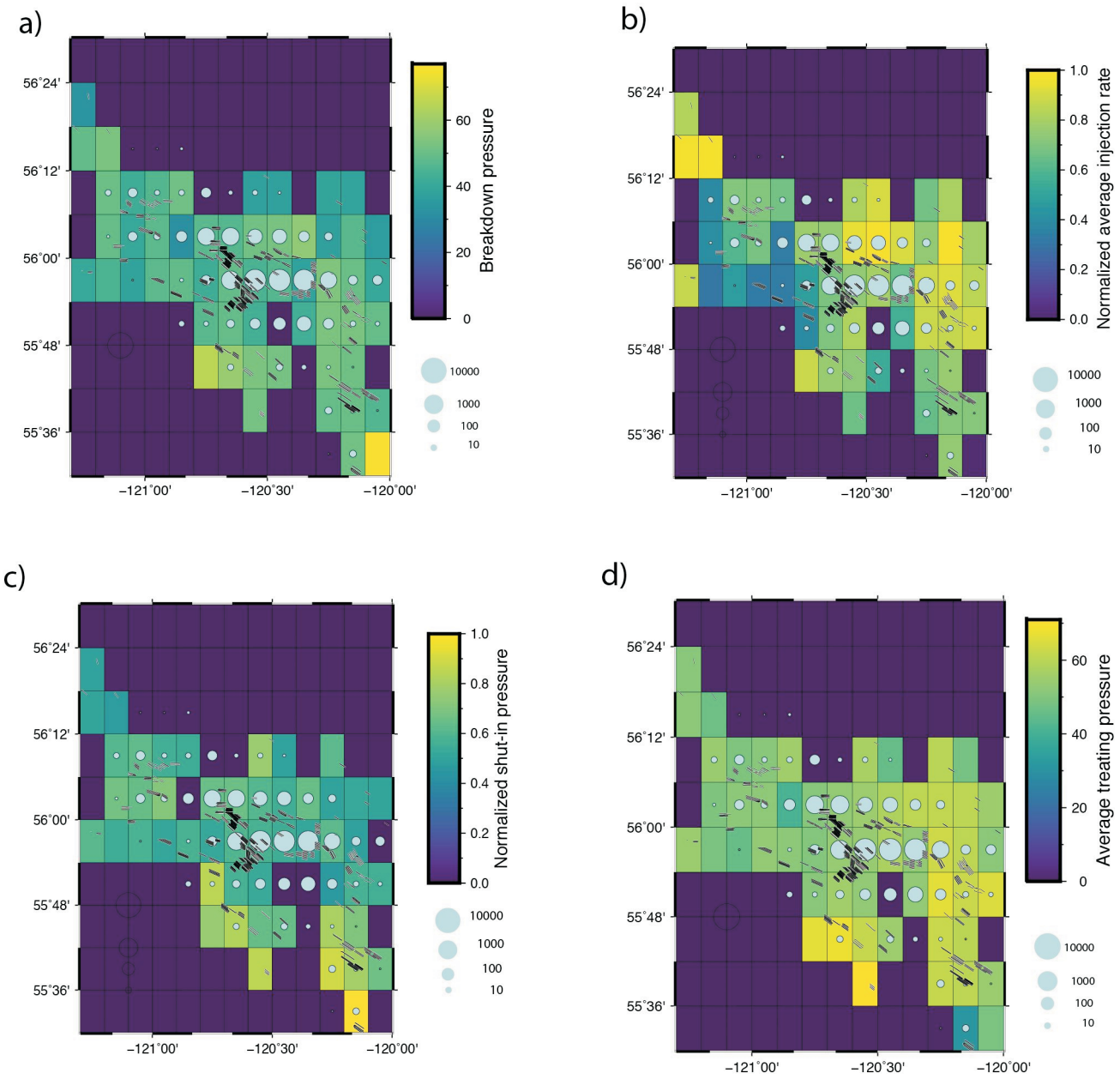

Figure 6. The spatiotemporal relationship between hydraulic-fracturing operational parameters and injection-induced earthquakes in the Kiskatinaw Seismic Monitoring and Mitigation Area, northeastern British Columbia. **a)** The background colour in each 0.1° × 0.1° cell represents the average breakdown pressure normalized by the maximum value within each cell. The size of the circle at the centre of the cells denotes the number of earthquakes in that cell. Diagrams **b)**, **c)** and **d)** are similar to a), showing the average injected rate, average shut-in pressure and average treating pressure, respectively.

brittle failures. This argument is consistent with the pervasive faulting and fracturing/slickenside structures observed within the core samples of the AM (Sanders et al., 2018); it is also compatible with a recently reported upward seismicity-migration pattern from the target member (Peña Castro et al., 2020; Schultz and Wang, 2020). In contrast, the geomechanical rock properties (e.g., higher clay and TOC content) in the UM may favour stable sliding that results in the strain causing the injection-related deformation being released by aseismic slip (Eyre et al., 2019).

Discussion

The volume of injected fluid has been regarded as one of the key controlling factors in inducing earthquakes within the WCSB. For example, Farahbod et al. (2015) found that in the Horn River Basin of northeastern BC, IIEs were observed only when the monthly HF-injection volume (summed over the entire basin) exceeded the level of 2.0×10^4 m^3. Schultz et al. (2018), relying on a greater quantity of data from the Fox Creek area, suggested that the cu-

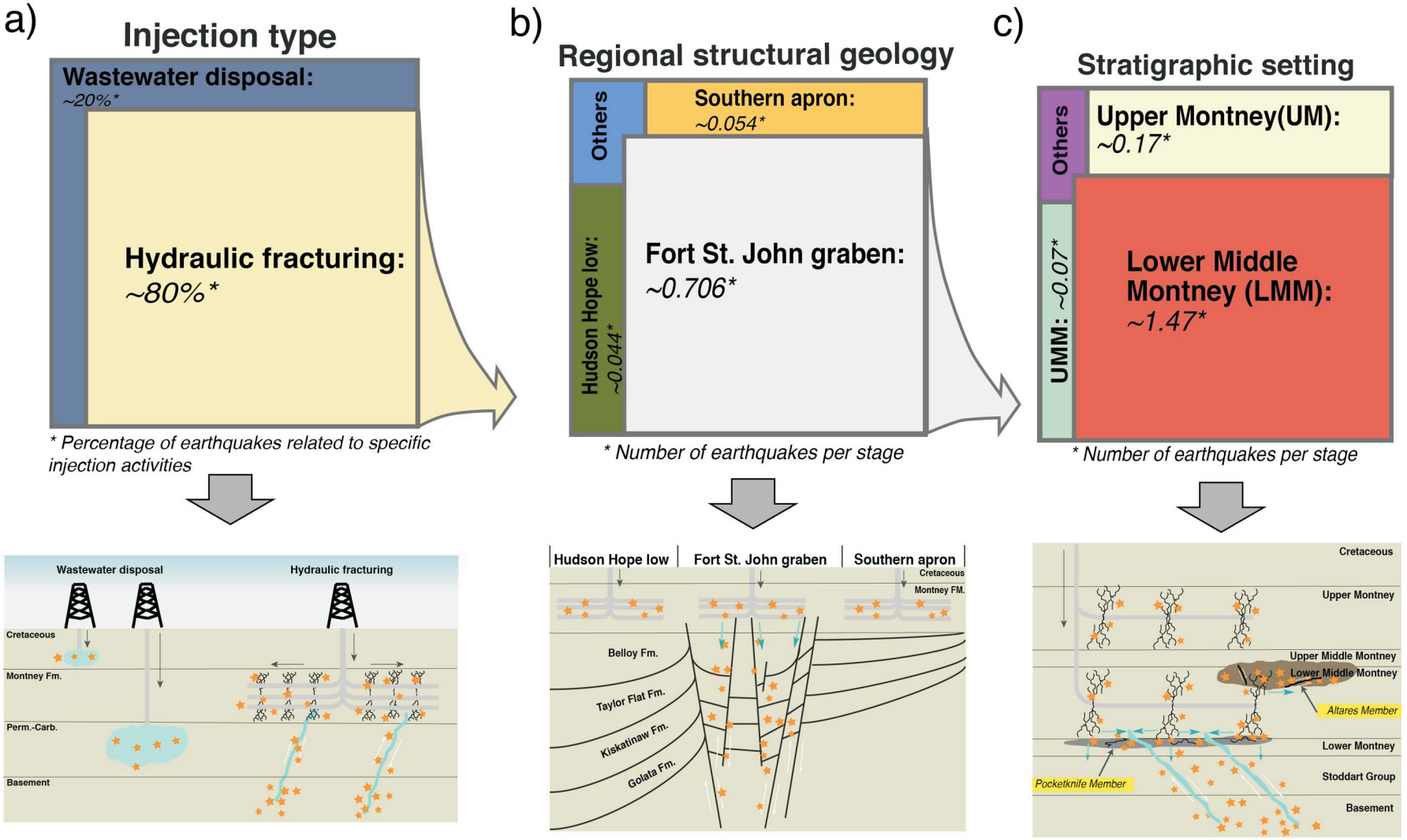

Figure 7. Schematic diagram showing the relative significance of physical factors controlling injection-induced earthquakes (IIEs) in the Kiskatinaw Seismic Monitoring and Mitigation Area, northeastern British Columbia. The bottom panels illustrate the corresponding seismogenic mechanisms of IIEs for the top three factors (top panels). **a)** Injection type is the most important factor: approximately 80% of all IIEs (orange stars, given a 3 day and 3 km spatiotemporal correlation-filter criterion) are related to hydraulic fracturing (HF), and can occur in the vicinity of injection depth and the crystalline basement via hydraulic conduits. **b)** Regional structural geology is the second most important factor. The number of earthquakes per HF stage is the highest within the area of the Fort St. John graben filled with subvertical faults (the blue arrows show the potential fluid migration along the graben faults). **c)** Stratigraphic setting is the third important factor: the number of earthquakes per HF stage is the highest when the lower Middle Montney (LMM) is the HF target. The higher IIE rate may be related to the presence of the Altares and Pocketknife members along the top and bottom sections of the LMM, respectively. Horizontal blue arrows show fluid migration along bedding contacts and possibly intersecting with graben faults, whereas the small vertical blue arrows show the slow diffusion via the permeable Permo-Carboniferous formations below the LMM.

mulative injected volume per each injection pad could be linearly related to the seismicity produced when volumes were approximately 10^4–10^5 m^3. However, observations in the KSMMA study area do not support a linear relationship between the cumulative injected volume and the number of IIEs (Figure 5d). Instead, the FSJG area has a much higher IIE/HF-stage ratio (~0.706) than the two neighbouring areas (0.044 and 0.054; Figure 2b). Since the cumulative injected volume in the FSJG area is also the highest, it is likely that the pervasive fault system in the graben and the large cumulative volume both contribute positively to the higher seismicity.

Based on observations in the study area, it seems that, for the cumulative volume to become an important controlling factor of IIEs, the cumulative injected volume must exceed a certain threshold before the widespread occurrence of IIEs (Figure 5d). Once the outbreak threshold is exceeded, the occurrence rate of IIEs can significantly outpace the rate of volume increase. As more fluid is injected into the rock formations, it could lead to more deformation by the poroelastic effects, pore-pressure diffusion to a broader region as well as additional creep and aseismic slip along pre-existing faults that, in turn, cause additional stress perturbations and earthquakes (Segall and Lu, 2015; Deng et al., 2016, 2020; Goebel et al., 2017; Eyre et al., 2019; Yu et al., 2019; Wang et al., 2021). The nonlinear relationship between the number of IIEs and injected volume probably further points to the important role played by regional/local geological structures.

Although the depth resolution to demonstrate that all IIEs associated with HF targeting the LMM are deeper than those targeting the UM or UMM was not determined, results of the STCF analysis clearly suggest that stimulating the relatively deeper LMM correlates with a higher rate of IIEs (Figure 5b). The relatively porous and permeable formations (Permo-Carboniferous) immediately beneath the Montney Formation (i.e., the Belloy Formation, Stoddart Group and Debolt Formation; Figure 1c) may play an important role. Specifically, these formations contain pervasive pre-existing faults, formed during the Paleozoic subsidence, that can be reactivated by injections to trigger IIEs (Barclay et al., 1990; O'Connell, 1994). They can also act as effective conduits for the fluid and stress perturbation caused by injections that reach the deeper, and presumably more seismogenic, crystalline basement (Skoumal et al., 2018). If the geomechanical perturbation caused by each HF stage is comparable regardless of the targeted formation, the probability of causing IIEs through HF stimulations to the LMM becomes higher due to its close proximity to the deeper Permo-Carboniferous formations and crystalline basement.

The sharp geomechanical rock-property contrast between the LMM and both the AM and PKM may also contribute to the higher seismogenic potential of the LMM, as the injected fluid can migrate more easily along the bedding contacts to a broader area (Sanders et al., 2018). Such horizontal migration may increase the probability of injected fluid reaching more subvertical faults within the FSJG and potentially triggering more IIEs in the crystalline basement (Figure 7c). The fact that HF stimulations targeting the LMM within the HHL and southern apron areas have caused considerably fewer IIEs than those within the FSJG should be noted. One interpretation could be that the total injected volume within the HHL and southern apron is below the threshold corresponding to the widespread occurrence of IIEs. Meanwhile, the possibility that the interactions between the inferred horizontal migration (due to the bedding contacts) and pervasive subvertical faults within the FSJG help to enhance the seismogenic potential of the LMM cannot be ruled out.

Overall, the highly heterogeneous distribution of IIEs in the KSMMA represents the combined effects of different physical mechanisms. When one factor (e.g., HF stimulation) collaborates with the others (e.g., the geological structure of subvertical or thrust faults [Riazi and Eaton, 2020], the existence of stratigraphic members with distinct geomechanical/hydrological characteristics and proximity to the crystalline basement), the likelihood of IIE occurrence becomes substantially higher (Figure 7).

Conclusion

The spatiotemporal correlation between injection operations and regional seismicity in the KSMMA was investigated. Findings indicate that ~80% of IIEs are associated with HF stimulations in the area. Conducting Monte Carlo tests using synthetic earthquake catalogues showed that the hypothesis whereby regional seismicity is randomly distributed can be statistically rejected (probability $<10^{-4}$). Additionally, HF stimulations performed in the FSJG area have a much higher probability of inducing earthquakes than those undertaken in the surrounding areas (~0.706 vs. <0.05 event per HF stage). Given the same setting of structural geology and injected volume, the seismogenic response to HF stimulations could vary significantly depending on which formation member is targeted. In the KSMMA, the number of HF stages targeting the LMM is only ~1/5 of that targeting the UM, yet the number of corresponding IIEs is higher (~1.47 vs. ~0.17 event per HF stage).

Based on observations, a comprehensive physical model to interpret the contrasting IIEs is proposed. The enhanced seismogenic potential of HF stimulations targeting the LMM could be explained by at least two reasons. Firstly, the LMM is in proximity to deeper permeable formations and subvertical graben faults that may facilitate the downward migration of injected fluid. The associated stress per-

turbation due to elevated pore pressure could help reactivate pre-existing faults in the basement. Secondly, the geomechanical heterogeneity of two geological units (AM and PKM) along the upper and lower boundaries of the LMM may enhance the seismogenesis of local IIEs. The lower TOC content, higher proportion of recrystallized calcite and sharp hydrogeological contrast to other Montney Formation members probably collectively contribute to the inferred geomechanical heterogeneity.

A key implication of this study is that decisions on the geographic location of injection wells and their targeted formations/members can make a big difference in effectively managing the seismic risk due to IIEs. Therefore, HF stimulations targeting members with a higher IIE-triggering capacity (e.g., the LMM in the FSJG area) should be closely monitored. On the other hand, formations without the characteristic conditions associated with IIEs can probably sustain more HF stimulations and/or larger injected volumes under the same regulatory framework. This aspect should be carefully considered when designing HF stimulations to achieve the optimal balance between stimulation efficiency and seismic safety.

Acknowledgments

The authors wish to thank A. Babaie Mahani and C. Salas for reviewing this paper. The Natural Resources Canada (NRCan) earthquake catalogue can be downloaded through the NRCan website, the seismic waveforms for NRCan stations are publicly available on the Incorporated Research Institutions for Seismology website (network code 1E and PQ) and the injection-well data can be accessed on the BC Oil and Gas Commission website. The enhanced earthquake catalogue produced using the source-scanning based on navigated automated phase-picking method can be obtained by sending a request to the corresponding author. Support for this study was jointly provided by Geoscience BC, with funding to B. Wang and R. Visser, and the Induced Seismicity Research Project of NRCan, with funding to H. Kao and H. Yu.

References

Atkinson, G.M., Eaton, D.W., Ghofrani, H., Walker, D., Cheadle, B., Schultz, R., Shcherbakov, R., Tiampo, K., Gu, J., Harrington, R.M., Liu, Y.J., van der Baan, M. and Kao, H. (2016): Hydraulic fracturing and seismicity in the Western Canada Sedimentary Basin; Seismological Research Letters, v. 87, no. 3, p. 631–647, URL <https://doi.org/10.1785/0220150263>.

Babaie Mahani, A. (2021): Seismic *b*-value within the Montney play of northeastern British Columbia, Canada; Canadian Journal of Earth Sciences, v. 58, no. 8, p. 720–730, URL <https://doi.org/10.1139/cjes-2020-0157>.

Babaie Mahani, A., Kao, H., Walker, D., Johnson, J. and Salas, C. (2016): Performance evaluation of the regional seismograph network in northeast British Columbia, Canada, for monitoring of induced seismicity; Seismological Research Letters, v. 87, no. 3, p. 648–660, URL <https://doi.org/10.1785/0220150241>.

Babaie Mahani, A., Malytskyy, D., Visser, R., Hayes, M., Gaucher, M. and Kao, H. (2020): Well-log-based velocity and density models for the Montney unconventional resource play in northeast British Columbia, Canada, applicable to induced seismicity monitoring and research; Seismological Research Letters, v. 92, no. 2A, p. 886–894, URL <https://doi.org/10.1785/0220200213>.

Bao, X. and Eaton, D.W. (2016): Fault activation by hydraulic fracturing in western Canada; Science, v. 354, no. 6318, p. 1406–1409, URL <https://doi.org/10.1126/science.aag2583>.

Barclay, J., Krause, F., Campbell, R. and Utting, J. (1990): Dynamic casting and growth faulting: Dawson Creek graben complex, Carboniferous–Permian Peace River embayment, western Canada; Bulletin of Canadian Petroleum Geology, v. 38, no. 1, p. 115–145, URL <https://doi.org/10.35767/gscpgbull.38a.1.115>.

BC Oil and Gas Commission (2021): Hydraulic fracture summary data; BC Oil and Gas Commission, URL <https://www.bcogc.ca/> [July 2021].

Davies, G.R., Watson, N., Moslow, T.F. and MacEachern, J.A. (2018): Regional subdivisions, sequences, correlations and facies relationships of the Lower Triassic Montney Formation, west-central Alberta to northeastern British Columbia, Canada—with emphasis on role of paleostructure; Bulletin of Canadian Petroleum Geology, v. 66, no. 1, p. 23–92.

Deng, K., Liu, Y. and Harrington, R. M. (2016): Poroelastic stress triggering of the December 2013 Crooked Lake, Alberta, induced seismicity sequence; Geophysical Research Letters, v. 43, no. 16, p. 8482–8491, URL <https://doi.org/10.1002/2016GL070421>.

Deng, K., Liu, Y. and Chen, X. (2020): Correlation between poroelastic stress perturbation and multidisposal wells induced earthquake sequence in Cushing, Oklahoma; Geophysical Research Letters, v. 47, no. 20, art. e2020GL089366, URL <https://doi.org/10.1029/2020GL089366>.

Eaton, D.W., Ross, G.M. and Hope, J. (1999): The rise and fall of a cratonic arch: a regional seismic perspective on the Peace River Arch, Alberta; Bulletin of Canadian Petroleum Geology, v. 47, no. 4, p. 346–361.

Ellsworth, W.L. (2013): Injection-induced earthquakes; Science, v. 341, no. 6142, art. 1225942, URL <https://doi.org/10.1126/science.1225942>.

Eyre, T.S., Eaton, D.W., Garagash, D.I., Zecevic, M., Venieri, M., Weir, R. and Lawton, D.C. (2019): The role of aseismic slip in hydraulic fracturing-induced seismicity; Science Advances, v. 5, no. 8, art. eaav7172, URL <https://doi.org/10.1126/sciadv.aav7172>.

Farahbod, A.M., Kao, H., Walker, D.M., Cassidy, J.F. and Calvert, A. (2015): Investigation of regional seismicity before and after hydraulic fracturing in the Horn River Basin, northeast British Columbia; Canadian Journal of Earth Sciences, v. 52, no. 2, p. 112–122.

Galloway, E., Hauck, T., Corlett, H., Pană, D. and Schultz, R. (2018). Faults and associated karst collapse suggest conduits for fluid flow that influence hydraulic fracturing-induced seismicity; Proceedings of the National Academy of Sciences, v. 115, no. 43, p. E10003–E10012, URL <https://doi.org/10.1073/pnas.1807549115>.

Goebel, T., Weingarten, M., Chen, X., Haffener, J. and Brodsky, E. (2017). The 2016 M_w 5.1 Fairview, Oklahoma earthquakes: evidence for long-range poroelastic triggering at >40 km from fluid disposal wells; Earth and Planetary Science Letters, v. 472, p. 50–61.

Healy, J.H., Rubey, W.W., Griggs, D.T. and Raleigh, C.B. (1968): The Denver earthquake; Science, v. 161, no. 3848, p. 1301–1310, URL <https://doi.org/10.1126/science.161.3848.1301>.

Ikari, M.J., Niemeijer, A.R., Spiers, C.J., Kopf, A.J. and Saffer, D.M. (2013): Experimental evidence linking slip instability with seafloor lithology and topography at the Costa Rica convergent margin; Geology, v. 41, no. 8, p. 891–894.

Kao, H., Visser, R., Smith, B. and Venables, S. (2018): Performance assessment of the induced seismicity traffic light protocol for northeastern British Columbia and western Alberta; The Leading Edge, v. 37, no. 2, p. 117–126, URL <https://doi.org/10.1190/tle37020117.1>.

Keranen, K.M. and Weingarten, M. (2018): Induced seismicity; Annual Review of Earth and Planetary Sciences, v. 46, no. 1, p. 149–174, URL <https://doi.org/10.1146/annurev-earth-082517-010054>.

Lei, X., Huang, D., Su, J., Jiang, G., Wang, X., Wang, H., Guo, X. and Fu, H. (2017): Fault reactivation and earthquakes with magnitudes of up to M_w 4.7 induced by shale-gas hydraulic fracturing in Sichuan Basin, China; Scientific Reports, v. 7, no. 1, 7971, URL <https://doi.org/10.1038/s41598-017-08557-y>.

Lei, X., Wang, Z. and Su, J. (2019): The December 2018 M_L 5.7 and January 2019 M_L 5.3 earthquakes in south Sichuan basin induced by shale gas hydraulic fracturing; Seismological Research Letters, v. 90, no. 3, p. 1099–1110.

Natural Resources Canada (2021): Search the earthquake database; Natural Resources Canada, URL <http://www.earthquakescanada.nrcan.gc.ca/stndon/NEDB-BNDS/bulletin-en.php> [July 2020].

O'Connell, S.C. (1994): Geological history of the Peace River Arch; *in* Geological Atlas of the Western Canada Sedimentary Basin, G.D. Mossop and I. Shetsen (comp.), Canadian Society of Petroleum Geologists, Calgary, Alberta, and Alberta Research Council, Edmonton, Alberta, p. 431–438.

Peña Castro, A.F., Roth, M.P., Verdecchia, A., Onwuemeka, J., Liu, Y., Harrington, R.M., Zhang, Y. and Kao, H. (2020): Stress chatter via fluid flow and fault slip in a hydraulic fracturing-induced earthquake sequence in the Montney Formation, British Columbia; Geophysical Research Letters, v. 47, no. 14, art. e2020GL087254, URL <https://doi.org/10.1029/2020GL087254>.

Raleigh, C., Healy, J. and Bredehoeft, J. (1976): An experiment in earthquake control at Rangely, Colorado; Science, v. 191, no. 4233, p. 1230–1237.

Riazi, N. and Eaton, D.W. (2020): Anatomy of a buried thrust belt activated during hydraulic fracturing; Tectonophysics, v. 795, art. 228640 URL <https://doi.org/10.1016/j.tecto.2020.228640>.

Sanders, S., Etienne, C., Gegolick, A., Kelly, D. and Zonneveld, J.-P. (2018): The Middle Montney Altares Member: lithology, depositional setting and significance for horizontal drilling and completion in the Altares field, British Columbia; Bulletin of Canadian Petroleum Geology, v. 66, no. 1, p. 318–337.

Schultz, R. and Eaton, D.W. (2018): Increased likelihood of induced seismicity in highly overpressured shale formations; Geophysical Journal International, v. 214, no. 1, p. 751–757, URL <https://doi.org/10.1093/gji/ggy167>.

Schultz, R. and Wang, R. (2020): Newly emerging cases of hydraulic fracturing induced seismicity in the Duvernay East shale basin: Tectonophysics, v. 779, art. 228393, URL <https://doi.org/10.1016/j.tecto.2020.228640>.

Schultz, R., Corlett, H., Haug, K., Kocon, K., MacCormack, K., Stern, V. and Shipman, T. (2016): Linking fossil reefs with earthquakes: geologic insight to where induced seismicity occurs in Alberta; Geophysical Research Letters, v. 43, no. 6, p. 2534–2542, URL <https://doi.org/10.1002/2015GL067514>.

Schultz, R., Atkinson, G., Eaton, D., Gu, Y. and Kao, H. (2018); Hydraulic fracturing volume is associated with induced earthquake productivity in the Duvernay play; Science, v. 359, no. 6373, p. 304–308.

Segall, P. and Lu, S. (2015): Injection-induced seismicity: poroelastic and earthquake nucleation effects; Journal of Geophysical Research: Solid Earth, v. 120, no. 7, p. 5082–5103, URL <https://doi.org/10.1002/2015JB012060>.

Shen, L.W., Schmitt, D.R. and Haug, K. (2019): Quantitative constraints to the complete state of stress from the combined borehole and focal mechanism inversions: Fox Creek, Alberta; Tectonophysics, v. 764, p. 110–123.

Skoumal, R.J., Brudzinski, M.R. and Currie, B.S. (2018): Proximity of Precambrian basement affects the likelihood of induced seismicity in the Appalachian, Illinois, and Williston Basins, central and eastern United States; Geosphere, v. 14, no. 3, p. 1365–1379.

Tan, F., Kao, H., Nissen, E. and Eaton, D. (2019): Seismicity-scanning based on navigated automatic phase-picking; Journal of Geophysical Research: Solid Earth, v. 124, no. 4, p. 3802–3818, URL <https://doi.org/10.1029/2018JB017050>.

Verberne, B., Spiers, C.J., Niemeijer, A.R., De Bresser, J., De Winter, D. and Plümper, O. (2014): Frictional properties and microstructure of calcite-rich fault gouges sheared at subseismic sliding velocities; Pure and Applied Geophysics, v. 171, no. 10, p. 2617–2640.

Visser, R., Smith, B., Kao, H., Babaie Mahani, A., Hutchinson, J. and McKay, J. (2017): A comprehensive earthquake catalogue for northeastern British Columbia and western Alberta, 2014–2016; Geological Survey of Canada, Open File 8335, 28 p., URL <https://doi.org/10.4095/306292>.

Visser, R., Kao, H., Smith, B., Goerzen, C., Kontou, B., Dokht, R.M.H., Hutchinson, J., Tan, F. and Babaie Mahani, A. (2020): A comprehensive earthquake catalogue for the Fort St. John–Dawson Creek region, British Columbia, 2017–2018; Geological Survey of Canada, Open File, 8718, 28 p., URL <https://doi.org/10.4095/326015>.

Wang, B., Harrington, R.M., Liu, Y., Kao, H. and Yu, H. (2020): A study on the largest hydraulic-fracturing-induced earthquake in Canada: observations and static stress-drop estimation; Bulletin of the Seismological Society of America, v. 110, no. 5, p. 2283–2294, URL <https://doi.org/10.1785/0120190261>.

Wang, B., Verdecchia, A., Kao, H., Harrington, R.M., Liu, Y. and Yu, H. (2021). A study on the largest hydraulic fracturing induced earthquake in Canada: numerical modeling and triggering mechanism; Bulletin of the Seismological Society of America, v. 111, no. 3, p. 1392–1404, URL <https://doi.org/10.1785/0120200251>.

Yu, H., Harrington, R.M., Liu, Y. and Wang, B. (2019): Induced seismicity driven by fluid diffusion revealed by a near-field hydraulic stimulation monitoring array in the Montney Basin, British Columbia: Journal of Geophysical Research:

Solid Earth, v. 124, no. 5, p. 4694–4709, URL <https://doi.org/10.1029/2018JB017039>.

Yu, H., Harrington, R.M., Kao, H., Liu, Y., Abercrombie, R.E. and Wang, B. (2020): Well proximity governing stress drop variation and seismic attenuation associated with hydraulic fracturing induced earthquakes: Journal of Geophysical Research: Solid Earth, v. 125, no. 9, art. e2020JB020103, URL <https://doi.org/10.1029/2020JB020103>.

Yuan, J., Kao, H. and Yu, J. (2020): Depth-scanning algorithm: accurate, automatic, and efficient determination of focal depths for local and regional earthquakes; Journal of Geophysical Research: Solid Earth, v. 125, no. 7, art. e2020JB019430, URL <https://doi.org/10.1029/2020JB019430>.

Zoback, M.D. and Lund Snee, J.-E. (2018): Predicted and observed shear on pre-existing faults during hydraulic fracture stimulation; *in* SEG International Exposition and 88th Annual Meeting; Society of Exploration Geophysicists, October 14–19, 2018, Annaheim, California, Technical Program 2018 Expanded Abstracts, p. 3588–3592, URL <https://doi.org/10.1190/segam2018-2991018.1>.

Zonneveld, J.-P. and Moslow, T. F. (2018): Palaeogeographic setting, lithostratigraphy, and sedimentary framework of the Lower Triassic Montney Formation of western Alberta and northeastern British Columbia; Bulletin of Canadian Petroleum Geology, v. 66, no. 1, p. 93–127.

Investigating Fault-Sealing Effects on Induced Seismicity and Pore Pressure Distribution in Northeastern British Columbia (Parts of NTS 093P, 094A): Observations

Z. Esmaeilzadeh[1], **Department of Geoscience, University of Calgary, Calgary, Alberta, zahra.esmaeilzadeh@ucalgary.ca**

D.W. Eaton, Department of Geoscience, University of Calgary, Calgary, Alberta

Esmaeilzadeh, Z. and Eaton, D.W. (2022): Investigating fault-sealing effects on induced seismicity and pore pressure distribution in northeastern British Columbia (parts of NTS 093P, 094A): observations; *in* Geoscience BC Summary of Activities 2021: Energy and Water, Geoscience BC, Report 2022-02, p. 49–60.

Introduction

The Montney shale gas play in northeastern British Columbia (BC) contains overpressured terranes, which preserve the signature of elevated formation pressures that formed during hydrocarbon migration near the time of maximum burial. The spatially varying pattern of overpressure signatures is thought to reflect loss of pressure along permeable fairways, such as faults, during uplift and exhumation. Other studies, however, show that distinct pressure terranes within the Montney play are likely fault bounded, implying that some faults continue to serve as seals that inhibit pressure migration. These two concepts can be reconciled within the framework of the fault-valve model, wherein a fault experiences a transient coseismic increase in permeability during an earthquake. According to this model, the fault seal rebuilds gradually over time during the ensuing interseismic period, such that complete release of overpressure within a fault-bounded compartment may require multiple fault activation cycles.

A local magnitude (M_L) 4.5 hydraulic-fracturing (HF) induced earthquake on November 30, 2018, and the ensuing seismicity sequence, occurred close to a major pressure boundary within the Septimus oil and gas field and surrounding area. The sequence was triggered by HF treatment in two horizontal wells, in the Lower–Middle Montney members, which straddled a major pressure boundary. Pressure readings from these wells show that the lateral pressure difference across the boundary was approximately 10 megapascals (MPa) over a distance <2.3 km, and provided evidence for a coseismic pressure drop of about 3 MPa. This paper reviews the available data from this area, with the objective of reappraising pressure terrane boundaries in light of recently mapped structural corridors, and evaluating the relationship between structural corridors, pressure terranes and log-derived geomechanical parameters. The study area encompasses the Septimus field, including the location of the November 2018 earthquakes, and covers a large part of the Kiskatinaw Seismic Monitoring and Mitigation Area (KSMMA; Figure 1). The datasets that have been compiled within this study area are summarized in Table 1.

Structural Corridors

The Western Canada Sedimentary Basin (WCSB) is a mature oil and gas basin with an extraordinary endowment of publicly accessible data. The basin contains structural elements of varying age, expressed as folding, faulting and fracturing, which provide a record of tectonic activity during basin evolution (Wozniakowska et al., in press). In a region of the WCSB, straddling the border between Alberta and BC and covering an area of approximately 130 000 km^2, Wozniakowska et al. (in press) used publicly available fault data, formation top data, LITHOPROBE seismic profiles and regional potential-field data to delineate regional structural elements. They adopted a structural-corridor approach, which helps to resolve the limited spatial extent of available seismic data and provides broader spatial coverage, enabling the investigation of structural trends throughout the entirety of the Montney play (Wozniakowska et al., in press). In this study, pressure terranes (Fox and Watson, 2019; Enlighten Geoscience Ltd., 2021) and property discontinuities are compared with these structural corridors (Figure 2a, b). As summarized in Table 2, these two independent interpretations correlate strongly within and/or at the boundaries of the Septimus High, Wilder Moderate (Mod.) High–Cecil Low and Wilder Mod. High–Monias Low pressure terranes.

Pore Pressure and Stress Mapping

The hydrogeological setting is considered one of the most important considerations in understanding induced seismicity (Fox and Watson, 2019). In very low permeability plays, structural features can cause significant pressure

[1]*The lead author is a 2021 Geoscience BC Scholarship recipient.*

This publication is also available, free of charge, as colour digital files in Adobe Acrobat® PDF format from the Geoscience BC website: http://geosciencebc.com/updates/summary-of-activities/.

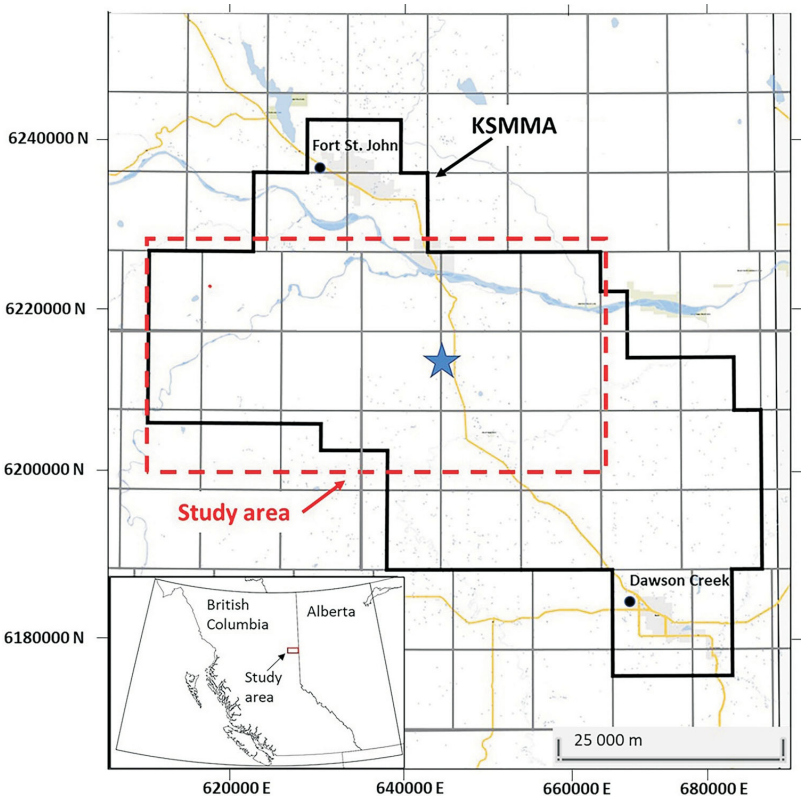

Figure 1. Location of the study area (red dashed outline) and Kiskatinaw Seismic Monitoring and Mitigation Area (KSMMA; black outline) in northeastern British Columbia. The star shows the approximate location of the November 30, 2018, earthquake sequence. All co-ordinates are in UTM Zone 10 North, NAD 83.

Table 1. List of data compiled for this study area, northeastern British Columbia. Well data and reservoir parameters were provided by geoLOGIC systems ltd. © 2021, seismic events from Visser et al. (2017) and Salvage and Eaton (2021) and structural corridor shapefiles from Wozniakowska et al. (in press). Abbreviations: N/a, not available; PVT, pressure-volume-temperature.

Data	Number of wells/ amount of data analyzed	Formation
Formation tops	8000	Debolt to Shaftesbury
Advanced core analysis	20	Montney
Fluid and PVT data	10	Montney
Production/injection data	1500	Montney
Diagnostic fracture injection test (DFIT)	149	Montney
Well logs	111	Debolt to Shaftesbury
Pressure data	1600	Debolt to Halfway
Well surveys	224	N/a
Seismic events	3639	N/a
Structural corridor shapefiles	134	N/a

compartmentalization (Fox and Watson, 2019; Wood et al., 2021). Pressure gradient maps of the Upper and Middle Montney members from Fox and Watson (2019) are shown in Figure 3a and b. The figure shows several transitions across the study area from relatively high (>14 kPa/m) to low (<10 kPa/m) pressure gradient values. The epicentral region of the November 30, 2018, earthquake sequence seems to correlate with a sharp contrast in lateral pore pressure in the Montney Formation.

To validate and update these results, Montney Formation pore pressure data were extracted from diagnostic fracture injection tests (DFITs) and routine pressure survey tests (PST). All tests were subjected to quality control (QC) evaluation to remove poor quality tests, to account for different gauge resolutions and to exclude the outliers. Pressure data with less than 10 days of shut-in duration were ignored. For individual wells, the pressure data were extrapolated to the initial reservoir pressure. For the Montney Formation, most of the pressure data are within the Upper Montney Member and the least amount of data are within the Lower Montney Member. The PST data include tests from the following categories: pressure gauge fall-off (PGFO), pressure gauge build-up (PGBU) and static gradient (SG). All of these tests were reviewed to ensure the best possible pressure value for each tested interval was included in the final maps. Figure 4 shows different ranges of pressure gradient in the Montney Formation measured with different tools. Since the mean value of all the methods are close and they all cover similar ranges of data, down-hole gauge pressure (PGFO, PGBU, SG) and DFIT data were used confidently. Due to limitations in memory and runtime for this model, only the pressure data from the wells with full-set logs (111 wells) were considered.

Diagnostic fracture injection tests, also known as minifrac tests, include a short injection test followed by a few hours of fall-off. During the injection, the rock formation breaks down to allow wellbore communication past the damage zone. The post–shut-in pressure decay is used to estimate reservoir parameters needed for fracture design. Interpretation of DFIT results provides estimates of reservoir pore pressure, fracture pressure, fracture closure pressure (approximately equivalent to minimum horizontal stress), permeability and rock elastic parameters, such as Young's modulus. In addition, the flow regime is identified to confirm the reservoir parameters. In this study, DFIT interpretation reports were available for 149 wells.

Within the Montney Formation, areas with strong lateral gradients in pore pressure appear to mark the locations of faults that bound pressure compartments and coincide with zones that appear to be more prone to induced seismicity.

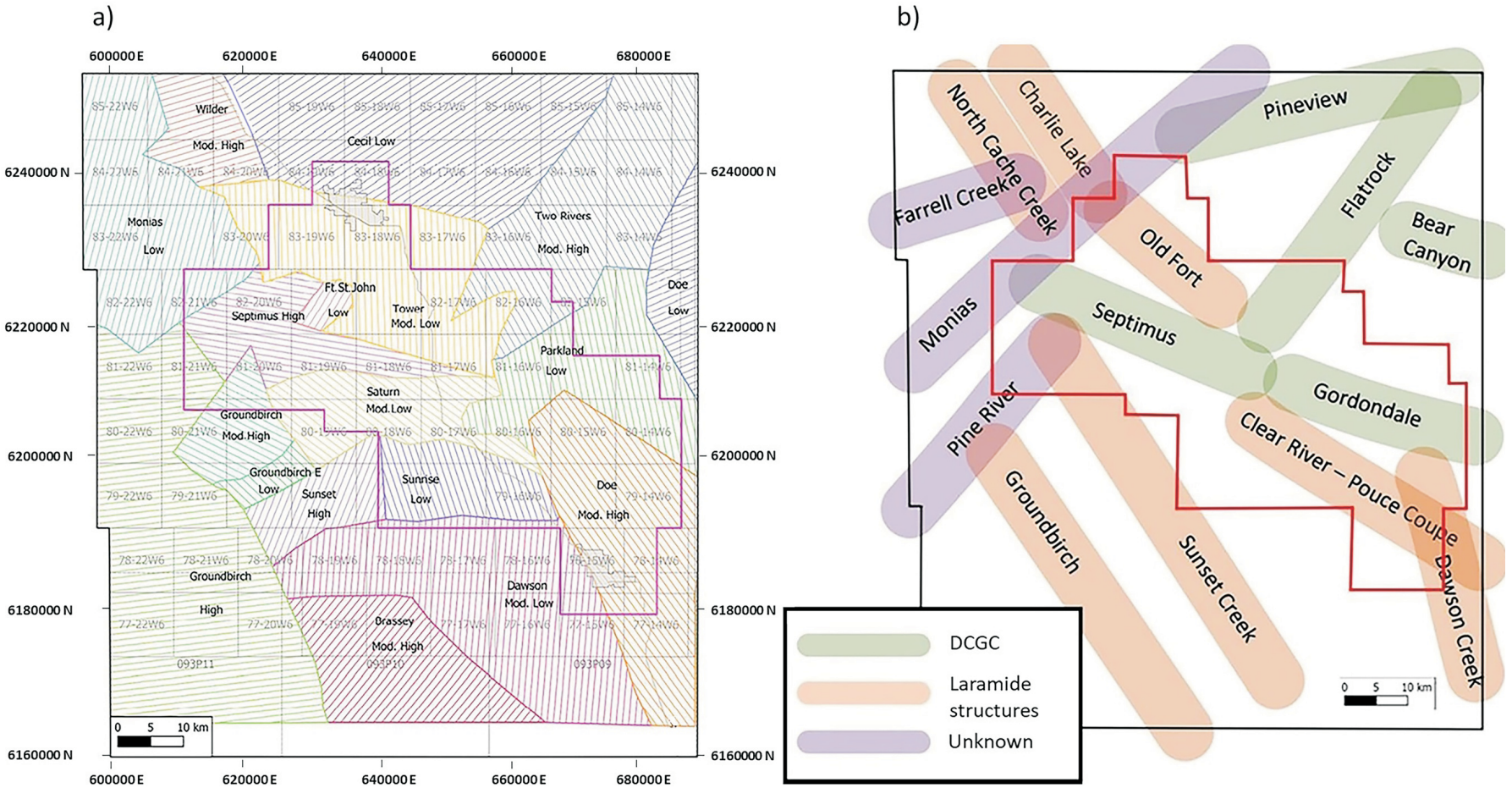

Figure 2. Comparison between **a)** pressure terranes (modified from Fox and Watson, 2019) and **b)** structural corridors (modified from Wozniakowska et al., in press), northeastern British Columbia. Some NTS map numbers (e.g., 093P11) and townships and ranges are noted in the background (e.g., 77-22W6, Twp. 77, Rge. 22, W 6th Mer.). All co-ordinates are in UTM Zone 10 North, NAD 83. Abbreviations: DCGC, Dawson Creek graben complex; E, east; Mod., moderate.

Table 2. Comparative summary of structural corridors and pressure terranes in the study area, northeastern British Columbia (see Figure 2). Abbreviations: Mod., moderate; N/a, not applicable.

Structural corridor	Pressure terrane	Degree of correlation
Septimus	Septimus High	Very high
Charlie Lake	Wilder Mod. High–Cecil Low	Very high
North Cache Creek	Wilder Mod. High–Monias Low	Very high
Dawson Creek	Doe Mod. High–Dawson Mod. Low	High
Groundbirch	Groundbirch High–various Lows	High
Old Fort	Septimus High–Ft. St. John Low	Partial
Flatrock	Two Rivers Mod. High	Partial
Monias	Septimus High–Monias Low	Partial
Clear River – Pouce Coupe	Saturn Mod. Low–Sunrise Low	Partial
Pine River	Groundbirch High	Partial
Bear Canyon	Two Rivers Mod. High–Parkland Low	Partial
Gordondale	N/a	None
Pineview	N/a	None
Farrell Creek	N/a	None
Sunset Creek	N/a	None

The epicentre of the M_L 4.5 event on November 30, 2018, also corresponds to an area with significant lateral pore pressure variation at the Montney Formation level. An analysis of fault structures and seals is in progress to characterize the leakage potential that causes permeability variations and hydrostatic gradient in fluid pressure along each fault plane. Pressure gradient maps of the Upper and Middle Montney members within the study area are presented in Figure 5a and b. The overall trend of the pore pressure and the location of hydraulic discontinuities align with previously published results (Figure 3). Pore pressure and other petrophysical and mechanical properties in this study have been populated using kriging interpolation.

In addition to down-hole gauge measurements, all of the available drill stem test (DST) data were collected and the DST pore pressure from the overlying Halfway and Doig formations and the underlying Belloy Formation was mapped. Although DST is the most accurate source of pressure data it is not cost-effective to complete DSTs in the Montney Formation unconventional reservoir due to low permeability and low flow capacity, thus only the routine tests (PGFO, PGBU, SG) and DFITs are available. Figure 6 displays the DST pressure gradient map of the Halfway Formation, which is more uniform than the Montney Formation and generally remains close to the hydrostatic gradient (10 kPa/m) throughout the study area. Notably, a series of Halfway Formation conventional pools along the southern bounding fault of the Fort St. John graben is evident from the distribution of producing wells.

Minimum horizontal stress and fracture pressure gradient maps from the Lower Montney Member to the Doig Formation were also generated based on the DFIT reports and the data provided by operators. These two different datasets have the same mean values and lie within the same data range, and mixing the two datasets does not cause any significant issues in stress analysis. Previous studies (Haghshenas and Qanbari, 2020) show that the tangent method, used in most DFIT interpretations, underestimates the actual fracture closure pressure (minimum horizontal stress [S_{Hmin}]). There is usually a 2–5% difference between the actual and measured values. This difference depends on the strength and average height of the asperities on the fracture walls. Therefore for stress modelling and HF simulation projects, correction to S_{Hmin} should be applied. Considering the absolute error in the S_{Hmin} estimation, this amount of error might be negligible, but the error is much more significant in fracture net pressure.

Pressure Difference and Seismicity Near the Suspended Well

When the November 30, 2018, earthquake sequence was initiated, zipper-HF was being carried out in two Lower–Middle Montney member wells (G and H), which was subsequently suspended. Over a two-week period (3 days before and 10 days after the November 30, 2018, mainshock), almost 600 events (M_L –0.3 to 4.5) were identified (Salvage and Eaton, 2021). Events appear tightly clustered, both spatially and in depth. Focal mechanism analysis suggests that this region of seismic activity is located within a transitional stress regime, with a mixture of reverse and strike-slip faulting over a small spatial extent (Salvage and Eaton, 2021). Figure 7 shows relocated seismic event hypocentres for the epicentral location of the November 30, 2018, earthquake sequence. A possible scenario to explain the observed pattern of seismicity, which includes small strike-slip events between the two wells, is that fault slip along the pressure-terrane boundary occurred aseismically, triggering dynamic rupture at a slightly greater depth (e.g., Debolt Formation). This hypothesis is currently being evaluated.

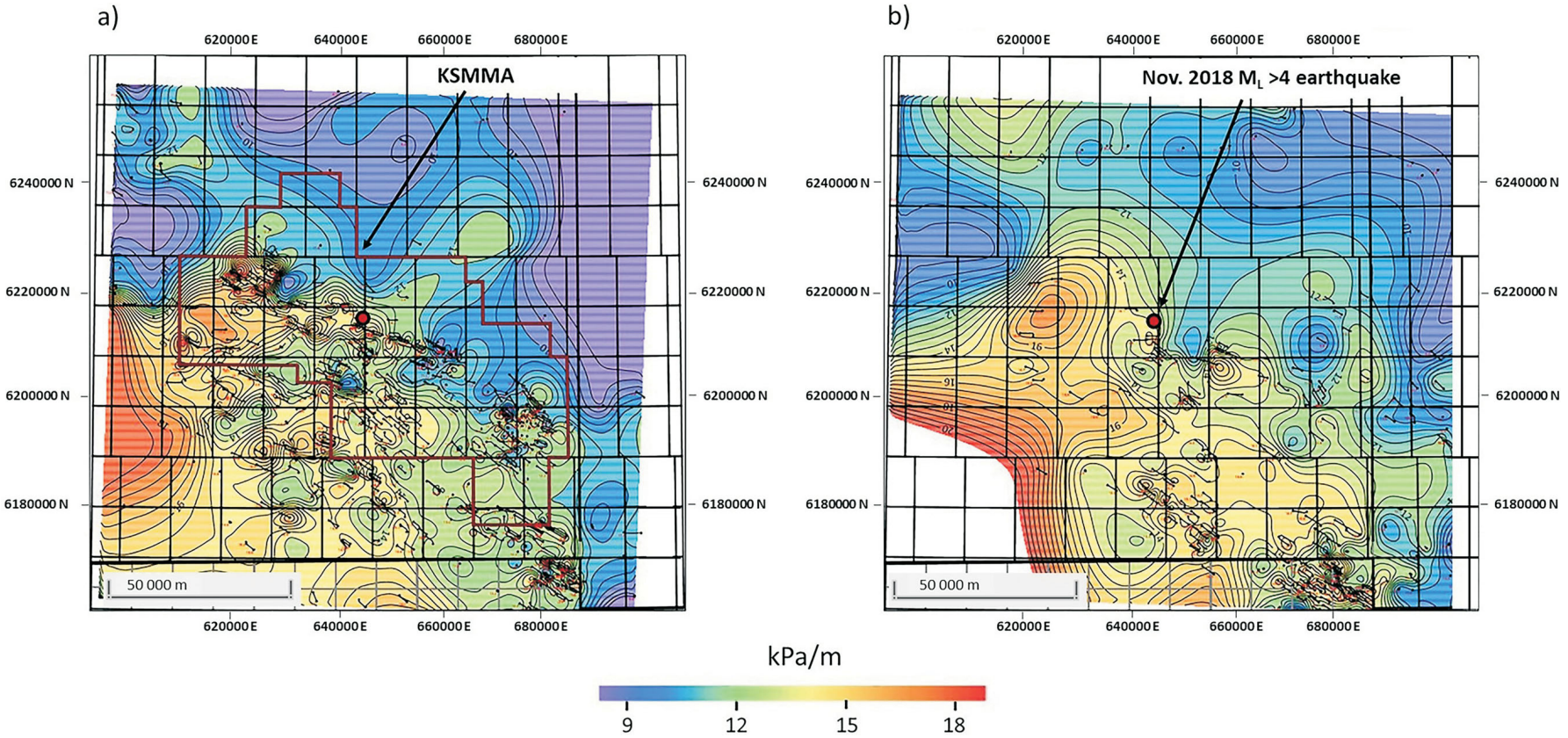

Figure 3. Pressure gradient (kilopascals per metre [kPa/m]) map of the **a)** Upper Montney and **b)** Middle Montney members of the Montney Formation (from Fox and Watson, 2019). Red circle shows the epicentral region of the local magnitude (M_L) 4.5 earthquake sequence, November 30, 2018. The earthquake location appears to correlate with significant lateral contrast in pore pressure gradient associated with the boundary between the Septimus High and the Tower Moderate Low pressure terranes (see Figure 2). Black symbols indicate well locations. All co-ordinates are in UTM Zone 10 North, NAD 83. Abbreviation: KSMMA, Kiskatinaw Seismic Monitoring and Mitigation Area.

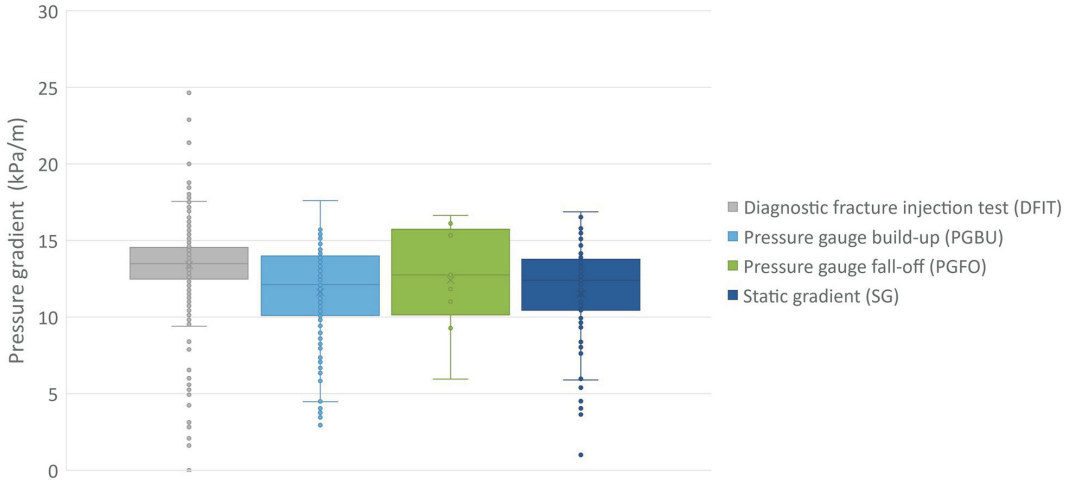

Figure 4. Box-and-whisker plot showing a comparison of pressure gradient data from different pressure measurement methods, compiled for the Montney Formation in this study. Abbreviation: kPa, kilopascal.

The initial static pressure of the G well was measured as approximately 38 MPa before the start of the HF operation. Following the earthquake sequence and for a period of about nine months, the formation pressures of the G well and the H well were measured as 35 and 28 MPa, respectively. The G well pressure drop of 3 MPa seems to be due to fluid leak-off into a nearby fault over the nine-month time interval. Also, the 10 MPa pressure difference between the two wells confirms the presence of a fault. It should be noted that H well is completed 47 m above the G well but this small difference in depth cannot cause such a large pressure difference. Also, based on close examination, the high pressure of the G well does not seem to be influenced by the fluid-injection pressure of the adjacent wells (<500 m distance), since no other nearby well shows abnormal pressure. Based on regional pore pressure gradient data, an extended normal fault (see 'Property Modelling' section, Figure 10) divides the entire study area into low- and high-pressure regions. The G and H wells are located in the high-pressure and low-pressure regions, respectively. Figure 8 demonstrates the pressure behaviour of the two wells before and after the November 30, 2018, earthquake. The pressure behaviour of these wells supports the fault-valve theory. Sibson (1990) introduced the concept of fault-valve theory, where a reactivated fault plane can act as an open valve for fluids, promoting leakage and causing a hydrostatic gradient in fluid pressure. This fluid pressure cycling may significantly increase the variations in fault strength. Changes in frictional strength over the interseismic period resulting from the fault-valve activity may substantially exceed the shear stress drop at failure. In such circumstances, recurrence intervals between successive events can be highly variable. In regions where large ruptures tend to nucleate, the largest fluid pressure fluctuations result from faults that remain active as a consequence of fluid overpressure. Geological evidence suggests that valve action may be especially important in the lower regions of a seismogenic zone due to severely misoriented faults in the prevailing stress field. The most extreme fault-valve action is likely to be associated with high-angle reverse faults (Sibson, 1992). When fluid flow reactivates faults in the form of aseismic slip or earthquakes, the resulting shear deformation can cause considerable enhancement of the hydraulic diffusivity (in some cases, one order of magnitude increase). As mentioned earlier, the epicentre of the November 30, 2018, M_L 4.5 mainshock strongly correlates with a significant lateral pore pressure difference. Similar behaviour is observed in some other wells in the study area. Observations suggest a relationship between pressure difference across the fault and the induced seismicity in the vicinity of HF operations. The higher the pressure difference and the smaller the depth offset between the two wells, the greater the seismicity rate and magnitude. It is also expected that this pressure difference will affect the efficiency of HF jobs and the geometry of the fractures. Detailed studies are underway to validate these observations through numerical and statistical analysis.

Permeability Model

Permeability plays an important role in reservoir characterization since the distribution of permeable conduits within a reservoir controls fluid pressure diffusion (Riazi and Eaton, 2020). The most common permeability estimation methods are permeability prediction from core data, permeability calculation based on conventional well logs, and permeability estimation from the nuclear magnetic resonance (NMR) logs (Di, 2015). As the cost of cutting, running tests and analyzing the core data is nearly 10 times greater than well log analysis (Yao and Holditch, 1993), many attempts have been made to find permeability predictors in well logs. One of the most common approaches is using permeability–porosity correlations. These correlations are widely used in the industry and are suitable for quick

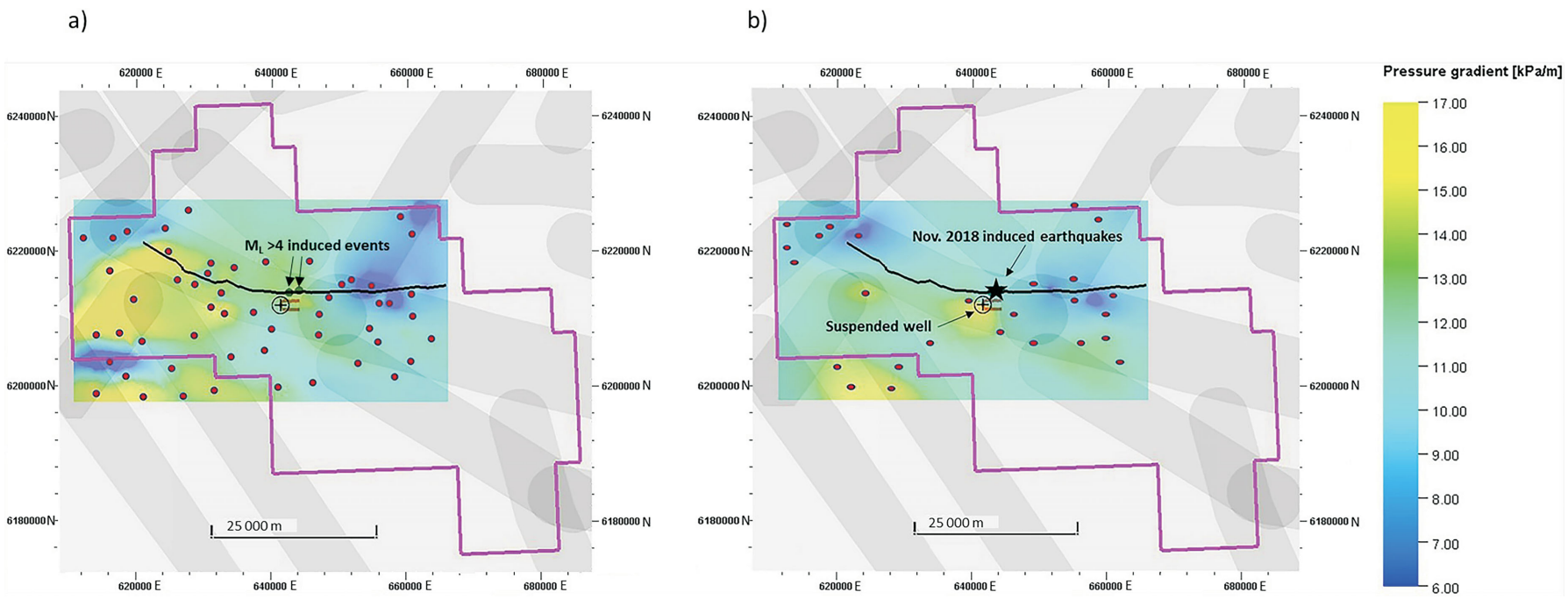

Figure 5. Pressure-gradient (kilopascals per metre [kPa/m]) maps of the **a)** Upper Montney and **b)** Middle Montney members based on data compiled in this study and populated using kriging interpolation. Data provided by geoLOGIC systems ltd. © 2021. Red dots show the distribution of pressure data points in the model. The star is the epicentre of the November 30, 2018, main-shock and the black line represents the southern bounding fault (projected to the surface from the Debolt Formation) of the Fort St. John graben. Magenta outline shows the Kiskatinaw Seismic Monitoring and Mitigation area. The suspended well symbol marks the pad location of the two horizontal wells (orange lines) in Figure 7. Structural corridors are indicated by translucent shading (see Figure 2). All co-ordinates are in UTM Zone 10 North, NAD 83.

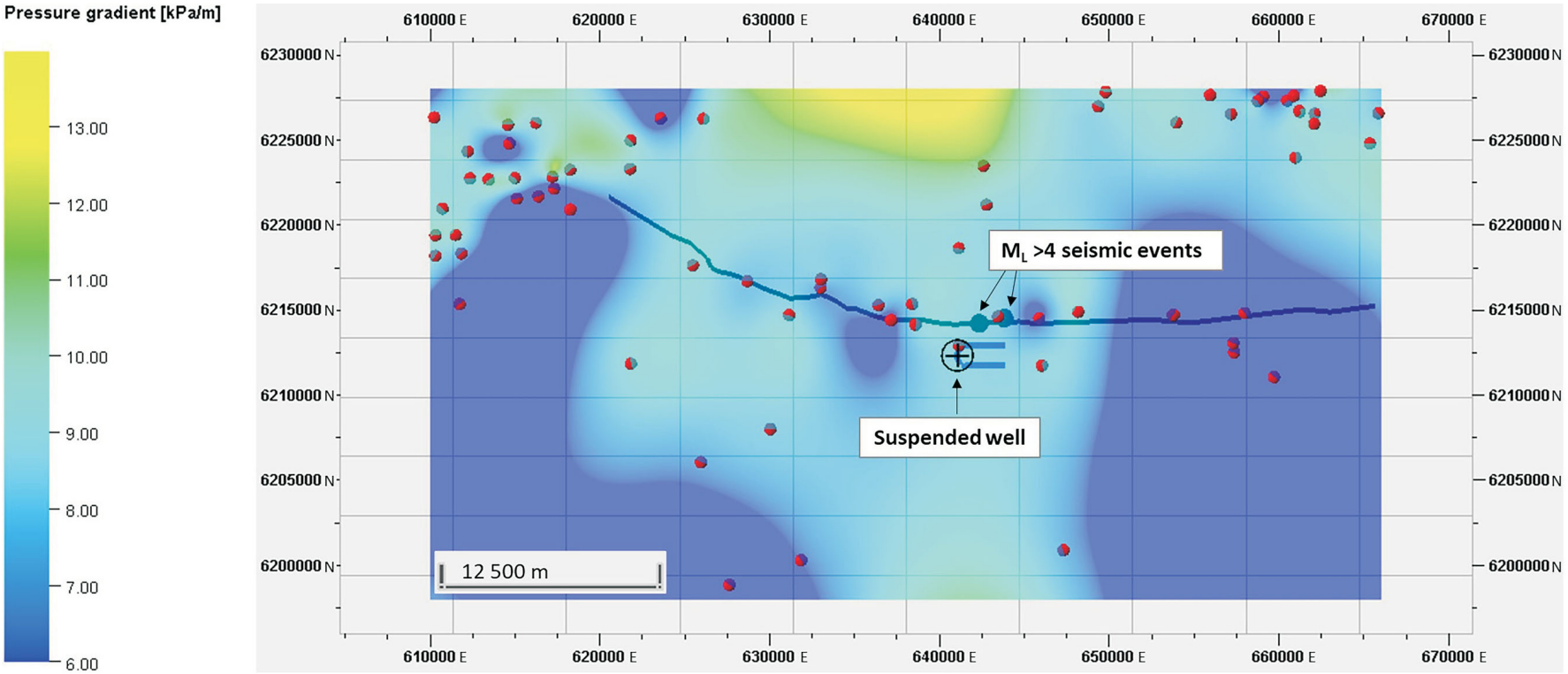

Figure 6. Pressure-gradient (kilopascals per metre [kPa/m]) map of the Halfway Formation, based on drill stem tests (DSTs). Red and grey dots show the locations of wells with pressure data. Data provided by geoLOGIC systems ltd. © 2021. The Halfway Formation overlies the Montney Formation but, unlike the Montney Formation, the Halfway Formation pore pressure gradient remains close to the hydrostatic gradient (10 kPa/m) throughout the study area. The southern bounding fault (projected to the surface from the Debolt Formation) of the Fort St. John graben is shown as the dark blue line. A number of conventional (structurally trapped reservoirs) producing wells are situated along the FSJG fault, providing independent validation of the fault location and upward deformation into the Halfway Formation. The suspended well symbol marks the pad location of the two horizontal wells (light blue line) in Figure 7. All co-ordinates are in UTM Zone 10 North, NAD 83. Abbreviation: M_L, local magnitude.

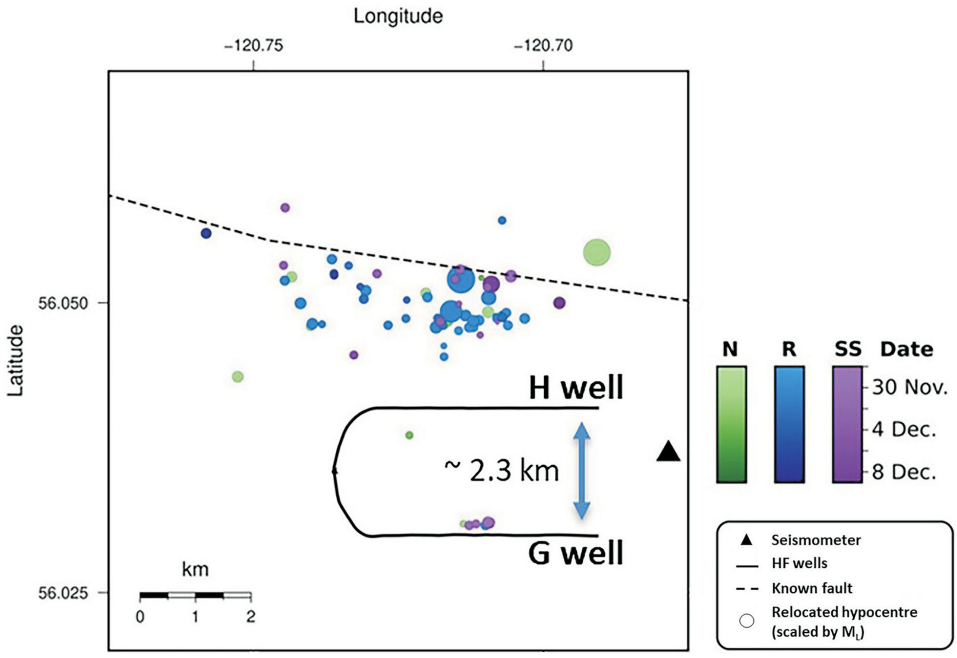

Figure 7. Epicentral location of the November 30, 2018, earthquake sequence coloured by type of event and shaded by timing of the event. The approximate location of the southern bounding fault (projected to the surface from the Debolt Formation) of the Fort St. John graben is shown by the dashed black line. Normal (N), reverse (R) and strike-slip (SS) mechanisms are shown by different colours. Figure is modified from Salvage and Eaton (2021). Abbreviations: HF, hydraulic fracturing; M_L, local magnitude.

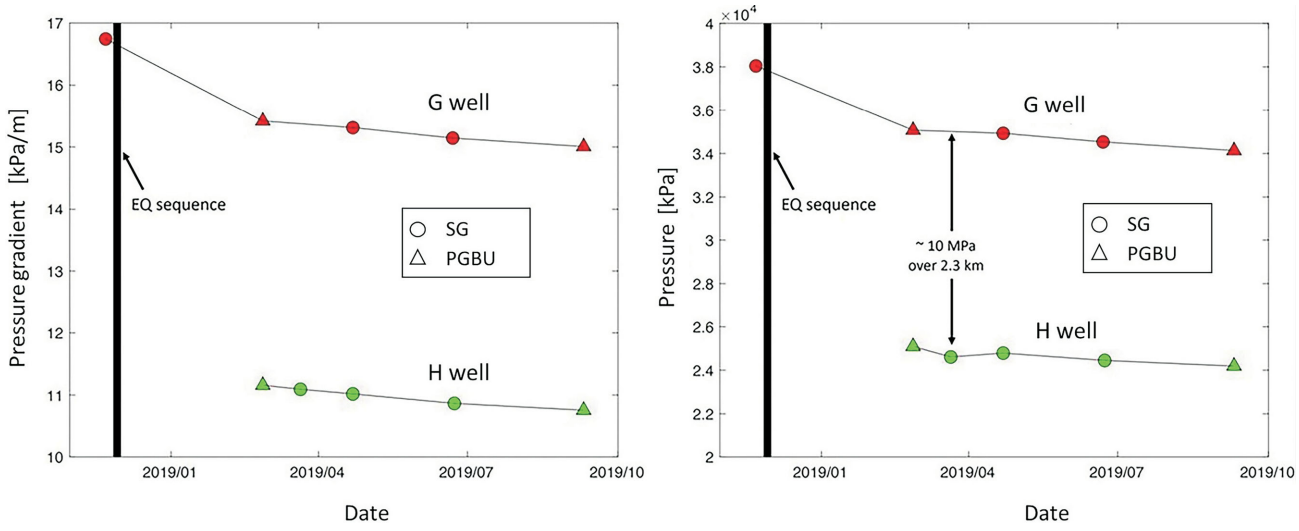

Figure 8. a) Bottom-hole pressure gradient and **b)** bottom-hole pressure for the G and H wells before and after the November 30, 2018, earthquake (EQ) sequence. There is an approximately 10 megapascal (MPa) pressure difference between the two wells, providing a tight constraint on the boundary between the Septimus High and Tower Moderate Low pressure terranes at this location (Figure 2). An apparent 3 MPa pressure drop after the mainshock may be related to fluid leak-off along the fault as predicted by the fault-valve model. Abbreviations: SG, static gradient test; PGBU, pressure gradient build-up test.

and still acceptable permeability estimation. For this study, the correlation used was

$$k = A\varphi^{a}$$

where k is permeability (m^2), A is an empirical constant, φ is fractional porosity and a is a porosity exponent. The coefficient and the exponent were calibrated with core data. Since there are many well logs in the study area, detailed porosity and permeability distribution maps were produced. The resulting permeability maps correlate well with the structural corridors (Figure 9). Permeabilities derived from DFIT reports, DSTs and core analysis were also used

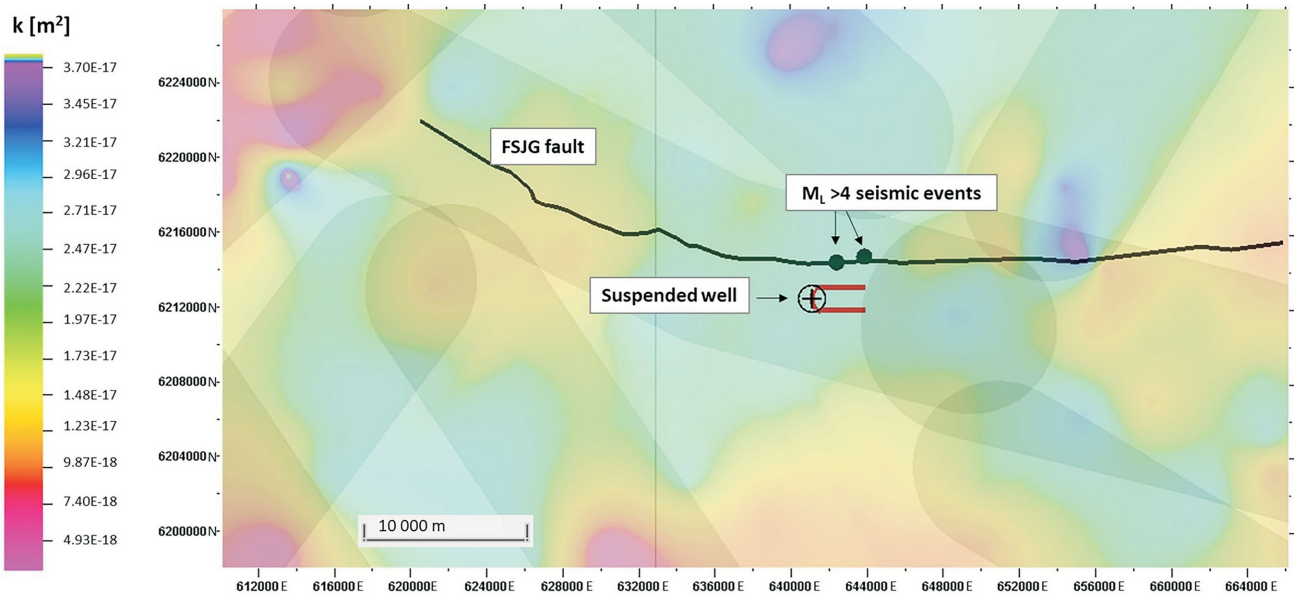

Figure 9. The Lower Montney Member permeability (k) map based on data compiled in this study using kriging interpolation. Data provided by geoLOGIC systems ltd. © 2021. Green dots show the locations of large magnitude events including the November 30, 2018, local magnitude (M_L) 4.5 mainshock. The green line represents the southern bounding fault of the Fort St. John graben (FSJG). The suspended well symbol marks the pad location of the two horizontal wells (red line) in Figure 7. Permeability shows a correlation with the structural corridors (indicated by translucent shading; see Figure 2). All co-ordinates are in UTM Zone 10 North, NAD 83.

for calibration. Log-derived permeabilities span a similar range of values.

Property Modelling

Well logs are arguably the best source of data for reservoir characterization and estimation of petrophysical properties at the macro scale. They can also be used to estimate dynamic elastic parameters, such as Poisson's ratio and Young's modulus. From more than 500 full suites of well logs, 100 wells were selected that had the best data quality and included (to the extent possible) the interval from the Debolt to Doig formations. An attempt was also made to have a relatively uniform distribution of well logs across the model area and a balance of locations across each fault. Logs used in this study included gamma-ray (GR), calliper (CAL), bulk density (RHOB, RHOZ), neutron and density porosity of sandstone (NPOR, DPHI), spontaneous potential (SP), photoelectric factor (PEF), shear and compressional sonic (DTS, DTP), shallow, medium and deep resistivity (Rxo, Rm, RD), and temperature (TEMP). Before log upscaling and property modelling, careful data cleaning and variogram analyses were performed for each zone to fit the best model based on the spatial correlation of the log samples. Petrophysical modelling was then carried out using the kriging interpolation method. To determine elastic rock properties in this study area, the following relationships were used for dynamic elastic moduli (Vishkai et al., 2017):

$$G_{dyn} = dynamic\ \ shear\ \ modulus = \frac{\rho_b}{\Delta t_s^{\ 2}}$$

$$K_{dyn} = dynamic\ \ bulk\ \ modulus = \frac{\rho_b}{\Delta t_p^{\ 2}} - \frac{4}{3} G_{dyn}$$

$$E_{dyn} = dynamic\ \ Young's\ \ modulus = \frac{9 G_{dyn} K_{dyn}}{G_{dyn} + 3K_{dyn}}$$

$$v_{dyn} = dynamic\ \ Poisson's\ \ ratio = \frac{\frac{1}{2}\left(\frac{\Delta t_s}{\Delta t_p}\right)^2 - 1}{\left(\frac{\Delta t_s}{\Delta t_p}\right)^2 - 1}$$

where ρ_b is bulk density (kg/m^3) and Δt_s and Δt_p are shear and compressional slowness (μs/m), respectively.

Faults are the most likely explanation for hydraulic disconnections. Structural discontinuities can impact the sedimentation processes, reflected in the dislocation of reservoir properties along the faults. Low diffusivity and transmissibility of the faults also result in sharp contrasts in hydraulic properties, such as pressure and permeability. The discontinuities in permeability, Young's modulus and the P-wave impedance, among other reservoir properties, show good correlation with the structural discontinuities. In areas with insufficient pressure data, the distribution of petrophysical and mechanical properties can help to infer the possible locations of the faults. Stratigraphic cross-sections and depth variations were inspected to confirm the location of a number of otherwise subtle faults (Figure 10).

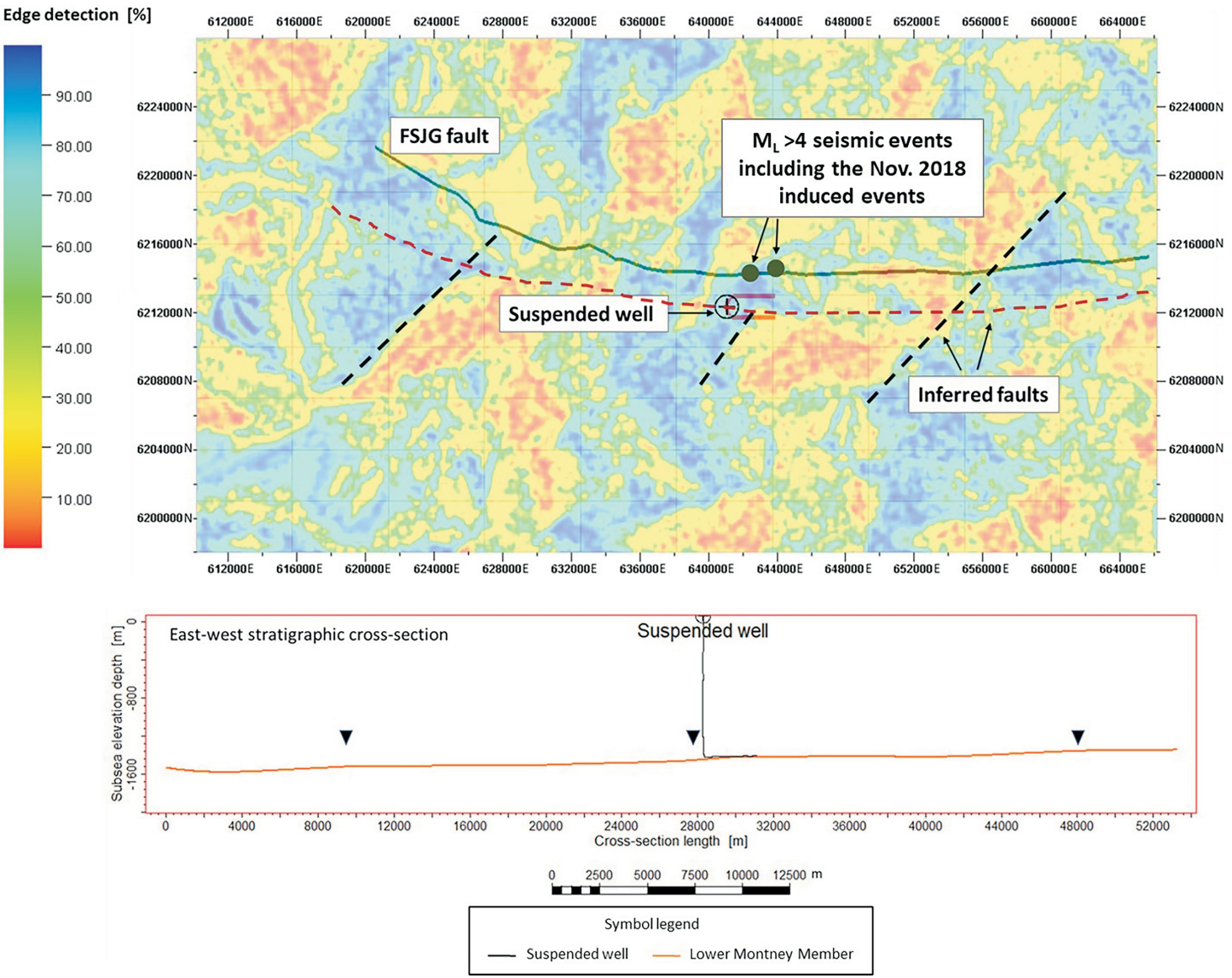

Figure 10. The Lower Montney Member edge detection map, expressed as a percent likelihood, based on log-derived Young's modulus. Data provided by geoLOGIC systems ltd. © 2021. Dashed lines are inferred faults based on property discontinuities. The inferred fault, shown as a red dashed line, correlates with a significant difference in the regional pore pressure gradient. The east-west stratigraphic cross-section (lower panel) shows the locations of these possible subtle faults. The suspended well symbol marks the pad location of the two horizontal wells (orange line) in Figure 7. All co-ordinates are in UTM Zone 10 North, NAD 83. Abbreviations: FSJG, Fort St. John graben; M_L, local magnitude.

Edge evidence is a statistical interpretation method in Schlumberger's Petrel, which can be used to enhance edges such as faults and salt body borders. It can detect sharp and/or fuzzy edges, whether short or long. This attribute can be used to enhance faults or the outline of geobody borders, if there is a suitable 'border' attribute that can be used as input. The edge evidence attribute searches locally in all directions for line segments where the values on the line differs significantly from the surrounding values. The result of the method is the best evidence of a line passing through that point. The better the evidence of a line, the higher the output value.

Conclusions

This compilation and other recent studies show that sealing faults act partially as pressure barriers, but seal preservation depends on the depth and reservoir pressure distribution. Observations suggest a relationship between the pressure difference across the fault and the induced seismicity rate and magnitude. The higher pressure difference seems to be correlated with higher seismicity rates and larger magnitudes. Also, variations in permeability and mechanical properties lie within the boundaries of structural corridors. In areas where pressure data are insufficient, the distribution of petrophysical and mechanical properties can help infer the locations of the possible faults.

Acknowledgments

This work was funded by a Natural Sciences and Engineering Research Council of Canada's Alliance grant and a scholarship from Geoscience BC. The authors would like to thank the BC Oil and Gas Commission and Geoscience BC for providing data; Schlumberger Canada Limited for the Petrel software platform; Itasca Consulting Group, Inc. for 3DEC™ software; and Halliburton Energy Services for GOHFER® software licensing. geoLOGIC systems ltd. is thanked for their contribution of data and software used in this study. All geoLOGIC systems ltd. data and geoSCOUT software is ©2021. Canadian Natural Resources Limited generously provided diagnostic fracture injection test data. The authors appreciate their peer reviewer, C. Wang, for taking the time and effort necessary to provide insightful guidance. All sponsors of the Microseismic Industry Consortium are thanked for their financial support.

References

Di, J. (2015): Permeability characterization and prediction in a tight oil reservoir, Edson Field, Alberta; M.Sc. thesis, University of Calgary, 113 p.

Enlighten Geoscience Ltd. (2021): Pressure, stress and fault slip risk mapping in the Kiskatinaw Seismic Monitoring and Mitigation Area, British Columbia; report prepared for the BC Oil and Gas Research and Innovation Society, Final Report ER-Seismic-2020-01, 81 p.

Fox, A.D. and Watson, N.D. (2019): Induced seismicity study in the Kiskatinaw Seismic Monitoring and Mitigation Area, British Columbia; report prepared for the BC Oil and Gas Commission, 51 p., URL <https://www.bcogc.ca/files/reports/Technical-Reports/final-report-enlighten-geoscience-kssma-phase-1-study-2019w-appendices-links.pdf> [November 2021].

Haghshenas, B. and Qanbari, F. (2020): Field-wide review of diagnostic fracture injection tests DFIT in Montney and Duvernay formations–part 1: stress and pressure distributions; Society of Petroleum Engineers Canada, Unconventional Resources Conference, September 28–October 2, 2020, virtual, paper no. SPE-199990-MS.

Riazi, N. and Eaton, D.W. (2020): Anatomy of a buried thrust belt activated during hydraulic fracturing; Tectonophysics, v. 795, art. 228640.

Salvage, R. and Eaton, D. (2021): How is induced seismicity affected by transitional stress regimes?; American Rock Mechanics Association, 55th U.S. Rock Mechanics Geomechanics Symposium, June 18–25, 2021, virtual, paper no. ARMA-2021-2078.

Sibson, R. (1992): Implications of fault-valve behaviour for rupture nucleation and recurrence; Tectonophysics, v. 211, no. 1–4, p. 283–293.

Sibson, R.H. (1990): Conditions for fault-valve behaviour; *in* Deformation Mechanisms, Rheology and Tectonics, R.J. Knipe and E.H. Rutter (ed.), Geological Society, Special Publication no. 54, p. 15–28.

Vishkai, M., Wang, J., Wong, R.C., Clarkson, C.R. and Gates, I.D. (2017): Modeling geomechanical properties in the Montney Formation, Alberta, Canada; International Journal of Rock Mechanics and Mining Sciences, v. 96, p. 94–105.

Visser, R., Smith, B., Kao, H., Babaie Mahani, A., Hutchinson, J. and McKay, J.E. (2017): A comprehensive earthquake catalogue for northeastern British Columbia and western Alberta, 2014–2016; Geological Survey of Canada, Open File 8335, 28 p.

Wood, J.M., Euzen, T., Sharp, L. and Leroux, S. (2021): Phase separation and secondary migration of methane rich gas accompanying uplift of an unconventional tight hydrocarbon system, Montney Formation, western Canada; Marine and Petroleum Geology, v. 124, art. 104808.

Wozniakowska, P., Eaton, D., Deblonde, C., Mort, A. and Ardakani, O. (in press): Identification of regional structural corridors in the Montney play using trend surface analysis combined with geophysical imaging; Geological Survey of Canada, Open File Report, OF-8814, 59 p.

Yao, C. and Holditch, S. (1993): Estimating permeability profiles using core and log data; Society of Petroleum Engineers, Eastern Regional Meeting, November 2–4, 1993, Pittsburgh, Pennsylvania, paper no. SPE-26921-MS.

BC Natural Gas Atlas: Description and Visualization Tools of Gas Geochemical Database for Northeastern British Columbia (Parts of NTS 093, 094)

M.J. Whiticar, School of Earth and Ocean Sciences, University of Victoria, Victoria, British Columbia, whiticar@uvic.ca

E. Wiebe, School of Earth and Ocean Sciences, University of Victoria, Victoria, British Columbia

Whiticar, M.J. and Wiebe, E. (2022): BC Natural Gas Atlas: description and visualization tools of gas geochemical database for northeastern British Columbia (parts of NTS 093, 094); *in* Geoscience BC Summary of Activities 2021: Energy and Water, Geoscience BC, Report 2022-02, p. 61–74.

Introduction

The objective of the British Columbia Natural Gas Atlas (BC-NGA) project, funded by Geoscience BC and the BC Oil and Gas Research and Innovation Society (BC OGRIS), is to create a thorough, searchable and mappable geochemical inventory of natural gases in northeastern BC. This accessible geochemical database will be a valuable resource for a broad range of users, for example, industry, government, non-governmental organizations (NGOs) and the general public. The project output is available at www.bcnga.ca and is the result of extensive efforts by C. Evans (Evans, 2019). For a detailed description of the BC-NGA project, the database and quality assurance–quality control (QA-QC) filters, refer to Whiticar and Evans (2020).

The primary goals of the BC-NGA project are to

1) produce a database of the unique natural gas compositional data assembled from past and active gas operations around northeastern BC (BC-NGA phase 1);
2) characterize and map the geochemical conditions of northeastern BC's major ongoing and future regions of petroleum exploration and production;
3) contribute to understanding the geological framework of natural gas deposits, from field to basin scales;
4) assist development of petroleum system models that help de-risk the exploration and production of plays by providing an understanding and prediction of generation occurrences, histories and potential productivity of natural gas in northeastern BC;
5) provide a robust baseline of gas signatures that help identify and track fugitive emissions of natural gas (into groundwaters and the atmosphere), for example, distinguish microbial gas from thermogenic gas;
6) offer a 'geochemical fingerprint' catalogue for different gas sources, useful in provenance studies at the production, well completion, processing and transport stages; and
7) establish a database to identify and track fugitive gas emissions into surface waters and the atmosphere.

In addition, the BC-NGA project seeks to

1) provide an important, unique, geochemical inventory and assessment of natural gas occurrences in BC;
2) establish a comprehensive, legacy, regional/play, natural gas character framework (e.g., baselines, stratigraphic control, source rocks);
3) enable critical multi-user participation by the energy industry, governments (e.g., First Nations, BC Ministry of Energy, Mines and Low Carbon Innovation, BC Oil and Gas Commission [BCOGC]), not for profit organizations (e.g., Geoscience BC), academic institutions (e.g., BC universities and colleges), NGOs and the public;
4) provide an open-access platform for database query, mapping, plotting and interpretation;
5) integrate BC-NGA into existing Canadian petroleum databases; and
6) contribute diagnostic subsurface gas geochemical data for northeastern BC to groundwater and fugitive gas emissions studies (e.g., Goetz et al., 2021).

The BC-NGA project involved accessing, incorporating and reporting the nonconfidential gas molecular and isotope geochemical data from the BCOGC repository, as well as adding calculated geochemical ratios and other parameters for gas typing and subsurface mapping.

Having detailed information on the geochemical characterization of natural gases, which should routinely include the stable isotope composition of the gases, benefits the operator, potentially allowing them to optimize the gas revenue stream by understanding where certain gas types occur. The systematic cataloguing of BC natural gases in this BC-NGA project will reveal information about the development, migration, segregation and compartmentalization of natural gases within petroleum systems. It will also define

This publication is also available, free of charge, as colour digital files in Adobe Acrobat® PDF format from the Geoscience BC website: http://geosciencebc.com/updates/summary-of-activities/.

the distribution of natural gas liquids, which will help gas producers and governments to target higher value assets and natural gas streams.

Additional information may be gained on the effectiveness of regional seals and the impact of geological structure on seal integrity. This information is critical to ensure shallow aquifers are not being compromised during hydraulic fracturing operations. Also, communication between wells (e.g., during hydraulic fracturing) can be tested with diagnostic gas geochemical tracers.

Although new wells are generally drilled with state-of-the-art completion methods and production equipment, there are concerns that the associated drilling, production and transmission activities allow gases to fugitively escape into the atmosphere or shallow groundwater. This includes the release of natural gas from poor well completions, compromised surface-casing cements and pressure cycling during hydraulic fracturing. There are also additional concerns regarding fugitive gas emissions from older, sometimes abandoned, wellbores where cementing practices were less rigorous than required.

The ability to identify a leaking gas source has many benefits for the public and industry. In the case of a leaking wellbore, operators can lower remediation costs by having a higher level of certainty as to the gas source (e.g., depth and location), thereby allowing the operator to quickly and efficiently plan remediation of a leaking wellbore. The identification of gas emission sources can also assist in the remediation of old and abandoned wellbores. The methodology would allow companies and others to pinpoint the horizon(s) that is (are) leaking, thereby reducing fugitive gas emissions, in addition to lost product and revenue.

The detection of fugitive emissions from natural gas upstream activities (exploration, production and transmission) is critical for the responsible development of the resource and for the health and safety of all communities. Cataloguing the geochemical fingerprint of the different types and sources of natural gas in the subsurface is a critical step in the development of a comprehensive air-quality monitoring network.

As new (and previous) wells and oil and gas reservoirs are drilled and tested, natural gas samples are collected for geochemical analyses. By routinely measuring the molecular and isotopic composition of these gases, important details are learned about the character of the gases present, their habitat, origin (e.g., microbial or thermogenic), type of organic source material (e.g., kerogen), maturity or rank levels. Secondary processes, such as degradation, oxidation, mixing and commingling, can also be identified.

In addition to providing a basic gas geochemical database, the BC-NGA is further enhanced with a QA-QC script. This feature improves the reliability of the data and provides quality assessment of the data, while maintaining the transparency of the original database.

In 2021, the BC-NGA database was updated to include the recent addition of data from 86 conventional producing gas wells, provided by Canadian Natural Resources Limited (CNRL). These wellhead data provide a valuable addition to the database of produced, conventional gases. Furthermore, this iteration of the BC-NGA website now offers an interactive, online, data selection and visualization package.

Updated and Enhanced BC-NGA Database

To streamline scripting, improve database performance and to enable interactive user features, the BC-NGA database was reprogrammed. The previous three database levels (Raw BC-NGA dataset, Primary BC-NGA dataset and User BC-NGA dataset) were initially designed to ensure and maintain data treatment transparency. These have been replaced by a single database that merges the three datasets, while maintaining transparency and fidelity. The current revised database is available for download as a .csv file from www.bcnga.ca. The most recent version, updated on October 01, 2021, contains 44 689 individual records (e.g., from wells and horizons). Prior to June 25, 2020, the records were manually compiled and processed and stored on the database; since June 25, 2020, the records have been automatically added and processed with QA-QC scripts within BC-NGA.

The BC-NGA database contains 157 fields (Table 1). It holds 64 basic parameters, such as the BCOGC well authorization number (WA#), location, sampling depth, mol % methane and $\delta^{13}CH_4$, as defined in Table 2. There are also 18 identifier fields, such as BCOGC formation code and data source. In addition, for the automated QA-QC process, there are 103 fields that contain the results of a specific data test (Table 3) and all data are flagged as pass (p), fail (f) or conditional (c). For example, if the mol % for CH_4 is >100%, it is recorded as 'f' (fail). However, any data flagged as fail (f) or conditional (c) are not removed from the database. This no-loss data retention is an important feature of the enhanced database. It allows for the easy identification of questionable data, and flags precisely why the data are considered questionable with the defined criteria. However, as the data are not eliminated from the database, this also allows users to custom set or remove the filter criteria (choices of p, f and c values) and/or develop their own filters to independently QA-QC and filter the database. The user can also select to download the entire database as a .csv file for offline work.

The enhanced BC-NGA database now includes a useful online feature that allows users to create individualized data subsets. A data subset is created online by selecting a suite

Table 1. List of 157 parameters in the British Columbia Natural Gas Atlas (BC-NGA) database. See Table 2 for parameter and label abbreviations. See Table 3 for explanation of quality assurance–quality control (QA-QC) control filters (fil).

Parameter name	Parameter name	Parameter name
1 id	54 C2_div_iC4_Mol_percent	106 fil_ao_Dryness_ratio_high
2 BCNGA_test_index	55 C2_div_C3_Mol_percent	107 fil_ap_any_delta_13C_high_or_low
3 WA_num	56 N2_div_O2_Mol_percent	108 fil_aq_any_delta_deuterium_high_or_low
4 data_pass_fail_p_f_c	57 d13C2_minus_d13C1	109 fil_ar_CO2_ISO_13C_low
5 Bottom_Depth	58 d13C2_minus_d13C3	110 fil_as_CO2_ISO_13C_high
6 Top_Depth	59 d13C1_minus_d13C3	111 fil_at_C1_ISO_13C_low
7 corrected_date	60 QA_QC_and_other_comments	112 fil_au_C1_ISO_13C_high
8 formatted_date	61 eastingUTM	113 fil_av_C2_ISO_13C_low
9 BCNGA_play_category	62 northingUTM	114 fil_aw_C2_ISO_13C_high
10 NGA_sample_type	63 Gas_lab_num_OGC_Primary	115 fil_ax_C3_ISO_13C_low
11 Primary_data_source	64 Primary_flag_summary	116 fil_ay_C3_ISO_13C_high
12 C1_Methane_Mol_percent	65 fil_xx_data_not_used	117 fil_az_ISO_C1_C2_difference
13 C2_Ethane_Mol_percent	66 fil_a_C1_low	118 fil_ba_ISO_C2_C3_difference
14 C3_Propane_Mol_percent	67 fil_b_C1_high	119 fil_bb_iC4_ISO_13C_low
15 iC4_iButane_Mol_percent	68 fil_c_C2_low	120 fil_bc_iC4_ISO_13C_high
16 nC4_nButane_Mol_percent	69 fil_d_C2_high	121 fil_bd_nC4_ISO_13C_low
17 iC5_iPentane_Mol_percent	70 fil_e_C3_low	122 fil_be_nC4_ISO_13C_high
18 nC5_nPentane_Mol_percent	71 fil_f_C3_high	123 fil_bf_nC5_ISO_13C_low
19 C6plus_Hexanes_Plus_Mol_percent	72 fil_g_iC4_low	124 fil_bg_nC5_ISO_13C_high
20 N2_Nitrogen_Mol_percent	73 fil_h_iC4_high	125 fil_bh_C1_ISO_D_low
21 O2_and_Ar_combined_Mol_percent	74 fil_i_nC4_low	126 fil_bi_C1_ISO_D_high
22 CO2_Carbon_Dioxide_Mol_percent	75 fil_j_nC4_high	127 fil_bj_C2_ISO_D_low
23 H2S_Sour_Gas_Mol_percent	76 fil_k_iC5_low	128 fil_bk_C2_ISO_D_high
24 He_Helium_Mol_percent	77 fil_l_iC5_high	129 fil_bl_C3_ISO_D_low
25 H2_Hydrogen_Mol_percent	78 fil_m_nC5_low	130 fil_bm_C3_ISO_D_high
26 C1_percent_rel_HC_percent	79 fil_n_nC5_high	131 fil_bn_bad_depth
27 C2_percent_rel_HC_percent	80 fil_o_nC6p_low	132 fil_bo_bad_date1
28 C3_percent_rel_HC_percent	81 fil_p_nC6p_high	133 fil_bp_bad_date2
29 iC4_percent_rel_HC_percent	82 fil_q_C1_low	134 fil_bq_unexpected_date
30 nC4_percent_rel_HC_percent	83 fil_r_C1_high	135 fil_br_unexpected_depth
31 iC5_percent_rel_HC_percent	84 fil_s_C2_low	136 fil_bs_N2_high
32 nC5_percent_rel_HC_percent	85 fil_t_C2_high	137 fil_bt_O2_high
33 C6plus_percent_rel_HC_percent	86 fil_u_C3_low	138 fil_bu_N2_ratio_O2_not_atmospheric
34 d13C_C1_permil	87 fil_v_C3_high	139 fil_bv_injection_or_disposal_well
35 d13C_C2_permil	88 fil_w_iC4_low	140 OGC_Bottom_Depth
36 d13C_C3_permil	89 fil_x_iC4_high	141 OGC_Top_Depth
37 d13C_iC4_permil	90 fil_y_nC4_low	142 NGA_bottom_depth
38 d13C_nC4_permil	91 fil_z_nC4_high	143 NGA_top_depth
39 d13C_iC5_permil	92 fil_aa_iC5_low	144 OGC_sample_date_text
40 d13C_nC5_permil	93 fil_ab_iC5_high	145 OGC_sample_date
41 d13C_CO2_permil	94 fil_ac_nC5_low	146 BCNGA_play_category_2
42 d2H_C1_permil	95 fil_ad_nC5_high	147 PRCL_formation_correlation
43 d2H_C2_permil	96 fil_ae_nC6p_low	148 OGC_Formation_code
44 d2H_C3_permil	97 fil_af_nC6p_high	149 Match_injection_disposal
45 d2H_iC4_permil	98 fil_ag_H2S_high	150 Gas_lab_num_OGC
46 d2H_nC4_permil	99 fil_ah_CO2_high	151 NGA_adjusted_gas_lab_number
47 d2H_iC5_permil	100 fil_ai_alkene_alkyne	152 Isotech_Lab_No
48 d2H_nC5_permil	101 fil_aj_Bernard_low	153 BCNGA_sample_type
49 Bernard_Ratio_C1_div_C2_plus_C3	102 fil_ak_Bernard_high	154 OGC_Sample_Point
50 Wetness_Ratio_sumC2_to_nC4_div_sumC1_to_nC4	103 fil_al_Bernard_error_DIV0	155 data_source
51 Dryness_Ratio_C1_div_sumC1_to_nC4	104 fil_am_Bernard_error_blank_C1	156 dindex
52 C1_div_C2_Mol_percent	105 fil_an_Wetness_ratio_high	157 sample_timestamp
53 iC4_div_nC4_Mol_percent		

Table 2. Glossary of parameter and label abbreviations used in the British Columbia Natural Gas Atlas (BC-NGA) database (shown in Table 1).

Abbreviation in database	Designation/definition
id	Sequential numbering (for sorting)
BCNGA_test_index	BC Natural Gas Atlas assigned unique identifier text field
WA_num	BCOGC designated well authorization number
data_pass_fail_p_f_c	QA-QC filter status
Bottom_Depth	Bottom of sample collection interval (m)
Top_Depth	Top of sample collection interval (m)
corrected_date	Manual date conversion from various text formats
formatted_date	Formatted date for user
BCNGA_play_category	Sampled geological unit using BC Ministry of Energy, Mines and Low Carbon Innovation (2006) atlas designations
NGA_sample_type	Type of sample collected
Primary_data_source	Origin of the data
C1 or Methane	Methane (CH_4)
C2 or Ethane	Ethane (C_2H_6)
C3 or Propane	Propane (C_3H_8)
iC4 or iButane	iso-Butane (C_4H_{10})
nC4 or nButane	n-Butane (C_4H_{10})
iC5 or iPentane	iso-Pentane (C_5H_{12})
nC5 or nPentane	n-Pentane (C_5H_{12})
C6plus or Hexanes Plus	Hexanes + higher alkanes
N2 or Nitrogen	Nitrogen (N_2)
O2 and Ar combined	Oxygen and argon combined (O_2 + Ar)
CO2 or Carbon Dioxide	Carbon dioxide (CO_2)
H2S or Sour Gas	Hydrogen sulphide (H_2S)
He or Helium	Helium (He)
H2 or Hydrogen	Hydrogen (H_2)
Mol_percent	mol % calculated from total gas with non-numerics removed
HC	Hydrocarbon(s)
Cx_percent_rel_HC_percent	Relative mol % calculated from C_1 to C_6+ hydrocarbons only (100*iC_x mol %/total HC)
d13C_Cx_permil	$\delta^{13}C$, stable carbon isotope ratio of compound (relative to VPDB standard)
d2H_Cx_permil	$\delta^{2}H$, stable hydrogen isotope ratio of compound (relative to VSMOW standard)
Bernard_Ratio_C1_div_C2_plus_C3	mol % C_1 divided by Σ mol % C_2 + mol % C_3, BR = $\%C_1/(\%C_2+\%C_3)$
BR	Bernard Ratio, BR = $\%C_1/(\%C_2+\%C_3)$
Wetness_Ratio_sumC2_to_nC4_div_sumC1_to_nC4	Σ mol % C_2 to n-C_4 divided by Σ mol % C_1 to mol % n-C_4
Dryness_Ratio_C1_div_sumC1_to_nC4	mol % C_1 divided by Σ mol % C_1 to mol % n-C_4
Cx_div_Cy_Mol_percent	Division of C_x by C_y (mol % C_x divided by mol % C_y x 100)
d13Cy_minus_d13Cx	Subtraction of $\delta^{13}C_x$ from $\delta^{13}C_y$
QA_QC_and_other_comments	Comment for corrections or changes as a result of filters
eastingUTM	UTM map co-ordinates (easting)
northingUTM	UTM map co-ordinates (northing)
Gas_lab_num_OGC_Primary	Analytical lab reference number
Primary_flag_summary	Concatenation of filtering flags ('fil') as text string
div	Divided by
rel	Relative
No or num	Number
fil_letter (e.g. fil_b_C1_high)	Filter criteria
QA_QC	Quality assurance and quality control
ISO	Isotope
VPDB	Vienna Pee Dee Belemnite (carbon isotope standard)
VSMOW	Vienna Standard Mean Ocean Water (hydrogen isotope standard)
BCOGC or OGC	British Columbia Oil and Gas Commission
PRCL	Petrel Robertson Consulting Ltd.
Isotech	Isotech Laboratories, Inc.

Table 3. Explanation of limits used for the quality assurance–quality control (QA-QC) filters (fil; shown in Table 1) for the British Columbia Natural Gas Atlas (BC-NGA) database. The abbreviation ±2σ used here means the statistical threshold of plus or minus 2 standard deviations from the approximate average value for that parameter over the entire database.

Abbreviation in database	Designation / definition
fil_xx_data_not_used	Report flagged as replicate or other problems (see columns "replicate_report" and "report_error")
fil_a_C1_low	Methane amount in total gas is abnormally <±2σ of 10 mol %
fil_b_C1_high	Methane amount in total gas is abnormally >±2σ of 99.8 mol %
fil_c_C2_low	Ethane amount in total gas is abnormally <±2σ of 0.05 mol %
fil_d_C2_high	Ethane amount in total gas is abnormally >±2σ of 13 mol %
fil_e_C3_low	Propane amount in total gas is abnormally <±2σ of 0.03 mol %
fil_f_C3_high	Propane amount in total gas is abnormally >±2σ of 6 mol %
fil_g_iC4_low	iso-Butane amount in total gas is abnormally <±2σ 0.03 mol %
fil_h_iC4_high	iso-Butane amount in total gas is abnormally >±2σ of 0.8 mol %
fil_i_nC4_low	n-Butane amount in total gas is abnormally <±2σ of 0.03 mol %
fil_j_nC4_high	n-Butane amount in total gas is abnormally >±2σ of 1.6 mol %
fil_k_iC5_low	iso-Pentane amount in total gas is abnormally <±2σ of 0.03 mol %
fil_l_iC5_high	iso-Pentane amount in total gas is abnormally >±2σ of 0.3 mol %
fil_m_nC5_low	n-Pentane amount in total gas is abnormally <±2σ of 0.03 mol %
fil_n_nC5_high	n-Pentane amount in total gas is abnormally >±2σ of 0.5 mol %
fil_o_nC6+_low	Hexane+ (C_6+) amount in total gas is abnormally <±2σ of 0.03 mol %
fil_p_nC6+_high	Hexane+ (C_6+) amount in total gas is abnormally >±2σ of 4 mol %
fil_q_C1_low	Methane relative % to C_1-C_6 hydrocarbons is <±2σ of 77%
fil_r_C1_high	Methane relative % to C_1-C_6 hydrocarbons is >±2σ of 99.8%
fil_s_C2_low	Ethane relative % to C_1-C_6 hydrocarbons is <±2σ of 1%
fil_t_C2_high	Ethane relative % to C_1-C_6 hydrocarbons is >±2σ of 13%
fil_u_C3_low	Propane relative % to C_1-C_6 hydrocarbons is <±2σ of 0.5%
fil_v_C3_high	Propane relative % to C_1-C_6 hydrocarbons is >±2σ of 6%
fil_w_iC4_low	iso-Butane relative % to C_1-C_6 hydrocarbons is <±2σ of 0.3%
fil_x_iC4_high	iso-Butane relative % to C_1-C_6 hydrocarbons is >±2σ of 1%
fil_y_nC4_low	n-Butane relative % to C_1-C_6 hydrocarbons is <±2σ of 0.3%
fil_z_nC4_high	n-Butane relative % to C1-C6 hydrocarbons is >±2σ of 1.9%
fil_aa_iC5_low	iso-Pentane relative % to C_1-C_6 hydrocarbons is >±2σ of <0.01%
fil_ab_iC5_high	iso-Pentane relative % to C_1-C_6 hydrocarbons is >±2σ of 1%
fil_ac_nC5_low	n-Pentane relative % to C_1-C_6 hydrocarbons is <±2σ of 0.3%
fil_ad_nC5_high	n-Pentane relative % to C_1-C_6 hydrocarbons is >±2σ of 0.7%
fil_ae_nC6+_low	Hexane plus relative % to C_1-C_6 hydrocarbons is <±2σ of 0.3%
fil_af_nC6+_high	Hexane + (C_6+) relative % to C_1-C_6 hydrocarbons is >±2σ of 4%
fil_ag_H2S_high	Hydrogen sulphide total gas is abnormally >±2σ of 7 mol %
fil_ah_CO2_high	Carbon dioxide total gas is abnormally >±2σ of 10 mol %
fil_ai_alkene/alkyne	Any unsaturated hydrocarbons amount in total gas is >0.0 mol %
fil_aj_Bernard_low	Bernard ratio $C_1/(C_2+C_3)$ < 0.1
fil_ak_Bernard_high	Bernard ratio $C_1/(C_2+C_3)$ >10 000
fil_al_Bernard_error_DIV0	Bernard ratio $C_1/(C_2+C_3)$ is an error where (C_2+C_3) = zero
fil_am_Bernard_error_blank_C1	Error in C_1 (RAW dB) means the Bernard ratio is not calculated
fil_an_Wetness_ratio_high	Ratio of sum of C_2, C_3, C_4 divided by sum C_1, C_2, C_3, C_4 >0.99
fil_ao_Dryness_ratio_high	Ratio of sum of C_1 divided by all C_1, C_2, C_3, C_4 >0.99
fil_ap_any_delta_13C_high_or_low	All $\delta^{13}C$ fields checked for known natural range of +30 ‰ to -120 ‰ VPDB
fil_aq_any_delta_deuterium_high_ or_low	All $\delta^{2}H$ fields checked for known natural range of 0 ‰ to -500 ‰ VSMOW
fil_ar_CO2_ISO_13C_low	$\delta^{13}C$-CO_2 is abnormally <±2σ of -30.0 ‰
fil_as_CO2_ISO_13C_high	$\delta^{13}C$-CO_2 is abnormally >±2σ of +15.0 ‰
fil_at_C1_ISO_13C_low	$\delta^{13}C$-CH_4 is abnormally depleted <±2σ of -55.0 ‰
fil_au_C1_ISO_13C_high	$\delta^{13}C$-CH_4 is abnormally enriched >±2σ of -33.0 ‰
fil_av_C2_ISO_13C_low	$\delta^{13}C$-C_2 is abnormally depleted <±2σ of -38.3 ‰
fil_aw_C2_ISO_13C_high	$\delta^{13}C$-C_2 is abnormally enriched >±2σ of -25.5 ‰
fil_ax_C3_ISO_13C_low	$\delta^{13}C$-C_3 is abnormally depleted <±2σ of -36.3 ‰

Table 3 (continued). Explanation of limits used for the quality assurance–quality control (QA-QC) filters (fil; shown in Table 1) for the British Columbia Natural Gas Atlas (BC-NGA) database. The abbreviation ±2σ used here means the statistical threshold of plus or minus 2 standard deviations from the approximate average value for that parameter over the entire database.

Abbreviation in database	Designation / definition
fil_ay_C3_ISO_13C_high	$\delta^{13}C$-C_3 is abnormally enriched >±2σ of -22.3 ‰
fil_az_ISO_C1_C2_difference	$\delta^{13}C$-CH_4 minus $\delta^{13}C$-C_2 >1 [positive indicates either error or "reversal"]
fil_ba_ISO_C2_C3_difference	$\delta^{13}C$-C_2 minus $\delta^{13}C$-C_3 >1 [positive indicates either error or "reversal"]
fil_bb_iC4_ISO_13C_low	$\delta^{13}C$-iC_4 is abnormally depleted <±2σ of -36.8 ‰
fil_bc_iC4_ISO_13C_high	$\delta^{13}C$-iC_4 is abnormally enriched >±2σ of -22.5 ‰
fil_bd_nC4_ISO_13C_low	$\delta^{13}C$-nC_4 is abnormally depleted <±2σ of -34.6 ‰
fil_be_nC4_ISO_13C_high	$\delta^{13}C$-nC_4 is abnormally enriched >±2σ of -21.7 ‰
fil_bf_nC5_ISO_13C_low	$\delta^{13}C$-nC_5 is abnormally depleted <±2σ of -33.1 ‰
fil_bg_nC5_ISO_13C_high	$\delta^{13}C$-nC_5 is abnormally enriched >±2σ of -23.4 ‰
fil_bh_C1_ISO_D_low	$\delta^{2}H$-CH_4 is abnormally depleted <±2σ of -298 ‰
fil_bi_C1_ISO_D_high	$\delta^{2}H$-CH_4 is abnormally enriched >±2σ of -151 ‰
fil_bj_C2_ISO_D_low	$\delta^{2}H$-C_2 is abnormally depleted <±2σ of -170 ‰
fil_bk_C2_ISO_D_high	$\delta^{2}H$-C_2 is abnormally enriched >±2σ of -133 ‰
fil_bl_C3_ISO_D_low	$\delta^{2}H$-C_3 is abnormally depleted <±2σ of -250 ‰
fil_bm_C3_ISO_D_high	$\delta^{2}H$-C_3 is abnormally enriched >±2σ of -145 ‰
fil_bn_bad_depth	Depth is blank or unknown
fil_bo_bad_date1	Sample date is blank or unknown
fil_bp_bad_date2	Analysis date is blank or unknown
fil_bq_unexpected_date	Sample date outside range, yyyymmdd format of 19750000 to 20190701
fil_br_unexpected_depth	Depth is outside expected range 400 to 7000 m
fil_bs_N2_high	Nitrogen amount in total gas > atmosphere mixing ratio (78.1 mol %)
fil_bt_O2_high	Oxygen amount in total gas > atmosphere mixing ratio (20.9 mol %)
fil_bu_N2_ratio_O2_not_atmospheric	N_2/O_2 ratio below 3.73 or above 3.74 (ratio of 78.1 to 20.9 mol %)
fil_bv_injection_or_disposal_well	Possible injection or disposal well sample

of one or more parameters, for example, mol % ethane, $\delta^{13}CH_4$ and play category, and then setting the upper and lower limits, range or value for each parameter (Figure 1). The database is filtered by these criteria and the subset created. This data subset can be downloaded as a separate .csv file for offline work or used online for the gas geochemical interpretative plotting routines, described below.

Gas Geochemical Interpretative Plots from BC-NGA Database

Over the past 60 years, geochemists have developed a suite of geochemical parameters that can define and distinguish different natural gases (e.g., Whiticar, 2021). Several review papers have been published on the interpretation of natural gases using geochemical parameters, including the applications of stable isotopes, for example, Schoell (1980), Stahl and Faber (1983), Galimov (1988), Clayton (1991), Whiticar (1994), Prinzhofer and Battani (2003) and Liu et al. (2019). From field and experimental studies, a range of interpretative diagrams have emerged with the broadest utility to classify natural gases and identify primary and secondary effects, such as source rock type, degree of maturation, migration and degradation. Table 4 is an abbreviated list, from Whiticar (2021), of the more common interpretative diagrams used in gas geochemistry.

For the BC-NGA, a selection of these gas geochemistry interpretative diagrams has been created using various combinations of parameters, for example, mol% CH_4, $\delta^{13}CH_4$ and $C_1/(C_2+C_3)$. These plots can be populated using the whole BC-NGA database or using the online-generated data subsets filtered by user criteria. Four examples of the 10 interpretative plots currently available in the online plotting tool are shown in Figures 2 to 5. The data plotted in the figures are an example of a data subset resulting from the chosen data filtering variables (mol % ethane, $\delta^{13}CH_4$, play category) and their respective values, shown in Figure 1.

Figure 2 is commonly termed the 'Bernard Diagram' (Bernard et al., 1976); it plots the relative molecular abundance of the light hydrocarbons C_1-C_3 as the Bernard ratio, that is, $C_1/[C_2+C_3]$ on a volume basis against the stable carbon isotope ratio, $\delta^{13}C_{CH4}$. The Bernard Diagram expands the presence and mixing of microbial gas with thermogenic gas, and is particularly useful for surface sediment studies.

Figure 3 is a modified $\delta^{13}C_{CH4}$ versus $\delta^{2}H_{CH4}$ plot (after Whiticar, 2021) that emphasizes thermogenic natural gases (i.e., associated, humic, etc.). This is a truncated version of the traditional 'CD diagram' or 'Whiticar plot' (e.g., Whiticar, 2020).

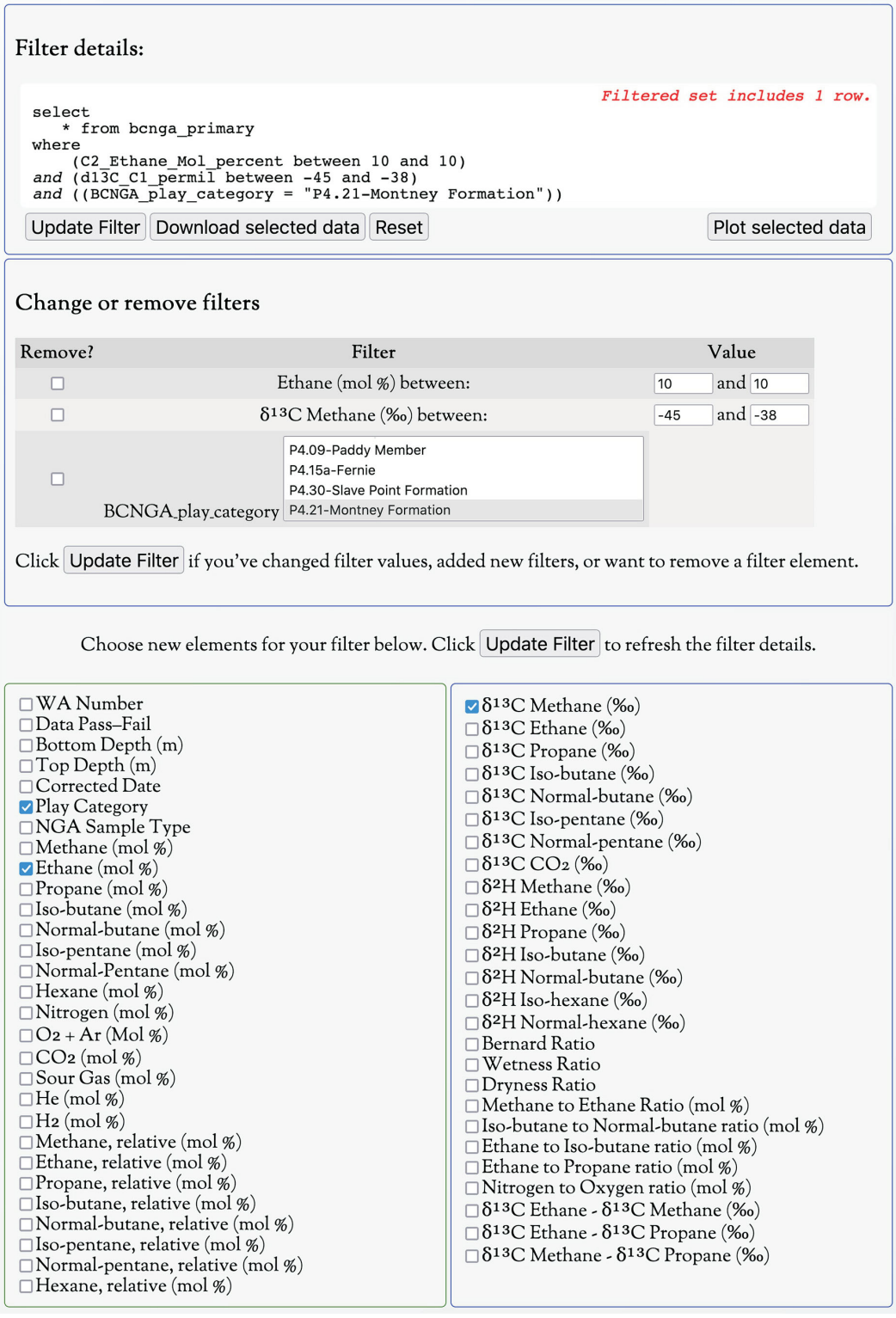

Figure 1. Example of a data subset from the British Columbia Natural Gas Atlas (BC-NGA) database on www.bcnga.ca created using a user-defined selection/filter mask.

Table 4. Examples of interpretative diagrams commonly used in gas geochemistry (from Whiticar, 2021).

Diagram name[1]	Parameters	Basic utility	Reference
Bernard Diagram	$\delta^{13}C_{CH4}$ *vs* $C_1/(C_2+C_3)$	Gas classification of thermogenic and microbial gases; scale emphasizes microbial gas	Bernard et al., 1976
Gas wetness	$\delta^{13}C_{CH4}$ *vs* $\%C_{2+}$ $\%C_2+ = (1-C_1/\sum C_{1-5})\bullet 100$	Gas classification of natural gas types; scale emphasizes thermogenic components	Schoell, 1983
CD diagram (Whiticar plot)	$\delta^{13}C_{CH4}$ *vs* δ^2H_{CH4}	Classification of all types of primary and secondary natural gas types and processes	Whiticar, 1994; Milkov and Etiope, 2018
Faber diagram	$\delta^{13}C_{CH4}$ *vs* $R_o\%$	Estimation of source maturity from methane to propane $\delta^{13}C$ values	Faber, 1987
CC diagram	$\delta^{13}C_{CO2}$ *vs* $\delta^{13}C_{CH4}$	Distinguishing different methanogenic pathways, methanotrophy and identifying biodegradation of oils	Whiticar, 1999; Milkov, 2011
Chung natural gas plot	$\delta^{13}C_{1-5}$ *vs* n/carbon #	Comparison of gases, identifying mixtures and alterations using C_{1-5} alkanes	Chung et al., 1988
Berner-Faber diagram	$\delta^{13}C_{C3H8}$ *vs* $\delta^{13}C_{C2H6}$	Distinguishing gas families, non-thermogenic mixtures and alterations, and estimating maturities	Berner and Faber, 1988, 1996; Rooney et al., 1995
Lorant diagram	$\Delta\delta^{13}C_2$-$\delta^{13}C_3$ *vs* C_2/C_3 (mol/mol)	Compare primary versus secondary cracking of gas in open and closed systems	Lorant et al., 1998
Delta-delta diagram	$\Delta\delta^{13}C_2$-$\delta^{13}C_1$ *vs* $\Delta\delta^{13}C_3$-$\delta^{13}C_2$	Identify mixing of two gases with different molecular and isotope compositions	Jenden et al., 1993
AlphaC-alphaD diagram	α_C *vs* α_D ($\delta^{13}C_{CO2}$:$\delta^{13}C_{CH4}$ *vs* δ^2H_{H2O}:δ^2H_{CH4})	Combination of carbon and hydrogen isotopes of methane to distinguish methanogenic pathways	Whiticar, 2020
Isotope rollover diagram	$\delta^{13}C_{C2H6}$ *vs* $\%C_{2+}$	Differentiate normal from high maturity isotope reversals (^{12}C enrichment of $\delta^{13}C_{C2H6}$)	Zumberge et al., 2012; Tilley and Muehlenbachs, 2013
CO_2-delta diagram	$\delta^{13}C_{CO2}$ *vs* $\Delta\delta^{13}C_2$-$\delta^{13}C_1$	Differentiate microbial-thermogenic gas mixtures from petroleum degradation	Milkov, 2011

[1]The plot names are the unofficial, 'in-house' names used by the author (MJW) and his colleagues over the decades. Some of the diagrams have other variations, names and updates, so apologies for any incorrect designations or attributions, and for the omissions.

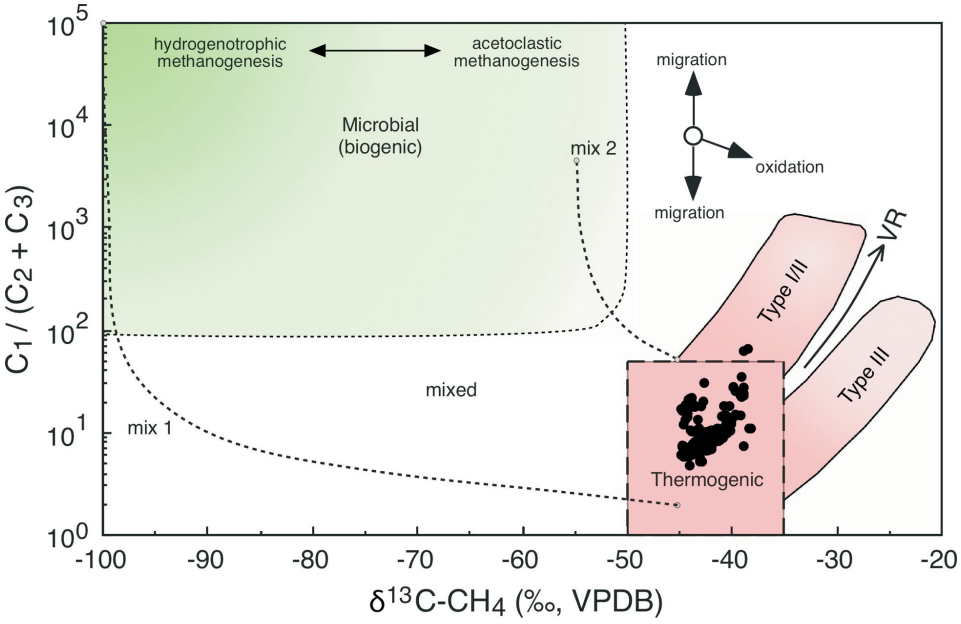

Figure 2. Example of Bernard Diagram (Bernard et al., 1976) created on the www.bcnga.ca website. The data plotted are from a data subset created using the chosen data filtering variables (mol % ethane, $\delta^{13}CH_4$, play category) shown in Figure 1. Abbreviations: VPDB, Vienna Pee Dee Belemnite (carbon isotope standard); VR, vitrinite reflectance (maturity indicator).

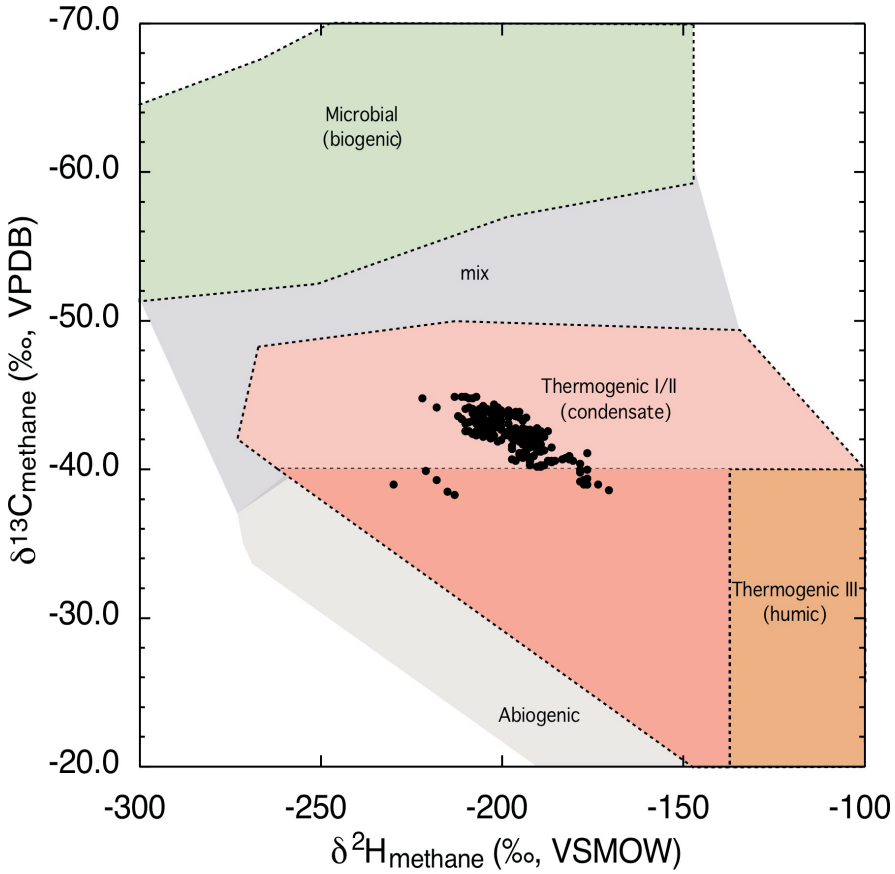

Figure 3. Example of truncated 'Whiticar plot' or 'CD diagram' (Whiticar, 2021) created on the www.bcnga.ca website. The data plotted are from a data subset created using the chosen data filtering variables (mol % ethane, $\delta^{13}CH_4$, play category) shown in Figure 1. Abbreviations: VPDB, Vienna Pee Dee Belemnite (carbon isotope standard); VSMOW, Vienna Standard Mean Ocean Water (hydrogen isotope standard).

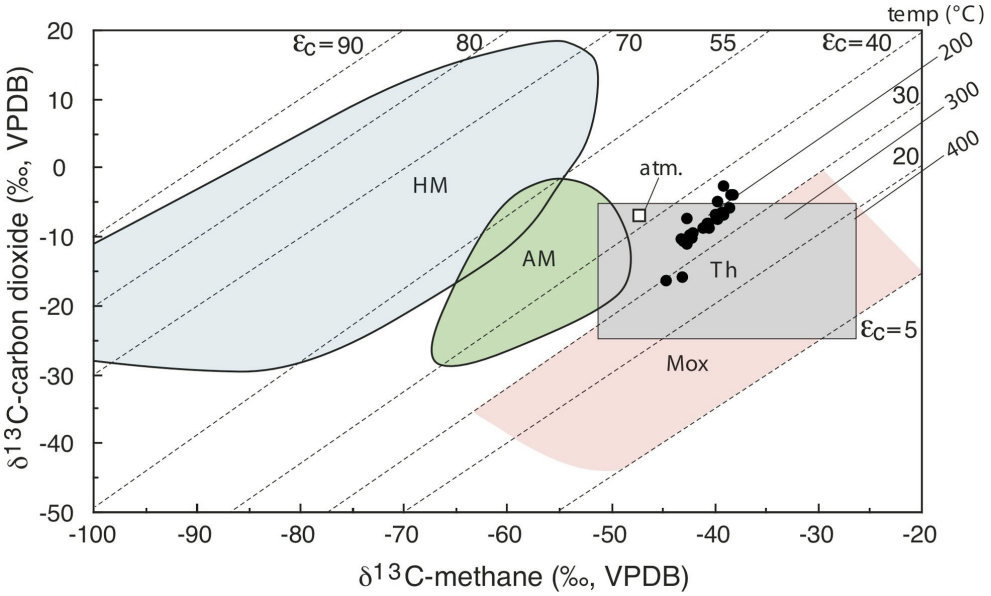

Figure 4. Example of 'CC diagram' (Whiticar, 1999; Milkov, 2011) created on the www.bcnga.ca website. The data plotted are from a data subset created using the chosen data filtering variables (mol % ethane, $\delta^{13}CH_4$, play category) shown in Figure 1. Abbreviations: ε_c, carbon isotope fractionation factor; AM, acetoclastic methanogenesis; atm., average tropospheric methane; HM, hydrogenotrophic methanogenesis; Mox, methane oxidation; Th, thermogenic methane; VPDB, Vienna Pee Dee Belemnite (carbon isotope standard).

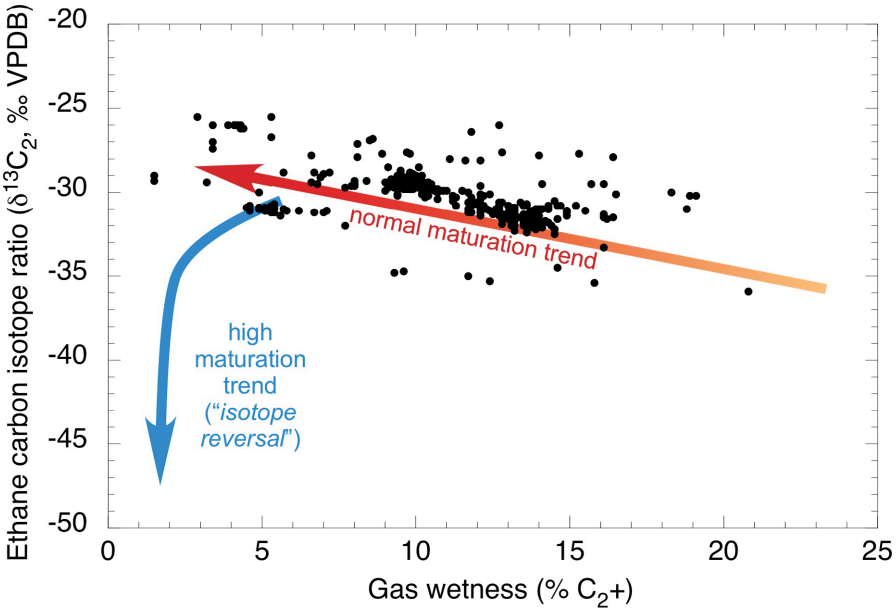

Figure 5. Example of isotope reversal ('rollover') diagram (Zumberge et al., 2012; Tilley and Muehlenbachs, 2013) created on the www.bcnga.ca website. The data plotted are from a data subset created using the chosen data filtering variables (mol % ethane, $\delta^{13}CH_4$, play category) shown in Figure 1. Abbreviation: VPDB, Vienna Pee Dee Belemnite (carbon isotope standard).

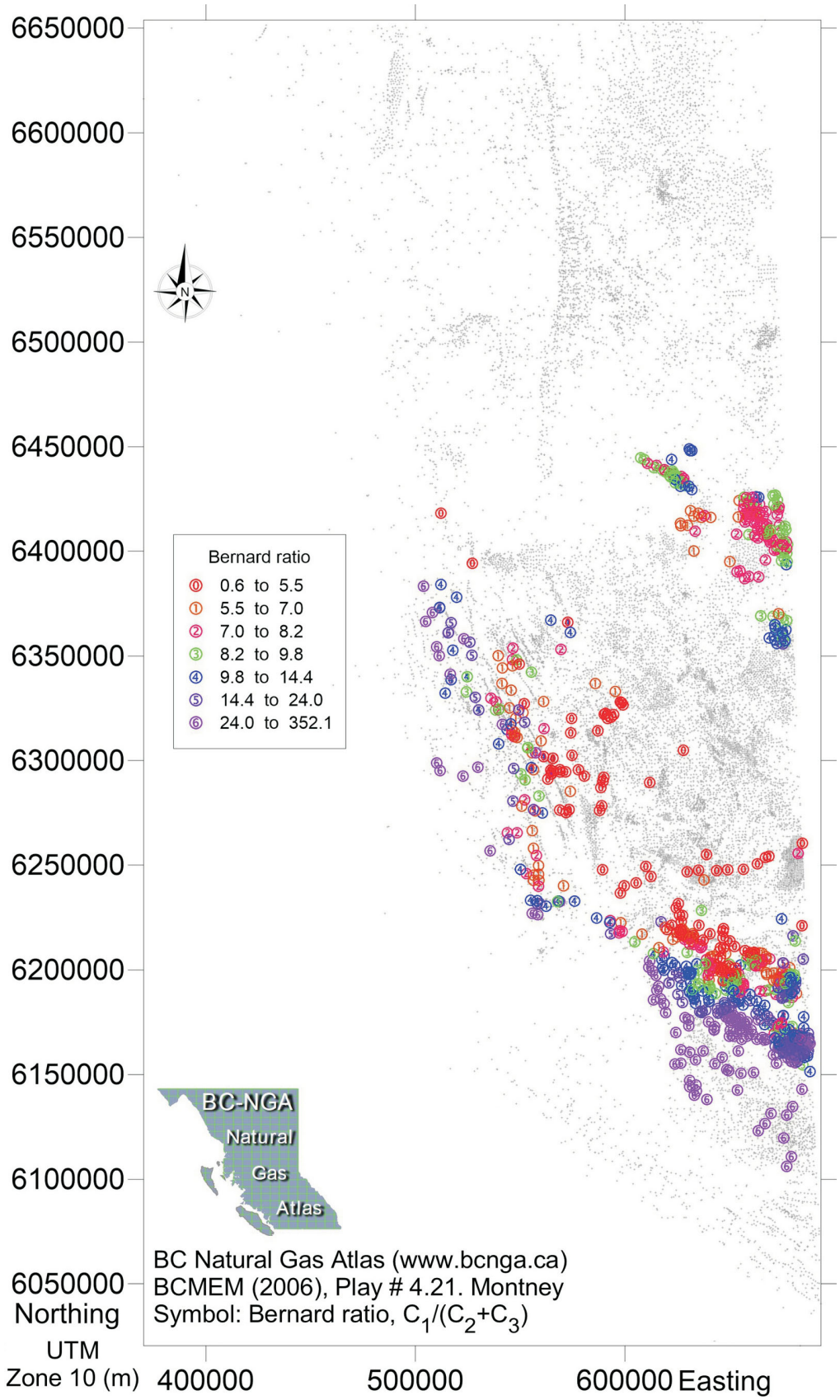

Figure 6. Example from the www.bcnga.ca map catalogue showing Bernard ratio distribution for the Montney Formation in northeastern British Columbia. Small black crosses (+) show the locations of data for the entire database. The map co-ordinates are in UTM Zone 10, NAD 83.

The interpretative plot of $\delta^{13}C_{CO2}$ versus $\delta^{13}C_{CH4}$ or 'CC diagram', illustrated in Figure 4 (Whiticar, 1994; Milkov, 2011), is particularly useful in identifying microbial methanogenic and methanotrophic gases and pathways, as well as helping understand the geothermometry and distinguishing thermogenic gas from abiogenic gas.

The final example diagram presented here is termed the 'isotope reversal' or 'isotope rollover' diagram (Figure 5). It is derived from Zumberge et al. (2012) and Tilley and Muehlenbachs (2013) and plots $\delta^{13}C_{C2H6}$ versus $\%C_{2+}$. This diagram can differentiate normal gas maturation trends or trajectories from the unusual high maturity isotope reversals (^{12}C enrichments of $\delta^{13}C_{C2H6}$).

Mapping of Gas Geochemical Parameters Using the BC-NGA Database

The BC-NGA website (www.bcnga.ca) offers an atlas of 349 geochemical distribution maps. The maps show specific geochemical parameters, such as ppm H_2S, dryness ratio, iC_4/nC_4 ratio and $\delta^{13}CH_4$, for northeastern BC. The maps are catalogued on the website according to the formation/play code (e.g., Dunvegan, Bluesky, Doig, Montney), which is based on the designation in BC Ministry of Energy, Mines and Low Carbon Innovation (2006).

The maps were generated by Evans (2019) using basic kriging with a spherical algorithm and a Gaussian variogram. Declustering was done manually based on the data analysis. Many well test intervals have two or three gas samples analyzed for molecular composition only. These samples are often inadequate to create a production profile and the geographic location is exactly the same. This creates estimation problems for the kriging algorithm and declustering is required. If all samples from a well test interval were flagged equally, only the first sample was used in creating the map. If the first sample was problematic, as identified in the flagging, the second or third sample was chosen. This declustering also applied to gas analysis from multiple legs on a single drilling pad, but instead of using the first sample (usually the motherbore of a horizontal well), the horizontal leg with the longest reach and most frequent testing was used for mapping. Figure 6 provides an example of a www.bcnga.ca map showing the distribution of the Bernard ratio for the Montney Formation in northeastern BC based on the BC-NGA database.

Summary

The British Columbia Natural Gas Atlas (BC-NGA) project and the associated upgraded website, www.bcnga.ca, now features a script to check for new natural gas geochemical data posted on the British Columbia Oil and Gas Commission site. This new nonconfidential data is downloaded and appended to the BC-NGA database, then automatically reformatted and passed through the quality assurance–quality control procedure before being made available to users on www.bcnga.ca. New sorting tools to select, filter and download user-defined data subsets have been created. In addition, to aid interpretation of the gas geochemical data, automated plotting of common interpretative diagrams has been added as a user feature. Maps of the distributions of common natural gas geochemical parameters for northeastern British Columbia are also presented on www.bcnga.ca.

It is anticipated that the BC-NGA database will be periodically updated, and thus will continue to provide a comprehensive and useful geochemical resource for those working on gas geochemical topics and issues in northeastern British Columbia.

Acknowledgments

The British Columbia Natural Gas Atlas (BC-NGA) team would like to thank C. Salas, R. Hughes and L. Wytrykush of Geoscience BC for their proactive support and assistance over the past five years. The support of the BC Oil and Gas Commission, in particular, J. Johnson, S. Venables and M. Hayes, is also recognized. The authors would like to thank S. Verenitch (School of Earth and Ocean Sciences, University of Victoria) and P. Eby (InnoTech Alberta) for conducting the stable isotope ratio analyses. The work of compiling and creating the initial BC-NGA database and manually conducting the quality assurance–quality control of the entries was carefully and tirelessly undertaken by C. Evans. His University of Victoria M.Sc. thesis details much of the gas geochemistry mapping included in the BC-NGA database.

The funding for BC-NGA is generously provided by grants from Geoscience BC and the BC Oil and Gas Research and Innovation Society (BC OGRIS) and is gratefully acknowledged. The authors also thank C. Evans for kindly reviewing and C.J. Dawson, with RnD Technical, for expertly editing the manuscript.

References

BC Ministry of Energy, Mines and Low Carbon Innovation (2006): Conventional natural gas play atlas, northeast British Columbia; BC Ministry of Energy and Mines and Low Carbon Innovation, Petroleum Geology Publication 2006-01, pt. 1, 46 p., URL <https://www2.gov.bc.ca/assets/gov/farming-natural-resources-and-industry/natural-gas-oil/petroleum-geoscience/oil-gas-reports/og_report_2006-1_nebc_atlas_part1.pdf> [November 2021].

Bernard, B.B., Brooks, J.M. and Sackett, W.M. (1976): Natural gas seepage in the Gulf of Mexico; Earth Planetary Science Letters, v. 31, no. 1, p. 48–54.

Berner, U. and Faber, E. (1988): Maturity related mixing model for methane, ethane and propane, based on carbon isotopes; Organic Geochemistry, v. 13, no. 1–3, p. 67–72.

Berner, U. and Faber, E. (1996): Empirical carbon isotope/maturity relationships for gases from algal kerogens and ter-

rigenous organic matter, based on dry, open-system pyrolysis; Organic Geochemistry, v. 24, no. 10, p. 947–955.

Chung, H.M., Gormly, J.R. and Squires, R.M. (1988): Origin of gaseous hydrocarbons in subsurface environments—theoretical considerations of carbon isotope distribution; Chemical Geology, v. 71, p. 97–104.

Clayton, C. (1991): Carbon isotope fractionation during natural gas generation from kerogen; Marine and Petroleum Geology, v. 8, no. 2, p. 232–240.

Evans, C. (2019): Molecular composition and isotope mapping of natural gas in the British Columbia Natural Gas Atlas; M.Sc. thesis, University of Victoria, 345 p.

Faber, E. (1987): Zur Isotopengeochemie gasfoermiger Kohlenwasserstoffe; Erdoel Erdgas Kohle, v. 103, p. 210–218.

Galimov, E.M. (1988): Sources and mechanisms of formation of gaseous hydrocarbons in sedimentary rocks; Chemical Geology, v. 71, no. 1, p. 77–95.

Goetz, M., Allen, A.J., Ladd, B., Gonzalez, P.S., Cahill, A.G., Kirste, D., Welch, L., Mayer, B., van Geloven, C. and Beckie, R.D. (2021): Peace Region scientific groundwater monitoring network installation study; Geoscience BC, Report 2021-16, 76 p., URL <http://www.geosciencebc.com/i/project_data/GBCReport2021-16/Geoscience%20BC%20Report%202021-16.pdf> [October 2021].

Jenden, P.D., Drazan, D.J. and Kaplan, I.R. (1993): Mixing of thermogenic natural gases in northern Appalachian Basin; American Association of Petroleum Geologists, Bulletin, v. 77, no. 6, p. 980–998.

Liu, Q., Wuk, X., Wang, X., Jin, Z., Zhu, D., Meng, Q. and Fu, Q. (2019): Carbon and hydrogen isotopes of methane, ethane, propane: a review of genetic identification of natural gas; Earth-Science Reviews, v. 190, p. 247–272.

Lorant, F., Prinzhofer, A., Behar, F. and Huc, A.Y. (1998): Carbon isotopic and molecular constraints on the formation and the expulsion of thermogenic hydrocarbon gases; Chemical Geology, v. 147, p. 249–264.

Milkov, A.V. (2011): Worldwide distribution and significance of secondary microbial methane formed during petroleum biodegradation in conventional reservoirs; Organic Geochemistry, v. 42, no. 2, p. 184–207.

Milkov, A.V. and Etiope, G. (2018): Revised genetic diagrams for natural gases based on a global dataset of >20,000 samples; Organic Geochemistry, v. 125, p. 109–120.

Prinzhofer, A. and Battani, A. (2003): Gas isotopes tracing: an important tool for hydrocarbons exploration; Oil & Gas Science and Technology, v. 58, no. 2, p. 299–311.

Rooney, M.A., Claypool, G.E. and Chung, H.M. (1995): Modeling thermogenic gas generation using carbon isotope ratios of natural gas hydrocarbons; Chemical Geology, v. 126, no. 3–4, p. 219–232.

Schoell, M. (1980): The hydrogen and carbon isotopic composition of methane from natural gases of various origins; Geochimica Cosmochimica Acta, v. 44, no. 5, p. 649–661.

Schoell, M. (1983): Genetic characterization of natural gases; American Association of Petroleum Geologists, Bulletin, v. 67, no. 12, p. 2225–2238.

Stahl, W. and Faber, E. (1983): Carbon isotopes as a petroleum exploration tool; World Petroleum Council, 11th World Petroleum Congress, August 28–September 2, 1983, London, England, paper WPC-20114, p. 147–159.

Tilley, B. and Muehlenbachs, K. (2013): Isotope reversals and universal stages and trends of gas maturation in sealed, self-contained petroleum systems; Chemical Geology, v. 339, p. 194–204.

Whiticar, M.J. (1994): Correlation of natural gases with their sources; Chapter 16, Part IV *in* The Petroleum System–From Source to Trap, L.B. Magoon and W.G. Dow (ed.), American Association of Petroleum Geologists, Memoir 60, p. 261–283.

Whiticar, M.J. (1999): Carbon and hydrogen isotope systematics of bacterial formation and oxidation of methane; Chemical Geology, v. 161, no. 1–3, p. 291–314.

Whiticar, M.J. (2020): The biogeochemical methane cycle; *in* Hydrocarbons, Oils and Lipids: Diversity, Origin, Chemistry and Fate, H. Wilkes (ed.), Handbook of Hydrocarbon and Lipid Microbiology, Springer, Cham, Switzerland, p. 669–746, URL <https://doi.org/10.1007/978-3-319-90569-3_5>.

Whiticar, M.J. (2021): Carbon isotopes in petroleum science; *in* Encyclopedia of Petroleum Geoscience, R. Sorkhabi (ed.), Encyclopedia of Earth Sciences Series, Springer, Cham, Switzerland, 19 p., URL <https://doi.org/10.1007/978-3-319-02330-4_310-1>.

Whiticar, M.J. and Evans, C. (2020): BC Natural Gas Atlas: creation of the geochemical database for northeastern British Columbia (parts of NTS 093, 094); *in* Geoscience BC Summary of Activities 2019: Energy and Water, Geoscience BC, Report 2020-02, p. 77–86, URL <http://www.geosciencebc.com/i/pdf/SummaryofActivities2019/EW/Project%202015-013_EW_SOA2019.pdf> [November 2021].

Zumberge, J., Ferworn, K. and Brown, S. (2012): Isotopic reversal ('rollover') in shale gases produced from the Mississippian Barnett and Fayetteville formations; Marine and Petroleum Geology, v. 31, no. 1, p. 43–52.

Geothermal Resource Potential of the Garibaldi Volcanic Belt, Southwestern British Columbia (Part of NTS 092J): Phase 2

S.E. Grasby, Geological Survey of Canada–Calgary, Calgary, Alberta, steve.grasby@canada.ca

A. Calahorrano-Di Patre, Simon Fraser University, Burnaby, British Columbia

Z. Chen, Geological Survey of Canada–Calgary, Calgary, Alberta

J. Dettmer, University of Calgary, Calgary, Alberta

H. Gilbert, University of Calgary, Calgary, Alberta

C. Hanneson, University of Alberta, Edmonton, Alberta

M. Harris, The University of British Columbia, Vancouver, British Columbia

S. Leiter, The University of British Columbia, Vancouver, British Columbia

J. Liu, Geological Survey of Canada–Calgary, Calgary, Alberta

M. Muhammad, Simon Fraser University, Burnaby, British Columbia

K. Russell, The University of British Columbia, Vancouver, British Columbia

M.J. Unsworth, University of Alberta, Edmonton, Alberta

G. Williams-Jones, Simon Fraser University, Burnaby, British Columbia

W. Yuan, Geological Survey of Canada–Calgary, Calgary, Alberta

Grasby, S.E., Calahorrano-Di Patre, A., Chen, Z., Dettmer, J., Gilbert, H., Hanneson, C., Harris, M., Leiter, S., Liu, J., Muhammad, M., Russell, K., Unsworth, M.J., Williams-Jones, G. and Yuan, W. (2022): Geothermal resource potential of the Garibaldi volcanic belt, southwestern British Columbia (part of NTS 092J): Phase 2; *in* Geoscience BC Summary of Activities 2021: Energy and Water, Geoscience BC, Report 2022-02, p. 75–80.

Introduction

Canada has committed to a target of net-zero emissions by 2050. This requires a significant increase in renewable energy supply for heating and electrical generation. Most renewables, though, have intermittent supply (e.g., wind, solar) that requires storage solutions to be integrated into existing energy grids. Compared to other renewables, geothermal energy has numerous advantages: its low environmental footprint, its ability to provide a stable baseboard–power supply and the fact that it is dispatchable (capable of quickly ramping up and down to adjust to demand). Driven at the time by concerns over energy security, the Geological Survey of Canada ran a Geothermal Energy Program from 1975 to 1985 that provided the first insight into geothermal energy potential in Canada (Jessop, 2008; Grasby et al., 2011). This program included highlighting the high-temperature resource potential of volcanic belts in western Canada (Yukon and British Columbia [BC]).

This publication is also available, free of charge, as colour digital files in Adobe Acrobat® PDF format from the Geoscience BC website: http://geosciencebc.com/updates/summary-of-activities/.

With renewed interest in geothermal energy, a new research project was initiated in the Garibaldi volcanic belt of southwestern BC (Figure 1), with a specific focus of reducing the exploration risk for geothermal energy associated with volcanic systems. The first phase of this project was a multidisciplinary field program, conducted in the Mount Meager area in the summers of 2019 and 2020 (Grasby et al., 2021), that focused on developing novel tools to better predict the occurrence of zones of high permeability in the subsurface. In 2021, the second phase of the project moved the focus to the Mount Cayley area, to test exploration tools developed in Phase 1 in an area with limited previous exploration. This paper reports on the nature of the field program and data collected in 2021.

Garibaldi Volcanic Belt

The Garibaldi volcanic belt represents a chain of young (less than 11 000 years old) volcanoes in southwestern BC, in a region also known to have abundant thermal springs. In the 1990s, Natural Resources Canada (NRCan), along with BC Hydro, conducted initial exploration drilling at the Mount Meager volcano that defined high-temperature geothermal resources, exceeding 250°C (Jessop, 2008; Witter,

2019). While the drilling defined a world-class thermal resource, the permeability was insufficient to allow economic development at that time. A lack of geoscience information regarding the regional controls on permeability posed a significant drilling risk for subsequent industry exploration in the region (Witter, 2019).

A project to reduce exploration risk was initiated in 2019 by the Geological Survey of Canada (GSC) of Natural Resources Canada (NRCan), in partnership with The University of British Columbia (UBC), Simon Fraser University (SFU), Douglas College (DC), University of Calgary (U of C) and University of Alberta (U of A), to develop a multidisciplinary approach to reduce exploration risk through an integrated geological and geophysical field campaign. Project funding is provided through NRCan's Renewable and Electrical Energy Division, together with Geoscience BC. The project incorporates a range of geoscience tools, including remote sensing, bedrock mapping, fracture measurements, geochemistry, and magnetotelluric (MT), gravity and passive-seismic surveys. The ultimate project goal is to develop new predictive tools for finding permeable aquifers at depth. Results will also aid development of new geothermal-resource models, thus creating greater certainty in national geothermal-resource assessments and supporting development of effective regulatory environments.

Mount Cayley Field Program

Field teams from UBC, SFU, U of A, U of C and GSC participated in the 2021 field program but worked independently to adhere to COVID-19 protocols. Field planning began with engagement with the Squamish Nation and co-development of a modified field plan that limited impacts in areas of special concern. This included movement of planned survey points to new locations that still meet science goals but did not disturb the areas of special concern and, in other areas, focusing survey work on previously disturbed lands, which had the additional benefit of easier field access. The local knowledge provided through the engagement process was of significant benefit to field operations. Fieldwork was focused on logging roads along the flanks of Mount Cayley. As well, the project team engaged an environmental monitor from the Squamish Nation to ensure that helicopter work to access higher levels on Mount Cayley did not cause any wildlife disturbance. The field program focused on establishing an array of broadband seismometers to record the nature of seismicity as potential information on subsurface magma chambers (U of C); an array of MT stations

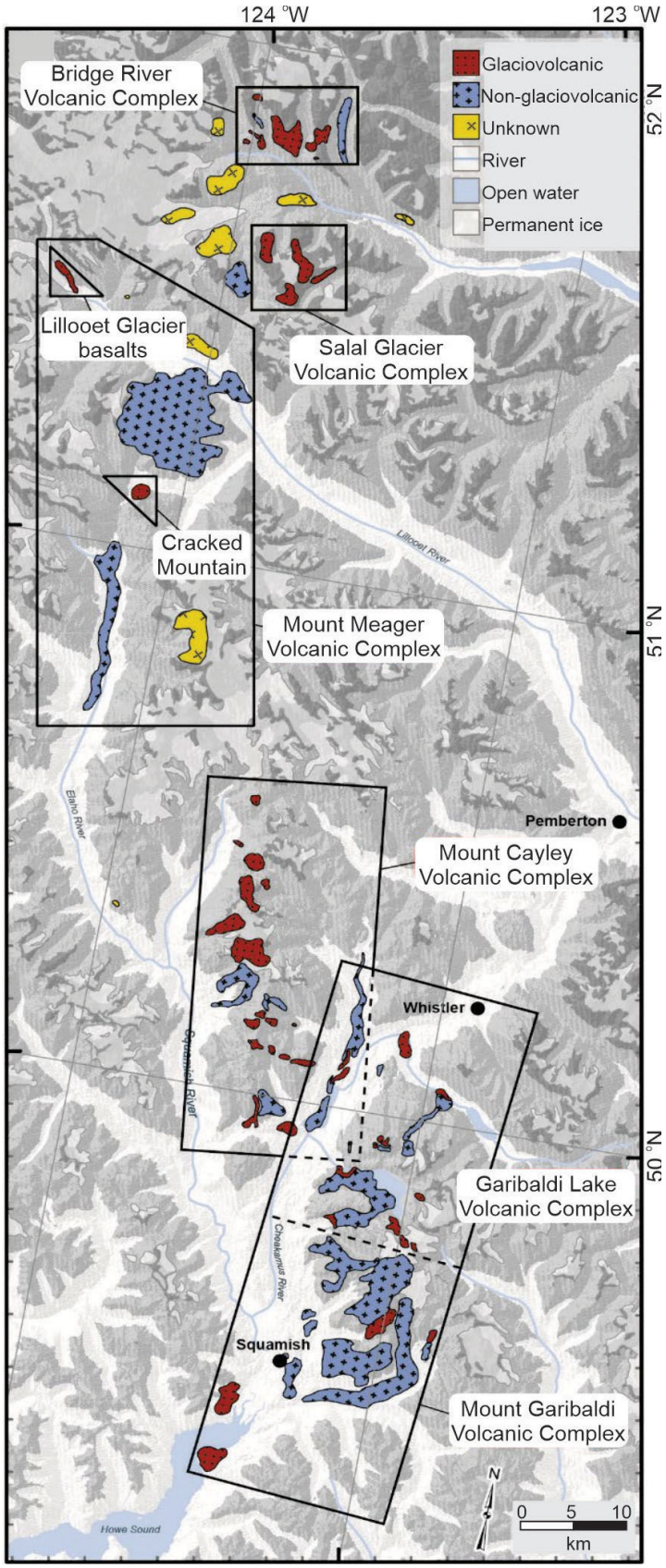

Figure 1. Volcanic complexes of the Garibaldi volcanic belt, showing the location of Mount Meager, the focus of Phase 1, and the Mount Cayley area, which is the focus of Phase 2.

focused on imaging the deeper volcanic plumbing (U of A); a gravity survey that will provide insight into potential magma chambers (SFU); bedrock mapping to provide information on the rock types of the geothermal reservoir (UBC); and fracture, rock property and thermal anomaly studies that will provide information on permeable networks, heat conduction and heat production, respectively (GSC).

Broadband Seismometers

Due to delays in equipment development and refurbishment, the seismometer stations have not yet been installed, but attempts will be made pending onset of winter snow.

Magnetotelluric (MT)

Magnetotelluric (MT) and audio-frequency magnetotelluric (AMT) data collection at the Mount Cayley Volcanic Complex was conducted in 2021 by the U of A MT group to understand the deeper structure of the volcanic system, which requires longer recording time and consequently reduced the total number of measurement locations. The deeper focus MT survey was designed to image pathways that carry fluids to a potential geothermal reservoir. These deep MT measurements will also define the size and content of any magma bodies beneath the volcano. With the deeper exploration targets, lower frequencies were used in a broadband-magnetotelluric (BBMT) survey. Along with stations around Mount Cayley, a north-south profile connecting with previous work on Mount Meager was also collected.

A key aspect of MT data analysis will be to elucidate zones of high and low resistivity found beneath Mount Cayley. This work, along with analysis of the new 3-D resistivity models from Mount Cayley and supported by other geological and geophysical datasets, can help define potential geothermal reservoirs.

Gravity

Gravity measurements, in conjunction with other geophysical methods, are particularly useful in mapping the magmatic and hydrothermal subsurface features of volcanoes. During the summer of 2021, gravity measurements were taken at 75 stations around the Mount Cayley Volcanic Complex (Figure 2) for the purpose of mapping its internal structure. Gravity was measured with a LaCoste & Romberg spring-gravity meter in order to develop a Bouguer anomaly map of the area. The network comprises both a dense distribution of sites near the volcanic edifice and more broadly spaced stations with increasing distance from the mountain. This distribution seeks to investigate the deep magmatic structures (depth >10 km). The measured Bouguer anomalies will be analyzed via an informed inverse-modelling approach, which combines information from geological and structural mapping, AMT, MT and seismic measurements. This will restrict the number of possible solutions for the inversion and ensure that the results best reflect plausible subsurface geological features.

Bedrock Mapping

Detailed bedrock mapping was conducted to enhance understanding of the spatial distribution of volcanic rocks that form the Mount Cayley Volcanic Complex. Resultant detailed maps will support the development of hydrogeological models for bulk-rock permeability to better characterize potential fluid flow at depth. High-density fracture zones appear to be associated with major fault and deformation belts. Identification and mapping of these zones using all available means (Landsat imagery and regional geophysical data, field observations, earthquake records) at a regional level will provide the basis for construction of geothermal-resource models. New sample collection will lead to refined radiometric dating that will aid definition of the youngest (and hottest) flow units with the greatest heat-generation potential.

Fracture Studies

Geological examination and fracture measurement followed traditional field methods. The field party observed, identified and recorded geological and geomorphological features, measured fracture attitudes (strike, dip direction, dip angle, density and spacing) of fracture/fault planes and collected rock samples for further laboratory analysis (Figure 3). The identified geological and geomorphological features and evidence of geological processes were analyzed in relation to tectonic and volcanic activities of the region and to assess their association with reservoir development at and around each station. Photos were taken at the outcrops where well-exposed fracture traces are present to fur-

Figure 2. Gravity meter on the top of Mount Brandywine. Photo by A. Calahorrano-Di Patre.

Figure 3. Field party collecting fracture measurements from outcrops along the south flank of Mount Cayley.

ther study the statistical characteristics of fracture spacing and density.

Thermal Anomalies

Ground temperature was measured using miniature temperature data loggers (HOBO Water Temp Pro v2). The temperature data logger is waterproof and has a resolution of 0.2°C and temperature range of –40°C to 70°C in air and up to 50°C in water. At each site, a single HOBO temperature logger was buried in soil with the sensor at a depth of approximately at 10 cm below the ground surface to avoid direct exposure to solar radiance. The improved deployment in 2021 had two HOBO temperature loggers at each site, one buried at a depth of 30–50 cm, depending on ground conditions, and the other on surface to account for solar radiance. The newly deployed loggers will be retrieved during the 2022 fieldwork season. For each site, a soil sample was taken for laboratory analysis to determine physical and thermal properties.

A thermal infrared camera was also used to take temperature images of various objects, ground-surface covers and water bodies. These images will be used to provide accurate ground temperature measurements to allow calibration of land-surface temperature maps derived from Landsat images, as well as for identifying ground-surface–temperature anomalies (Figure 4), particularly for groundwater seeps.

Conclusions

The summer 2021 field program faced some challenges due to COVID-19 restrictions but was still a success, with abundant new geophysical and geological data collected. These data are still being processed and will be incorporated into ongoing research projects. Final results will be integrated into a new 3-D model of the geothermal and volcanic plumbing of the Mount Cayley complex. Results will provide new methods to help predict the occurrence of permeability at depth and greatly reduce the risk associated with drilling for geothermal reservoirs in the volcanic systems of British Columbia.

Acknowledgments

Funding for this project was provided by Geoscience BC and Natural Resources Canada. The authors thank

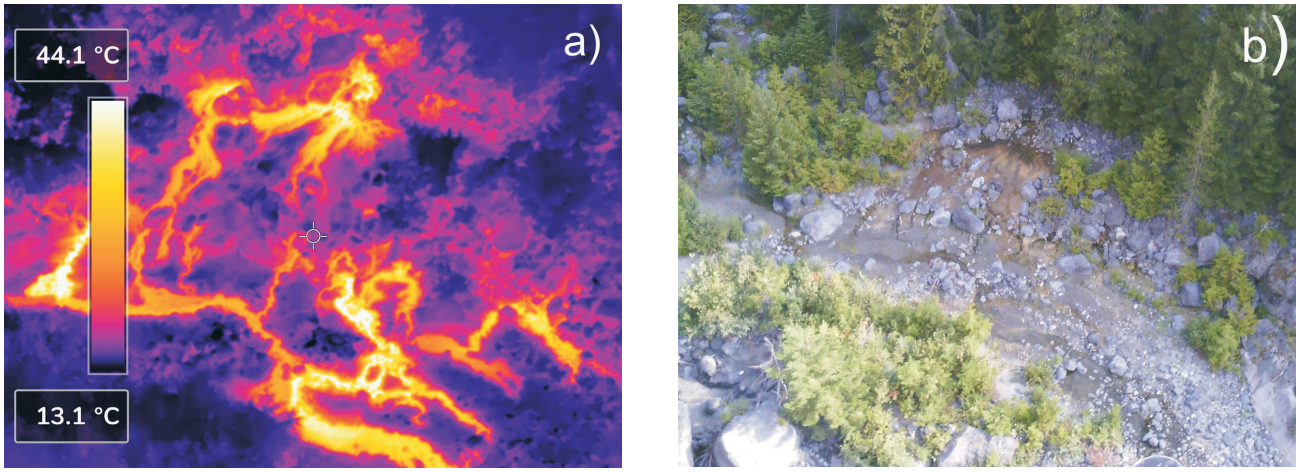

Figure 4. Comparison of image from thermal infrared camera **(a)** and true colour image **(b)**, showing the ability to identify ground-temperature anomalies. Photo taken by W. Yuan from a helicopter about 500 m above ground level.

O. Ardakani for his helpful review of an earlier draft of the paper.

Natural Resources Canada, Lands and Minerals Sector contribution 20210397

References

Grasby, S.E., Allen, D.M., Bell, S., Chen, Z., Ferguson, G., Jessop, A., Kelman, M., Ko, M., Majorowicz, J., Moore, M., Raymond, J. and Therrien, R. (2011): Geothermal energy resource potential of Canada; Geological Survey of Canada, Open File 6914, 322 p., URL <https://doi.org/10.4095/288745> [November 2021].

Grasby, S.E., Ansari, S.M., Barendregt, R.W., Borch, A., Calahorrano-DiPatre, A., Chen, Z., Craven, J.A., Dettmer, J., Gilbert, H., Hanneson, C., Harris, M., Hormozzade, F., Leiter, S., Liu, J., Muhammad, M., Quane, S.L., Russell, J.K., Salvage, R.O., Savard, G., Tschirhart, V. et al. (2021) Garibaldi Geothermal Energy Project – Phase 1: Final Report; Geoscience BC Report 2021-08, 276 p., URL <http://www.geosciencebc.com/i/project_data/GBCReport2021-08/GBCR%202021-08%20Garibaldi%20Geothermal%20Energy%20Project%20-%20Phase%201.pdf> [November 2021].

Jessop, A. (2008): Review of National Geothermal Energy Program, Phase 2 – geothermal potential of the Cordillera; Geological Survey of Canada, Open File 5906, 86 p., URL <https://doi.org/10.4095/225917> [November 2021].

Witter, J. (2019): South Meager geothermal project – new perspectives from recently unearthed data; Geoscience BC, Report 2019-07, 5 p., URL <http://www.geosciencebc.com/i/pdf/Report-2019-07-Innovate-Geothermal.pdf> [November 2021].

Magnetotelluric Investigations of Geothermal Systems Centred in Southern British Columbia (Parts of NTS 082, 083, 092, 093)

C. Hanneson[1], **Department of Physics, University of Alberta, Edmonton, Alberta, cedar@ualberta.ca**

M.J. Unsworth, Department of Physics and Department of Earth and Atmospheric Sciences, University of Alberta, Edmonton, Alberta

Hanneson, C. and Unsworth, M.J. (2022): Magnetotelluric investigations of geothermal systems centred in southern British Columbia (parts of NTS 082, 083, 092, 093); *in* Geoscience BC Summary of Activities 2021: Energy and Water, Geoscience BC, Report 2022-02, p. 81–94.

Introduction

British Columbia (BC) has a range of significant geothermal resources in settings that include volcanic systems, fault-hosted systems and hot dry rock. Volcanic systems are found in the Garibaldi volcanic belt (GVB), including at Mount Meager, and fault-hosted systems are found near the southern Rocky Mountain Trench (SRMT). Both fault-hosted geothermal systems and hot dry rock resources are found in the Columbia Mountains.

Geophysical exploration using electromagnetic (EM) methods—including magnetotelluric (MT) surveys—is widely used in geothermal studies. These methods have been used to investigate two areas in southern BC, at different spatial scales:

1) Southeastern BC: a regional study at a large spatial resolution with horizontal model discretization of 5 km. This study had the aim of correlating regional-scale crustal structures with small-scale geothermal systems.
2) Mount Meager: a study surrounding the Mount Meager massif at a smaller spatial resolution with horizontal model discretization of 250 m. This study had the aim of imaging deep hydrothermal systems and magma bodies associated with a Holocene volcanic centre.

The study of the Mount Meager volcanic system is part of a multidisciplinary research program (the Garibaldi volcanic belt geothermal energy project) that includes magnetotelluric, passive seismic and gravity surveys, bedrock mapping, fracture analysis, and thermal-spring geochemistry (Grasby et al., 2020).

Tectonic and Geological Settings

The studied areas are located in the Canadian Cordillera and adjacent Western Canada Sedimentary Basin (WCSB; Figure 1). The Cordillera is an orogenic belt that covers much of BC and Yukon, as well as the western edges of Alberta and the Northwest Territories, and it is commonly divided into five morphogeological belts based on bedrock type and geomorphology. From west to east, they are: 1) the Insular Belt, 2) the Coast Belt, 3) the Intermontane Belt, 4) the Omineca Belt, and 5) the Foreland Belt. The SRMT separates the Omineca and Foreland belts.

The Juan de Fuca Plate, situated offshore southwestern BC and northwestern Washington, subducts beneath the North American Plate at the Cascadia subduction zone (Figure 1). The tectonic convergence rate between these two plates is ~40 mm/year (Kreemer et al., 2014). Dehydration of the subducting slab releases volatiles into the overlying mantle of the North American Plate, lowering its melting point and creating a region of partial melt, which leads to volcanism at the surface (Stern, 2002). The chain of volcanoes resulting from this subduction is called the Cascade volcanic arc.

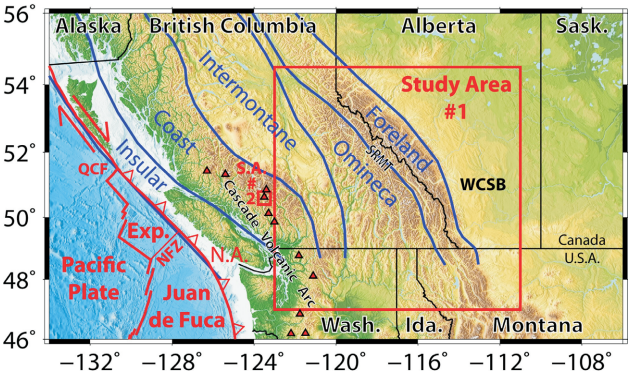

Figure 1. Southwestern Canada and northwestern United States showing the two study areas (red boxes). Study area 1 is centred on southeastern British Columbia but extends east into the province of Alberta and south into the states of Washington, Idaho and Montana. Study area 2 is centred on Mount Meager in the Cascade volcanic arc. Provincial, state and federal boundaries (black lines), morphogeological boundaries (blue lines), plate boundaries (red lines) and major volcanic centres (red triangles) are also shown. Abbreviations: Exp., Explorer Plate; Ida., Idaho; N.A., North American Plate; NFZ, Nootka fault zone; QCF, Queen Charlotte fault; S.A., study area; Sask., Saskatchewan; SRMT, southern Rocky Mountain Trench; Wash., Washington; WCSB, Western Canada Sedimentary Basin.

[1]*The lead author is a 2021 Geoscience BC Scholarship recipient.*

This publication is also available, free of charge, as colour digital files in Adobe Acrobat® PDF format from the Geoscience BC website: http://geosciencebc.com/updates/summary-of-activities/.

The northernmost segment of the Cascade volcanic arc (north of latitude 48°N) trends roughly northwest, whereas the rest of the arc trends generally north. The former, extending from Glacier Peak to Silverthrone Caldera, is the GVB (Figure 2); the latter (south of the area shown in Figure 2), from Mount Rainier in central Washington to Mount Lassen in northern California, is called the High Cascades (Mullen et al., 2017). North of the Nootka fault zone (Figure 1), the plate boundary transitions from convergent to transform, with strike-slip motion occurring north of the Queen Charlotte fault, and the Cascade volcanic arc dies out. In contrast to the Juan de Fuca Plate, the Explorer Plate is subducting at a rate of only 5–20 mm/year (Hutchinson et al., 2020).

Magnetotelluric Theory

The MT method uses natural EM signals to image the electrical resistivity of the subsurface and is widely used in geothermal exploration (Muñoz, 2014). The low-frequency radio wave sources are generated by global lightning activity and interactions between solar wind and the Earth's ionosphere. This EM method measures time series of electric and magnetic fields at the surface of the Earth, then converts them into frequency-domain transfer functions that describe the impedance of the Earth. The impedance ($\boldsymbol{Z}$) as a function of angular frequency, ω, is defined as a 2 by 2 tensor with $Z_{ij}(\omega) = E_i(\omega)/H_j(\omega)$ for $i,j = \{x,y\}$, where E is the electric field strength and H is the magnetic field strength. The vertical magnetic transfer function, referred to as the tipper ($\boldsymbol{T}$), is defined as a vector with $T_{zk}(\omega) = H_z(\omega)/H_k(\omega)$ for $k = \{x,y\}$. These transfer functions are used to calculate the electrical resistivity at depth. The theoretical foundations of the MT method were developed by Cagniard (1953) and a detailed description is given by Chave and Jones (2012).

The MT method has two main advantages that make it suitable for geothermal exploration:

1) It can effectively image aqueous and magmatic fluids, both of which are relevant to geothermal exploration. The electrical resistivity of the crust varies over several orders of magnitude: dry crystalline rock has a resistivity in excess of 1000 Ω•m, whereas the presence of aqueous fluids or partial melt can lower this to values in the range 1–10 Ω•m. Thus, MT data can help distinguish fluid-rich zones.

2) It can resolve crustal features over a broad range of depths, allowing for investigation of both fine-scale crustal structure and deeper resistivity anomalies. The frequency of the passive radio-wave source controls the depth of exploration according to the skin depth (δ), which is defined in metres as $\delta \approx 500(\rho T)^{1/2}$, where ρ is the bulk resistivity and T is the period of the signal. Therefore, longer periods give information about deeper structures and signals are more attenuated in lower resistivity materials. This broad depth range is a distinct advantage over other EM methods that are more limited in scale.

Resistivity models derived from MT data are an excellent way to detect fluids in bedrock during geothermal exploration; however, there are other causes of low resistivity in the near surface and all possible explanations must be considered in a program of geothermal exploration. These include presence of hydrothermal alteration minerals (Ussher et al., 2000; Hersir et al., 2015), graphite films (Frost et al., 1989) and sulphide minerals (Varentsov et al., 2013). Additional geophysical and geological data are helpful in distinguishing between different low-resistivity materials.

The techniques available for the analysis of MT data have drastically improved over the past decade due to increased computing power. In the past, one-dimensional and two-dimensional (1-D and 2-D) inversions were used to derive models of subsurface resistivity from MT data, but this greatly limited the application of the method in complex geological environments. Magnetotelluric data can now be inverted to produce three-dimensional (3-D) resistivity models using new inversion codes that are run on multiprocessor clusters (Kelbert et al., 2014; Lindsey and Newman, 2015). Topography can be modelled in 3-D and recent advances have allowed 3-D anisotropy to be modelled as well (Kong et al., 2021).

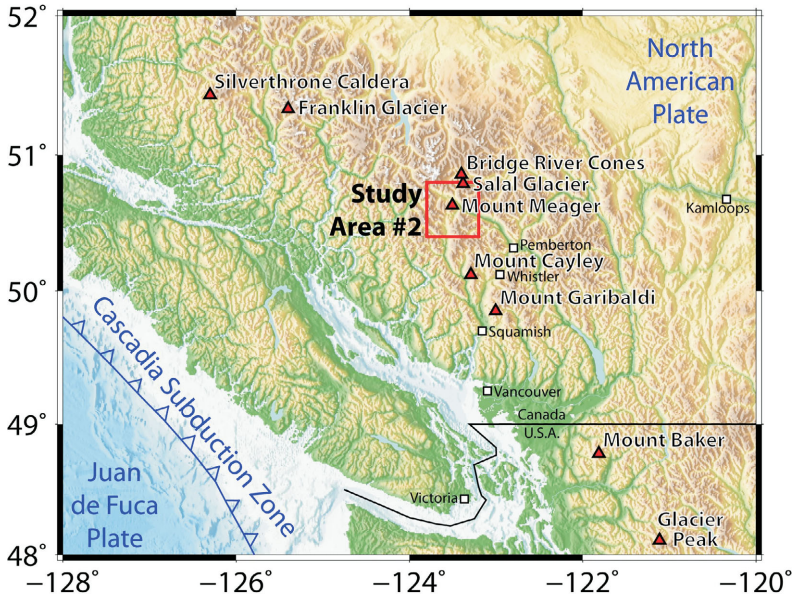

Figure 2. Southwestern British Columbia and northwestern Washington showing study area 2. Major volcanic centres of the Garibaldi volcanic belt are shown as red triangles, cities and towns are shown as squares.

Study Area 1: Southeastern BC

Geothermal Background

Study area 1 is centred on the SRMT, a major fault-controlled valley in southeastern BC. The region surrounding the SRMT is characterized by relatively high heat flow (~75 mW/m^2), and surface geothermal features such as the Radium and Fairmont hot springs occur along the valley floor, making it a promising target for exploration for geothermal resources. Faults that occur within and adjacent to the SRMT include: the SRMT fault, Purcell thrust fault, Redwall fault and Lussier fault (Figure 3). The SRMT fault underlies the SRMT for much of its length, though there are limited outcrop exposures of the fault itself. The fault dips steeply west and estimates of normal dip-slip displacement range from 2 to 10 km (McDonough and Simony, 1988; Gal and Ghent, 1990; van der Velden and Cook, 1996). The across-fault continuity of several transverse features, both structural and stratigraphic, indicate that it does not exhibit significant strike-slip offset (McMechan and Thompson, 1989), though Finley (2020) suggested the possibility of post-Eocene dextral offset on the order of tens of kilometres. The Purcell thrust fault lies within the SRMT from latitude 51.5°N (north of Golden) to latitude 50.5°N (near Invermere). This fault is regarded as an out-of-sequence thrust fault that developed during the last stages of Mesozoic compression. Notably, no thermal springs occur along the SRMT where the Purcell thrust occurs, suggesting this structure may not be conducive to fluid circulation or that there is limited fluid supply at depth.

The Redwall and Lussier faults are parallel to and east of the SRMT, between the towns of Radium and Cranbrook. The nature of these faults is not well understood, and they have variably been interpreted as dextral, sinistral or thrust faults (North and Henderson, 1954; Charlesworth, 1959; Foo, 1979). Many thermal springs near the southern portion of the SRMT in fact coincide with these faults rather than the SRMT fault itself, hence their inclusion in this study.

Within study area 1, MT data collected at more than 300 locations during the current and previous studies cover mainly the Omineca, Foreland and Intermontane belts of the Canadian Cordillera (Figure 3). In this region, heat flow is anomalously high, 70–120 mW/m^2, compared with the national average of 64 ±16 mW/m^2 (Majorowicz and Grasby, 2010). For comparison, an average of 85–90 mW/m^2 is observed in the Basin and Range province to the south, which hosts many of the United States' high-temperature (>150°C) geothermal systems (Wisian and Blackwell, 2004). The presence of more than 40 thermal springs within study area 1 is suggestive of the region's geothermal potential.

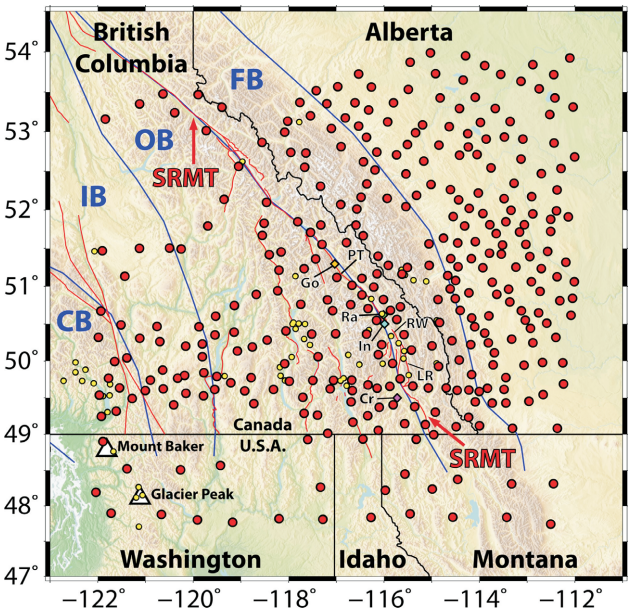

Figure 3. Magnetotelluric stations (red dots) used in the geophysical inversion to produce the electrical resistivity model shown in Figures 6 and 7. The approximate extent of the southern Rocky Mountain Trench is indicated by the red arrows. Provincial, state and federal boundaries (black lines), morphogeological boundaries (blue lines), major faults (red lines), Cascade arc volcanoes (white triangles), thermal springs (yellow dots) and population centres mentioned in the text (coloured diamonds) are also shown. Abbreviations: CB, Coast Belt; Cr, Cranbrook; FB, Foreland Belt; Go, Golden; IB, Intermontane Belt; In, Invermere; LR, Lussier River fault; OB, Omineca Belt; PT, Purcell thrust fault; Ra, Radium; RW, Redwall fault; SRMT, southern Rocky Mountain Trench.

It has previously been suggested that the locations of these thermal springs are controlled by faults (Grasby and Hutcheon, 2001) that allow deep circulation and consequent heating of meteoric water. Thermal springs in this study area include the Wolfenden, Radium, Fairmont, Red Rock, Lussier, Ram Creek and Wildhorse hot springs near the SRMT (Grasby and Hutcheon, 2001; Allen et al., 2006). Aqueous geothermometry has indicated that the spring water reaches temperatures of ~40–100°C, implying circulation depths of ~2–5 km (Grasby and Hutcheon, 2001). Although these temperatures are on the lower limit of what can be used to efficiently produce electricity, there is interest in using these systems for direct-use geothermal heating (Tuya Terra Geo Corp. and Geothermal Management Company, Inc., 2016). It is also important to note that convection and advection can have a cooling effect and may lower geothermal resource potential; therefore, thermal springs do not always indicate high geothermal potential (Grasby and Ferguson, 2010).

Data and Methods

Study 1 used data from 336 MT sites in an area spanning from latitude 47.7 to 54°N and longitude 112 to 122°W (Figure 3). These data included 110 LITHOPROBE sites, 22 EarthScope USArray sites and 19 sites from other previ-

ous studies. The University of Alberta MT research group collected an additional 185 MT soundings between 2002 and 2018. The large extent of the grid (i.e., extending south into the United States and east almost to the Saskatchewan border) enhances the model precision in southeastern BC, our area of interest, by extending the data coverage beyond the southern Omineca Belt on all four sides. In previous decades, inversion of MT data was limited to 1-D and 2-D, producing resistivity models that were limited in their ability to adequately represent Earth structure. The development of new inversion algorithms that run on multiprocessor clusters has allowed 3-D inversion to become practical in recent years. The MT transfer functions (impedance and tipper) were jointly inverted using the ModEM algorithm (Kelbert et al., 2014). The inversion used data at 18 periods, logarithmically spaced between 1 and 18 000 s. Tipper data were omitted at the two longest periods; when they were included, they resulted in the highest misfit of any single-component single-period misfit. Furthermore, Meqbel et al. (2014) omitted tipper data at periods longer than 6500 s to avoid external source bias, which aligns with our methods.

The 336 sites were chosen from a total of more than 700 based on the high quality of their data and to ensure that station spacing was as uniform as possible. The median distance between a station and its nearest neighbour was 22 km. The data were measured in geomagnetic co-ordinates: magnetic north and east for x and y, respectively. For the inversion, the data were rotated to a geographic co-ordinate system: geographic north and east for x and y, respectively. The following error floors were applied to the impedance ($\boldsymbol{Z}$) and tipper ($\boldsymbol{T}$) data: 5% of $(|Z_{xy}||Z_{yx}|)^{1/2}$ to Z_{xy} and Z_{yx}, 10% of $(|Z_{xy}||Z_{yx}|)^{1/2}$ to Z_{xx} and Z_{yy}, and 0.03 to T_{zx} and T_{zy}, where Z is a complex-valued 2 by 2 tensor and T is a complex-valued 2 by 1 vector. These are the same error floors used by Wang (2019).

Study area 1 was approximately 700 km by 700 km; therefore, a relatively coarse mesh was used, as explained below. The model cells were 5 km by 5 km in the horizontal plane, with 12 padding cells increasing geometrically by a factor of 1.4 away from the central grid. Given the areal extent of the study area, this was the finest grid that could be modelled using a reasonable amount of memory on a parallel computing cluster; the inversion required roughly 500 GB of memory for nearly four weeks. During data selection, locations were chosen to ensure that a minimum of two vacant grid cells separated any two MT sites. The uppermost layer was 50 m thick, and the layer thickness increased geometrically by a factor of 1.15 downward. The total model volume was 2689 km from north to south, 2709 km from east to west, and 1105 km from surface to base, allowing for a significant buffer around the study area. At the longest period in our dataset, the skin depth in a 100 Ω•m half-space is 679 km; therefore, the model extended approximately 1.5 skin depths in all directions. Due to the coarseness of the mesh and the computing resources needed, topography and bathymetry were not included in the model. The 3-D rectangular model mesh used for this study had 1.76 million cells: 172 in the north-south direction, 176 in the east-west direction, and 58 in the vertical direction.

Model covariance length scale, γ, is a measure of model smoothing applied across cell boundaries, where a higher number allows more smoothing. The preferred inversion used $\gamma = 0.3$ in the horizontal directions and $\gamma = 0.4$ in the vertical direction, thereby allowing for lateral resistivity variations that were less smooth than variations with depth. The model had a tear halfway through the sedimentary basins of the upper crust, as determined by the CRUST 1.0 model (Laske et al., 2013), meaning that γ was reduced to zero at model cell interfaces corresponding to half of the sedimentary layer thickness, hence no smoothing was imposed across the tear. This tear allowed for sharp resistivity transitions, as might be expected from the layered sedimentary geology of the WCSB. Typical sedimentary strata in this region are Cretaceous siliciclastic rocks overlying Devonian carbonate rocks; since the latter are more resistive, it is reasonable to place a tear within the sedimentary layer. This initial condition had little effect on the resistivity structure beneath the Cordillera, but it was used because it did affect the resistivity structure beneath the WCSB (not presented here). The inversion started with a regularization parameter (λ) of 1 and this value decreased, one order of magnitude at a time, to a minimum value of 10^{-8} by the end of the inversion. With high values of λ, the inversion will prioritize a smooth model; with low values of λ, the inversion will prioritize low data misfit. This created smooth models at early iterations, then allowed more complex structures to emerge as the inversion progressed.

Upward of twenty 3-D inversions were run to examine the available data and dependence on control parameters. The preferred inversion used a starting model with 10 Ω•m above the tear in the sedimentary rocks and 100 Ω•m everywhere else. After 297 iterations, the inversion converged to a root-mean-square (r.m.s.) misfit of 2.23 from a starting value of 16. Additional inversions are currently in progress and the model is yet to be finalized; however, it is unlikely to change significantly.

Study Area 2: Mount Meager

Geothermal Background

Study area 2 is centred on Mount Meager (Figure 2), which is the volcano active most recently in the Canadian portion of the GVB, with a major eruption ~2400 years ago (Hickson, 1994). The Mount Meager area drew attention as a geothermal target in the 1970s because of two thermal spring systems: Meager Creek springs and Pebble Creek spring (Souther, 1981). Early exploration work included

geothermometry, DC resistivity surveys and diamond drilling (Fairbank et al., 1981). Lewis and Jessop (1981) measured heat flow of 132 mW/m^2 in a drillhole near Mount Meager, which was elevated compared to a mean of 79 mW/m^2 in three other drillholes, each more than 10 km from Mount Meager. Based on these studies, this volcano is one of the most promising geothermal targets near to infrastructure in Canada, and has been the subject of research since the 1970s (Jessop, 1998). However, a number of barriers to development have been identified and need to be addressed.

One challenge to development at Mount Meager has been the distance to the power grid. This has improved in recent years since Innergex Renewable Energy Inc. (Innergex) has been operating two run-of-river hydroelectric plants near Mount Meager since 2017, as part of their Upper Lillooet River hydro project. Electricity generated at these two facilities is transmitted to the BC Hydro transmission system by a 230 kV transmission line. The proximity of this high-voltage line to Meager Creek has increased the economic feasibility of a geothermal power plant in the area; however, Innergex would be under no obligation to enter a corporate relationship with a geothermal developer. Meager Creek Development Corporation is planning to produce green hydrogen instead of delivering power to the grid, removing this particular hurdle. Green hydrogen is produced from water by electrolysis using renewable electricity.

Another challenge to development comes from landslide hazards. A large rockslide and debris flow occurred at Mount Meager on August 6, 2010, that displaced 48.5 million cubic metres of material (Guthrie et al., 2012; Allstadt, 2013). Meager Creek was temporarily dammed, and the flood risk led to the evacuation of 1500 residents of Pemberton (Guthrie et al., 2012). Therefore, landslide hazard assessment is an important consideration for ongoing geothermal development at Mount Meager.

A remaining challenge comes from uncertainties in the permeability and porosity of the rocks in the reservoir. This question can be addressed with geophysical studies that image the subsurface structure, as described in this paper.

Data and Methods

Within study area 2, the available broadband MT data were recorded at 73 stations within an area covered by latitudes 50.48 to 50.74°N and longitudes 123.29 to 123.71°W, as shown in Figure 4. These data included seven soundings collected in 1982 by the Pacific Geoscience Centre (Flores-

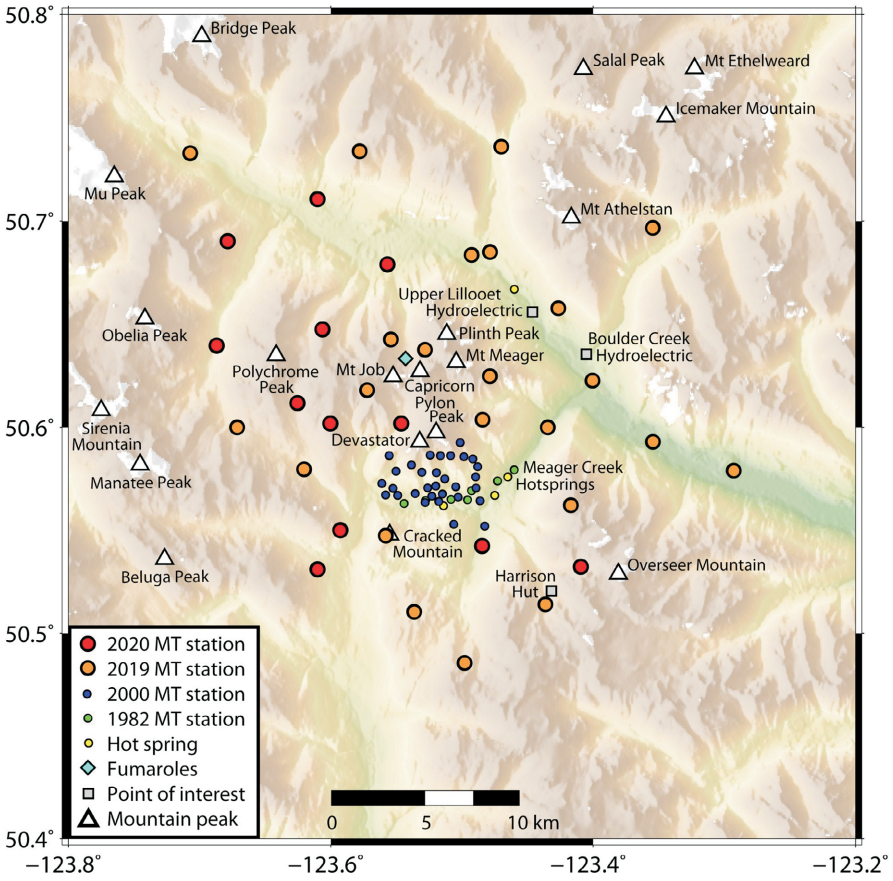

Figure 4. Study area 2 showing locations of all 73 available broadband magnetotelluric data sites.

Luna, 1986), 31 soundings collected in 2000 by Frontier Geosciences Inc. (Candy, 2001), and 35 soundings collected by the University of Alberta for this study, 23 sites in 2019 and 12 sites in 2020 (Unsworth et al., 2021). These time series were processed using robust algorithms (Egbert and Eisel, 1998) based on the theory of Egbert and Booker (1986). These frequency-domain data were edited manually to remove outliers.

For this study, a resistivity model was obtained from joint inversion of impedance and tipper data using 29 periods (0.0025–1000 s) and 66 of the 73 available data sites (Figure 5). The data sites consist of two from 1982, 30 from 2000, 22 from 2019 and 12 from 2020. An inversion with 64 data sites (2000–2020 data) and another with 34 data sites (2019–2020 data) will be performed at a later stage in this study to test the robustness of the model and possible influence of time variations; however, 20 to 40 years is a relatively short amount of time when considering the evolution of a magma body and its associated hydrothermal systems (Arnórsson, 2014; Karakas et al., 2017).

A 5% relative error floor was applied to the impedance data and a 0.03 absolute error floor was applied to the tipper data. As for study 1, the ModEM algorithm (Kelbert et al., 2014) was used to invert the data. The inversion started from a 100 Ω•m half-space with an r.m.s. misfit of 11.7 and converged to a resistivity model with a misfit of 2.0 after 670 iterations.

The 3-D rectangular model mesh used for this study had 2.1 million cells: 148 in the north-south direction, 136 in the east-west direction, and 105 in the vertical direction. The cells were 250 by 250 m in the horizontal plane, with 15 padding cells increasing geometrically by a factor of 1.35 away from the central grid (Figure 5). The upper layers were 50 m thick, then layer thickness increased geometrically by a factor of 1.1 below topography. The top 12 layers, higher than all the MT sites, were removed to decrease the total model size and the computing resources needed.

Resistivity Models

Southeastern BC

Although the resistivity model developed for study area 1 extends to depths in excess of 300 km, this paper only presents results for the uppermost 80 km and focuses on crustal features. Attention is drawn to features near the SRMT, and

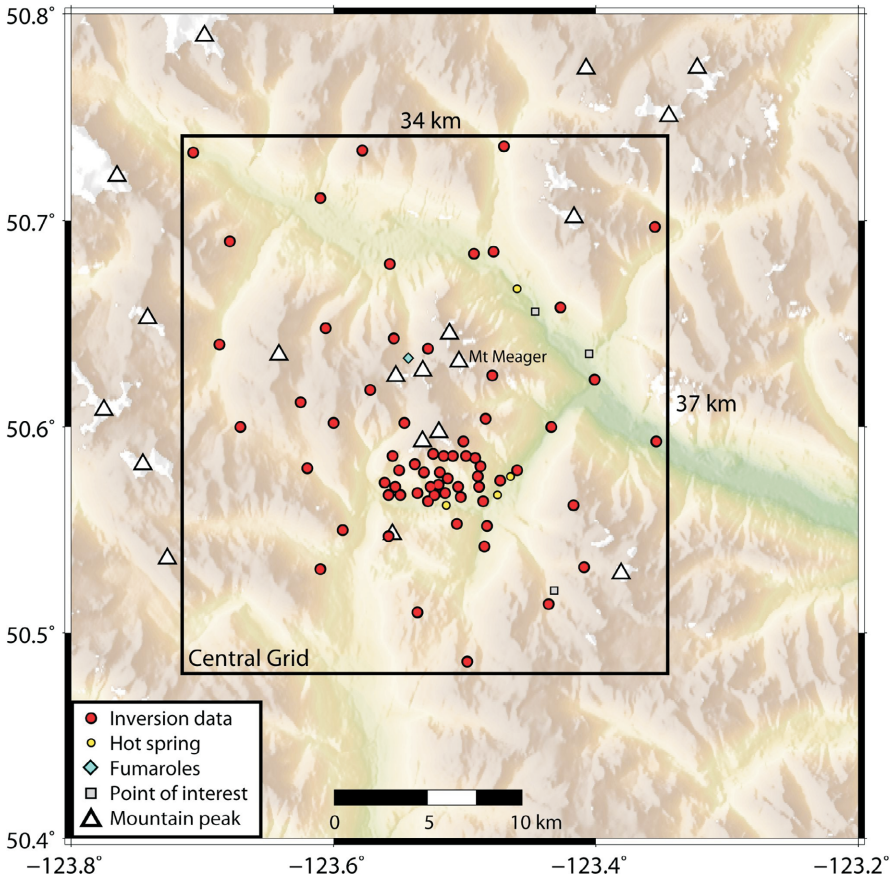

Figure 5. Extent of central grid of study area 2 showing locations of the 66 magnetotelluric data sites included in the inversion that produced the resistivity model shown in Figures 8 and 9. Points of interest and mountain peaks are as labelled in Figure 4.

the potential for future geothermal exploration is discussed.

In the model, the Canadian Cordillera in southeastern BC is characterized by resistive upper crust and numerous discrete mid- and lower-crustal conductors. To the east, beneath the plains of Alberta, the high-resistivity North American craton is overlain by the low-resistivity WCSB. Three horizontal slices of the preferred resistivity model are presented in Figure 6.

A band of low resistivity west of the BC–Alberta border is observed at crustal depths of 5–30 km (e.g., Figure 6a–b). This lateral change in resistivity structure corresponds roughly to the well-documented facies boundary between the Paleozoic carbonate platform to the east and the shale-dominated oceanic basin to the west. Rocks in the shale basin are more commonly deformed in a ductile manner, and show pervasive penetrative cleavage and low-grade metamorphism, whereas the eastern carbonate rocks are typically deformed in a brittle manner, and are unmetamorphosed. It has been suggested that the facies boundary is the trace of a continental suture (Johnston, 2008; Chen et al., 2019), which may explain the contrasting electrical properties observed on either side. At depths greater than 25 km, there could be partial melting in the southern Omineca Belt (Ledo and Jones, 2001) and several large conductors extend below this depth in our model (Figure 6c). At shallower depths, low resistivity is more likely caused by interconnected saline fluids. Figure 6c shows the model layer at a depth of 51–58 km, which is close to the depth of the Moho near the SRMT (Bennett et al., 1975).

A cross-section of the resistivity model for study area 1 is presented in Figure 7. The profile A-B-C is roughly parallel to the SRMT (see Figure 3) and passes close to eight thermal springs. The northernmost of them, Canoe River hot spring, is correlated with a large, low-resistivity anomaly that was named the Valemount conductor (VC) in this study. This oblong, northwest-trending crustal conductor is least resistive (<1 Ω•m) beneath the Canoe River hot spring and is 10–20 km thick for much of its length. To the northwest of the hot spring, the conductor dips at ~45° to a depth of ~60 km, and to the southeast it extends horizontally for more than 100 km. The VC is the deepest of the various conductors resolved in our model beneath the SRMT. The depth to the base of a conductor is poorly resolved by the MT method, therefore it cannot be determined if the VC extends into the mantle. It must also be noted that the Moho in Figure 7 is approximated by a straight line at 55 km depth although its depth is likely variable along the profile. The VC is located in the footwall of the SRMT fault, a westward-dipping normal fault. The low resistivity could be caused by saline fluids in porous fractured rocks near the fault and/or conductive minerals (e.g., graphite, sulphides or clays) deposited by prior fluid flow; however, interpretations are still in progress. Lee (2020) interpreted a shallow crustal conductor near the SRMT fault in the same region as more likely caused by graphite or sulphides than aqueous fluids.

The seven hot springs on profile B-C (Figure 7) occur near faults. Wolfenden and Radium hot springs are near the southern end of the Purcell thrust fault and the northern end of the Redwall fault; Fairmont and Red Rock hot springs

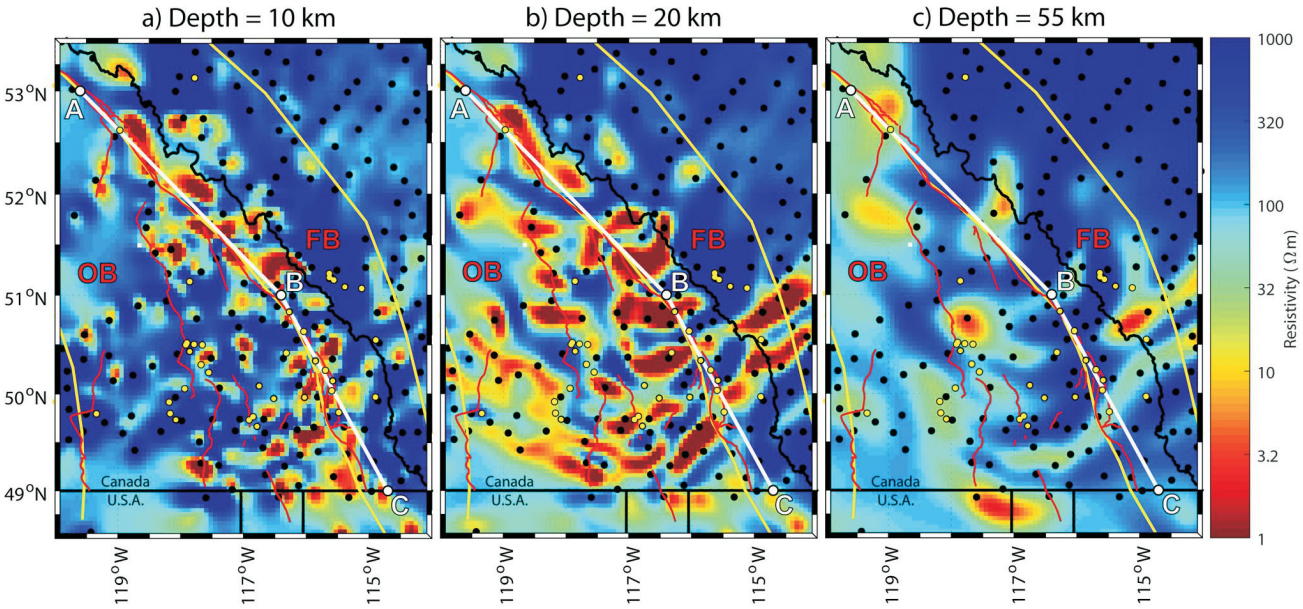

Figure 6. Horizontal slices of the resistivity model in the area bounded by latitudes 48.5–53.5°N and longitudes 114–120°W, at depths of **a)** 9–11 km, **b)** 19–22 km, and **c)** 51–58 km. Provincial and federal boundaries (black lines), morphogeological boundaries (yellow lines), surface traces of major faults (red lines), thermal springs (yellow dots) and magnetotelluric sites (black dots) are also shown. Abbreviations: FB, Foreland Belt; OB, Omineca Belt. A cross-section along profile A-B-C is shown in Figure 7.

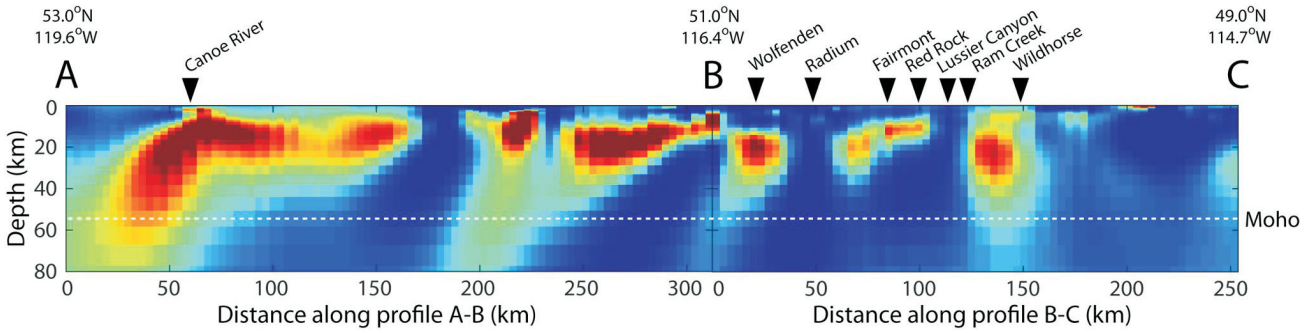

Figure 7. Cross-section of the resistivity model for southeastern British Columbia in the vicinity of the southern Rocky Mountain Trench, along with the locations of eight nearby thermal springs. The location of profile A-B-C and the resistivity colour scale are shown in Figure 6. Approximate depth of the Moho (white dashed line at 55 km depth) is from a seismic refraction model (Bennett et al., 1975).

are near the Redwall fault; and Lussier Canyon, Ram Creek and Wildhorse hot springs are near the Lussier River fault. There are a few mid-crustal conductors beneath this cluster of hot springs, predominantly in the 11–33 km depth range (Figure 7). The observed low resistivity is likely caused by aqueous fluids as these depths are within the 400–700°C temperature range (Hyndman and Shearer, 1989; Currie and Hyndman, 2006). The pattern of subparallel, discrete conductors in the middle of profile A-B-C could be caused by electrical anisotropy (e.g., Heise and Pous, 2001) and will be subject to further investigation, such as forward modelling and anisotropic 3-D inversion.

Low resistivity (0.1–10 Ω•m) is observed in the upper and middle crust, extending ~100 km to the northwest from point B, but there is a conspicuous absence of hot springs in this region. This section of the profile is near the Cretaceous Purcell thrust fault, which was not reactivated by Eocene extension nor modern transpression and is therefore likely not permeable. This low-resistivity anomaly is shallowest beneath the Columbia River northwest of Golden, BC. The low resistivity could be caused by conductive minerals deposited by prior fluid flow associated with the extinct Purcell thrust; however, the possibility of saline fluids trapped beneath an impermeable layer or diffused within a permeable layer such that they do not form a discrete hot spring at the surface cannot be excluded. This region is recommended for future geophysical research, for example, a higher-frequency MT survey with shorter interstation distances. If possible, the resulting dataset should be inverted using a 3-D anisotropic inversion program (e.g., Kong et al., 2021). Conductors associated with other clusters of hot springs, in the central-southern Omineca Belt for example, will be presented and discussed in future publications.

The resistivity model for study area 1 shows broad similarities with previous MT studies in the Canadian Cordillera. Rippe et al. (2013) used 2-D inversion of MT data to create a pair of subparallel resistivity models of the southern Canadian Cordillera, and they imaged a crustal conductor beneath the Intermontane and Omineca belts. These authors showed that the mid-crust of the southern Canadian Cordillera was characterized by low resistivity, which was interpreted as most likely a layer of aqueous fluids that may be underlain by partial melt. On their southern profile, the upper surface of the crustal conductor was at a depth of ~20 km; a similar but less pronounced conductor, also at ~20 km depth, was observed on their northern model. These lower crustal conductors were interpreted as saline fluids and/or partial melt, with the weaker northern conductor inferred to be due to the reduced extension. Our model shows a similar crustal conductor, but it is shallower and has a more complex 3-D structure than in the 2-D studies. Rippe et al. (2013) also showed that the low resistivity of the upper mantle was consistent with the presence of a shallow asthenosphere at depths greater than 60 km. This agreed with a lithosphere thickness of 50–60 km concluded by Currie and Hyndman (2006) based on thermal constraints and other observations.

Mount Meager

The resistivity model for study area 2 is presented in Figures 8 and 9; the model should be considered preliminary, as discussed below in ‘Conclusions’.

The uppermost kilometre of the model has highly variable resistivity. Near Mount Meager, the resistivity is generally low (Figure 8a). This is likely caused by saline aqueous fluids (brines) and hydrothermally altered rock.

There is a large conductor 5 to 8 km below sea level, between Mount Meager and Meager Creek (Figure 8b). It is more than 7 km wide (Figure 9a), more than 10 km long (Figure 9b) and more than 3 km thick. This anomaly is likely caused by brines and partially melted rock, and it occurs beneath the areas investigated with MT in 1982 and 2000 (Figure 4). The finer details of the resistivity model may change as the model is refined, but this large feature is certainly robust.

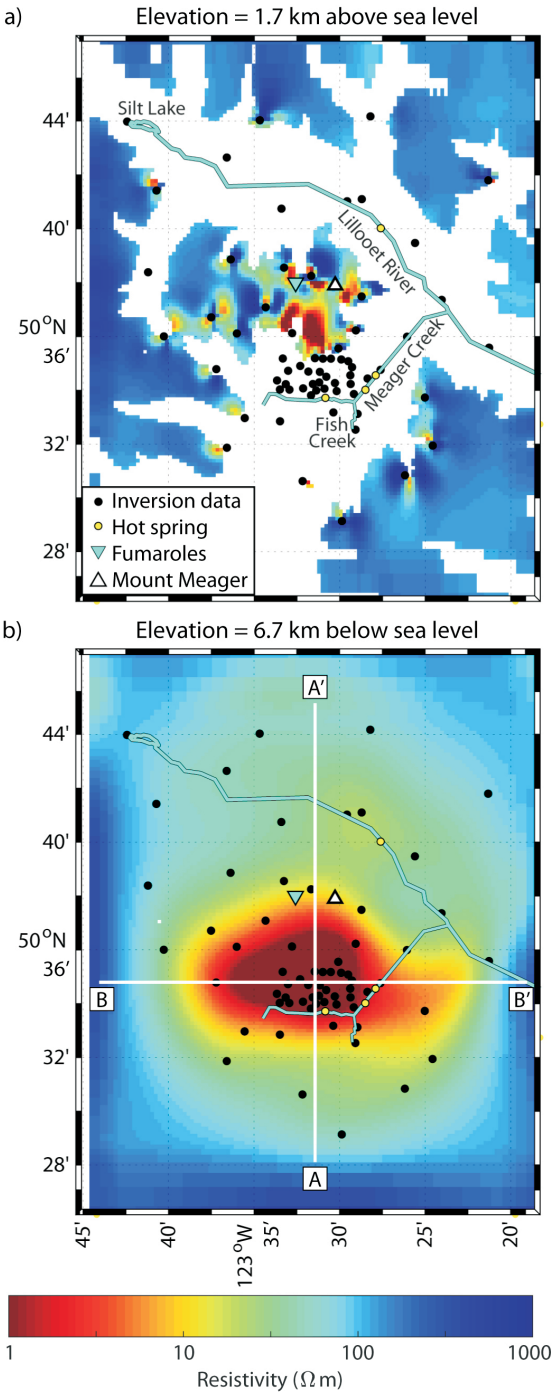

Figure 8. Horizontal layers of the 3-D resistivity model for study area 2 at **a)** 1.7 km above sea level, and **b)** 6.7 km below sea level. Cross-sections indicated by lines A-A' and B-B' are shown in Figure 9.

Two general conclusions are very likely at this early stage: 1) there are localized regions of near-surface brines and hydrothermally altered rock beneath the Mount Meager massif, and 2) there is a magma body beneath the Mount Meager massif in the depth range of 7 to 10 km. Detailed descriptions of these features will require further analysis, but these conclusions are not inconsistent with the last volcanic episode on Mount Meager happening so recently, the degree of hydrothermal alteration seen in the near surface as a result of landslide failures, and the presence of long-

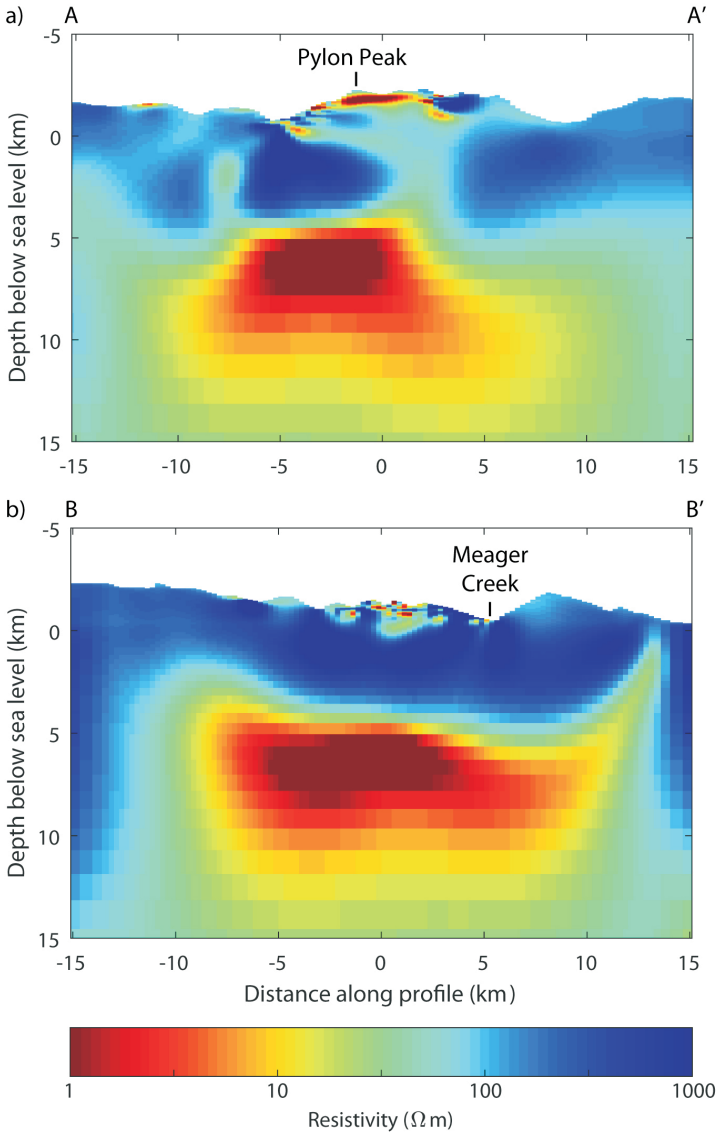

Figure 9. Cross-sections of the 3-D resistivity model for study area 2 from **a)** south to north (A-A'), and **b)** west to east (B-B'). Locations of the cross-sections are shown on Figure 8b.

lived fumaroles (Hickson et al., 1999; Stewart et al., 2003; Hickson, 2017). Implications for development of geothermal resources are also being considered.

Conclusions

The 3-D resistivity model presented in this paper for study area 1 shows that the mid-crustal layer is composed of a number of discrete low-resistivity zones. Some of these appear to underlie regions with known geothermal manifestations, but others do not. It may be that some of these discrete zones are representative of 'blind' geothermal systems that do not have surface manifestations. However, the observed pattern may also be indicative of strong crustal anisotropy that is poorly resolved with this isotropic inversion.

As these results are still preliminary, further research is needed in two new directions: 1) application of a new 3-D anisotropic magnetotelluric inversion algorithm to test if the pattern of discrete conductors is caused by electrical anisotropy or a reasonable representation of the geology, and 2) use of denser grids for the magnetotelluric data in areas of interest to detect fluid pathways from the mid-crustal layer to the surface. A finer model mesh and higher frequency data at additional locations would allow the resolution of smaller and shallower features. Two examples of possible target areas are: 1) a region encompassing the Redwall and Lussier River faults, where there are several known hot springs; and 2) the southern Rocky Mountain Trench northwest of Golden, where there is a notable ab-

sence of thermal springs. Modelling of the upper-crustal (e.g., top 5 km) resistivity structure, especially with the addition of topography, could image specific hydrothermal systems associated with known hot springs, and possibly locate potential blind geothermal systems.

The resistivity model presented in this paper for study area 2 is preliminary and the following research steps are currently in progress or being planned: 1) variation of smoothing parameters, e.g., the regularization parameter (λ) and model covariance length scale (γ); 2) testing of different data subsets, e.g., without the 1982 and/or 2000 data; and 3) testing of data sensitivity and model resolution, e.g., forward modelling and synthetic inversions.

After the resistivity model has been finalized, more detailed interpretations will be made and will include: 1) estimation of fluid content and relevant parameters using constraints from geophysical and chemical experiments; 2) estimation of melt fraction using constraints from petrological experiments, as was done by Comeau et al. (2015) and Cordell et al. (2018); and 3) joint interpretations using results from the gravity and seismic investigations also being carried out for the Garibaldi volcanic belt geothermal energy project. Audio-magnetotelluric (AMT) data were also collected for this project in 2019 (Craven et al., 2020) and the regional model presented in this paper will assist the AMT interpretations. The two resistivity models, with different spatial scales, will be compared and possibly merged into one.

Acknowledgments

Funding was provided by a Natural Sciences and Engineering Research Council of Canada Discovery Grant to M.J. Unsworth and an award from the Future Energy Systems program at the University of Alberta. Additional resources and support were provided by Natural Resources Canada and Geoscience BC. The authors are grateful to J.K. Russell for reviewing this paper and thank T. Finley for providing invaluable feedback and discussions; G. Egbert, A. Kelbert and N. Meqbel for use of ModEM; and Compute Canada for access to high-performance cluster computing. The authors also thank S. Grasby, J. Craven, A. Williamson and Z. Vestrum for all of their help; C. Candy at Frontier Geosciences Inc. for access to the 2000 magnetotelluric data; and the outstanding pilots from No Limits Helicopters.

References

Allen, D.M., Grasby, S.E. and Voormeij, D.A. (2006): Determining the circulation depth of thermal springs in the southern Rocky Mountain Trench, south-eastern British Columbia, Canada using geothermometry and borehole temperature logs; Hydrogeology Journal, v. 14, p. 159–172, URL <https://doi.org/10.1007/s10040-004-0428-z>.

Allstadt, K. (2013): Extracting source characteristics and dynamics of the August 2010 Mount Meager landslide from broadband seismograms: seismic inversion of Mount Meager landslide; Journal of Geophysical Research: Earth Surface, v. 118, p. 1472–1490, URL <https://doi.org/10.1002/jgrf.20110>.

Arnórsson, S. (2014): The roots of volcanic geothermal systems—Their birth, evolution and extinction; *in* Proceedings 5th African Rift Geothermal Conference, Arusha, Tanzania, 29–31 October 2014, 8 p.

Bennett, G.T., Clowes, R.M. and Ellis, R.M. (1975): A seismic refraction survey along the southern Rocky Mountain Trench, Canada; Bulletin of the Seismological Society of America, v. 65, p. 37–54.

Cagniard, L. (1953): Basic theory of the magneto-telluric method of geophysical prospecting; Geophysics, v. 18, p. 605–635, URL <https://doi.org/10.1190/1.1437915>.

Candy, C. (2001): Crew Development Corporation Report on a magnetotelluric survey, South Meager Geothermal Project, Pemberton, British Columbia (Project FGI-581); report prepared for Frontier Geosciences Inc., 168 p.

Charlesworth, H.A.K. (1959): Some suggestions on the structural development of the Rocky Mountains of Canada; Journal of the Alberta Society of Petroleum Geologists, v. 7, p. 249–256.

Chave, A.D. and Jones, A.G. (2012): The Magnetotelluric Method: Theory and Practice; Cambridge University Press, Cambridge, U.K., 604 p.

Chen, Y., Gu, Y.J., Currie, C.A., Johnston, S.T., Hung, S.-H., Schaeffer, A.J. and Audet, P. (2019): Seismic evidence for a mantle suture and implications for the origin of the Canadian Cordillera; Nature Communications, v. 10, article no. 2249, 10 p., URL <https://doi.org/10.1038/s41467-019-09804-8>.

Comeau, M.J., Unsworth, M.J., Ticona, F. and Sunagua, M. (2015): Magnetotelluric images of magma distribution beneath Volcán Uturuncu, Bolivia: implications for magma dynamics; Geology, v. 43, p. 243–246, URL <https://doi.org/10.1130/G36258.1>.

Cordell, D., Unsworth, M.J. and Díaz, D. (2018): Imaging the Laguna del Maule Volcanic Field, central Chile using magnetotellurics: evidence for crustal melt regions laterally-offset from surface vents and lava flows; Earth and Planetary Science Letters, v. 488, p. 168–180, URL <https://doi.org/10.1016/j.epsl.2018.01.007>.

Craven, J.A., Hormozzade, F., Tschirhart, V., Ansari, M., Bryant, R. and Montezadian, D. (2020): Overview of the 2019 audiomagnetotelluric survey of the Mount Meager geothermal reservoir; Chapter 6 *in* Garibaldi Geothermal Energy Project, Mount Meager 2019 - Field Report, Geoscience BC, Report 2020-09, p. 126–147, URL <https://https://geoscan.nrcan.gc.ca/starweb/geoscan/servlet.starweb?path=geoscan/fulle.web&search1=R=326818> [October 2021].

Currie, C.A. and Hyndman, R.D. (2006): The thermal structure of subduction zone back arcs; Journal of Geophysical Research: Solid Earth, v. 111, URL <https://doi.org/10.1029/2005JB004024>.

Egbert, G.D. and Booker, J.R. (1986): Robust estimation of geomagnetic transfer functions; Geophysical Journal International, v. 87, p. 173–194, URL <https://doi.org/10.1111/j.1365-246X.1986.tb04552.x>.

Egbert, G.D. and Eisel, M. (1998): EMTF: Programs for robust single station and remote reference analysis of magnetotelluric data: UNIX (and PC) version; software manual, 35 p.

Fairbank, B.D., Openshaw, R.E., Souther, J.G. and Stauder, J.J. (1981): Meager Creek Geothermal Project: an exploration case history; Geothermal Resources Council Bulletin, v. 10, p. 3–7, URL <https://doi.org/10.4095/103409>.

Finley, T. (2020): Fault-hosted geothermal systems in southeastern British Columbia; M.Sc. thesis, University of Alberta, 208 p.

Flores-Luna, C.F. (1986): Electromagnetic induction studies over the Meager Creek geothermal area, British Columbia; Ph.D. thesis, University of Toronto, 222 p.

Foo, W.K. (1979): Evolution of transverse structures linking the Purcell Anticlinorium to the western Rocky Mountains near Canal Flats, British Columbia; Ph.D. thesis, Queen's University, 146 p.

Frost, B.R., Fyfe, W.S., Tazaki, K. and Chan, T. (1989): Grain-boundary graphite in rocks and implications for high electrical conductivity in the lower crust; Nature, v. 340, p. 134–136, URL <https://doi.org/10.1038/340134a0>.

Gal, L.P. and Ghent, E.D. (1990): Metamorphism in the Solitude Range, southwestern Rocky Mountains, British Columbia: comparison with adjacent Omineca Belt rocks and tectonometamorphic implications for the Purcell Thrust; Canadian Journal of Earth Sciences, v. 27, p. 1511–1520, URL <https://doi.org/10.1139/e90-161>.

Grasby, S.E. and Ferguson, G. (2010): Controls on the distribution of thermal springs in the Canadian Cordillera; *in* Proceedings World Geothermal Congress 2010, Bali, Indonesia, 25–29 April 2010, 4 p.

Grasby, S.E. and Hutcheon, I. (2001): Controls on the distribution of thermal springs in the southern Canadian Cordillera; Canadian Journal of Earth Sciences, v. 38, p. 427–440.

Grasby, S.E., Ansari, S.M., Calahorrano-Di Patre, A., Chen, Z., Craven, J.A., Dettmer, J., Gilbert, H., Hanneson, C., Harris, M., Liu, J., Muhammad, M., Russell, K., Salvage, R.O., Savard, G., Tschirhart, V., Unsworth, M.J., Vigouroux-Caillibot, N. and Williams-Jones, G. (2020): Geothermal resource potential of the Garibaldi volcanic belt, southwestern British Columbia (part of NTS 092J); *in* Geoscience BC Summary of Activities 2019: Energy and Water, Geoscience BC, Report 2020-02, p. 103–108, URL <https://www.geosciencebc.com/i/pdf/SummaryofActivities2019/EW/Project%202018-004_EW_SOA2019.pdf> [October 2021].

Guthrie, R.H., Friele, P., Allstadt, K., Roberts, N., Evans, S.G., Delaney, K.B., Roche, D., Clague, J.J. and Jakob, M. (2012): The 6 August 2010 Mount Meager rock slide-debris flow, Coast Mountains, British Columbia: characteristics, dynamics, and implications for hazard and risk assessment; Natural Hazards and Earth System Sciences, v. 12, p. 1277–1294, URL <https://doi.org/10.5194/nhess-12-1277-2012>.

Heise, W. and Pous, J. (2001): Effects of anisotropy on the two-dimensional inversion procedure; Geophysical Journal International, v. 147, p. 610–621, URL <https://doi.org/10.1046/j.0956-540x.2001.01560.x>.

Hersir, G.P., Árnason, K. and Vilhjálmsson, A.M. (2015): 3D inversion of magnetotelluric (MT) resistivity data from Krýsuvík high temperature geothermal area in SW Iceland; *in* Proceedings World Geothermal Congress 2015, Melbourne, Australia, 19–25 April 2015, 14 p.

Hickson, C.J. (1994): Character of volcanism, volcanic hazards, and risk, northern end of the Cascade magmatic arc, British Columbia and Washington State; Geological Survey of Canada, Bulletin 481, p. 231–250, URL <https://doi.org/10.4095/203253>.

Hickson, C.J. (2017): Mount Meager data compilation; Geoscience BC, Project 2017-006, URL <http://www.geosciencebc.com/projects/2017-006/> [October 2021].

Hickson, C.J., Russell, J.K. and Stasiuk, M.V. (1999): Volcanology of the 2350 B.P. eruption of Mount Meager Volcanic Complex, British Columbia, Canada: implications for hazards from eruptions in topographically complex terrain; Bulletin of Volcanology, v. 60, p. 489–507, URL <https://doi.org/10.1007/s004450050247>.

Hutchinson, J., Kao, H., Riedel, M., Obana, K., Wang, K., Kodaira, S., Takahashi, T. and Yamamoto, Y. (2020): Significant geometric variation of the subducted plate beneath the northernmost Cascadia subduction zone and its tectonic implications as revealed by the 2014 MW 6.4 earthquake sequence; Earth and Planetary Science Letters, v. 551, article no. 116569, 11 p., URL <https://doi.org/10.1016/j.epsl.2020.116569>.

Hyndman, R.D. and Shearer, P.M. (1989): Water in the lower continental crust: modelling magnetotelluric and seismic reflection results; Geophysical Journal International, v. 98, p. 343–365, URL <https://doi.org/10.1111/j.1365-246X.1989.tb03357.x>.

Jessop, A.M. (1998): Geothermal energy in Canada; Geoscience Canada, v. 25, p. 33–41.

Johnston, S.T. (2008): The Cordilleran ribbon continent of North America; Annual Review of Earth and Planetary Sciences, v. 36, p. 495–530, URL <https://doi.org/10.1146/annurev.earth.36.031207.124331>.

Karakas, O., Degruyter, W., Bachmann, O. and Dufek, J. (2017): Lifetime and size of shallow magma bodies controlled by crustal-scale magmatism; Nature Geoscience, v. 10, p. 446–450, URL <https://doi.org/10.1038/ngeo2959>.

Kelbert, A., Meqbel, N., Egbert, G.D. and Tandon, K. (2014): ModEM: a modular system for inversion of electromagnetic geophysical data; Computers & Geosciences, v. 66, p. 40–53, URL <https://doi.org/10.1016/j.cageo.2014.01.010>.

Kong, W., Tan, H., Lin, C., Unsworth, M., Lee, B., Peng, M., Wang, M. and Tong, T. (2021): Three-dimensional inversion of magnetotelluric data for a resistivity model with arbitrary anisotropy; Journal of Geophysical Research: Solid Earth, v. 126, issue 8, August 2021, e2020JB020562, URL <https://doi.org/10.1029/2020JB020562>.

Kreemer, C., Blewitt, G. and Klein, E.C. (2014): A geodetic plate motion and global strain rate model; Geochemistry, Geophysics, Geosystems, v. 15, p. 3849–3889, URL <https://doi.org/10.1002/2014GC005407>.

Laske, G., Masters, G., Ma, Z. and Pasyanos, M. (2013): Update on CRUST1.0 - A 1-degree global model of Earth's crust; Geophysical Research Abstracts, v. 15, Abstract EGU2013-2658, URL <http://igppweb.ucsd.edu/~gabi/rem.html> [November 2021].

Ledo, J. and Jones, A.G. (2001): Regional electrical resistivity structure of the southern Canadian Cordillera and its physical interpretation; Journal of Geophysical Research: Solid Earth, v. 106, p. 30755–30769, URL <https://doi.org/10.1029/2001JB000358>.

Lee, B. (2020): Improving exploration for geothermal resources with the magnetotelluric method; Ph.D. thesis, University of Alberta, 288 p.

Lewis, J.F. and Jessop, A.M. (1981): Heat flow in the Garibaldi volcanic belt, a possible Canadian geothermal energy resource area; Canadian Journal of Earth Sciences, v. 18, p. 366–375, URL <https://doi.org/10.1139/e81-028>.

Lindsey, N.J. and Newman, G.A. (2015): Improved workflow for 3D inverse modeling of magnetotelluric data: examples from

five geothermal systems; Geothermics, v. 53, p. 527–532, URL <https://doi.org/10.1016/j.geothermics.2014.09.004>.

Majorowicz, J. and Grasby, S.E. (2010): Heat flow, depth–temperature variations and stored thermal energy for enhanced geothermal systems in Canada; Journal of Geophysics and Engineering, v. 7, p. 232–241, URL <https://doi.org/10.1088/1742-2132/7/3/002>.

McDonough, M.R. and Simony, P.S. (1988): Structural evolution of basement gneisses and Hadrynian cover, Bulldog Creek area, Rocky Mountains, British Columbia; Canadian Journal of Earth Sciences, v. 25, p. 1687–1702, URL <https://doi.org/10.1139/e88-159>.

McMechan, M.E. and Thompson, R.I. (1989): Structural style and history of the Rocky Mountain fold and thrust belt; Chapter 4 *in* Western Canada Sedimentary Basin: A Case History, Canadian Society of Petroleum Geologists, p. 47–71.

Meqbel, N.M., Egbert, G.D., Wannamaker, P.E., Kelbert, A. and Schultz, A. (2014): Deep electrical resistivity structure of the northwestern U.S. derived from 3-D inversion of USArray magnetotelluric data; Earth and Planetary Science Letters, v. 402, p. 290–304, URL <https://doi.org/10.1016/j.epsl.2013.12.026>.

Mullen, E.K., Weis, D., Marsh, N.B. and Martindale, M. (2017): Primitive arc magma diversity: new geochemical insights in the Cascade Arc; Chemical Geology, v. 448, p. 43–70, URL <https://doi.org/10.1016/j.chemgeo.2016.11.006>.

Muñoz, G. (2014): Exploring for geothermal resources with electromagnetic methods; Surveys in Geophysics, v. 35, p. 101–122, URL <https://doi.org/10.1007/s10712-013-9236-0>.

North, F.K. and Henderson, G.G.L. (1954): The Rocky Mountain Trench; *in* Guide Book, Fourth Annual Field Conference, Banff–Golden–Radium, Canadian Society of Petroleum Geologists, p. 82–100.

Rippe, D., Unsworth, M.J. and Currie, C.A. (2013): Magnetotelluric constraints on the fluid content in the upper mantle beneath the southern Canadian Cordillera: implications for rheology; Journal of Geophysical Research: Solid Earth, v. 118, p. 5601–5624, URL <https://doi.org/10.1002/jgrb.50255>.

Souther, J.G. (1981): Canadian Geothermal Research Program; *in* Energy Resources of the Pacific Region, AAPG Studies in Geology, v. 12, p. 391–400.

Stern, R.J. (2002): Subduction zones; Reviews of Geophysics, v. 40, p. 3-1–3-38, URL <https://doi.org/10.1029/2001RG000108>.

Stewart, M.L., Russell, J.K. and Hickson, C.J. (2003): Discrimination of hot versus cold avalanche deposits: implications for hazard assessment at Mount Meager, B.C.; Natural Hazards and Earth System Sciences, v. 3, p. 713–724, URL <https://doi.org/10.5194/nhess-3-713-2003>.

Tuya Terra Geo Corp. and Geothermal Management Company, Inc. (2016): Direct-use geothermal resources in British Columbia, Section A: Summary of findings; Geoscience BC, Report 2016-07, 38 p., URL <http://www.geosciencebc.com/projects/2015-022/> [October 2021].

Unsworth, M.J., Hanneson, C., Williamson, A.R. and Vestrum, Z.E. (2021): Final report on the 2019-2020 broadband magnetotelluric study at Mount Meager: implications for structure of the hydrothermal and magmatic system; Chapter 5 *in* Garibaldi Geothermal Energy Project - Phase 1: Final Report, Geoscience BC, Report 2021-08, p. 79–146, URL <http://www.geosciencebc.com/i/project_data/GBCReport2021-08/GBCR%202021-08%20Garibaldi%20Geothermal%20Energy%20Project%20-%20Phase%201.pdf> [October 2021].

Ussher, G., Harvey, C., Johnstone, R. and Anderson, E. (2000): Understanding the resistivities observed in geothermal systems; *in* Proceedings World Geothermal Congress 2000, Kyushu - Tohoku, Japan, May 28–June 10, 2000, p. 1915–1920.

van der Velden, A.J. and Cook, F.A. (1996): Structure and tectonic development of the southern Rocky Mountain trench; Tectonics, v. 15, p. 517–544, URL <https://doi.org/10.1029/95TC03288>.

Varentsov, I.M., Kulikov, V.A., Yakovlev, A.G. and Yakovlev, D.V. (2013): Possibilities of magnetotelluric methods in geophysical exploration for ore minerals; Izvestiya, Physics of the Solid Earth, v. 49, p. 309–328, URL <https://doi.org/10.1134/S1069351313030178>.

Wang, E. (2019): Multidimensional magnetotelluric studies of the Precambrian Alberta basement; Ph.D. thesis, University of Alberta, 397 p.

Wisian, K.W. and Blackwell, D.D. (2004): Numerical modeling of Basin and Range geothermal systems; Geothermics, v. 33, p. 713–741.

Pilot Collaborative Water Monitoring Program, Northeastern British Columbia (NTS 094A, Parts of 093O, P, 094B, G, H): Year One Update

S.L. Lapp, British Columbia Oil and Gas Commission, Fort St. John, British Columbia, suzan.lapp@bcogc.ca

E.G. Johnson, British Columbia Ministry of Energy, Mines and Low Carbon Innovation, Victoria, British Columbia

D.L. Cottrell, Shell Canada Ltd., Calgary, Alberta

W.T. Van Dijk, Matrix Solutions Inc., Edmonton, Alberta

B.P. Shepherd, Matrix Solutions Inc., Grande Prairie, Alberta

R.L. Rolick, British Columbia Oil and Gas Commission, Fort St. John, British Columbia

Lapp, S.L., Johnson, E.G., Cottrell, D.L., Van Dijk, W.T., Shepherd, B.P. and Rolick, R.L. (2022): Pilot Collaborative Water Monitoring Program, northeastern British Columbia (NTS 094A, parts of 093O, P, 094B, G, H): year one update; *in* Geoscience BC Summary of Activities 2021: Energy and Water, Geoscience BC, Report 2022-02, p. 95–102.

Program Background

In 2020 the Pilot Collaborative Water Monitoring Program came to fruition as the union of three distinct projects to address the needs brought forward through such programs as the Province of British Columbia's (BC) Northeast Water Strategy and Regional Strategic Environmental Assessment, and results of the *Scientific Review of Hydraulic Fracturing in British Columbia* (Scientific Hydraulic Fracturing Review Panel, 2019). The three projects include

1) Northeast BC Hydrometric Monitoring Project: an installation of four to six hydrometric stations to measure surface water quantity.
2) Co-ordinated Groundwater, Surface Water and Climate Monitoring Project, Northeast BC: co-location of supplemental monitoring to greatly expand collected knowledge at the monitoring sites, increase the opportunity for research and understanding into watershed processes, and increase the capacity and participation of local First Nations as a partner in water monitoring. Supplemental monitoring includes installation of groundwater monitoring wells for water quantity and quality where it is anticipated there will be groundwater–surface water interaction; surface water quality monitoring including benthic invertebrate sampling; installation or improvement of local climate stations to monitor factors that affect surface and groundwater, such as rainfall, snowfall, humidity, wind and solar radiation; and training of local First Nations to capture measurements and maintain equipment.
3) Traditional Knowledge Project: an innovative venture to bridge communication barriers through the gathering of Traditional Knowledge at each monitoring site at specific seasonal times with the hope of braiding Traditional Knowledge with Western-style scientific observations.

By co-locating groundwater monitoring stations near hydrometric stations, not only will project costs be reduced, but results of the research will hopefully answer several key questions using the datasets produced (groundwater quantity and quality, surface water quality, and climate data). This co-ordinated approach will also maximize the return on 'foundational science' through a more complete baseline monitoring program, which will augment the existing approved Surface Water Quantity Monitoring Program (Geoscience BC project number 2019-016), and the approved Traditional Knowledge Program (Geoscience BC project number 2019-018). The baseline data will allow for advanced analysis to support assessment of groundwater–surface water interaction, watershed water balance calculations, and meteorological data to support a variety of assessments.

Project Updates

This program was initiated with a virtual kick-off workshop on December 2, 2020, with members of the six Treaty 8 First Nations from within the boundary of the study area (Figure 1) in attendance, along with program partners from the BC Oil and Gas Commission (BCOGC), the BC Ministry of Energy, Mines and Low Carbon Innovation (EMLCI), Shell Canada Ltd. and Matrix Solutions Inc. (Matrix). The six First Nation communities included Blueberry River First Nations (BRFN), Doig River First Nation (DRFN), Halfway River First Nation (HRFN), McLeod

This publication is also available, free of charge, as colour digital files in Adobe Acrobat® PDF format from the Geoscience BC website: http://geosciencebc.com/updates/summary-of-activities/.

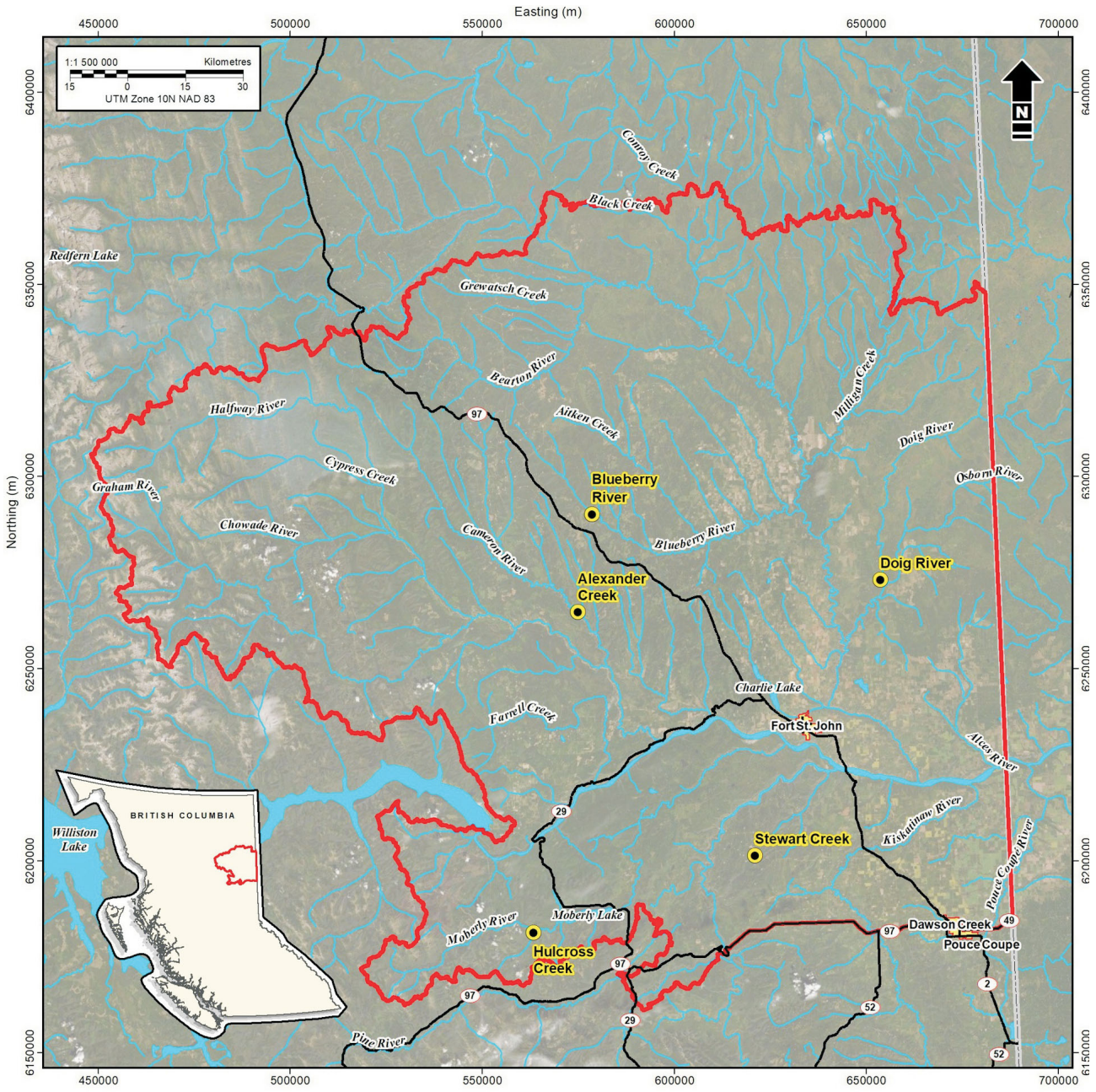

Figure 1. Location of study area (outlined in red) and water monitoring sites.

Lake Indian Band (MLIB), Saulteau First Nations (SFN), and West Moberly First Nations (WMFN). All First Nations expressed interest in participating in the research and monitoring partnership.

Site Criteria

Throughout the winter and spring of 2021 ongoing virtual meetings were conducted with each First Nation community within the study area to discuss co-locating water and climate monitoring sites based on specific site criteria and priorities and/or concerns expressed by each of the First Nations. Field reconnaissance was conducted in the early summer of 2021 with representatives of each First Nation community to confirm the site of the hydrometric station. Criteria for site selection was a mix of features, including

- vehicle accessibility to the monitoring site;
- watersheds with high cumulative disturbance on both water quantity and quality (Johnson, 2020; Sentlinger and Metherall, 2020), which is a monitoring criteria of primary interest to the local First Nation communities;
- whether the stream size was amenable to the type of hydrometric monitoring proposed (not too large or too small); and

- if the site could accommodate well drilling on Crown land.

To further refine the selection conditions, discipline-specific siting criteria were also considered, to meet standards for scientific data collection such as the desirable criteria for basic hydrometric stations, as outlined in the *Manual of British Columbia Hydrometric Standards* (Resources Information Standards Committee, 2018), and desirable class for sensor-siting classification for climate monitoring stations, as proposed in the *Manual of Surface Weather Observation Standards* (Environment and Climate Change Canada, 2019).

After potential sites were initially identified, they were further discussed with various subject matter experts from the BC Ministry of Forests, Lands and Natural Resource Operations and Rural Development (FLNRORD) and the BC Ministry of Environment and Climate Change Strategy, for considerations around benthic sampling (as part of the Canadian Aquatic Benthic Invertebrate Network); as potentially part of the Provincial Groundwater Observation Well Network; as a location to supply water quality data; and for considerations around surface water–groundwater interaction.

There is more flexibility in the location of climate monitoring stations, and the team is actively working with FLNRORD and BC Hydro to understand if certain infrastructure can be improved to serve multiple purposes instead of installing new stations. Figure 1 shows the location of the five chosen monitoring sites; Table 1 summarizes the hydrometric station site information; and Table 2 lists what monitoring was carried out at each site.

Table 1. Summary of the monitoring site locations and associated First Nation communities. All co-ordinates are in UTM Zone 10N, NAD 83. Abbreviations: BRFN, Blueberry River First Nations; DRFN, Doig River First Nation; HRFN, Halfway River First Nation; MLIB, McLeod Lake Indian Band; SFN, Saulteau First Nations; WMFN, West Moberly First Nations.

Location	First Nation	Easting	Northing
Blueberry River on Mile 98 Road	BRFN	578627	6290276
Doig River at Doig River First Nation	DRFN	653587	6273135
Alexander Creek on Mile 95 Road	HRFN	574248	6271384
Stewart Creek at Stewart Creek Road	MLIB	620969	6201392
Hulcross Creek on Moberly Forest Service Road	SFN/WMFN	563289	6181243

Proposed Monitoring

Hydrometric Stations

A total of five hydrometric stations were installed in the late summer and early fall of 2021; installation at each site took between two and three days. First Nation community members were invited to participate in the equipment installation and ongoing monitoring of the station associated with their community. Water Officers from FLNRORD based in Fort St. John also participated in the installation of the stations and will continue to collaborate with the BCOGC to monitor water quantity at these locations. At each hydrometric station the equipment consists of OTT HydroMet GmbH's OTT PLS sensors with Sutron XLink 100 loggers. The final visit to each of the stations for the 2021 field season was conducted in October to winterize them. Figure 2 shows the location of the hydrometric station installations.

Groundwater Wells

The purpose of water wells is to monitor the groundwater level in the shallow subsurface (unconfined aquifer), water quality in shallow groundwater, and ultimately—in coordination with the surface water monitoring—provide information about surface water–groundwater interaction. As such, wells were sited proximal to hydrometric stations. Some locations provided the added opportunity for testing the possible existence of a paleovalley at a slightly deeper horizon. Research on paleovalleys in this region has been supported by Geoscience BC with mapping, airborne and ground-based geophysical surveys, and drilling. Where possible, water wells will be installed to a depth sufficient to test any proposed paleovalley.

The sites selected for groundwater monitoring (Blueberry River, Alexander Creek, Stewart Creek and Hulcross Creek) were the most suitable, based on the objective of

Table 2. Summary of the proposed monitoring at each of the five chosen sites. An 'X' in a cell indicates that type of monitoring is being carried out at that site; an asterisk (*) indicates a site that is being discussed with the BC Ministry of Forests, Lands and Natural Resource Operations and Rural Development to assess suitability of use of wildfire stations at these sites as climate monitoring sites for this study. All sites are being assessed for suitability of benthic invertebrate sampling for use by the Canadian Aquatic Benthic Invertebrate Network (CABIN). Other abbreviations: BRFN, Blueberry River First Nations; DRFN, Doig River First Nation; HRFN, Halfway River First Nation; MLIB, McLeod Lake Indian Band; SFN, Saulteau First Nations; WMFN, West Moberly First Nations.

Location	First Nation	Hydrometric station	Groundwater well	Water quality	CABIN	Climate station
Blueberry River on Mile 98 Road	BRFN	X	X	X	X	Regional*
Doig River at Doig River First Nation	DRFN	X		X	X	Regional*
Alexander Creek on Mile 95 Road	HRFN	X	X	X	X	X
Stewart Creek at Stewart Creek Road	MLIB	X	X	X	X	X
Hulcross Creek on Moberly Forest Service Road	SFN/WMFN	X	X	X	X	Regional

Figure 2. Photos showing the hydrometric station equipment and data collection at **a)** Hulcross Creek, **b)** Blueberry River, **c)** Alexander Creek, **d)** Doig River and **e)** Stewart Creek.

monitoring interactions between surface water and groundwater in the Quaternary deposits overlying bedrock. Initial desktop analysis indicated that groundwater near the Doig River hydrometric site was deep and confined, and several existing wells in the vicinity gave no indication of shallow groundwater. Therefore, no well was proposed at the Doig River location. Geological and airborne geophysical surveys indicate the possibility of a paleovalley at the Alexander Creek and Blueberry River sites, therefore the wells at these sites will be drilled to a greater depth.

After the sites for water well installation were selected, applications were submitted to FLNRORD for permits to drill and install wells on Crown land, with the installations originally planned for September 2021. The drilling program was delayed due to permit requirements that included sign-off by all local First Nations. The monitoring wells have been designed to meet requirements for future inclusion in the Provincial Groundwater Observation Well Network. A pressure-logging instrument will be deployed in each monitoring well to record groundwater levels.

The monitoring wells are scheduled to be installed in late 2021 by Matrix and Anderson Water Services Ltd., a drilling contractor based in Fort St. John. The drilling and well construction details will be provided in a future report.

Water Quality

There is general consensus that insufficient water quality monitoring data exists in northeastern BC (Northeast Water Strategy, 2017, 2018). Sampling water quality in conjunction with stream volume helps identify any linked parameters, such as dissolved solids and dissolved oxygen. Sampling for water quality at monitoring sites was proposed for four specific time frames annually during the open-water season: once in spring, twice in summer, and once in fall. Surface water quality monitoring in 2021 was planned for all five monitoring locations during the four time frames, however, due to the time required earlier in the year to select and establish the monitoring sites and receive consensus among partners, sampling was carried out only twice at all but the Stewart Creek location: once in late summer and once in the fall. Details of the sampling completed at each site are given in 'Site Status', below.

Surface water quality monitoring for the program includes sampling both field and laboratory parameters. Routinely sampled field parameters include dissolved oxygen, temperature, pH and electrical conductivity, while sampled laboratory parameters include the same routine field parameters in addition to turbidity, major ions, total and dissolved metals, total organic carbon, coliforms and total plate count, biochemical and chemical oxygen demand, and hydrocarbons.

Additionally, sampling of benthic invertebrates was proposed at the start of the program for two monitoring sites; however, it was later determined that Matrix would investigate site suitability and benthic community diversity at as many sites as possible. The Canadian Aquatic Biomonitoring Network (CABIN) program assesses the aquatic health of streams through the collection of benthic invertebrate samples. Sampling for benthic invertebrates at the selected sites will be completed by a Matrix staff member certified by CABIN (Figure 3). Each site will be registered into the CABIN database by a Matrix staff member, which will identify any potential reference sites for evaluation of relative stream health. Determination of the necessity for future assessments will be made based on results of the 2021 assessments.

Climate Stations

Climate data will be used to assess the water balance at each of the monitoring sites. Climate data parameters include total accumulation of precipitation and snow, air temperature, wind speed and direction, barometric pressure, and relative

Figure 3. Examples of benthic invertebrate sampling at **a)** Alexander Creek and **b)** Blueberry River.

humidity. Climate stations do not need to be placed at the same exact location as the hydrometric sites and monitoring wells. Having the climate monitoring stations located in the vicinity of the other monitoring equipment is sufficient for research needs, and results are superior when the station is located away from road activity, in a sheltered spot where it is not unduly influenced by wind.

If there is not an existing climate station in proximity to the monitoring locations, a new climate station will be installed using a combination of provincial and federal government criteria for properly siting sensor equipment.

Site Status

Blueberry River at Mile 98 Road

This site is within 10 km of the community of Wonowon. The contributing watershed area is 312 km^2. The hydrometric station was installed between August 24 and 26, 2021.

Matrix completed sampling of surface water quality and benthic invertebrates on August 17, 2021, with two members from the Blueberry River First Nations. At that time, Matrix learned the BRFN had already established a monitoring site for benthic invertebrates at this location in 2019 and intend to continue sampling for CABIN at this site with First Nations members who have been trained by CABIN. Nevertheless, for the purpose of the co-ordinated program, Matrix collected benthic invertebrate samples at this site and will share the results of analyses with the BRFN.

Water quality was sampled a second time on October 20, 2021.

Climate data for the Blueberry River site will be sourced from regional climate monitoring stations. Matrix is in communication with the managers of FLNRORD Wildfire Management Branch's wildfire climate stations to see if the Geoscience BC program can support improvement of their Wonowon climate station to serve multiple purposes in 2022 and beyond.

A groundwater monitoring well will be installed on the west side of Blueberry River in late 2021. The site is within a mapped paleovalley associated with Blueberry River. The objectives of drilling a groundwater monitoring well at this site include confirming the presence of a paleovalley, identifying Quaternary aquifers, and monitoring groundwater quality and levels to assess interactions with Blueberry River.

Doig River at Doig River First Nation

Installation of the hydrometric station at this site was completed on August 18, 2021. The contributing watershed area is 2416 km^2. A community meeting was held on October 5, 2021, to discuss the hydrometric program and to conduct a field visit with DRFN members.

Matrix completed sampling of surface water quality and benthic invertebrates at Doig River on August 18, 2021, which coincided with the installation of the hydrometric station. Water quality was sampled a second time on October 20, 2021.

Climate data for the Doig River site will be sourced from regional climate monitoring stations. Matrix is in communication with the managers of FLNRORD Wildfire Management Branch's wildfire climate stations to see if the Geoscience BC program can support improvement of their Osborn climate station to serve multiple purposes in 2022 and beyond.

Alexander Creek at Mile 95 Road

The site is within 15 km of the Halfway River First Nation. The contributing watershed area is 134 km^2. Installation of a hydrometric station was completed at the site on August 19, 2021.

Matrix completed sampling of surface water quality and benthic invertebrates on August 17, 2021, which coincided with the installation of the hydrometric station. Three representatives from HRFN were present at the time of the site visit. Surface water quality was sampled a second time on October 20, 2021.

A new climate station was installed in early November 2021, approximately 1.5 km west of the Alexander Creek monitoring site. The climate station is equipped with sensors to record air temperature, year-round precipitation, snow-water equivalent, wind, relative humidity and barometric pressure.

A groundwater monitoring well will be installed on the west side of Alexander Creek. The site is located within a mapped paleovalley associated with Cameron River. The objectives of groundwater monitoring at this site include confirming the presence and characteristics of the paleovalley, and monitoring groundwater within the paleovalley to assess groundwater interactions with Alexander Creek.

Stewart Creek at Stewart Creek Road

The station is located within the McLeod Lake Indian Band's summer area and south of Stewart Lake. Installation of the hydrometric station was completed on October 15, 2021. The contributing watershed area is 24 km^2.

Matrix did not complete sampling of water quality during the month of August due to site selection and reaching consensus among participants taking longer than expected. However, water quality was sampled on October 21, 2021. Two members of the MLIB arrived on site at the end of the

sampling, but Matrix staff reviewed the sampling procedures they had completed with the First Nations members. No benthic invertebrate sampling was completed at this site in 2021.

A new climate station was installed approximately 0.5 km west of the Stewart Creek monitoring site in early November 2021. The climate station is equipped with sensors to record air temperature, year-round precipitation, snow-water equivalent, wind, relative humidity and barometric pressure.

A groundwater monitoring well will be installed at the Stewart Creek site. The objectives of groundwater monitoring at this site include characterizing the Quaternary geology, identifying Quaternary aquifers, and monitoring groundwater quality and levels to assess interactions with Stewart Creek.

Hulcross Creek at Moberly Forest Service Road

The Hulcross Creek site is located west of the West Moberly and Saulteau First Nations, within the Moberly Lake watershed. The contributing watershed area is 132 km^2. Installation of a hydrometric station at the site was completed on August 25, 2021.

Matrix completed sampling of surface water quality at Hulcross Creek on August 25, 2021. There were no representatives from WFMN or SRFN present at the time of the sampling. Water quality was sampled a second time on October 21, 2021.

Sampling for CABIN data was conducted by Matrix on August 17, 2021; however, due to a location error the work was completed at Dixie Creek, east of Hulcross Creek. Despite the location error, the results of the benthic invertebrate sampling will be shared with SFN and WMFN as it may be of value for other watershed studies.

Climate data for the Hulcross Creek monitoring site will be sourced from publicly available information from Environment and Climate Change Canada's climate monitoring station at the Chetwynd Municipal Airport.

A groundwater monitoring well will be installed at the Hulcross Creek location. The site is near the southern edge of a mapped paleovalley associated with Moberly River. The objectives of groundwater monitoring at this site include confirming the presence of the paleovalley, identifying Quaternary aquifers, and monitoring groundwater levels and quality to assess potential interactions with Hulcross Creek.

Traditional Knowledge

One of the objectives of this project is to include a holistic understanding of First Nation values and First Nations' relationship with water. Extensive conversations were carried out to construct a feasible plan for interacting with the local First Nations and to gather Traditional Knowledge related to water quantity. Special thanks to A. Garibaldi (EMLCI) for her assistance and insights.

Once the scope of this stage of the project was decided upon, a request for proposals was extended. Integral Ecology Group was the successful proponent to gather Traditional Knowledge from selected local First Nations.

At this initial stage, the plan is to visit the monitoring sites with First Nations members three times during the 2022 field season: at low water, high water, and at some point when water levels are moderate. First Nation attendees will be asked for their thoughts, input and stories about the site. Their responses will be gathered and collated into a summary report. The results of this element of the project will be available in late 2022 or early 2023.

The information gained from this pilot project will help form the foundation for understanding how First Nations think about water quantity in northeastern BC. The information may also be used to develop relevant indicators and thresholds for assessing water quantity specifically and water health more generally.

Summary and Next Steps

Work on the program moved forward successfully in 2021 following a one-year setback resulting from the COVID-19 outbreak. The project team was able to successfully engage with all six First Nation communities within the study area, and identified five monitoring locations in collaboration with the First Nation communities.

Hydrometric Study

Hydrometric equipment was installed at each location and is ready to capture spring freshet in 2022.

During the winter of 2021–2022 the data will be assessed for quality assurance and quality control as outlined in the *Manual of British Columbia Hydrometric Standards* (Resources Information Standards Committee, 2018). Data collection at the hydrometric stations will be reinstated in the spring to capture a full open-water season of data, including freshet. As water quantity information becomes available it will be posted for the public to access through the BC Water Portal (www.waterportal.geoweb.bcogc.ca) and the provincial database Aquarius (https://aqrt.nrs.gov.bc.ca).

Groundwater Study

Groundwater monitoring wells will be installed at four locations in late 2021 and equipped with pressure transducers. In 2022, groundwater monitoring will include measuring static water levels, downloading pressure transducer results, and collecting groundwater samples.

Water Quality Study

Water quality was sampled twice during 2021 at most sites (once at Stewart Creek). Water quality will be sampled at each site four times during the open-water season of 2022. The 2022 sampling schedule for benthic invertebrates for the Canadian Aquatic Benthic Invertebrate Network will be determined based on the results of the 2021 suitability assessment and analytical results.

Climate Study

Two climate stations were installed in 2021: at the Alexander Creek and Stewart Creek sites. Publicly available climate data will be downloaded from a climate station located near the Hulcross Creek site. At the Doig River and Blueberry River sites, climate data will be collected by installing new stations in 2022 or upgrading existing wildfire stations.

First Nations Training

Training of First Nations' community members is planned for 2022, to develop skills and facilitate ongoing participation in the program. The training will consist of a classroom-based training session, as well as field-based training during field monitoring. The training will cover hydrometric monitoring, climate station monitoring and maintenance, groundwater monitoring and water quality sampling.

The program team is also exploring future funding options to ensure the monitoring continues past the March 2023 expiration of the Geoscience BC funding.

Acknowledgments

Special thanks to C. van Geloven with the BC Ministry of Forests, Lands and Natural Resource Operations and Rural Development for conducting the peer review, and Geoscience BC for providing the project funding.

References

Environment and Climate Change Canada (2019): Manual of Surface Weather Observation Standards, (MANOBS), Eighth Edition; Monitoring and Data Services Directorate, Meteorological Service of Canada, 187 p., URL <https://www.canada.ca/en/environment-climate-change/services/weather-manuals-documentation/manobs-surface-observations.html> [October 2021].

Johnson, E.J. (2020): Cumulative watershed disturbance model for surface water quality and quantity; report prepared for Regional Stratigraphic Environmental Assessment WATER Working Group for Northeast BC, 32 p., URL <https://doi.org/10.13140/RG.2.2.31708.3164>.

Northeast Water Strategy (2017): A disturbance-sensitivity based approach to prioritizing water monitoring in northeast B.C., Part 1: Report; BC Ministry of Environment and Climate Change Strategy, 119 p., URL <https://www2.gov.bc.ca/assets/gov/environment/air-land-water/water/northeast-water-strategy/disturbance_sensitivity_based_approach.pdf> [October 2020].

Northeast Water Strategy (2018): Surface water quality data summary for northeast British Columbia; BC Ministry of Environment and Climate Change Strategy, 59 p. URL <https://www2.gov.bc.ca/assets/gov/environment/air-land-water/water/northeast-water-strategy/news_ne_wq_summary_2018.pdf> [October 2020].

Resources Information Standards Committee (2018): Manual of British Columbia Hydrometric Standards, Version 2.0, December 2018; BC Ministry of Environment and Climate Change Strategy, Knowledge Management Branch, 160 p., URL <https://www2.gov.bc.ca/assets/gov/environment/natural-resource-stewardship/nr-laws-policy/risc/man_bc_hydrometric_stand_v2.pdf> [September 2021].

Scientific Hydraulic Fracturing Review Panel (2019): Scientific review of hydraulic fracturing in British Columbia; BC Ministry of Energy, Mines and Low Carbon Innovation, 220 p., URL <https://www2.gov.bc.ca/assets/gov/farming-natural-resources-and-industry/natural-gas-oil/responsible-oil-gas-development/scientific_hydraulic_fracturing_review_panel_final_report.pdf> [October 2020].

Sentlinger, G.I. and Metherall, C. (2020): RSEA hydrology and allocation baseline, rev. 0.9.5; unpublished report prepared for Regional Stratigraphic Environment Assessment, 157 p.

Geoscience BC

t: 604 662 4147
e: info@geosciencebc.com

SUITE 1101–750 WEST PENDER ST
VANCOUVER, BC V6C 2T7 CANADA

www.geosciencebc.com